LEVEL III

TECHNICAL REPORT RR-80-3

PROCEEDINGS OF THE WORKSHOP ON MILLIMETER AND SUBMILLIMETER ATMOSPHERIC PROPAGATION APPLICABLE TO RADAR AND MISSILE SYSTEMS, HELD AT REDSTONE ARSENAL, ALABAMA, 20-22 MARCH 1979

Oskar M. Essenwanger
Dorathy A. Stewart
(Editors)
Research Directorate
US Army Missile Laboratory

February 1980

U.S. ARMY MISSILE COMMAND
Redstone Arsenal, Alabama 35809

Approved for public release;
distribution unlimited.

DISPOSITION INSTRUCTIONS

DESTROY THIS REPORT WHEN IT IS NO LONGER NEEDED. DO NOT RETURN IT TO THE ORIGINATOR.

DISCLAIMER

THE FINDINGS IN THIS REPORT ARE NOT TO BE CONSTRUED AS AN OFFICIAL DEPARTMENT OF THE ARMY POSITION UNLESS SO DESIGNATED BY OTHER AUTHORIZED DOCUMENTS.

TRADE NAMES

USE OF TRADE NAMES OR MANUFACTURERS IN THIS REPORT DOES NOT CONSTITUTE AN OFFICIAL INDORSEMENT OR APPROVAL OF THE USE OF SUCH COMMERCIAL HARDWARE OR SOFTWARE.

UNCLASSIFIED

SECURITY CLASSIFICATION OF THIS PAGE *(When Data Entered)*

REPORT DOCUMENTATION PAGE		READ INSTRUCTIONS BEFORE COMPLETING FORM
1. REPORT NUMBER RR-80-3	2. GOVT ACCESSION NO.	3. RECIPIENT'S CATALOG NUMBER
4. TITLE *(and Subtitle)* PROCEEDINGS OF THE WORKSHOP ON MILLIMETER AND SUBMILLIMETER ATMOSPHERIC PROPAGATION APPLICABLE TO RADAR AND MISSILE SYSTEMS		5. TYPE OF REPORT & PERIOD COVERED Technical Report 6. PERFORMING ORG. REPORT NUMBER
7. AUTHOR(s) Dr. Oskar M. Essenwanger and Dr. Dorathy A. Stewart (editors)		8. CONTRACT OR GRANT NUMBER(s)
9. PERFORMING ORGANIZATION NAME AND ADDRESS Commander US Army Missile Command ATTN: DRSMI-RRA Redstone Arsenal, AL 35809		10. PROGRAM ELEMENT, PROJECT, TASK AREA & WORK UNIT NUMBERS
11. CONTROLLING OFFICE NAME AND ADDRESS Commander US Army Missile Command ATTN: DRSMI-RPT Redstone Arsen AL 35809		12. REPORT DATE February 1980 13. NUMBER OF PAGES 183
14. MONITORING AGENCY NAME & ADDRESS *(if different from Controlling Office)*		15. SECURITY CLASS. *(of this report)* UNCLASSIFIED 15a. DECLASSIFICATION/DOWNGRADING SCHEDULE

16. DISTRIBUTION STATEMENT *(of this Report)*

Approved for public release; distribution unlimited.

17. DISTRIBUTION STATEMENT *(of the abstract entered in Block 20, if different from Report)*

18. SUPPLEMENTARY NOTES

19. KEY WORDS *(Continue on reverse side if necessary and identify by block number)*

Millimeter, Submillimeter, Atmospheric Propagation, Dimers, Attenuation, Superradiance, Fog, Water Vapor, Radar, Hydrometeors, Guidance, Terminal Homing, Turbulence, Mobile Measurement Facility

20. ABSTRACT *(Continue on reverse side if necessary and identify by block number)*

A workshop on millimeter and submillimeter wave propagation through the atmosphere was held on 20-22 March 1979 at Redstone Arsenal, Alabama. This workshop served as a forum where scientists in diversified fields exchanged information on the latest results and discussed controversial issues and unresolved problems.

Continued on next page

DD FORM 1 JAN 73 1473 EDITION OF 1 NOV 65 IS OBSOLETE

UNCLASSIFIED

SECURITY CLASSIFICATION OF THIS PAGE *(When Data Entered)*

20. ABSTRACT Continued

The first few papers were concerned with MICOM needs. They specified the operating regions of interest for tactical applications and explained the rationale for the selection of these regions. The Terminal Homing Measurements Program was described.

Several papers discussed absorption by water vapor. Classical theories do not adquately describe the measured absorption in window regions between strong absorption lines. Alternate methods of explaining the discrepancies are to introduce reasonable modifications to existing models of line shapes or to consider the effect of water vapor dimers.

Other effects on atmospheric propagation and instrumentation for measuring these effects were also discussed. Absorption and scattering by hydrometeors, dust and smoke were considered. Additional papers were concerned with terrain effects, turbulence, natural atmospheric emissions, refractivity gradients, and the relatively new method of pulse generation by swept-gain superradiance.

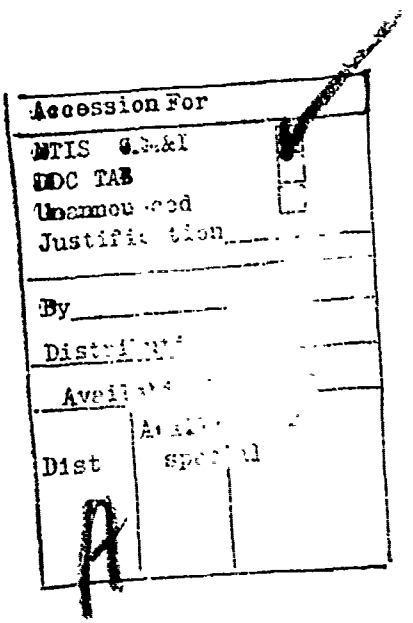

TABLE OF CONTENTS

AUTHORS

PROCEEDINGS OF THE

WORKSHOP ON MILLIMETER AND SUBMILLIMETER ATMOSPHERIC

PROPAGATION APPLICABLE TO RADAR AND MISSILE SYSTEMS

20-22 MARCH 1979

INTRODUCTION

The workshop on millimeter and submillimeter wave propagation which was held on 20-22 March 1979 at Redstone Arsenal (Alabama) served two purposes:

(1) To provide a survey of the present state-of-the-art in a special field which recently has received increased attention by MICOM*, the Army, and DoD.

(2) To furnish a forum where scientists who work in diversified fields with applications to the special topic could come together and exchange information on the latest results, discuss controversial issues or unresolved problems, and stimulate a better cooperation between researchers in this special but narrow field of work.

Thus, these proceedings comprise a mixture between old and new results. The survey papers on the state-of-the-art were largely presented by invited speakers. Other contributions dealt with the most recent results which may not have found their final interpretation at the time of the meeting. The editors feel, however, that they should be included as an exchange of scientific knowledge about ongoing research or experiments to stimulate further progress and reduce duplications in the field of research. Some of the particular topics where solutions are urgently needed were discussed by MIRADCOM* personnel.

Users see some benefits and advantages in systems which operate at millimeter and submillimeter wavelengths. For example, these wavelengths provide better resolution than longer wavelengths and are less sensitive to low visibility conditions than shorter wavelengths. Ideal data would consist of careful systematic measurements at many near-millimeter wavelengths over a period of several years at numerous geographic locations. However, ideal data on propagation and associated atmospheric conditions are seldom available. But research has progressed in recent years as the workshop has proved.

In the first session personnel from the Advanced Sensors Directorate, Technology Laboratory, discuss MIRADCOM* needs. They specify the operating regions of interest for tactical applications and explain the rationale for the selection of these regions. The Terminal Homing Measurements Program is described. Propagation measurement and modeling needs in the areas of battlefield characterization, atmospheric transmission, turbulence, aerosol backscatter, and anomalous effects are presented.

Sessions 2 through 6 deal with the present state of knowledge of millimeter and submillimeter propagation. Absorption by molecular water vapor causes severe attenuation at near-millimeter wavelengths. Wavelengths must be selected to operate in the window regions between strong absorption bands, and classical theories do not adequately describe the measured absorption in window regions. Alternate methods of explaining the discrepancies are to introduce reasonable modifications to existing models of line shapes or to consider the effect of water vapor dimers. Absorption and scattering by hydrometeors such as fog and rain are considered from both theoretical and experimental points of view. Other particles such as dust and smoke are discussed. Additional papers are concerned with topics such as terrain effects, natural, atmospheric emissions, refractivity gradients, and a point of view from a system engineer.

*Effective 1 July 1979 the US Army Missile Research & Development Command (MIRADCOM) combined with the US Army Missile Materiel Readiness Command (MIRCOM) to form the US Army Missile Command (MICOM).

Session 7 includes information about modeling and turbulence. Papers in this session contain models of clear air scintillation as well as adverse weather conditions.

Sessions 8 and 9 are concerned with instrumentation. One paper describes the relatively new method of pulse generation by swept-gain superradiance. The remaining papers provide information about research in atmospheric propagation. Both active and passive systems of measuring propagation characteristics are described. Attention is also given to instrumentation for characterizing the state of the atmosphere.

This collection of papers shows that the workshop accomplished the goals. Information among specialists in diverse fields was exchanged. The discussion included ongoing programs. It is expected that future cooperation fostered by the meeting will reduce duplication of effort and increase the effectiveness of future research. Thus, these proceedings should be useful to scientists in the fields of atmospheric science, physics, engineering and chemistry.

The publication time for these proceedings could have been considerably reduced if all authors had complied with the editors' requested time schedule and the guidelines for manuscripts which were issued.

The editors wish to thank the authors who put considerable effort into the preparation of their manuscripts. Mrs. Clara B. Brooks deserves special thanks for her diligence in the inevitable correcting and the necessary retyping of the manuscripts.

December 1979.

Dr. Oskar M. Essenwanger
Dr. Dorathy A. Stewart

MICOM NEEDS IN MILLIMETER PROPAGATION RESEARCH: INTRODUCTION TO SESSION 1

Mr. William C. Pittman

US Army Missile Command

Redstone Arsenal, Alabama

The subject of this session deserves some explanation. The term MICOM Needs has reference to the Millimeter Propagation Needs to allow the orderly evolutionary development of Army weapon systems using millimeter guidance sensors. The session is therefore framed from the exploratory development perspective. There are of course other sessions of the workshop. Achieving Army objectives in this area will not only require strong emphasis on the immediate needs for exploratory development, but a balanced allocation of resources for fundamental research as well, with special attention to the need to develop improved meteorological and millimeter instrumentation, and suitable calibration standards for this instrumentation. We therefore must not forget that we owe a note of thanks to those far-sighted individuals in the universities, private sector institutions, and Government who have maintained the research base in millimeter and submillimeter technology, often in the face of severe funding constraints, to reach the level of technological maturity we have achieved today.

Mr. Hodgens, the first speaker, will present the rationale for operations at millimeter wavelengths, propagation characterization needs, and three missile guidance concepts, one of which will be described in a film. Mr. Green will then continue with the presentation of concepts for air defense suppression, short range air defense, and indirect fire. Mr. Hodgens will then close the first part of the session with a summary of the propagation needs related to these concepts. Mr. Haraway will then take these needs for his point of departure to present the plans, problems and gaps in millimeter propagation as part of the Terminal Homing Measurements program. Mr. Anderson will summarize the work in optical propagation being done in his group, and outline the opportunities for extending the modeling of propagation from the optical to the millimeter and submillimeter region.

Mr. Robert Haraway, who manages MICOM's Terminal Homing Measurements program, has been a member of the Joint Technical Coordinating Group Subcommittee on Signatures and Backgrounds, and is currently a member of the Steering Committee on the Mobile Millimeter Wave Measurements Facility. Mr. Hammond Green's technical area is Millimeter Terminal Homing Seekers and he is a member of the ARPA Millimeter Guidance Steering Committee. Mr. Tony Hodgens is engaged in in-house independent research on beam encoding techniques for millimeter beamrider, and has been active in establishing the technical foundation of our Millimeter Guidance Program. Mr. Huey Anderson is the technical group leader for the Optical Propagation work at MICOM.

MILLIMETER PROPAGATION NEEDS FOR NEXT GENERATION GUIDANCE CONCEPTS

Tony Hodgens
Augustus H. Green
RF Guidance Technology
Advanced Sensors Directorate
Technology Laboratory
US Army Missile Command

ABSTRACT

Rationale for operation at millimeter wavelengths is presented and the operating regions of interest for tactical applications are specified. Battlefield characterization requirements are discussed and related to the guidance concept development cycle. Based upon present understanding of projected battlefield conditions, a baseline adverse environment has been established. These conditions are presented and related to the need for an upgraded battlefield characterization. Propagation data and modeling requirements are presented with current data base problems outlined. The need for a propagation data handbook is delineated.

1. INTRODUCTION

Successful armor deployment has historically occurred very frequently during periods of adverse weather (fog, rain, snow, etc.). This fact, coupled with the everpresent battlefield contaminants (smoke and dust from artillery rounds and vehicles) as well as the increased propensity of the enemy to use tactical aerosols, has led to an increased emphasis, DoD wide, for weapons systems which will operate in these environments.

Millimeter wavelength sensors offer the potential of improved adverse environment penetration while providing the relatively narrow beamwidths necessary for resolution and suppression of multipath and clutter effects. The rapid development of the state-of-the-art in millimeter wave technology is also expected to support the development of weapons systems operating at these wavelengths.

This paper is limited to atmospheric propagation data needs for support of development of millimeter wave missile guidance concepts. It is recognized that propagation factors represent only one facet of weapons system development. Other effects related to the battlefield scenario such as multipath, clutter, etc., are not addressed.

2. RATIONALE FOR OPERATION AT MILLIMETER WAVELENGTHS

The attenuation due to atmospheric gases, for standard conditions, over the spectral range 1μ to 10 cm wavelength is shown in Figure 1 (Lukes, 1968). From this figure it is evident that even for clear air operation, reasonable values of attenuation are attained only at wavelengths greater than 1 mm or less than 25μ. Figure 2 illustrates the incremental attenuation due to some naturally occurring aerosols over the same spectral range. The rain and cloud models were derived from Deirmendjian (1975). The fog model was derived from Chu and Hogg (1968).

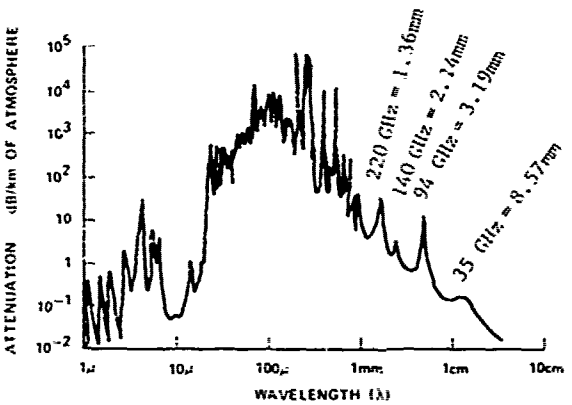

Figure 1. ATTENUATION DUE TO ATMOSPHERIC GASES (Lukes, 1968)

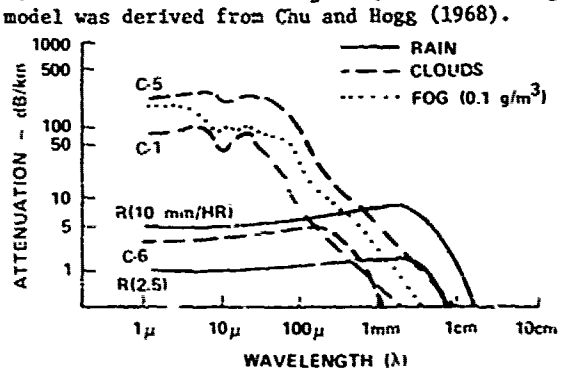

Figure 2. INCREMENTAL ATTENUATION DUE TO NATURALLY OCCURRING AEROSOLS (Deirmendjian, 1975; Chu and Hogg, 1968)

The R(2.5) and R(10) models represent 2.5mm/hr and 10mm/hr rain rates, respectively. The C-5 cloud model represents a heavy stratus cloud, the C-1 cloud model represents a fair weather cumulus cloud, and the C-6 cloud model represents the large droplet component of a nimbostratus cloud. The fog model approximates a 100 meter

visibility radiation fog. For these conditions, successful operation is limited to wavelengths greater than 1 mm.

From a propagation standpoint alone, it would appear that operation at wavelengths greater than 1 cm would be most desirable; however, other factors must be considered. Figure 3 depicts the general trends for atmospheric transmission in adverse weather as well as that for angular resolution.

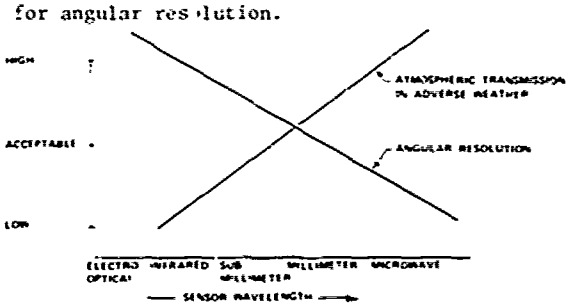

Figure 3. TRENDS - ANGULAR RESOLUTION - TRANSMISSION TRADEOFF FOR ADVERSE WEATHER.

Relatively small beamwidths are required for resolution and the suppression of multipath and clutter effects. From a weapons system standpoint, aperture size is also very important. The millimeter region appears to be the optimum trade between adverse weather transmission and angular resolution. Tables 1 and 2 (Georgia Institute of Technology, 1978) list additional comparisons of the millimeter wavelengths versus the optical, IR, and microwave wavelengths.

TABLE 1. MILLIMETER VS OPTICAL & IR FOR MISSILE GUIDANCE (Georgia Institute of Technology, 1978)

ADVANTAGES	DISADVANTAGES
• IMPROVED TRANSMISSION IN SMOKE AND FOG PROVIDING BETTER LOW VISIBILITY OPERATION	• LOWER RESOLUTION
• HARDER TO JAM - MORE COVERT	• HIGHER CLUTT
• IMPROVED EMP SAFETY	• LACK OF RELEVANT DATA
• POTENTIALLY LOWER COST SYSTEMS	• VIDEO DETECTION MORE DIFFICULT AND LOWER SENSITIVITY
• REDUCED BACKGROUND	• COMPONENT TECHNOLOGY NOT AS ADVANCED
• CAN EMPLOY BOTH RF AND OPTICAL TECHNOLOGY	• SOLID STATE AND TUBE SOURCES ARE CHIRPED LESS MONOCHROMATIC
	• CURRENTLY LARGER AND HEAVIER

Based on the apparent advantages of millimeter wave operation as well as the rapidly advancing state-of-the-art in the technology area, four atmospheric windows in the millimeter region have been designated by MIRADCOM as guidance thrust areas. These regions, as shown in Figure 4, are the 35, 94, 140, and 220 GHz windows.

3. BATTLEFIELD CHARACTERIZATION

Figure 5 depicts a typical guidance concept development cycle. For a given millimeter guidance concept, a characterization of the battlefield, tactical considerations, and the existing propagation data base are all used to estimate effects on system performance. From these efforts additional propagation data requirements are identified.

TABLE 2. MILLIMETER VS MICROWAVE FOR MISSILE GUIDANCE (Georgia Institute of Technology, 1978)

ADVANTAGES	DISADVANTAGES
• HIGHER RESOLUTION	• POOR HEAVY RAIN TRANSMISSION
• REDUCED MULTIPATH	• ATMOSPHERIC CLEAR ABSORPTION IS HIGHER
• LOW OFF AXIS DETECTABILITY	• LARGER RAIN BACKSCATTER
• TRACKING THROUGH PLUMES SHOULD BE IMPROVED	• CURRENT RECEIVER NOISE FIGURES ARE POORER
• COMPONENTS ARE SMALLER ALLOWING MORE COMPACT ONBOARD MISSILE SYSTEMS	• HIGHER PRECISION IN MANUFACTURING REQUIRED FOR COMPONENTS & ANTENNAS
• CLUTTER LOOKS MORE DIFFUSE DOPPLER SHIFT IS GREATER AND CLUTT SHOULD BE LESS	• PRESENT DAY SOLID STATE SOURCE EFFICIENCIES FALLING AS f^2
• BOTH RF AND OPTICAL TECHNIQUES CAN BE EMPLOYED	• POOR SOURCE STABILITY
	• POWER HANDLING CAPABILITY IS INFERIOR IN WAVEGUIDE COMPONENTS
	• CURRENTLY HIGHER COST FOR SYSTEMS

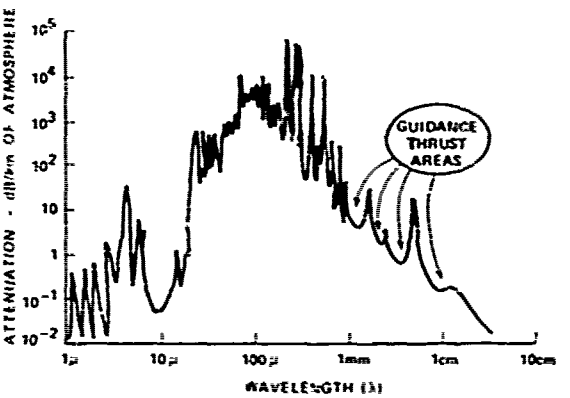

Figure 4. GUIDANCE THRUST AREAS.

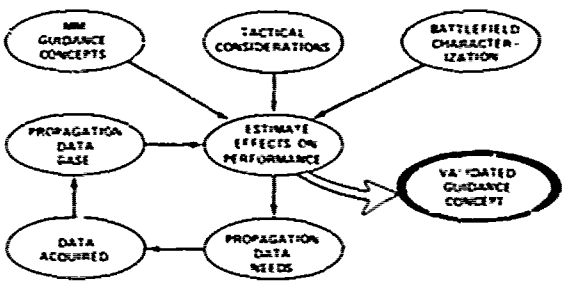

Figure 5. GUIDANCE CONCEPT DEVELOPMENT CYCLE.

As data are collected, the propagation data base is updated and the cycle of performance estimates is continued. This cycle proceeds until validation of the guidance concept. Note that the two items of primary importance are the battlefield characterization and the propagation data base. Both items are in states of continual refinement. The battlefield characterization will vary with projected battlefield locale, weather conditions, and changes in enemy tactics. The battlefield should be characterized as to the probability of occurrence of a given condition (or conditions) to include hours and duration of occurrence. The conditions generally fall into three areas: natural environments, induced environments, and tactical

aerosols. Natural environments include parameters such as rain, fog, snow, humidity, etc. The induced environments are those which are common to all battlefields. These may include debris from artillery rounds, dust dispersed into the atmosphere from tracked vehicles, and smoke from brush fires. Tactical aerosols include smoke and chaff intentionally injected into the atmosphere by the enemy in an attempt to defeat a sensor system.

While all of the required data are not readily available, and also are in a state of continual change, it was nevertheless necessary to establish a set of conditions as a starting point for estimates of system performance. These conditions are stated in Table 3 and are representative of typical central Germany environments. The clear air characteristics are based on the definition of a standard atmosphere.

TABLE 3. BASELINE ENVIRONMENTAL CONDITIONS

CONDITION	CHARACTERISTICS
CLEAR AIR	TEMPERATURE 15° C WATER VAPOR 6 g/m^3 SEA LEVEL
FOG	RADIATION VISIBILITY 100m LIQUID WATER 0.1 g/m^3 WATER VAPOR 9 g/m^3 SEA LEVEL
RAIN	RATE 4 mm/hr TEMPERATURE 14°C WATER VAPOR 13 g/m^3 SEA LEVEL
SMOKE	WHITE PHOSPHORUS CONCENTRATION 0.1 g/m^3 DIAMETER 1.1 MICRON
DUST	CONCENTRATION 2 X 10^{-4} g/m^3 DIAMETER 6-60 MICRON

The fog conditions represent thick, low visibility fogs of the radiation type. This definition encompasses over eighty percent of morning fogs on an annual basis. The rain conditions were chosen to include the 80th percentile seasonal rain and the 90th percentile annual rain. It should be noted that the maximum seasonal rain occurs in July when approximately 30 percent of the days with rain are thunderstorm days. The smoke and dust conditions were based upon previous system studies.

4. MILLIMETER GUIDANCE CONCEPTS

An outline of some of the potential applications of millimeter wavelengths to missile systems operating in adverse environments is presented. A brief description of each system concept is given below in order to illustrate the different types of propagation paths and problems that might be encountered.

4.1 Direct Fire Anti-Tank

Figure 6 illustrates the operation of a beamrider missile system. Target tracking is established with a precision tracking/guidance beam once the radar has been cued by an adjunct acquisition device. The missile is launched and immediately acquired by a broad concentric capture beam. An onboard rearward looking receiver intercepts and decodes the spatially coded beam and processing electronics interprets the missile position within the beam to generate guidance commands. The missile is guided toward the radar line-of-sight until it acquires the precision tracking/guidance beam. The missile decodes the precision guidance beam in the same fashion and flys the line-of-sight of the precision beam to the target. The pointing beam is used to both track the target as well as provide guidance information to the missile.

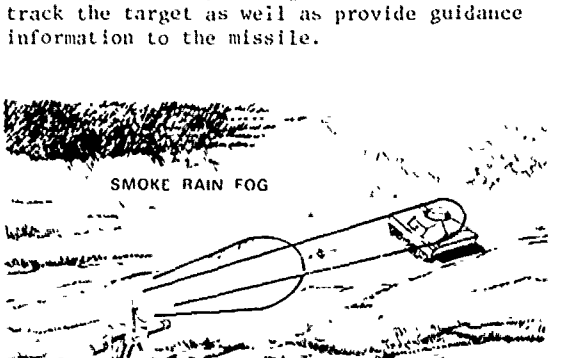

Figure 6. BEAMRIDER GUIDANCE.

Figure 7 depicts a form of command guidance referred to as differential guidance. Here the radar tracks both the target and the missile and determines their angular displacements from the radar boresight. The radar measures ϕ_1 and ϕ_2 (reference Figure 7) and based on their vector difference determines ϕ_3, the required correction for the missile to fly the target line-of-sight. Note that this concept, as opposed to the beamrider, does not require that the radar boresight remain on the target.

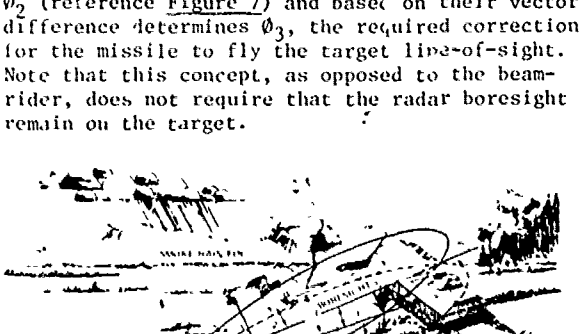

Figure 7. DIFFERENTIAL GUIDANCE - CLOS.

Both the beamrider and the differential guidance concepts have similar propagation paths, i.e., near earth, relatively horizontal paths.

4.2 Indirect Fire

Figure 8 is illustrative of attacking armored vehicles from essentially a vertical approach and, because the target may be beyond line-of-sight, the missile must operate autonomously. This system concept is called indirect fire. A missile or missiles can be delivered to some point in space at which target search begins following required maneuvers to stabalize the missile and to attain the necessary velocity for the missile to perform its functions. A radar beam is transmitted to search a specified ground area for the desired target. Upon detection and acquisition, a stable line-of-sight is generated to provide the necessary information to maintain track and guide the missile to impact. In the terminal phase a radiometric mode may be used to achieve a centroid aimpoint. Since the missile must perform during conditions of smoke, medium to heavy fog, rain and haze, propagation phenomena must be well understood for the near vertical trajectories which are not normally encounted for most system applications.

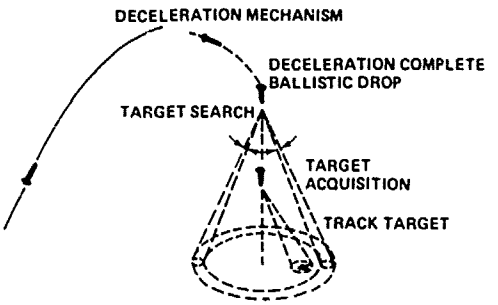

Figure 8. INDIRECT FIRE SYSTEM CONCEPT.

4.3 Dual Mode RF/RF Air Defense Suppression.

Figure 9 depicts an operational concept for a dual mode RF/RF Air Defense Suppression missile. In this concept an attack helicopter detects radiation from an air defense system which is a potential threat. Information is generated which locates the threat and cues a missile to the proper coordinates. The missile detects the radiation from the threat and after lock is established, is launched toward the target. Since most air defense systems operate within the microwave region, the missile performs its search, detect, acquire and initial tracking functions using the target's radiated energy. The missile will transfer to tracking operation within the millimeter region when accurate terminal tracking is required or when the threat "turns off" its radiation. It is conceivable that a passive radiometric mode could be used to achieve a centroid aimpoint. This particular system concept would utilize propagation paths similar to that for direct fire guidance.

4.4 Missile Fire Control

Figure 10 is a conceptual drawing for implementation of a fire control system operating within the millimeter spectrum.

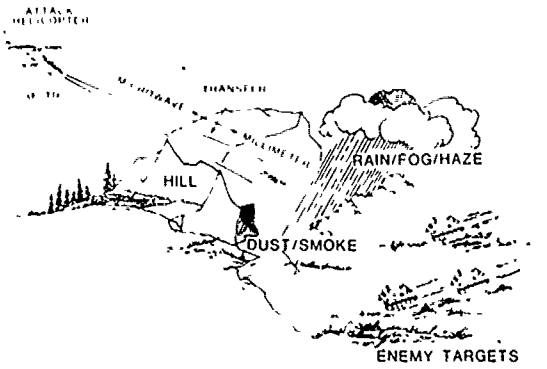

Figure 9. DUAL MODE RF/RF AIR DEFENSE SUPPRESSION.

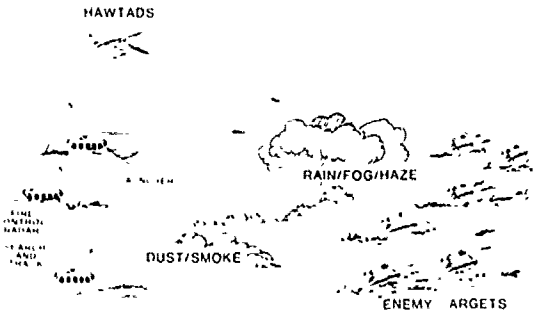

Figure 10. FIRE CONTROL SYSTEM.

For the type of systems shown, the effectiveness will be limited to ranges of less than ten kilometers because of atmospheric attenuation effects upon millimeter wavelengths. However, the advantage of this spectrum is the resolution gained by the shorter wavelengths and the penetrability through adverse environments when compared with optical systems. The fire control system may be either airborne or ground based. In the airborne case, the fire control system may be totally self contained within the weapon system wherein the system provides not only target position coordinates but also identifies the target or targets to be attacked. Similarly for the ground based case, the fire control radar assumes total control over separate launches which receive firing commands from the fire control radar. As a third option, an airborne and ground based system would be integrated to provide more flexibility for control of the battlefield.

4.5 Short Range Air Defense

Figure 11 illustrates a short range air defense system using millimeter wavelengths for the target acquisition/tracking radar. During periods of adverse environments on the tactical battlefield, these wavelengths can penetrate through obscurants when optical systems cannot provide the required performance. The radar searches, detects, acquires and tracks

these targets which are of a threat to the defense forces. The fire control system, which may be an integral part of the radar, determines which targets are most threatening and commands missiles to be launched against specified targets. The propagation paths will usually be over short ranges (less than 10 kilometers) and for depression angles generally less than 45 degrees.

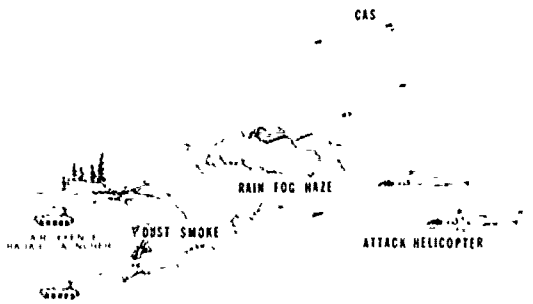

Figure 11. SHORT RANGE AIR DEFENSE.

5. PROPAGATION DATA NEEDS - MILLIMETER GUIDANCE SYSTEMS.

All of the system concepts discussed in the previous section generally have the same requirements as to atmospheric propagation data needs. The major differences in the data requirements lie in the propagation paths for the various systems. No attempt is made herein to emphasize one set of requirements as they will be system peculiar.

Table 4 outlines the perceived propagation needs from the system developer's standpoint. For convenience, the requirements have been grouped into five areas: aerosol backscatter, atmospheric and aerosol attenuation, anomalous absorption phenomena, turbulence effects, and atmospheric transmission/scattering models. For each category, the desired effort is listed along with a summary of current data base problems.

The data base deficiencies outlined for each category have several common elements. Experimental data are limited or nonexistent in all areas; this is particularly true at the higher frequencies of interest. There is a distinct lack of data in Central European type environments. For many of the reported measurements, insufficient recording of meteorological parameters is a vital factor which may explain some of the data variability. Aerosol particle size distribution measurements are also lacking; these data are necessary as precipitation rates alone do not provide adequate data correlation. Few measurements have been performed to examine the effects of various depression angles on millimeter wave propagation.

Specific data needs lie in the area of turbulence, anomalous absorption, temperature/humidity effects, and modeling.

A recent study (Collins, 1978) performed for MIRADCOM was inconclusive as to the severity of turbulence effects on a millimeter beamrider system; also the combined effects of turbulence and water vapor inhomogeneities are not presently understood.

Many experimental observations (Liebe, 1978) have confirmed the existence of anomalous absorption effects. This term is generally used to describe absorption effects that currently cannot be explained with the existing oxygen and water vapor absorption theory. This phenomenon has been frequently observed under various conditions, particularly at high humidities and low temperatures. Currently no unified treatment of the problem exists that has a physical basis.

No set of measurements of absorption due to water vapor as a function of temperature and composition sufficient to constitute a reliable guide for extrapolation of the values to significantly different conditions exists. This is especially true near saturation. The relative humidity is greater than 95% during heavy fog (Middleton, 1963) and is typically 80% or higher during rain.

Modeling efforts to date appear to be very specialized, applying only to specific conditions. Model validations cannot occur until the experimental data base has been expanded.

Currently, when the system developer requires particular propagation information, a thorough literature search must be performed which requires the expenditure of considerable time. A suggestion is therefore made for the preparation of a millimeter propagation handbook. The objective of this handbook would be to compile existing propagation data in a manner easily accessible by personnel involved in systems analysis, design and use. The approach would entail the establishment of an indexing system for general subjects, each followed by specific categories of effects. The handbook should be updated on an annual basis. Figure 12 illustrates a table of contents and a typical page from such a handbook.

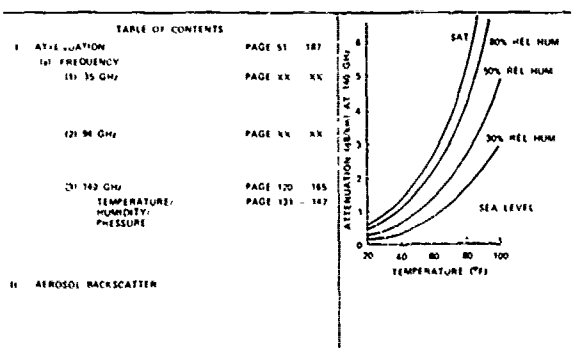

Figure 12. MILLIMETER PROPAGATION HANDBOOK - EXAMPLE.

TABLE 4. PROPAGATION DATA NEEDS - MILLIMETER GUIDANCE SYSTEMS

ITEM	DESIRED EFFORT	CURRENT DATA BASE PROBLEMS
• AEROSOL BACKSCATTER	• PROVIDE ACCURATE DATA BASE TO DETERMINE ENERGY RETURN THAT MAY CAUSE TARGET MASKING • ANALYSIS NEEDED AS A FUNCTION OF PARTICLE SIZE DISTRIBUTION, PRECIPITATION RATE POLARIZATION, DEPRESSION ANGLE AND METEOROLOGICAL CONDITIONS	• LIMITED EXPERIMENTAL DATA • MUCH OF DATA NOT ADEQUATELY CHARACTERIZED • LACK OF DATA IN CENTRAL EUROPEAN ENVIRONMENT
• ATTENUATION	• DEVELOP ATMOSPHERIC TRANSMISSION DATA BASE • MEASUREMENTS IN CLEAR AIR UNDER VARIOUS TEMPERATURE HUMIDITY CONDITIONS PROVIDE ANALYSIS OF TEMPERATURE/HUMIDITY EFFECTS • MEASUREMENTS IN RAIN FOG, SNOW, SMOKE AND DUST WITH PARTICLE SIZE DISTRIBUTIONS CHARACTERIZED • SUPPORTING METEOROLOGICAL DATA WITH MEASUREMENTS • MEASUREMENTS AT VARIOUS DEPRESSION ANGLES	• CLEAR AIR EXPERIMENTAL DATA HIGHER THAN PREDICTED BY THEORY • TEMPERATURE/HUMIDITY EFFECTS NOT WELL UNDERSTOOD FEW MEASUREMENTS • LIMITED RAIN, FOG, SNOW DATA • AEROSOL PARTICLE SIZE DISTRIBUTIONS NOT CHARACTERIZED • INSUFFICIENT METEOROLOGICAL DATA
• TURBULENCE EFFECTS	• DETERMINE EFFECTS OF TURBULENCE AS A FUNCTION OF FREQUENCY • PROVIDE DATA AS A FUNCTION OF ATMOSPHERIC CONDITIONS • DETERMINE ATTENUATION PHASE VARIATION, FADING EFFECTS AND FREQUENCY OF FLUCTUATION • PROVIDE CAPABILITY TO MEASURE FLUCTUATION RATES AS HIGH AS 50 Hz • ANALYZE DATA TO ESTABLISH ORIGIN OF FLUCTUATION EFFECTS	• NO EXPERIMENTS PERFORMED TO CHARACTERIZE TURBULENCE AND ITS EFFECTS ON MILLIMETER PROPAGATION • RECENT THEORETICAL STUDIES INCONCLUSIVE AS TO SEVERITY OF TURBULENCE EFFECTS • COMBINED EFFECTS OF TURBULENCE AND WATER VAPOR INHOMOGENEITIES NOT UNDERSTOOD
• ANOMALOUS ABSORPTION EFFECTS	• ESTABLISH VALIDITY OF ANOMALOUS ABSORPTION EFFECTS • DETERMINE ATTENUATION TIME EXTENT OF ABSORPTION ATMOSPHERIC CONDITIONS FLUCTUATION EFFECTS STATISTICS OF OCCURRENCE, SEASONAL OCCURRENCE AND VARIATION AS A FUNCTION OF TIME OF DAY • PERFORM BOTH MONOCHROMATIC AND BROAD BAND MEASUREMENTS • PROVIDE ANALYSIS ON SOURCE OF ANOMALOUS EFFECTS	• ABSORPTION IN WINDOW REGIONS OFTEN HIGHER THAN PREDICTED BY THEORY - ESPECIALLY UNDER HIGH HUMIDITY CONDITIONS • NO UNIFIED TREATMENT OF THE PROBLEM EXISTS THAT HAS A PHYSICAL BASIS
• ATMOSPHERIC TRANSMISSION SCATTERING MODELS	• TRANSMISSION/SCATTERING MODELING IN MM WINDOW REGIONS • CHARACTERIZATION IN CLEAR AIR AND IN THE PRESENCE OF AEROSOLS • ANOMALOUS ABSORPTION EFFECTS TO BE EMPLOYED WITH AEROSOL MODELS AND METEOROLOGICAL PARAMETERS	• LIMITED DATA BASE

REFERENCES

Chu, T. S. and D. C. Hogg, 1968: Effects of precipitation on propagation at 0.63, 3.5, and 10.6 microns. The Bell System Tech. J., 47, 723-759.

Collins, S. A., Jr., 1978: Scientific Services on the Effects of Atmospheric Turbulence on Millimeter Transmission. Scientific Services Agreement D. O. No. 0684, Army Research Office, Battelle - Columbus Laboratories, Durham, North Carolina 27707, August 1978.

Deirmendjian, D., 1975: Far Infrared and Submillimeter Wave Attenuation by Clouds and Rain. Rand Corporation Report P-5419, April 1975.

Georgia Institute of Technology, 1978: Published material for Georgia Institute of Technology short course in Millimeter Wave Systems and Technology.

Liebe, Hans J., 1978: Millimeter Wave Attenuation in Moist Air-Laboratory Measurements and Analysis. Research Proposal Submitted to US Army Research Office. Institute for Telecommunication Sciences, Boulder, Colorado, 80303, December 1, 1978. Contract ARO-30-79 has been awarded to Dr. Liebe.

Lukes, G. D., 1968: Penetratability of Haze, Fog, Clouds and Precipitation by Radiant Energy Over the Spectral Range 0.1 Micron to 10 Centimeters. The Center for Naval Analyses of the University of Rochester, Rochester, New York, Report No. 61, May 1968.

Middleton, W. E. K., 1963: Vision Through The Atmosphere. University of Toronto Press.

TARGET AND ENVIRONMENTAL MEASUREMENTS PROGRAM: MILLIMETER WAVE PROPAGATION PLANS, PROBLEMS, AND GAPS

Robert C. Haraway
US Army Missile Command
Redstone Arsenal, Alabama

ABSTRACT

The following is a brief overview of the Measurements Program in Advanced Sensors Directorate, Technology Laboratory, MICOM, as it relates to the problem of assessing environmental effects on sensor guidance systems. This program is conducted in close coordination with the research and development of guidance sensors and is designed to meet sensor development requirements for target and environmental characteristics.

1. INTRODUCTION

This program was established during the Exploratory Development phase of Army laser guidance systems. At that time, there was serious concern at all levels of Army R&D management for the effects of the tactical environment on laser guided systems. The Measurements Program focused primarily on the laser guidance problem for the first one to two years. During that time, the technology for infrared and millimeter-wave land combat guidance sensors was developing rapidly and it became obvious that these sensor development programs also required data on targets and environmental effects. The program was therefore expanded to include the characterization of targets and environmental effects in the infrared and millimeter-wave spectral regions. The program objective is the development of a data base and the definition of the technology required for development of land combat guidance sensors which will maintain acceptable operational capabilities under adverse tactical conditions, including smoke, dust, adverse weather, background clutter and false targets.

2. PROGRAM FUNCTIONS

The functions involved in the conduct of the program are depicted in Figure 1. In general, the effort has been about evenly divided between in-house and contract support. Typically, a measurements project or task is defined in-house, and a Measurements Plan and Scope of Work are prepared. This is followed by the selection and installation of instruments in the field, on towers, or aboard a special measurements helicopter. Data are then collected and analyzed on a quick-look basis to insure data quality and avoid excessive data collection and duplication. In-depth data analysis may be accomplished either in-house or on contract. Frequently, contracts are also employed to provide technical support for the development sensors or seekers used as measurement instruments.

Resulting data and analyses from the program are issued through technical reports which are distributed to the R&D community directly and through the Defense Documentation Center, and the Guidance and Control Information and Analysis Center (GACIAC).

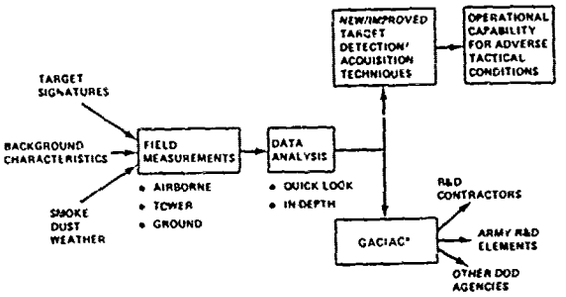

Figure 1. Measurements program.

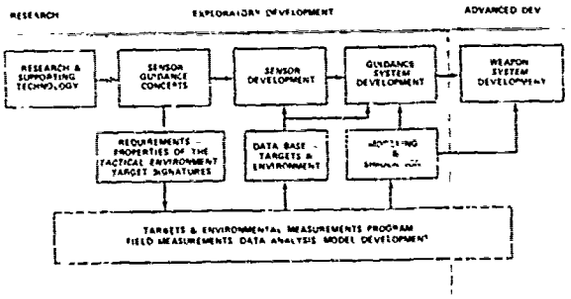

Figure 2. Sensor/guidance development-measurements interface.

3. SENSORS DEVELOPMENT/MEASUREMENT INTERFACE

From the beginning, the Measurements Program has been closely interrelated with the MICOM Sensor Development Program for weapons guidance applications, as illustrated in Figure 2. As early as possible in the sensor development process, the requirements of the anticipated tactical environment are identified and field measurements initiated to provide data on those effects which ultimately determine system performance. The program therefore provides a data base for sensor design and development,

art later for modeling and simulation in the prediction of sensor guidance system performance.

To further emphasize the close working relationship between the Measurements and Sensor Development Programs, it should be pointed out that developmental sensors are frequently used for measurements instrumentation. The use of developmental sensors offers the advantage that the resulting data represent state-of-the-art sensor performance capabilities.

4. TACTICAL PROBLEMS AND OBJECTIVES

The general scope of the program is illustrated in Figure 3. It will be noted that this effort is designed to address the broad Science and Technology (S&T) Objectives contained in the Army Science & Technology Objectives Guide. These objectives call for weapons capabilities in battlefield environments, including adverse weather, smoke and dust.

Although this chart indicates primary activity at millimeter frequencies up to and including 94 GHz, there is also major interest in the higher millimeter frequencies, particularly for guidance applications such as beam-rider, where high-resolution antenna beam patterns are required.

Up to the present time, the program emphasis has been primarily in two areas: the characterization of targets and background, and the measurements of smoke and dust effects on laser and infrared sensor guidance. With accelerated efforts on development of millimeter guidance sensors, the program will include increased emphasis on assessment of millimeter wave propagation capabilities in adverse environments.

5. DEFINING PROPAGATION TASK OBJECTIVES

As noted earlier, the Measurements Program efforts have been based on the anticipated tactical environment for guidance systems under development, in support of the MICOM R&D mission. Consistent with this approach, in defining objectives for millimeter propagation work to be accomplished, we must begin with an examination of current guidance systems concepts. Other papers in this session outline these concepts and the related needs for propagation research and analysis. It appears now that the initial task is that of defining the various areas of work required, in a priority order directly related to the atmospheric effects most likely to limit systems performance. To illustrate, Figure 4 shows the various tactical geometries associated with systems under investigation. These various systems applications involve propagation paths which vary from the horizontal near-earth, to those with vertical incidence angles. Associated with these systems concepts are design objectives, including target detection and acquisition ranges, which are dependent on weather and other environmental conditions. Other objectives include beam pointing, resolution, and tracking capability, which may be affected by turbulence, which in turn may exhibit a dependence on the propagation path angle of incidence. Other examples relating propagation effects to guidance applications could be suggested, but the point to be made here is that we need to determine what the most significant effects on system performance will be, as early in development programs as possible.

6. PROGRAM PLANNING

It is known that various atmospheric effects may degrade millimeter systems performance. Preliminary plans include the following:

a. PROPAGATION MEASUREMENTS THROUGH VARIED WEATHER CONDITIONS
   (1) MULTIPLE WAVELENGTHS (35/94/140/220/340 GHz)
   (2) COMPARATIVE PERFORMANCE
   (3) AS A FUNCTION OF GUIDANCE GEOMETRY
   (4) VARIOUS GEOGRAPHIC ENVIRONMENTS

b. SMOKE, DUST MEASUREMENTS

c. COMBINED EFFECTS

d. SYSTEM-RELATED EFFECTS (MULTIPATH, EXHAUST PLUME EFFECTS)

GUIDANCE SENSOR	TARGET DETECTION & DISCRIMINATION	BATTLEFIELD SMOKES, HAZE, DUST	ADVERSE WEATHER	S&T OBJECTIVES
LASER (1.06 MICRONS & 10.6 MICRONS)	TARGET REFLECTANCE OF US & FOREIGN ARMOR. BACKGROUNDS & FALSE TARGETS. DESIGNATOR & SEEKER MEASUREMENTS	SMALL SCALE FIELD EXPERIMENTS SUPPORT TACTICAL SCALE FIELD TESTS. SMOKE/DUST MODELING	NIGHT/FOG ATMOSPHERIC PROPAGATION MEASUREMENTS. ATMOSPHERIC MODELING ANALYSIS	CLOSE COMBAT CAPABILITIES: HELICOPTER BORNE MISSILES ANTI-TANK MISSILES
INFRARED (3-5 MICRONS & 8-14 MICRONS)	TARGET SIGNATURES OF US & FOREIGN ARMOR BACKGROUNDS & FALSE TARGETS SEEKER MEASUREMENTS	SAME - WITH 3-5 & 8-14 MICRON THERMOVISION & SEEKER SENSORS	SAME - WITH 3-5 & 8-14 MICRON THERMOVISION & SEEKER SENSORS	FIRE SUPPORT CAPABILITIES INDIRECT FIRE PRECISION MUNITIONS INDIRECT FIRE MISSILES
MICROWAVE/ MILLIMETER (20 GHz, 35 GHz, 70 GHz, 94 GHz)	TARGET SIGNATURES OF US & FOREIGN ARMOR BACKGROUNDS & FALSE TARGETS. SEEKER MEASUREMENTS	SAME - WITH 35 GHz & 94 GHz SEEKER SENSORS.	MET. DATA TAKEN ON 35 GHz & 94 GHz TOWER & AIRBORNE SENSOR EXPERIMENTS 35 GHz RADAR DETECTION & DISCRIMINATION EXPERIMENTS	

Figure 3. Tactical problems and objectives.

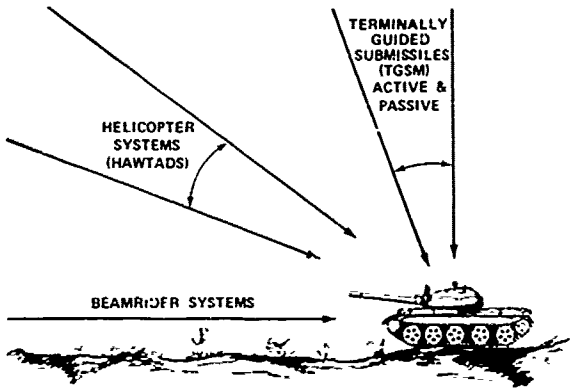

Figure 4. Propagation path geometries.

They are exploratory in nature, and intended to initially assess the spectral bands indicated for the various system applications being considered. Initial plans call for comparative measurements at multiple frequencies over the same propagation path, and under near simultaneous conditions. Other measurements will deal with the effects of guidance geometry, as sensor instrumentation becomes available. The collection of data in multiple spectral bands, for widely separated geographic locations has not been considered feasible in the past. However, the current development of an Army mobile measurements facility, will offer this capability. This facility is covered in more detail by other papers in this proceedings, e.g., session 9.

Smoke and dust measurements will be conducted at Redstone Arsenal and also in conjunction with large-scale Army experiments on specially-instrumented ranges. These normally include a wide range of laser and infrared instrumentation, and millimeter capabilities will be added as available. Combined effects refers, for example, to the combination of certain smokes and high humidity, which may be more severe than smoke in a dry environment.

Finally, there are system related effects which must be evaluated under carefully controlled conditions.

7. PROBLEMS

One problem which has severely limited thorough investigation of millimeter propagation effects on guidance systems has been the lack of availability of millimeter instrumentation for necessary measurements, particularly at the shorter wavelengths. Propagation measurements for assessing the effects of varied weather conditions require the commitment of instrumentation for extended periods of time, and of course require sensitive, stable equipment. Current millimeter instrumentation development efforts within the Army will probably alleviate this problem.

Similarly, there has been a problem in the availability of meteorological instrumentation for characterizing weather conditions of particular concern in tactical systems application, including fogs and light to moderate rain. Contributing to this problem has been the interest in collecting data at several stations along a propagation path rather than only at one location.

System-related priorities refers to the problem of determining or defining those propagation effects which are most critical in terms of proposed systems applications. In other words, we need to know as early as possible of tactical limitations imposed on proposed systems by certain weather conditions, in order to evaluate the potential usefulness of such systems.

The development of useful models for the various weather conditions of tactical interest, which are needed for realistic systems simulation, is viewed here as a problem. Actually, the development of such models will depend on the acquisition of an adequate data base representative of the weather conditions of interest. The problem anticipated with modeling is that of defining sets of "typical" conditions which are of reasonable size yet cover a realistic range of real-world situations.

The design of experiments is considered here as a problem, from the viewpoint that efficient, careful planning of field experiments is essential in order to achieve an assessment of planned Army guidance systems capabilities on a timely basis.

EXTENSION OF ENVIRONMENTAL MODELLING FROM THE OPTICAL THROUGH THE MM REGION

H. Anderson
US Army Missile Command
Redstone Arsenal, Alabama

Abstract and manuscript not available.

A SURVEY OF MILLIMETER RADIO AND SUBMILLIMETER RADIO WAVE PROPAGATION

Archie W. Straiton
Electrical Engineering Research Laboratory
The University of Texas at Austin
Austin, Texas

ABSTRACT

The transition in the use of radio wavelengths longer than a few centimeters to those of millimeter and shorter lengths creates additional transmission and reflection problems. This paper will discuss the effects of the length of these waves approaching (1) the resonant wavelengths of atmospheric gases, (2) the size of raindrops and other particulate matter, and (3) lengths very small compared to nearly all radar targets of interest.

1. INTRODUCTION

It is a pleasure to see the increasing interest in the transmission of millimeter radio waves through the atmosphere. Studies in this field have provided new insight into the area of the electromagnetic spectrum.

Table 1 appeared in Barrow (1938), Light, Photometry and Illuminating Engineering It gives a description of the electromagnetic spectrum with an undefined gap between 10^9 Hz and 6×10^{11} Hz.

Form of Energy	Hertz
Wireless telegraph wave	10^5 to 10^7
Hertzian waves	10^7 to 10^9
Infrared rays	6×10^{11} to 4×10^{14}
Visible light	4×10^{14} to 7.7×10^{14}
Ultraviolet light	7.7×10^{14} to 3×10^{15}

Frequency of Energy

Table 1

Even in 1961 an encyclopedia defined the lower frequency limit of infrared as being indefinitely defined but extending to approximately 350 microns (0.35 mm) which was the limit where heat measuring techniques could still be used.

This defined infrared as the region where it was possible to use incoherent heat measuring instrumentation while the radio wave region was where it was possible to use radio instrumentation. The mysterious region in Table 1 between 10^9 Hz (30 cm) and 6×10^{11} Hz (0.5 mm) was a region which could not be studied by either approach.

The title of this meeting and the papers included show that the barrier between radio and infrared waves has been broken by approaches from both sides. The developments of the laser and of the microwave bolometer have made obsolete the definitions based on coherent and incoherent systems.

The advances which have been made in understanding and using wavelengths between 0.1 mm and 1.0 mm have left us in a state of confusion for a simple name for this band. Such titles as millimeter waves and beyond, submillimeters, or far-infrared are not very specific and add more confusion when we speak of wavelengths less than 0.1 mm.

We have about run out of superlatives for radio bands when we call dekameter waves "high frequency", meter waves "very high frequency", decimeter wave "ultra high frequency", centimeter waves "super high frequency", and the millimeter waves "extreme high frequency". It is hard to top ultra, super and extreme.

There does not seem to be an accepted word for 10^{-4}. My suggestion is that of dropping to the micron (10^{-6} m) as a base and

calling the bands above 300 GHz as shown in Table 2.

Band	Frequency (terahertz)	Wavelength (meters)
hectomicron	0.3 to 3	10^{-4} to 10^{-3}
dekamicron	3 to 30	10^{-5} to 10^{-4}
micron	30 to 300	10^{-6} to 10^{-5}

Title for Bands with $\lambda < 1$ m m

Tab.e 2

The previous comments indicate that the spectrum under discussion at this meeting has some of the properties of radio waves and some of infrared.

Starting from the lower frequencies three effects of the reduction in wavelength from those in more conventional radio use receive the greatest attention and will be reviewed briefly. These are (1) the interaction of the millimeter and hectomicron waves with the molecular rotation energy states of oxygen and water vapor, (2) the absorption and scattering by water drops, snow flakes and other solid particles in the atmosphere and (3) a change in the type of interaction with surfaces including antennas, ground, trees, buildings, targets, etc. whose dimensions become very large compared to the wavelength.

2. INTERACTION WITH ATMOSPHERIC GASES

Two types of molecules have interaction with radio waves. Some molecules including water vapor have a permanent electric dipole and others including oxygen have magnetic dipoles. A very simplified model is that of a spinning baton with fixed charge separation or fixed magnetic poles.

By quantum theory, each mode of rotation is associated with a certain energy level. Changes from lower to higher energy levels occur when an electromagnetic frequency associated with the energy change falls on the spinning molecule. The process is reversed when an unbalance in the upper energy population levels causes the spin to revert to a lower level and the molecule to radiate energy at a frequency near the resonant absorption one.

At very low pressures the interaction of a polar molecule and an electromagnetic field tends to be limited to a series of very narrow bands of frequencies. Some broadening at very low pressures is caused by doppler effects of the spinning molecule and two closely spaced peaks instead of one will appear in the presence of a magnetic field. This later situation is found in the upper atmosphere but is of no consequence near the earth.

At very low pressures, saturation of the molecules in the higher levels may result in a reduction of the energy absorption rate. Charles Tolbert of our laboratory checked this effect at 4.3 millimeters by measuring the atmospheric attenuation during the day using solar radiation and during the night using lunar radiation. He found no difference within the accuracy of measurements.

At pressures near ground level the only important source of line broadening is the collision of molecules. A line width is defined by the difference between the two frequencies at which the absorbed power is reduced to one half of the peak value. This line width is primarily dependent on the pressure, the temperature and the gas mixture.

In the laboratory the line width factor, the resonant frequency and peak attenuation can be measured with precision. The extrapolation of the low pressure measurements to the far wings of the absorption lines has resulted in some discrepancy between absorption as calculated from the line width factor determined at low pressure and the loss found under actual field data.

Fig. 1 shows the center frequencies between 10 and 300 GHz of gases commonly found in the atmosphere. Twenty-one oxygen

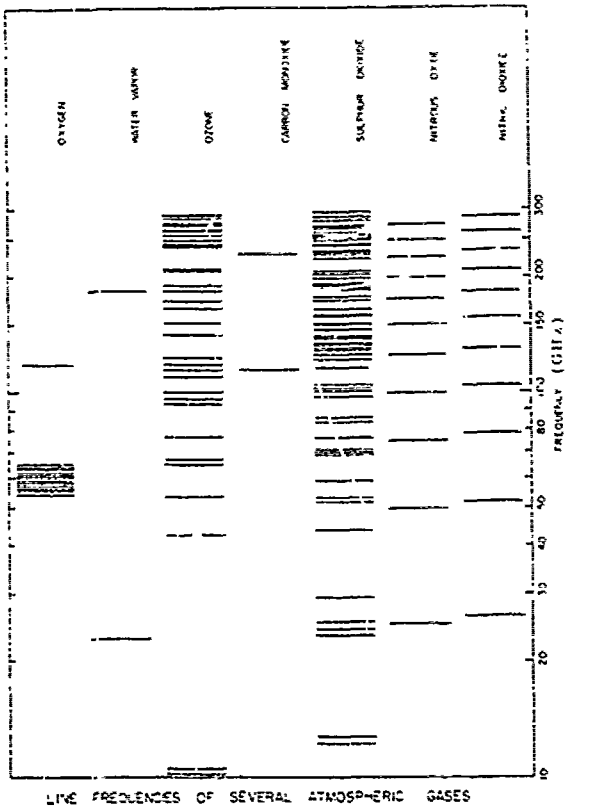

LINE FREQUENCIES OF SEVERAL ATMOSPHERIC GASES

FIG 1

lines are clustered between 5 to 6 mm and one falls at 2.5 mm. One water vapor line is at 22 GHz and one at 173 GHz. Hundreds of other water vapor lines are in the 1 to 1000 micron region. Ozone effects are limited to higher elevations and the ozone density is not enough to cause appreciable attenuation. The other gases shown are in small enough amounts so that they are not major contributors to radio transmission loss under usual conditions.

Recently our millimeter radio astronomy observatory at McDonald Observatory in West Texas was able to detect a CO layer in the upper atmosphere at the 230 GHz line. The radiation received from the sun around 230 GHz as a function of frequency is shown in Fig. 2. The receiver used had

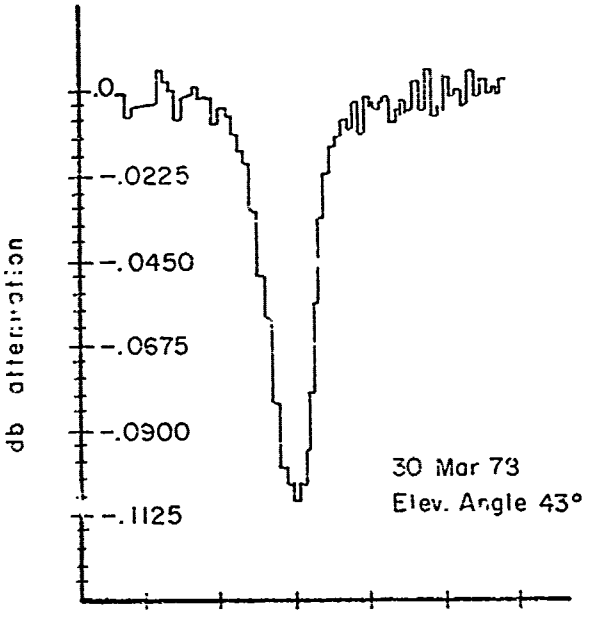

Solar Radiation Absorption by CO

Fig. 2

128 filters each with a bandwidth of 100 kilohertz. From the half power bandwidth the height of the layer was estimated to be approximately 50 km. The line was also measured in emission with the peak replacing the minimum at the line center.

The absorption as a function of frequency is given in most papers on millimeter waves either in terms of the loss per kilometer at sea level or the loss on a vertical path from sea level to outer space. These usually assume a standard atmosphere which may or may not be a good representation for a given geographical location and time. A plot of sea level attenuation has the same general features but with different units and numbers compared to the loss on a vertical path.

Many groups have shied away from using frequencies near the first water vapor line at 22 GHz but for many purposes such as satellite communication, its gas loss would not be a major deterent.

The three windows in the millimeter band between the peaks of the absorption lines provide ranges of frequencies over which the attenuation has relatively low values. Since water vapor density changes with time and location, it is difficult to say that one particular frequency in the window as around 90 GHz is optimum without taking into account the mean water vapor density. The intensity and width of the lines can be studied conveniently in the laboratory where temperature and pressures may be controlled. Tolbert et al. (1964) and Schulze and Tolbert (1963) reported studies made in a 15 cm diameter tube 152 meters long.

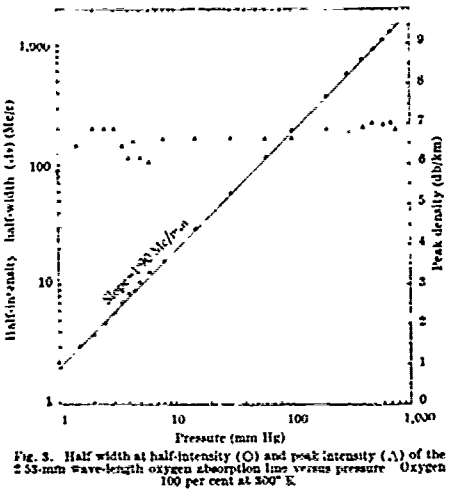

Fig. 3. Half width at half-intensity (O) and peak intensity (Δ) of the 2.53-mm wave-length oxygen absorption line versus pressure. Oxygen 100 per cent at 300° K.

Figure 3 from their work shows the dependence of line width and of the maximum attenuation on pressure. Note that the linewidth is linearly dependent on pressure and the maximum attenuation factor remains essentially constant as the pressure is reduced to about 2 mm Hg.

The precision measurements attained in the laboratory are not possible when the tests are made through the actual atmosphere. In the first place, the content of the atmosphere

is a variable quantity. Meteorologists did not know how fast that vapor density and temperature actually fluctuated until the resonant cavity atmospheric refractometer was developed. This device which measures the refractive index of the air as determined by water vapor, pressure and temperature is constantly changing both in time at one location and in space. We are never quite sure what exact value should be used to associate with radio data particularly for longer ranges. We resort to models of the atmosphere which may be excellent statistical averages but which cannot be relied upon for a particular time or place. Terrain, wind directions, weather fronts, and surface features can all change the meteorological factors that control the atmospheric gas absorption.

It is particularly difficult to measure the attenuation of the 22 GHz water vapor line through the actual atmosphere. The loss is so small per kilometer that an extended test range must be used. All of the variables causing erratic data frequently mask the true value of attenuation. Since water vapor density variation is desired, absolute power levels measured over enough days to be able to draw a graph of attenuation vs water vapor density are necessary. To get the oxygen loss this graph must be extrapolated to zero water vapor. This process does not lend itself to very high accuracy because it is difficult to get high and low water vapor density periods in a reasonable time span. The measurement of losses due to water vapor and oxygen through the actual atmosphere is easier at frequencies where the loss is high because of the short distances required.

The measurement of gas attenuation from earth to space can be made by tracking the sun or moon as it moves across the sky on relatively clear days. It is assumed that the atmosphere is horizontally stratified so that the attenuation will vary in proportion to the secant of the angle from the zenith. The usual reference is to the ground level humidity and a "standard" atmosphere which relates the total water vapor along a trans-atmospheric path to the ground level condition. This is a rough approximation but must not be relied upon for high precision attenuation predictions. Extrapolation of radio attenuation data from one location to another is risky as shown by the disagreement in the results obtained by various experimenters in different climatological areas.

At the so-called windows below 40 GHz, and around 90, and 140 GHz, the atmospheric gases do not become a serious problem if paths are length limited and when satellite paths are kept at 20° or higher above the horizon.

3. INTERACTION WITH RAIN DROPS

The most damaging factor to millimeter wave propagation is precipitation along the radio path. Fortunately, unlike polar gases, rain is present only part of the time. The interaction of an electromagnetic wave and a single spherical rain drop is well understood. If the wavelength is many times larger than the drop diameter, the absorption and scattering will be small. The wavelength dependence is well known and agreement between theory and measurements for homogeneous drops has been verified. As the wavelength approaches the drop dimensions, resonance effect occurs and the scattering from the drops increases rapidly. For wavelengths much shorter than the dimensions, the rain drops act essentially as shields which block out the fraction of the wave falling on them. Millimeter waves over short ranges do well in fogs because the drop sizes are small compared to the wavelength but optical or micron laser beams are obliterated.

If the number and size of drops along a given transmission path were known, the loss could be calculated with considerable reliability. Since such information is never known accurately, it is necessary to relate the drop distribution to the rain fall rate on the ground. The Marshall-Palmer and Laws and Parsons models are commonly used to relate the number of drops of various sizes to the rain rate. There are a number of obvious limitations to this process. In the first place the models are statistical ones and the actual distribution will vary both with time and space. The most common method of measuring rain rate is with tipping bucket gauges which are step by step integrating devices. At low rain rate the integration may be over time periods which hide the peak loss. An example of the variability of rain attenuation at 2.15 mm is shown in Fig. 4. This not only shows the scatter in the data but also the excess of the loss over the theoretical values for periods of very light rains.

For short paths with closely spaced gauges, the agreement between averaged measurements and theory may be good. However, for longer paths the distribution of the rain is quite variable with the heavy rain limited in range while lighter rains are commonly more widely distributed.

For satellite paths a knowledge of the number of drops and their sizes along the path is meager. Rain gauges are almost useless for

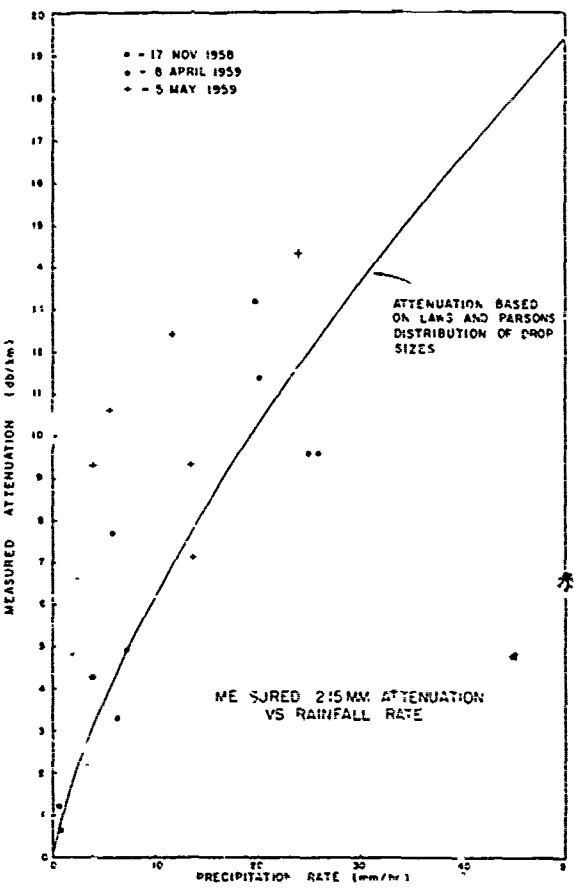

Rain Attenuation vs Rain Rate

Fig. 4

a correlation with attenuation.

In connection with the ATS-5 satellite at 12.7 GHz observed at angle from zenith of 32°, it was our experience that very little rain attenuation occurs unless a thunderstorm was in the vicinity of the receiver. No attenuation in excess of 10 dB occurred unless a thunderhead with a height of 10 km or more was present. The height and width of thunderstorms are roughly the same so that a spaced diversity system provides a reduction in the time of a potential outage. The probability of the individual receivers and the combination having attenuations exceeding various levels were measured. The space diversity reduced the probability of attenuation in excess of 10 dB by going from a single receiver to spaced receivers for which the spacing was 11 km.

The attenuation through the total atmosphere may also be measured by the radiation both from the atmospheric gases and from rain. The correlation of the loss calculated from such antenna temperature data and actual measurements is good for relatively small losses. If the atmosphere is nearly opaque, the radiometer will see only the nearest part of the sky path and not give a correct value of the losses.

A further complication of the rain studies is that the drops in falling tend to flatten. This causes greater attenuation for polarization along the major axis. Wind blown drops become canted and the maximum attenuation may not be for horizontal polarization. However, the differences in the reactions of the two polarizations of the radio waves is small compared to uncertainties as to the rain rate and drop distribution along the path.

The greatest unknown in millimeter and hectomicron radio propagation is the lack of adequate meteorological information over extended links, either between earth points or from earth to a satellite. We cannot at this time predict for a long path exactly what will happen at a particular time. As a result, we need to accumulate statistical data so that we may predict the probable length of time that attenuation greater than a certain level will be experienced. When we consider the translation of results from one location to another and that the propagation data changes with frequency, we now have only a minimal amount of data for engineering design. The Weather Bureau has collected rain data for a hundred years but no season fits exactly the long term statistical average.

4. INTERACTION WITH SURFACES

The third aspect of the reduction of wave length is the effect that this change has on the reaction with surfaces. Various arbitrary definitions for a smooth surface have been used based on the maximum phase difference between the shortest and longest path involved in reflection from a surface area. If we assume that a delay of less than 1/8 wavelength will not cause serious phase interference, we may calculate the roughness in a surface as a function of the angle of incidence, assuming no shadowing of one part by another. Such calculations are shown in Table 3 for wavelengths of 1 cm and 1 mm.

Fig. 5 illustrates this change in forward reflection with frequency over a fairly smooth bare ground surface (Straiton, 1952). This figure shows that the forward reflection increases as the angle approach grazing and decreases as the wavelength is decreased.

Wavelength	Allowable Path Differ	Angle from normal	Allowed Surface Variations
1 cm	1.25 mm	90°	0.67 mm
		30°	1.34 mm
		10°	3.86 mm
		2°	1.92 cm
1 mm	1.25 μm	90°	62 μm
		30°	124 μm
		10°	386 μm
		2°	1.92 mm

cm - Centimeter, mm - Millimeter, μm - Micrometer

Roughness Criteria for 1 cm and for 1 mm

Table 3

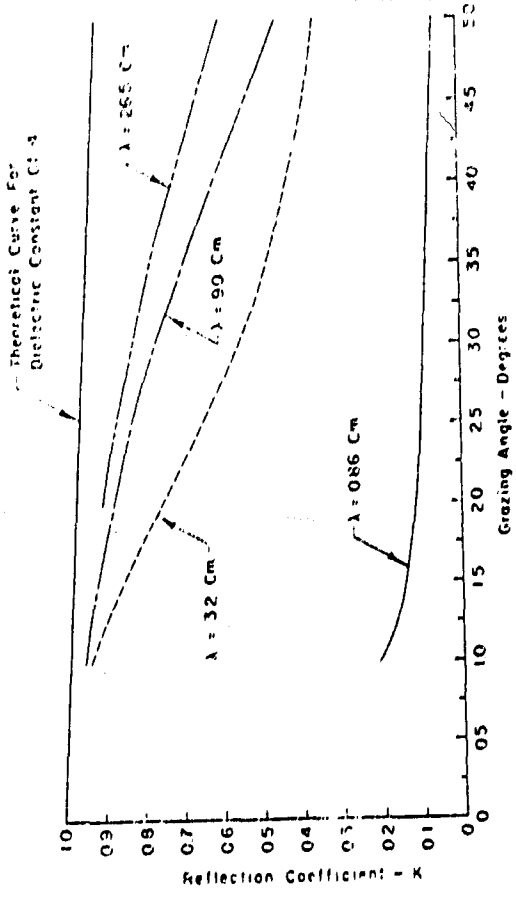

Forward Reflection of Fairly Smooth Ground

Fig. 5

The decrease in forward scatter is accompained by an increase in scatter in all directions including return to the transmitting point. This enhanced backscatter may show an object which does not return a signal to the transmitter as a well defined shadow in the brightened background noise.

At millimeter and hectomicron wavelengths complex radar targets respond as individual facets rather than as a whole. The term glint originally was associated with changes in phases of returns whose magnitudes remained essentially constant. For the wavelengths under discussion at this conference it is more likely that "glint" is associated with changes in magnitude. At slightly different angles of observation small changes in angle of incidence from normal to flat surfaces cause rapid reduction in the backscatter.

Passive measurements of surfaces alone or combined with active measurements may provide valuable data. Since radiometry is based on heat sources, angles of observation and phasing are not as important as with coherent radiation. Since the depth of penetration of the ground decreases with increasing frequency, the shorter waves appear to come from nearer the surface than do longer ones. This is illustrated by measuring the radiation from an area on the moon through a lunar cycle. Curves for such measurements at 35 and 94 GHz are shown in Fig. 6. It is noted the 94 GHz

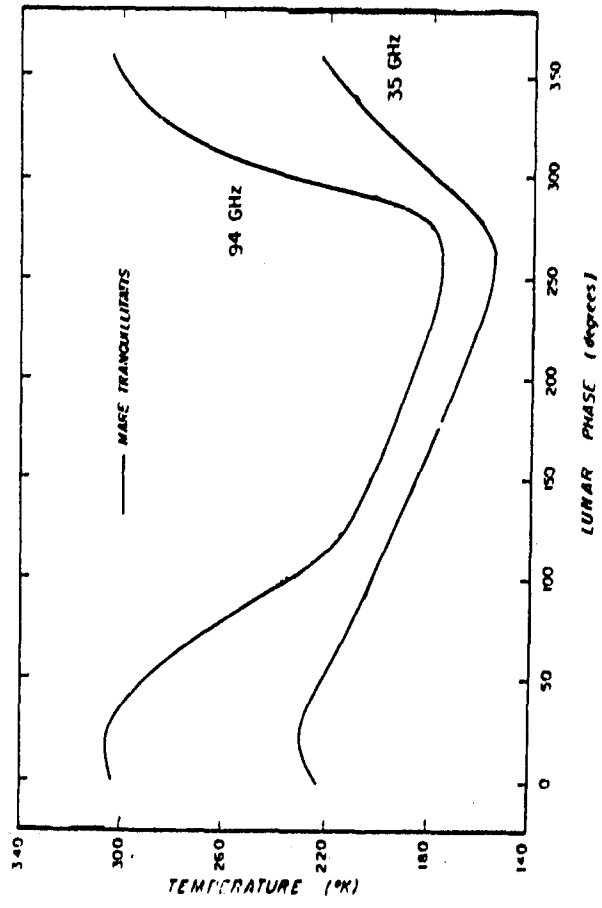

Lunar Brightness vs Lunar Phase

Fig. 6

radiation more nearly follows the illumination of the moon while 35 GHz radiation is less and remains more nearly constant indicating that the source is further under the lunar surface. Measurement of the temperature of a smooth lake shows it to appear very cold when viewed from nearly normal incidence because the sky reflected in the lake is in a region of small atmospheric attenuation. However only a slight amount of wind roughness of the surface made its temperature look much warmer because the incoming waves came from angles further from the zenith.

The point that I would like to emphasize is that millimeter radio wave propagation is not an area in which measurements can be made or results predicted with a high degree of accuracy. Perhaps this meeting will dispel some of the uncertainty that exists.

REFERENCES

Barrow, W. E., 1938: Light, Photometry and Illuminating Engineering, Second Edition. McGraw-Hill Book Co., New York.

Schulze, A. E. and C. W. Tolbert, 1963: Shape intensity and pressure broadening of the 2.53 mm wave-length oxygen absorption line. Nature, 200, 745-750.

Straiton, A. W., 1952: Preliminary Study of the Reflection of Millimeter Radio Waves from Fairly Smooth Ground. EERL, Univ. of Texas Rept. No. 60, 29 February 1952.

Tolbert, C. W., L. C. Krause, and A. W. Straiton, 1964: Attenuation of the Earth's atmosphere between the frequencies 100 and 140 gigacycles per second. J. Geophys. Res., 69, 1349-1357.

RAIN EFFECTS IN THE 10 TO 100 GHz FREQUENCY RANGE

Robert K. Crane

Environmental Research & Technology, Inc.

696 Virginia Road, Concord, Massachusetts 01742

ABSTRACT

Rain can significantly affect the operation of active or passive sensor systems operating within 10 to 100 GHz or higher frequencies. Reasonable models are available for the estimation of the magnitude of the specific attenuation and backscatter cross section per unit volume produced by rain of known intensity. Occurrence prediction models are also available. Model calculations are presented and combined with observations.

1. INTRODUCTION

Active or passive observations of targets on the surface of the earth at frequencies in the 10 to 100 GHz range may be adversely affected by the presence of rain or cloud along the observation path, in the vicinity of the target, or above the target. The effects of rain or cloud on system performance may be simulated given the characteristics of the system and models for attenuation and scattering by the rain. The validity of the simulation results depends upon the veracity of the rain or cloud model. In this brief report, models for prediction of attenuation and scattering by rain are reviewed and compared with experimental observations.

Calculations of the scattering properties of rain drops have been made many times over the past four decades. The results of these calculations have been used to model attenuation effects for radar and communication systems and to calibrate weather radar systems for use in measuring rainfall. The adequacy of the calculations for the estimation of attenuation over a wide frequency range has received considerable attention. Medhurst (1965) reviewed the results of experiments made prior to 1964 and concluded that the measurements and theory did not agree. He suggested that a purely empirical approach should be used for the estimation of specific attenuation at a given rain rate. deBettencourt (1974) reviewed the state of the experimental observations made prior to 1972 and also concluded that an empirical procedure should be used for the estimation of specific attenuation although he could not find conclusive evidence that the theory and observations disagreed. Crane (1971, 1975) and Waldteufel (1973) reviewed the available data and reached the conclusion that theory and observation do agree and that the theoretical relationship between specific attenuation and rain rate should be used; they found that the difficulties lay in the problems of measuring the rainfall intensity along a path. Crane (1974) in a carefully controlled experiment showed that good agreement existed between measurements and theory. Joss et al. (1974) reached a similar conclusion after careful analysis of another experiment. Today, the adequacy of model computations for the estimation of specific attenuation for a given rainfall rate is generally accepted for frequencies below 40 GHz.

A similar situation exists for the estimation of the backscatter cross section per unit volume (reflectivity) for a given rain rate. At frequencies below 10 GHz, the adequacy of the theory for the calculation of reflectivity is well established. Uncertainties in the relationship between reflectivity and rain rate are due primarily to uncertainties in the drop size distribution that should be used for the rain filled volume. Secondary problems exist associated with the drop shape distribution to be used but the corrections for shape are generally less than 2 dB. Crane (1978) recently reviewed the calibration procedures for the SPANDAR S-band radar at Wallops Island, Virginia and found that with a good radar calibration procedure, a detailed knowledge of the drop size distribution and corrections for drop shape, radar observations and cross section estimates based on rain rate observations agree to within 0.9 dB rms. The uncertainty in the comparison was primarily associated with difficulties in estimating the rain rate for comparison with the radar measurements.

In recent years, models have become available for the statistical prediction of the occurrence and severity of rain effects. Crane (1979) has developed a climatological model using rain rate climate regions for the world-

wide analysis of rain effects. Comparisons between the global model predictions and observations result in rms deviations of the observations about model predictions of less than 30 percent of the value predicted by the model, for terrestrial paths up to 60 km in extent at 11 GHz and up to 7 km in extent at 36.5 GHz.

Thus, it is concluded that models for the prediction of rain effects are well established for use at frequencies below 40 GHz. At higher frequencies the possibility of uncertainties still exists. The uncertainties are primarily associated with the estimation of the size distribution of rain and cloud particles in the region of interest and are not associated with theoretical problems.

2. ATTENUATION AND SCATTERING BY RAIN

2.1 Attenuation

Model calculations for specific attenuation and reflectivity have been available for many years. Crane (1966) made a series of calculations using the standard assumptions: spherical rain drops with homogeneous dielectric properties distributed in space in accordance with a Poisson process. He reported the results of caluculations made for 35, 70, and 94 GHz using both a model drop size distribution and a number of measured distributions. More recently, Crane (1977) published an analysis of the sampling errors associated with drop size measurements which showed that a significant fraction of the spread of the calculations for individual drop size distributions about calculations based on the use of the Laws and Parsons distributions (Laws and Parsons, 1943) was caused by sampling effects.

Calculations of specific attenuation and of the backscatter cross section per unit volume are presented in Figures 1 and 2 respectively, for two model distributions, the Laws and Parsons (L & P) distributions (Laws and Parsons, 1943) and the Marshall-Palmer (M-P) distribution (Marshall and Palmer, 1948). The essential difference between the two distributions is in the number of small drops, the M-P distribution containing significantly more small drops than L&P. The results of the calculations show that the number of small drops can seriously affect the estimate of attentuation at frequencies above 30 GHz and rain rates above 10 mm/h.

The summary of observations compiled by deBettencourt (1974) shows good agreement between the theoretical estimates and observations when the observations are culled to remove (1) observations made prior to 1950, (2) observations made with a large separation between the measurement path and the rain

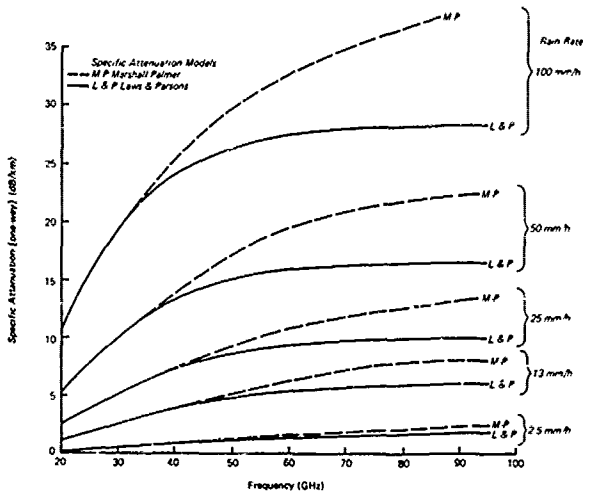

Figure 1 One Way Specific Attenuation vs Frequency for Rain

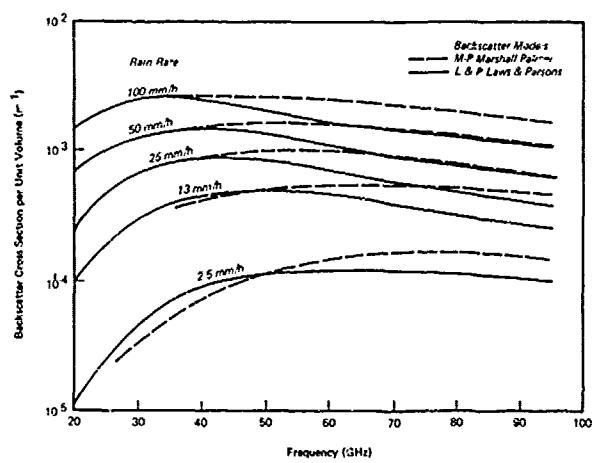

Figure 2 Reflectivity vs Frequency for Rain

gauges, and (3) observations with known difficulties in the interpretation of the rain gauge data. The summary figure from deBettencourt is reproduced in Figure 3 together with the recent published measurements of Sander (1975). The questionable data are marked by (X), the acceptable data by (●). The theoretical power law curve was based on a regression of a large number of calculations based upon individual drop size distribution measurements reported by Crane (1971). The theoretical data are close to the L&P distribution results. The k and b coefficients in the power law relationship between specific attenuation and rain rate show good agreement between observations and theory at frequencies up through 100 GHz.

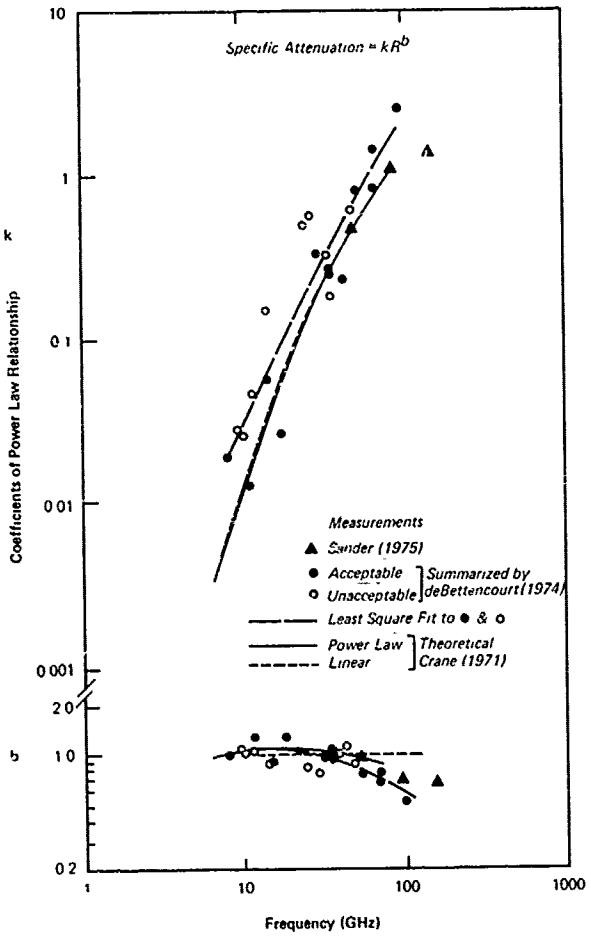

Figure 3 Coefficients of Power Law Relationships Between Specific Attenuation and Rain Rate

Multiwavelength radar measurements by the Ballistic Research Laboratories (BRL) at McCoy AFB in Florida show a similar good agreement between measured and estimated specific attenuation values at both 70 and 95 GHz. The raw observations obtained from Richard and Kammerer (1975) together with the theoretical calculations made using both the L&P and M-P distributions are presented in Figure 4 for 70 and 95 GHz. With the exception of some apparently spuriously low values of specific attenuation at rain rates between 1 and 10 mm/h, the agreement is good. The data were obtained by comparing the cross section of a corner reflector observed during rainy conditions with the cross section expected in the absence of rain. Considering that the rain was not measured along the relatively short path (450 m) but only at the target and that the measurements depend upon the radar calibration, the agreement is excellent.

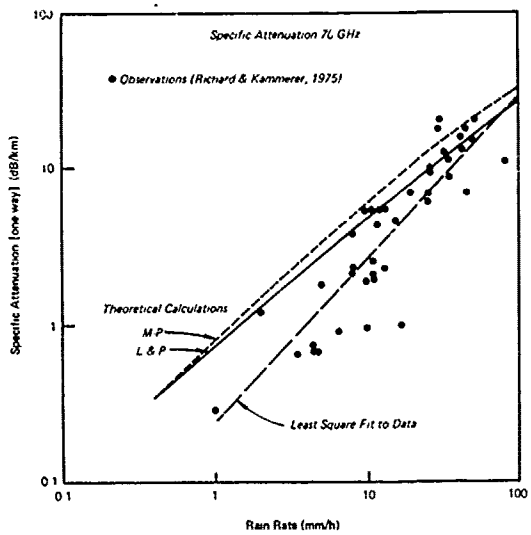

a. Observations at 70 GHz

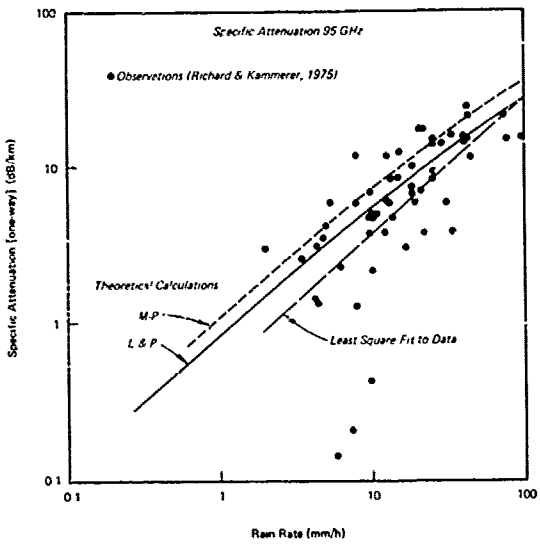

b. Observations at 95 GHz

Figure 4 Specific Attenuation Observations

2.2 Backscatter

Very little data exist for the verification of the theory for the estimation of the backscatter cross section per unit volume for frequencies above 20 GHz. However, adequate checks on the theory have been made at lower frequencies and no complications exist which

could invalidate the theory at one frequency after it has been validated at another. The multiwavelength data obtained by BRL do provide additional evidence and support for the theoretical calculations at higher frequencies. Figures 5 and 6 provide summaries of the cross section measurements made by BRL at 35, 70, and 95 GHz. The measurements displayed in Figure 5 are reproduced from the report by Richard and Kammerer (1975). The measurements displayed in Figure 6 are reproduced from the companion report by Currie et al. (1975). The two sets of figures represent two different analyses of the same data.

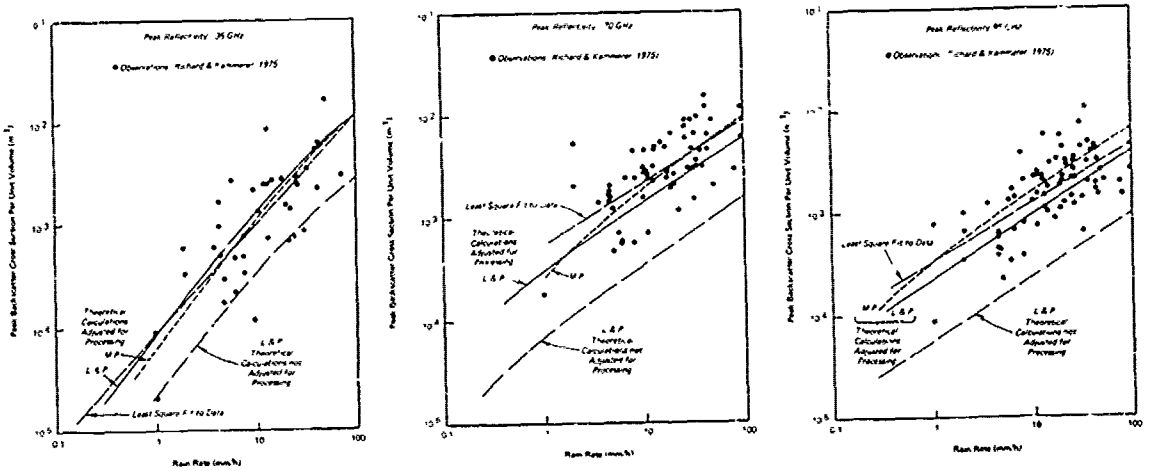

a. Observations at 35 GHz b. Observations at 70 GHz c. Observations at 95 GHz

Figure 5 Peak Reflectivity Observations

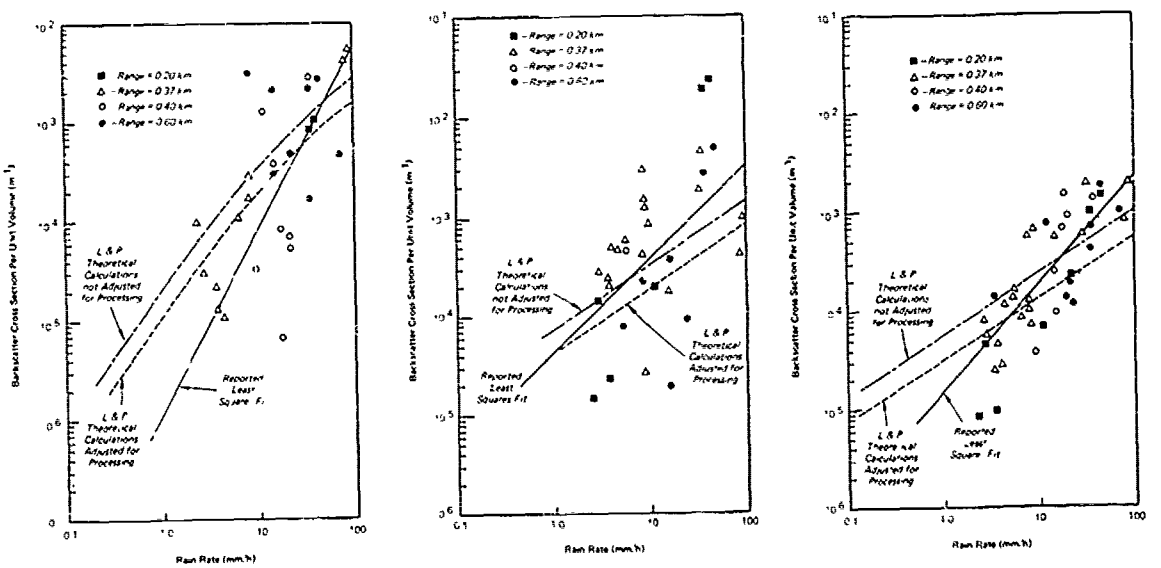

a. Average at 35 GHz b. Average at 70 GHz c. Average at 95 GHz

Figure 6 Average of the Logarithm of Reflectivity Obtained by Currie et al. (1975)

Richard and Kammerer reduced A-scope photograph data. They determined the peak rain reflectivity from the A-scope data using the radar returns from range intervals in front of and behind the corner reflector and reported the peak backscatter cross section per unit volume for the range to the corner reflector. Precise radar calibration and attenuation estimation were not necessary since the corner reflector cross section value was corrected for possible rain contamination and the peak rain cross section value was calculated using the known cross section of the corner reflector as reference. Processing adjustment should be made to the theoretical calculations prior to comparison with the observations (as indicated in figure 5) to compensate for the use of the peak value instead of the logarithm of the average reflectivity as assumed in most theoretical analyses. The unadjusted L&P curves are also presented for reference. From prior experience, it is known that the signal return (pulse to pulse variation) from rain has a Rayleigh distribution (Atlas, 1964). The highest signal value from 50 independent samples from a Rayleigh process is 6 dB above the mean (for a linear receiver, e.g. see Crane, 1973). Since roughly 50 independent pulses were sampled in the process of detecting the peak value, a 6 dB adjustment was used for the theoretical calculations plotted in Figure 5. Richard and Kammerer experimentally determined the adjustment to be 5.9 dB.

The data reported by Currie et al (1975) were obtained from the same set of measurements on the same radars as the BRL results. They used magnetic tape recorded A/D output from the logarithmic receiver at a single range gate which could be moved in range. In post processing analysis, they averaged the recorded output and converted the values directly to cross section per unit volume estimates. In transforming to reflectivity estimates the path attenuation had to be estimated and used to correct the radar observations. They used the empirical relationship of deBettencourt 1974) and the measured surface rain rate values to make the attenuation estimates. Since that relationship tends to overestimate attenuation (see Figure 3), the correction will produce reflectivity estimates that are too high at high rain rates. This tendency is evident in their data. The data also were not adjusted for the difference between the average of power and the average of the logarithm of the power for a Rayleigh process (Atlas, 1964). This last adjustment (2.5 dB) has been included as a correction to the theoretical calculations in Figure 6. Since the data reported by Currie et al. require both precise radar calibration and precise attenuation correction (the total attenuation values are as large as 10 dB two way for the 450 m path at rain rates in excess of 10 mm/h) they are considered to be less reliable than the BRL results and will not be considered further.

The BRL measurements (Figure 5) are in excellent agreement with the adjusted theoretical calculations. At 35 GHz, the reported least square fit power law relationship for the BRL observations is within 2 dB of the adjusted theoretical calculations. At 95 GHz, the reported least square fit power law lies between the two sets of adjusted theoretical calculations (L&P and M-P). It is known that the L&P distributions tend to underestimate the number of small drops while the M-P distribution tends to overestimate the number of small drops. Based on experience, the observations should lie between the two distributions. However, the precision of the BRL measurements is not great enough to select one drop size distribution model over the other.

A careful examination of the available observations is sufficient to reveal the veracity of the theoretical calculations. Insufficient data are available to select the best drop size distribution for use with the theoretical calculations. Since the drop size distribution may change from one location to another depending upon the existence of ice (or snow) aloft in a storm, the relatively humidity of the environment surrounding the falling drops, and the presence of low level clouds or fog, the establishment of the appropriate dropsize distribution is a meteorological problem, not a question of the adequacy of the theoretical model.

3. PREDICTION OF THE DISTRIBUTION OF ATTENUATION OF BACKSCATTER CROSS SECTION

Crane (1979) has developed a global model for the prediction of attenuation. The model is briefly reviewed in this section and a procedure is recommended for the estimation of the back scatter cross section. The occurrence of rain is characterized by an expected annual rain rate distribution. The distribution depends upon the geographic location as depicted in Figure 7. The expected rain rate distributions are depicted in Figure 8.

The attenuation along a terrestrial path is calculated using rain rate at the desired percentage of the year (from Figure 8), the path length, D, and the coefficients of the power law relationship between specific attenuation and rain rate for the frequency of interest (k and b of Figure 3; see Olsen

et al.,1978). The attenuation is given by:

$$A(R,D) = KR^b \left[\frac{e^{ubd}-1}{ub} - \frac{v^b e^{cbd}}{cb} + \frac{v^b e^{cbD}}{cb} \right], D>d = kR^b \frac{(e^{ubD}-1)}{ub}, D \leq d \quad (1)$$

where:

A is attenuation (dB)
R is point rain rate (from Fig. 8)
k,b are specific attenuation vs rain rate coefficients
D is path length
and u,v,c,d are empirical constants depending only on rain rate.

$$u = \frac{\ln(v e^{cd})}{d}$$

$$v = 2.3\, R^{-0.17}$$

$$c = 0.026 - 0.03 \ln R$$

$$d = 3.8 - 0.6 \ln R$$

If D is greater than 22.5 km, the value 22.5 km should be used in the calculation of attenuation together with an adjusted rain rate, value R', found by entering Figure 8 at an adjusted probability of occurrence $P' = P \left(\frac{22.5}{D}\right)$ where P is the probability of occurrence of interest.

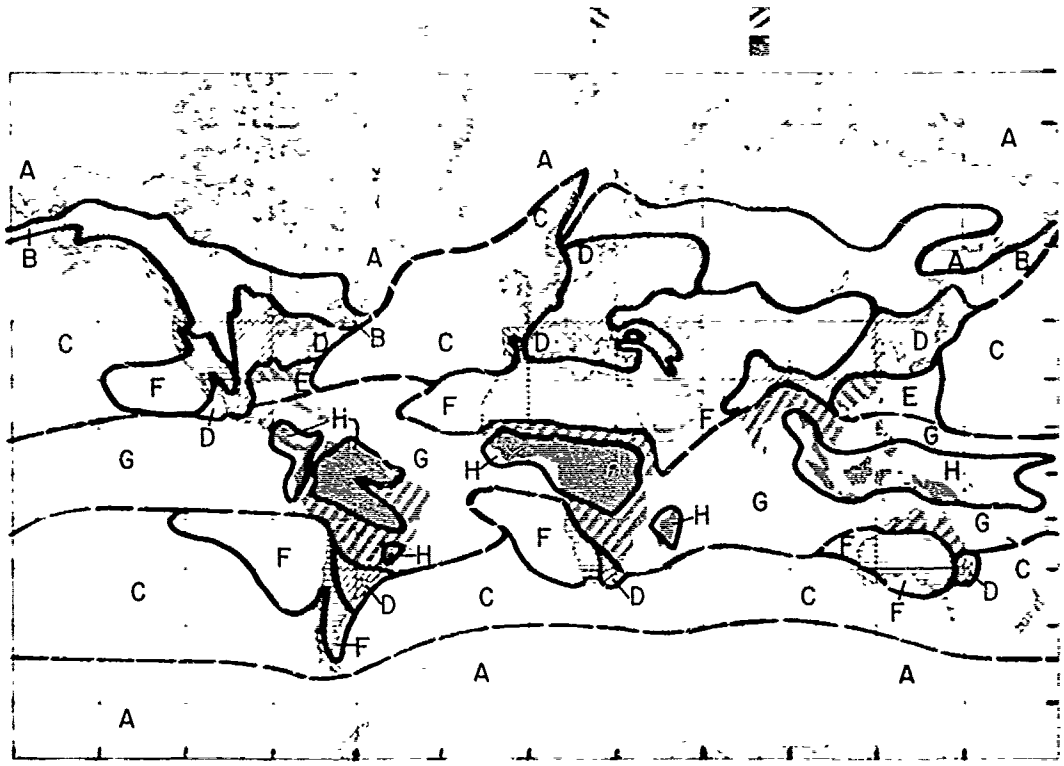

Figure 7 Global Rain Climate Boundaries

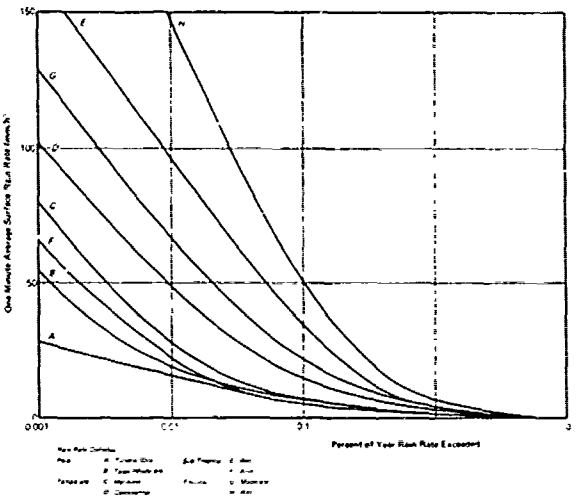

Figure 8 Point Rain Rate Distributions for Climate Regions A to H

Observations are in reasonable agreement with this prediction model as indicated in Figure 9 (taken from Harden et al.,1978). Two model curves are presented, one for the region C model rain rate distribution and the other for the average rain rate distribution over the geographic region of the observations (England). At 11 GHz, excellent agreement is evident. At 36.5 GHz, agreement is evident for path lengths less than 7 km. It is believed that equipment dynamic range limitations may be important at the longer path lengths.

Backscatter cross section estimates require both the prediction of attenuation along the path and the estimation of the scattering cross section at an endpoint of the path. The model used to calculate attenuation by rain includes a model to estimate the rain rate or attenuation along the path given the rain rate at one endpoint of the path. For application to the preparation of cross section estimates, the rain rate is obtained for desired probability of occurrence from Figure 8 and used to obtain the scattering cross section per unit volume (by interpolation in Figure 2) and the attenuation to be expected simultaneously between the radar and the scattering volume using equation 1. In using equation 1, D is the range to the target. If D > 22.5 km, use 22.5 km for D but do not adjust the rain rate as explained above.

4. CONCLUSIONS

A model has been presented for the calculation of attenuation and for the calculation of scattering cross section per unit volume and the attenuation to be simultaneously expected along the path to the radar. For frequencies below 40 GHz, the model predictions are in agreement with available observations. For frequencies above 40 GHz agreement is still evident but some uncertainty exists as to the best drop size distribution to be used for studying either the specific attention or the backscatter cross section unit volume. The model provides estimates which fall within the scatter of the observations at the higher frequencies (above 40 GHz) but insufficient measurements are available to reduce the scatter enough to select the best drop size distribution model.

5. ACKNOWLEDGMENTS

The analysis of the use of frequencies above 30 GHz reported in this paper was supported by MIT Lincoln Laboratory; the work on the development of attenuation prediction models was supported by NASA.

REFERENCES

Atlas, D., 1964 : Advances in radar meteorology. In Advances in Geophysics, Vol. 10, pp. 317-478, Academic Press.

Crane, R.K., 1966 : Microwave Scattering Parameters for New England Rain. MIT Lincoln Laboratory Tech. Rept. 426.

Crane, R.K., 1971 : Propagation phenomena affecting satellite communication systems operating in the centimeter and millimeter wavelength bands. Proc. IEEE, 59, 173-188.

Crane, R.K., 1973 : Virginia Precipitation Experiment - Data Analysis. NASA/GSFC Doc. X-750-73-55, NASA Goddard Space Flight Center, Greenbelt, Maryland.

Crane, R.K., 1974 : The rain range experiment - propagation through a simulated rain environment. IEEE Trans. Antennas and Propagat., AP-22, 321-328.

Crane, R.K., 1975 : Attenuation due to rain - a mini review. IEEE Trans. Antennas and Propagat., AP-23, 750-752.

Crane, R.K., 1977 : Prediction of the effects of rain on satellite communication systems. Proc. IEEE, 63, 456-474.

Crane, R.K., 1978 : Evaluation of Uncertainties in the Estimation of Hydrometeor Mass Concentrations Using SPANDAR Data and Air-

craft Measurements. Scientific Report No. 1, AFGL-TR-78-0118, Contract F19628-76-C-0069, Environmental Research & Technology, Inc.

Crane, R.K., 1979 : Prediction of attenuation by rain. submitted for publication, IEEE Trans. on Communication.

Currie, N.C., F.B. Dyer and R.D. Hayes, 1975: Analysis of Radar Rain Return at frequencies of 9.375, 35, 70 and 95 GHz. EES/GIT Project A-1485 Tech. Rept. 2, Engineering Experiment Station, Georgia Institute of Technology.

deBettencourt, J.T., 1974: Statistics of millimeter-wave rainfall attenuation. J. Rech. Atmos., 8, 89-119.

Harden, B.N., J.R. Norbury, and W.J.K. White, 1978 : Estimation of attenuation by rain on terrestrial radio links in the UK at frequencies from 10 to 100 GHz. Microwave, Optics and Acoustics, 2, 97-104.

Joss, J., R. Cavalli and R.K. Crane, 1974: Good agreement between theory and experiment for attenuation data. J. Rech. Atmos., 8, 299-318.

Laws, J.O. and D.A. Parsons, 1943: The relation of raindrop-size to intensity. Trans. Amer. Geophys. Union, 24, 452-460.

Marshall, J.S. and W. McK. Palmer, 1948: The distribution of raindrops with size. J. Meteor., 5, 165-166.

Medhurst, R.G., 1965: Rainfall attenuation of centimeter waves: Comparison of theory and measurement. IEEE Trans. Antennas and Propagat., AP-13. 550-564.

Olsen, R.L., D.V. Rogers, and D.B. Hodge, 1978: The aR^b Relation in the Calculation of Rain Attenuation. IEEE Trans Antennas and Propagation, AP-26, 318-329.

Richard, V.W. and J.E. Kammerer, 1975: Rain Backscatter Measurements and Theory at Millimeter Waves. BRL Rept. 1838, USA Ballistics Research Laboratories, Aberdeen Proving Ground, Maryland.

Sander, J., 1975: Rain attenuation of millimeter waves at λ = 5.77, 3.3 and 2 mm. IEEE Trans. Antennas and Propagat., AP-23, 213-220.

Waldteufel, P., 1973: Attenuation des ondes hyperfrequences par la pluie: une mise an point. Ann. Telecommun., 28, 255-272.

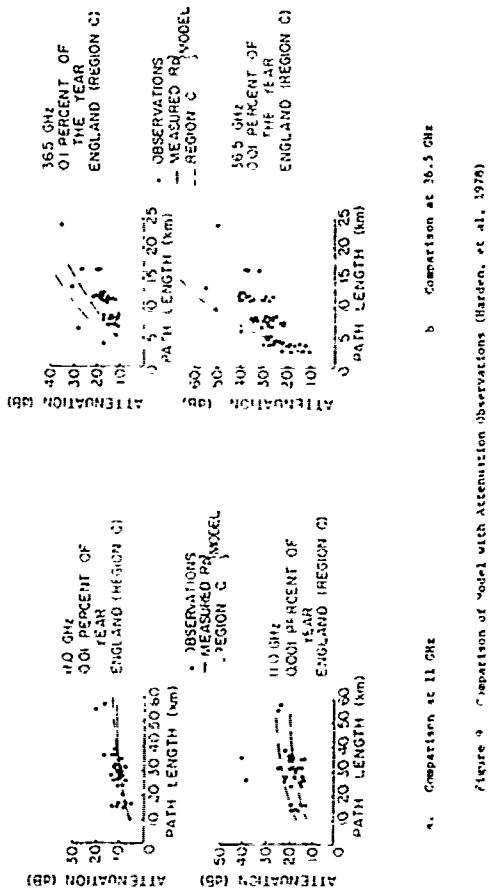

a. Comparison at 11 GHz

b Comparison at 36.5 GHz

Figure 9 Comparison of Model with Attenuation Observations (Harden, et al, 1978)

TERRAIN INTERACTIONS AT MICROWAVE FREQUENCIES

J. R. Lundien

Environmental Laboratory

U. S. Army Engineer Waterways Experiment Station

Vicksburg, Mississippi

ABSTRACT

The sensitivity of microwave measurements to environmental conditions has been documented many times and has often been the limiting condition for operation of various radio equipment. In the case of early radar studies, considerable work was conducted towards improving detection of military targets and decreasing sensitivity to background or surface "clutter." More recently, the surface itself has been considered to be an important target because of the applications to monitoring the character of land use, changes in the surface of the ocean, and various other quantities of economic significance.

A summary is presented of one such effort in defining the ability of microwave systems operating in pulsed- and continuous-wave modes to rapidly acquire terrain data through noncontact measurements. These studies consisted of analysis of both laboratory and field measurements of terrain materials and included the use of computer models to extrapolate the results still further. Test results, using swept-frequency radar measurements as examples, indicate that estimates can be made of power reflections from the surface of layered materials and that the amplitude of the subsurface contributions can be determined. Also, interference patterns, produced in the power reflection curves, can be used to calculate the thickness of each layer of the structure.

1. INTRODUCTION

Quantitative terrain information is required in many mapping studies for the Army. Uncalibrated radar systems have been used to great advantage in gathering data that can be interpreted to give relative or qualitative descriptions about the earth's surface conditions, but, without considerable ground truth support, the accuracy and resolution of such data are normally low. The ability to penetrate atmospheric haze and clouds, operate at any hour of the day, and reveal geologic detail not observed by visual sensor systems has generated considerable interest in the use of active microwave measurements for soil characteristics. The soil characteristics which are usually selected for investigation are: (a) soil physical properties (e.g. type, moisture content, density, etc.); (b) surface and subsurface structure; and (c) spatial and temporal distribution of the properties. In studies at the U.S. Army Engineer Waterways Experiment Station (WES), emphasis was placed on requirements to define direct relationships between microwave measurements and terrain properties that could be further exploited in noncontact, nondestructive remote sensing surveys. Three investigations conducted at WES will be described in this paper: (a) radar responses to laboratory-prepared samples of terrain materials; (b) swept-frequency radar measurements of terrain materials; and (c) mathematical models for feasibility studies and for improvement of data analysis procedures.

2. LABORATORY STUDIES OF RADAR RESPONSES

Laboratory measurements at WES have been made on soils and vegetation to determine their electrical properties at P-, L-, C-, X-, and K_a-band frequencies (297 MHz to 35 GHz) (Lundien 1966, Lundien 1971). The measurements at P-, C-, X-, and K_a-bands were conducted in an outdoor test facility shown in Figure 1.

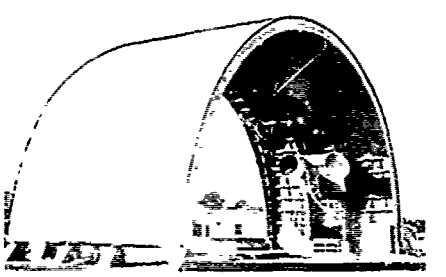

Figure 1. P-, C-, X-, and K_a-band radar test facility.

The principal parts of the facility were the wooden arch structure, the antenna carriage, and the instrument control room. Measurements with the four-band radar system mounted on the back of the antenna carriage were made on test materials (soils and vegetation) positioned in the center of the arch. Microwave absorbent materials were placed on the sample holder and the surrounding area to ensure that radar

measurements were of the test materials alone (see Figure 2). The data were analyzed to

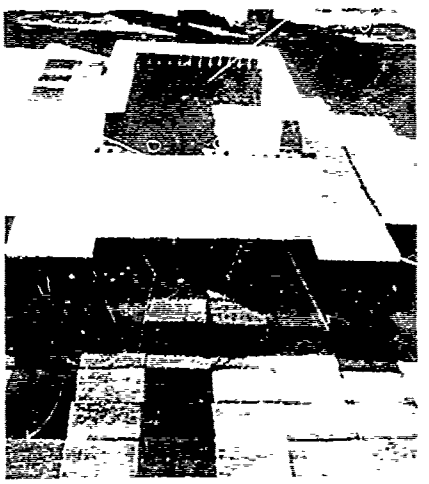

Figure 2. Microwave-absorbent material layout for soil tests.

determine the proportion of transmitted radar energy that was reflected from samples in two separate procedures: (a) tests in which incidence angle was varied (signature test, see Figure 3) were used to determine the

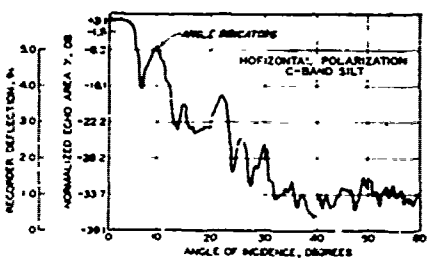

Figure 3. Typical radar signature at C-band.

feasibility of measuring sample moisture content of bare and vegetation-covered soil; and (b) tests in which the sample depth was varied (depth-of-penetration tests, see Figure 4)

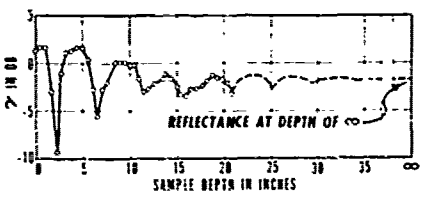

Figure 4. P-band depth-of-penetration test results for Yuma sand; moisture content = 19.7%.

were used to measure sample moisture content and density and the penetration capabilities of the waves at the various frequencies.

The results of computations at P-band frequencies for the relative dielectric constant and electrical conductivity of sand, silt, and clay soils are shown in Figures 5 and 6, respectively. Figure 7 shows similar

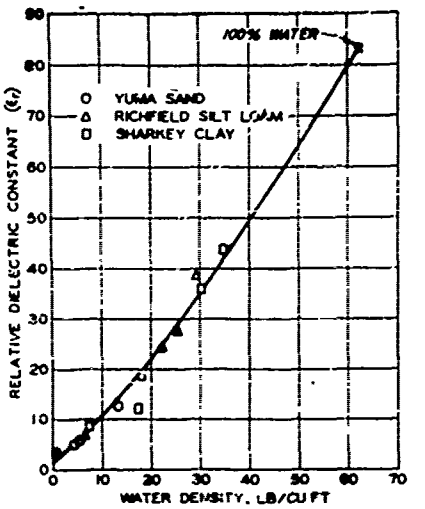

Figure 5. Relative dielectric constant versus moisture content, 300 MHz.

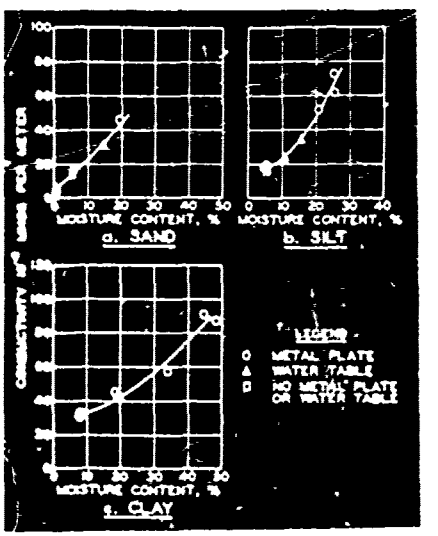

Figure 6. Conductivity versus moisture content (P-band).

results for the relative dielectric constant of sand, silt, and clay soils from another series of laboratory tests at WES with an L-band interferometer (1.0 to 1.5 GHz). Both sets of results at the P- and L-band indicate a nearly linear relationship between the relative dielectric constant and the soil water content which is slightly soil dependent. The clay soils tend to group on the lower part of the curve, the sand soils tend to group on the

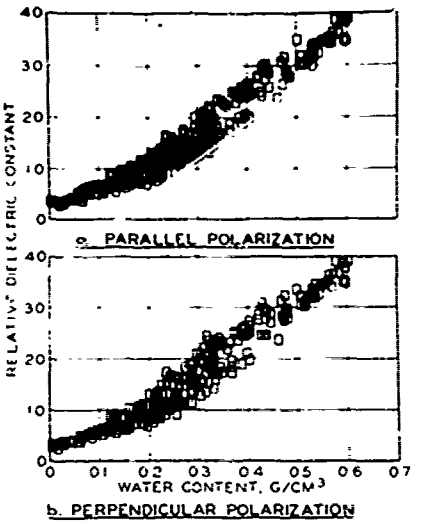

Figure 7. Effect of water content on relative dielectric constant. Sand, silt and clay soils measured at a frequency of 1.074 GHz.

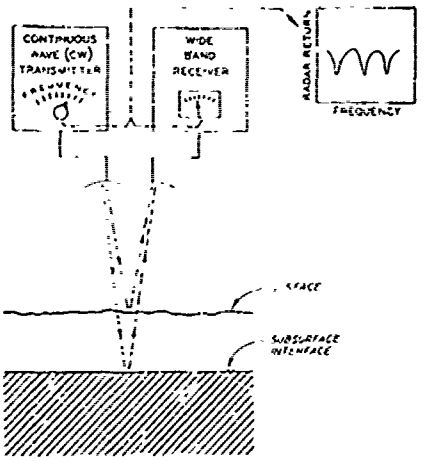

Figure 8. Simplified block diagram for swept-frequency radar system.

high part of the curve, and the silt soils are intermediate. This effect may be partially caused by the manner in which water is held in these soils instead of the soil type itself. Some of the water in a soil is held directly on the surface of the soil particles (absorbed) in a physical state different from that of liquid water or free water held in the spaces between the particles. The absorbed water has a relative dielectric constant that is much less than that of free water; thus, soils with small particles (large surface areas with correspondingly large amounts of absorbed water) have relative dielectric constants less than soils with large particles (smaller surface areas with correspondingly less amounts of absorbed water.

Although the test results indicated that standard single-frequency radar systems are not generally suitable for directly obtaining quantitative information on the electrical properties of target materials, the information required for such calculations may be obtained from measurements with specially designed microwave systems (such as the swept-frequency radar system). Further, the electrical properties were found to be strongly correlated to soil water content and sensitive to the type of soil.

3. SWEPT-FREQUENCY RADAR MEASUREMENTS

A simplified block diagram of a swept-frequency radar system is shown in Figure 8. The swept-frequency radar transmitter consists of a signal oscillator that can be varied in frequency. The transmitter signal is directed through the transmitting antenna down to the surface of the target where it is partially reflected and partially transmitted. The velocity of the signal that is transmitted into the target material decreases so that the wave length becomes shorter in the target material than it is in air. The signal continues to travel in the target material until it strikes another interface between materials whose electrical properties contrast. It again is partially reflected and partially transmitted and continues on in that manner indefinitely (though greatly attenuated). The reflected waves from the surface and subsurface interfaces combine vectorially as they travel back to the receiving antenna, the signal is then amplified in the wide band receiver, and the output can be displayed as a function of frequency. If the subsurface reflection combines out of phase with the surface reflection, an amplitude subtraction results, and the net return to the receiver is a minimum. If either the frequency or the sample depth is varied slightly, the wave amplitudes can add and the return to the receiver would be a maximum. At frequencies above a few hundred megahertz, the imaginary part of the relative dielectric constant for most terrain materials is small; therefore, an estimate for the real part of the relative dielectric constant can be computed from the power reflectance value.

Figure 9 shows the swept-frequency radar system in operation at WES (Lundien 1972). All the equipment necessary for radar measurements and ground truth measurements was carried on three trucks. The antenna system consists of two antenna pairs; the large antennas were used to transmit and receive the frequencies of 250 to 4000 MHz, and the small antennas were used to transmit and receive the frequencies of 4000 to 8000 MHz. The position of the antennas could be controlled from the instrument van by electric motors mounted on the end of a hydraulic boom. The instrument van also carried all of the electronic equipment (i.e. signal oscillators, amplifiers, the analog-to-digital converters, and the digital recording equipment).

A series of measurements with the

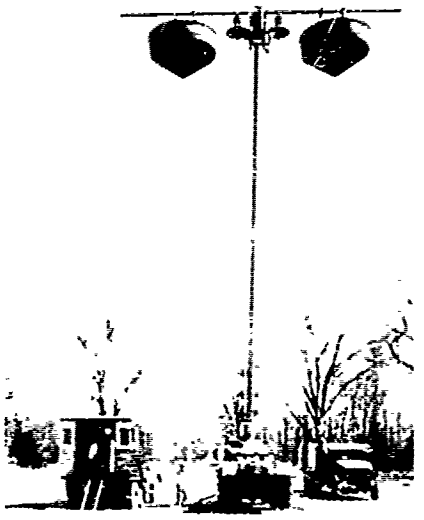

Figure 9. Truck-mounted swept-frequency radar system.

swept-frequency radar system were made on a section of asphalt highway on the interstate highway system near Vicksburg, Miss. Figure 10 shows the results of measurements at one

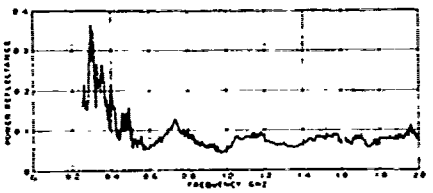

Figure 10. Swept-frequency radar measurement of asphalt highway.

site on this highway. The cyclic patterns contained in this power reflectance versus frequency curve are a measure of interface reflections from the layered target. The periodic frequencies can be extracted from this measured curve with curve fitting techniques and used to calculate the layer thicknesses. Also, the average surface reflectance can be computed from this curve and used to obtain the relative dielectric constant of this material.

Another method of extracting the cyclic patterns from the measured data is by use of a correlation program, and the results from such a program are shown in Figure 11. A peak in the correlation curve is found whenever a layer interface reflection is processed. One peak in the correlation data occurs for the interface between the asphalt pavement and the clay gravel base material, and another peak occurs for the interface between the clay gravel base and the silt foundation. The results of the correlation program have been plotted versus optical depth and must be corrected for the change in wave velocity in each material to obtain the actual layer

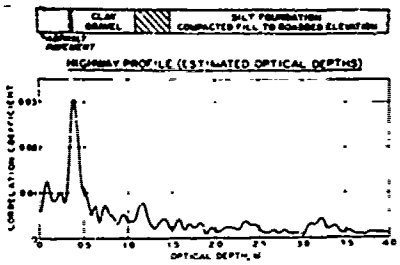

Figure 11. Swept-frequency radar test results. Asphalt highway correlation curve for sta 724.

thickness. The other peaks seen in this optical thickness curve could be caused by minor errors in the digital processing and correlation calculations. A summary of the results of interstate highway layer thickness measurements with the swept-frequency radar system is shown below.

	Ground Measurement cm	Swept-Frequency Radar Measurement cm
Site 1 - sta 724		
Asphalt concrete	22.6	24.2
Clay gravel base	13.3-18.6	18.2
Site 2 - sta 654		
Asphalt concrete	21.0	22.1
Clay gravel base	20.9-26.2	26.3
Site 3 - sta 634		
Asphalt concrete	21.4	20.2
Clay gravel base	30.9-36.2	31.0

At all three sites there appears to be very good agreement between ground measurements and the asphalt concrete (a difference of 1.6 cm or less at each site). Ground measurements for the clay gravel base material show this layer to vary in thickness across the width of the highway by approximately 5 cm. The highway is constructed this way to maintain the proper drainage in the base material. In each case, the swept-frequency radar thickness measurement follows the trend of the ground measurements.

4. MATHEMATICAL MODELS FOR MICROWAVE MEASUREMENTS

In order to generate data to conduct feasibility studies and to improve data analysis procedures for microwave measurements, a theoretical model was developed at WES based on plane-wave propagation to calculate the power reflectance for various terrain conditions. For the model, layer interfaces were assumed to be flat and parallel to the surface and the last layer in a formation was assumed

to be very deep in comparison with the operating wavelengths. In most cases, these assumptions are proper because of narrow antenna beamwidths and transmitted power would be limited to very small values, thus, signals could only propagate to depths that are compatible with foundation thicknesses.

The theoretical effort is based on complex electrical impedances of the various dielectric and magnetic materials that make up the layered embankment. Each layer in the embankment was assumed to have its own characteristic impedance as calculated by the equation below (Lundien 1978):

$$Z_{on} = \sqrt{\mu_n^*/\epsilon_n^*} \qquad (1)$$

$$\mu_n^* = \mu_o \mu_{rn}(1-j \tan \delta_m) \qquad (2)$$

$$\epsilon_n^* = \epsilon_o \epsilon_{rn}(1-j \tan \delta_d) \qquad (3)$$

where:

Z_{on} = characteristic impedance for the n^{th} layer, ohms

μ_n^* = complex magnetic permeability for n^{th} layer, Henry/m

ϵ_n^* = complex dielectric constant for n^{th} layer, Farad/m

μ_o = free space magnetic permeability, Henry/m

μ_{rn} = relative magnetic permeability for the n^{th} layer, dimensionless

$j = \sqrt{-1}$

$\tan \delta_m$ = magnetic loss tangent, dimensionless

ϵ_o = free space dielectric constant, Farad/m

ϵ_{rn} = relative dielectric constant for the n^{th} layer, dimensionless

$\tan \delta_d$ = dielectric loss tangent, dimensionless

These impedances cause a change in the power reflection at the surface of the layered embankment as computed by the equation shown below:

$$R = \left|(Z_{in} - Z_{air})/(Z_{in} + Z_{air})\right|^2 \qquad (4)$$

where:

$$Z_{in} = Z_{on}\{Z_{in+1}\cosh(\gamma_n t_n) + Z_{on}\sinh(\gamma_n t_n)\}/\{Z_{on}\cosh(\gamma_n t_n) + Z_{in+1}\sinh(\gamma_n t_n)\}$$

$$\gamma_n = j\omega\sqrt{\epsilon_n^* \mu_n^*}$$

and

R = power reflectance

Z_{air} = characteristic impedance for air (377 ohms)

Z_{in} = load impedance for n^{th} layer, ohms

γ = propagation factor, m^{-1}

t = layer thickness, m

ω = angular frequency, radians/sec

A computer program was written to compute power reflection for the frequency range over which the radar system is assumed to operate. In the first step for this computer program, all the input data for each layer are defined along with the controls for radar operation. The program calculates impedances at each interface starting at the lowest frequency and for the deepest material. The program cycles up through each layer, transforming impedances as it goes until it reaches the surface. At that point, a power reflectance is calculated and the next frequency is selected. The operation continues until all the frequencies have been exhausted.

One of the first steps in the validation process for the mathematical model was to compare the results of model calculations with actual measured data. The model was used to compute the reflectance from the asphalt highway previously tested with the swept-frequency radar. The results are shown in Figure 12. This model was proved useful for estimating the reflectance values for a wide range of terrain conditions and constructed foundations (see Figure 13).

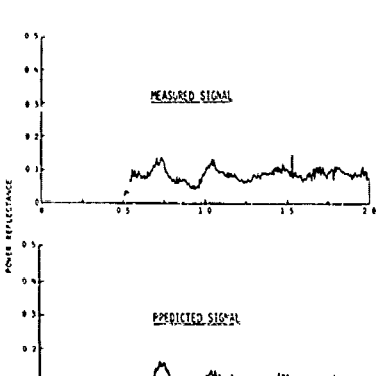

Figure 12. Comparison of predicted and measured reflection curves for asphalt highway.

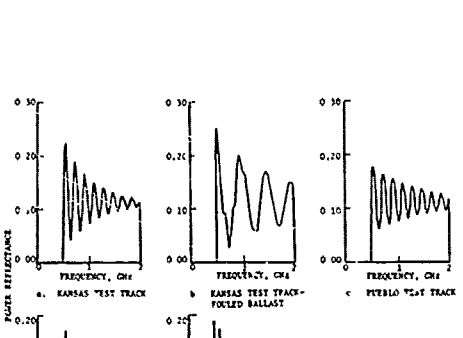

Figure 13. Power reflectance curves for railroad foundations.

5. SUMMARY

Because of the interest in surface and subsurface terrain conditions for these investigations, the wavelengths used in the microwave systems were selected to emphasize penetration into the layered materials and ranged from tens of millimeters to hundreds of millimeters. Radar systems operating at these wavelengths and using swept-frequency techniques for processing signals can be used to measure reflectivity and optical thickness of layered media, thus providing a means for estimating the dielectric constant and the physical thickness of the layers. Swept-frequency radar measurements were also found to vary with the surface roughness of the ground in a predictable manner and thus may offer the means to separate the effects of target geometry from the measurements of electrical properties.

REFERENCES

Lundien, J. R., 1966: Terrain analysis by electromagnetic means; Report 2, Radar responses to laboratory prepared soil samples. Technical Report 3-693, U. S. Army Engineer Waterways Experiment Station, CE, Vicksburg, Miss.

Lundien, J. R., 1971: Terrain analysis by electromagnetic means; Report 5, Laboratory measurements of electromagnetic propagation constants in the 1.0- to 1.5-GHz microwave spectral region. Technical Report 3-693, U. S. Army Engineer Waterways Experiment Station, CE, Vicksburg, Miss.

Lundien, J. R., 1972: Determining presence, thickness, and electrical properties of stratified media using swept-frequency radar. Technical Report M-72-4, U. S. Army Engineer Waterways Experiment Station, CE, Vicksburg, Miss.

Lundien, J. R., 1978: Feasibility study for railroad embankment evaluations with radar measurements. Miscellaneous Paper S-78-10, U. S. Army Engineer Waterways Experiment Station, CE, Vicksburg Miss.

SIMULATION OF MILLIMETER WAVE PROPAGATION IN THE ATMOSPHERE

Jerry Hopponen

Lockheed Missiles & Space Co., Inc.

Sunnyvale, California

ABSTRACT*

1. INTRODUCTION

Molecular resonances of oxygen and water vapor make clear, non-turbulent air a natural filter over the EHF (10-300 GHz) range with transfer, shielding, and emission properties not found at lower frequencies. Dispersive absorption causes attenuation, signal transit time variation, and background noise affecting signal-to-noise ratios, phase, and direction of ray propagation. The application of these effects in appropriate engineering problems is facilitated with the advent of modern digital computers which allow the latest physical theories to be applied to aid in the design of EHF systems.

Computer simulation of atmospheric transfer properties requires an accurate correlation between the physical state and the electromagnetic characteristics of the medium. One approach, employed here, is to translate the pertinent results of microwave molecular spectroscopy into a tractable form which, in turn, is used to calculate attenuation, phase dispersion, and noise for modeled radio paths in the clear atmosphere. The complex refractivity N (in parts per million) describes the interaction between millimeter waves and atmospheric molecules such as O_2 and H_2O.

The spectroscopic basis for calculating N is presented by Liebe (1977) and Rosenkranz (1975). Various trace gases will not be considered in this general paper. Once N is obtained, a ray tracing methodology simulates the deterministic aspects of EHF signal propagation.

2. METHODS

It is assumed that ray tracing theory is applicable to the simulation of the effects of clear air on signals between 10 and 300 GHz. Only atmospheric characteristics are involved, so no edge diffraction, surface reflections, or hardware effects are included. The frequency range is restricted since below about 10 GHz the lower atmosphere has little effect but the ionosphere may cause changes in signal direction, strength, and polarization. Coupling between environmental conditions and the mathematical formalism is through the complex refractivity

$$N = N_o + N_{oxy} + N_{wv},$$

where N_o is the (real) frequency-independent refractivity of moist air, N_{oxy} is the (complex) dispersive refractivity due to oxygen absorption, and N_{wv} is the (complex) water vapor refractivity. The dispersive contributions are calculated by Liebe's formulation (1977) which includes line broadening by foreign gases and also has Zeeman and Doppler broadening approximated. The non-dispersive part is calculated by the formula of Thayer (1974) and has corrections for non-ideal gas behavior.

Vertical profiles of atmospheric temperature, pressure, and water vapor content, as obtained from, for example, standard references or balloon ascents, are used in conjunction with the formulation for N to obtain profiles of the complex refractive index. Figure 1 shows attenuation

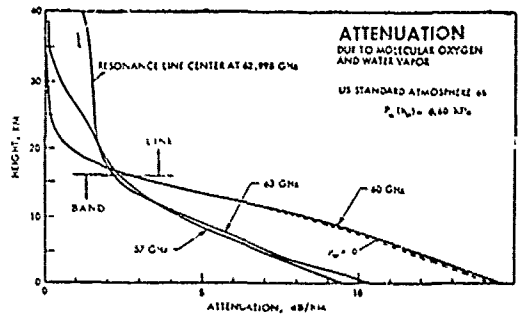

Figure 1. Attenuation Due to Molecular Oxygen and Water Vapor

(imaginary part of N, Im (N)) at 57, 60, and 63 GHz through a standard atmosphere. Figure 2 shows the real part of N, Re (N), expressed as

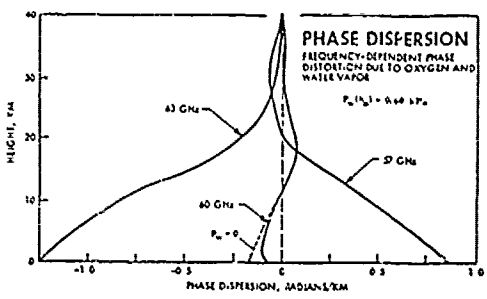

Figure 2. Phase Dispersion Due to Oxygen and Water Vapor

*ABSTRACT is at the end of the paper. Author did not comply with format.

phase dispersion. Although 60 GHz attenuation predominates in the lower atmosphere, the reduced pressure above 20 km causes line collapse, resulting in relatively small attenuation. By contrast, 57 and 63 GHz are close to absorption line centers which entails the continuing attenuation at these frequencies. This effect offers the possibility of selective shielding by the atmosphere.

In order to blend the complex refractive index profiles into a ray tracing program, several additional points must be considered. The spherical form of Snell's Law yields an expression for curved ray path length as

$$S(\theta, h) = ds/dh = \left\{ 1 - \left[\frac{n(h_o)}{n(h)} \frac{(r_o + h_o)}{(r_o + h)} \cos \theta_o \right]^2 \right\}^{-\frac{1}{2}}$$

where θ_o is the ray elevation angle at the initial height h_o and

$$n(h) = 1 + 10^{-6} \mathrm{Re}\,(N(h)).$$

Evaluation of $S(\theta_o, h)$ at points between consecutive reporting altitudes is accomplished by first interpolating the (real) refractive index n (h). Although several interpolation methods are widely used (e.g., linear or exponential), a method based on the gas law and the hydrostatic equation (Hopfield, 1969) is adopted since it is derived from physical principles. Interpolation of temperature and attenuation between data points is done linearly. For small values of θ_o (less than one degree) the expression for $S(\theta_o, h)$ becomes numerically unstable but can be approximated by a closed-form quadratic expression similar to that given by Blake (1968).

The interpolation methods above are incorporated into a computer program to evaluate such quantities as

$\int_o^H S(\theta_o, h)\, dh$ (ray path length),

$\int_o^H n(h)\, S(\theta_o, h)\, dh$ (radio range), and

$\int_o^H \alpha(h)\, S(\theta_o, h)\, dh$ (attenuation), where

$\alpha(h)$ is power attenuation.

Here H is taken to be 80 km instead of ∞ as the contribution of the atmosphere above this level is very small. The noise temperature due to radiation downwelling to the Earth's surface along a ray of elevation θ_o is

$$T_D = \int_o^H \alpha(h)\, T(h)\, T_D(h)\, S(\theta_o, h)\, dh$$

where $T_D(h) = \exp\left(-\int_o^h \alpha(t)\, S(\theta_o, t)\, dt\right)$. Radiation upwelling to a height K yields a noise temperature

$$T_U = \int_o^K \alpha(h)\, T(h)\, T_u(h)\, S(\theta_o, h)\, dh,$$

where $T_U(h) = \exp\left(-\int_h^K \alpha(t)\, S(\theta_o, t)\, dt\right)$.

All integrals may be evaluated numerically by adaptive Romberg integration, which shifts to higher order methods to accelerate convergence. To facilitate computing, special numerical methods can be devised to greatly reduce the time required in obtaining both T_D and T_U. The resulting ray trace program proceeds in a surface-to-space fashion and provides information useful to EHF system design.

3. RESULTS

Computer ray tracing with a vertical ray path through standard summer and winter atmospheres reveals the seasonal variation of attenuation shown in Figure 3. The shaded window regions exhibit less change than the narrow absorption bands where attenuation may vary over 30 dB. The

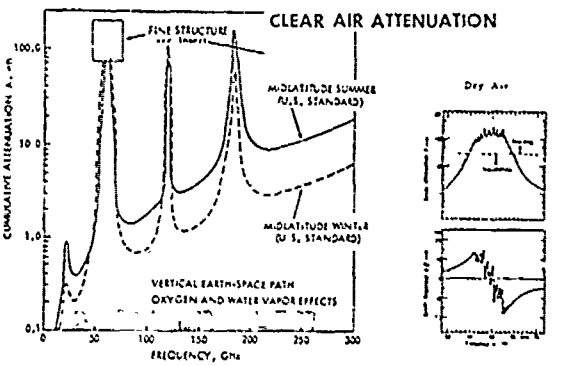

Figure 3. Clear Air Attenuation

crossover in the 60 GHz band (which is taken to include the isolated 1^- line at 118.75 GHz) reflects an intricate temperature dependence. The behavior around 60 GHz is exemplified by the two inserts, the bottom one showing phase dispersion, but is not calculated owing to the number of additional computations required.

The effect of dispersion on ray bending and phase delay is most pronounced at low elevation angles and is shown in Figure 4 for 0^o and 45^o.

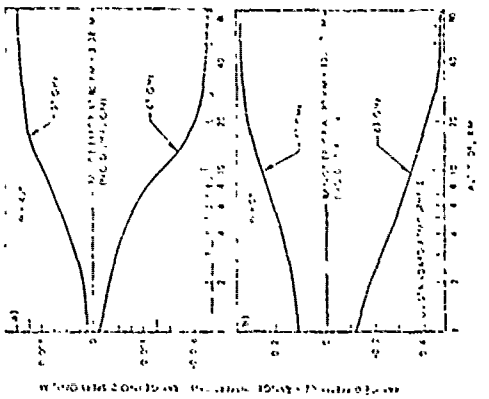

Figure 4. Effect of Dispersion in Refractivity

Radio range was computed both with and without dispersion: the difference is plotted as a function of altitude. As suggested by the lower insert of Figure 3, the dispersive effect at 57 and 63 GHz is much more in evidence than at 60 GHz, which is approximated by the straight line through the center of the chart. The wavelengths are roughly 5 mm, so the range difference is relatively large.

Noise temperature due to atmospheric emission is a consideration in determining overall signal-to-noise ratio of millimeter wave systems operating through air. Figure 5 shows an extreme seasonal variation of noise temperature due to radiation upwelling along a vertical ground-to-space

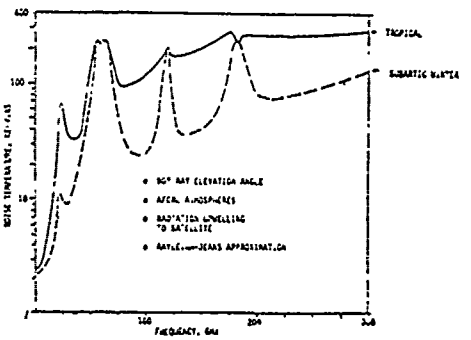

Figure 5. Noise Temperature for a Tropical and Subarctic Atmosphere

path. Surface contributions, which may appear in the window regions, are not included. Although the strong absorption regions show little seasonal change, the other bands may show changes exceeding 70 kelvins.

Downwelling radiation yields nearly the same noise temperature as upwelling radiation, except when absorption is strong as shown in Figure 6.

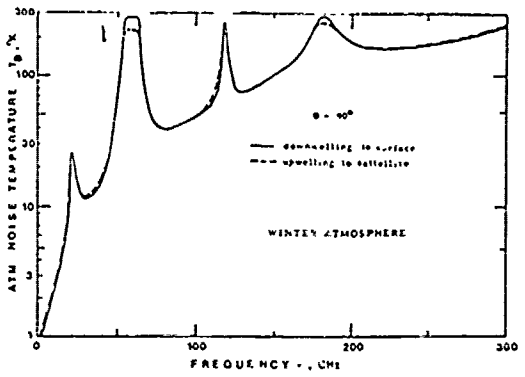

Figure 6. Noise Temperature for a Winter Atmosphere

When atmospheric penetration is limited, the noise detected by a ground-based antenna is roughly proportional to ambient air temperature. Figures 3, 5 and 6 can be used for a coarse approximation to the effect of the atmosphere on annual, vertical, earth-to-satellite link performance.

4. CONCLUSIONS

Molecular absorption by atmospheric gases poses an ever-present constraint on the design of systems in the 10-300 GHz band. Transfer and emission characteristics can be predicted from profiles of meterological data. Accurate computer calculations of radio wave propagation effects require a sound basis in physical theory, laboratory verification, and numerical methods. The major uncertainties for predicting system performance lie in the variable nature of the air mass in general and also in anomalous water vapor absorption in the window regions.

REFERENCES

Blake, L. V., 1968: Ray height computations for a continuous non-linear refractive index profile, Radio Sci., 3 (1), 85-95.

Hopfield, H. A., 1969: Low quartic tropospheric refractivity profile for correcting satellite data. J. Geophysical Res., 74, 4487-4499.

Liebe, H. J., Grimmestad, G. G., and Hopponen, J. D., 1977: Atmospheric oxygen microwave spectrum-experiement versus theory. IEEE Trans., AP-25, 327-335.

Rosenkranz, P. W., 1975: Shape of the 5mm oxygen band in the atmosphere. IEEE Trans., AP-23 (4), 498-506.

Thayer, G. D., 1974: An improved equation for the radio refractive index of air. Radio Sci., 9, 803-807.

ABSTRACT

Design of millimeter wave systems is facilitated by computer simulation of the atmosphere's contribution to signal attenuation, phase delay, dispersive ray bending, and noise temperature. The discussion begins with the complex refractive index of air, which couples the mathematical formalism to the assumed physical environment, and proceeds to the integral expressions for curved path length, radio range, cumulative attenuation, and noise temperature due to upwelling and downwelling atmospheric emission. Numerical methods pertinent to the evaluation of these intergrals are described. The overall methodology of the ray tracing computer program permits use of actual air data as well as standard atmospheric models, and models propagation through inhomogeneous clouds. Results are presented on seasonal variation of attenuation, the effect of dispersion in refractivity, comparison of upwelling and downwelling noise temperatures, and the effect of climatic extremes on noise temperature at several viewing angles.

H_2O NEAR MILLIMETER ABSORPTION: THE EFFECTS OF LINE SHAPE VARIATIONS

Dr. Douglas R. Brown and Donald E. Snider

US Army Atmospheric Sciences Laboratory

White Sands Missile Range, New Mexico

ABSTRACT

The fundamental atmospheric attenuator in the NMMW domain is water vapor. The laboratory H_2O NMMW absorption spectrum contains an anomalous component variously ascribed to far line wings, water dimers, or water clusters. Statistical line broadening theory argues for the modification of traditional line shapes. We introduce the Super Kinetic line profile to incorporate the results of statistical line broadening theory, and demonstrate a possible resolution of the NMMW H_2O spectrum anomaly.

As has been known for some time, the use of standard theoretical techniques to compute near millimeter H_2O vapor absorption gives results which do not agree with experimental measurements in the psuedo windows between strong H_2O lines: the measurements are consistently higher than the predictions of theory (Burch, 1968). This discrepancy has been ascribed to poorly known line widths (Frenkel & Woods, 1966), far line wing contributions ignored in the computation, dimers (Gebbie et al., 1968), water clusters (Liebe, 1979), and various induced dipole effects (Waters, 1976).

We will briefly present our reasons for believing a natural modification of the standard theoretical approach for computing water vapor absorption provides marked improvement in comparison to experimental data.

1. GASEOUS ABSORPTION COEFFICIENT

The gaseous absorption coefficient for a single line can be defined for our purposes as the product of three factors,

$$\kappa(\nu) = \text{Line Strength} \times \text{Number Density} \times \text{Line Profile } (\nu) \quad (1)$$

$$= S \times N \times \phi(\nu)$$

where the frequency dependence has been confined to the line profile function $\phi(\nu)$. In general, the line strength S depends primarily on the molecular model including such quantities as the dipole moment, the energy levels of the line in question and the molecular partition function. The line strength can be measured quite accurately and theory and experiment are in good agreement. The number density, N, depends for the most part on environmental factors such as temperature and pressure, once the basic active constituent has been fixed. The line profile function, $\phi(\nu)$ is a statistical quantity describing the average distribution in frequency of the photons absorbed by the active gas. As such, it is a potentially complicated function of the molecular model and the collision process.

In our review of the H_2O vapor absorption problem it was the line profile that we were led to consider as a possible source of error in theoretical computations. The use of different line profiles, such as Van Vleck & Weisskopf (Van Vleck & Weisskopf, 1945) or the Gross (Gross, 1955) line profile, provide different predicted absorption and thus the theory - measurement discrepancy also varies., There further appears to be no foundation for either to be

selected as the "correct" profile for H_2O vapor line shapes. A similar discrepancy exists in the infrared domain in the 8 to 12 micron, and 3.5 to 5 micron window where H_2O associated absorption cannot yet be predicted by theory. The existence of a similar discrepancy in two widely separated domains where theory cannot predict H_2O vapor band absorption in windows near H_2O vapor band absorption is at the least a remarkable coincidence. We believe that it might be more than that, rather that a similar mechanism is responsible, in part, for both.

2. LINE PROFILE DERIVATIONS

The two profiles commonly employed in the calculation of molecular millimeter absorption are the Van Vleck & Weisskopf (VVW) profile and the Gross (henceforth termed the Kinetic) profile. The derivations of these profiles are fundamentally analogous. Each is based upon classical principles of one dimensional harmonic oscillators, interacting with a spatially uniform time varying electric field. The differences between the two are primarily due to the assumptions as to which final state the perturbed oscillators are allowed to relax, and how that relaxation is allowed to occur. Gross in his derivation employs a kinetic equation to solve for the absorption, while VanVleck and Weisskopf solve the oscillator equation itself. The resulting expressions are then quantized to provide the actual profile functions.

Implicit assumptions have been made in these derivations that have become clear as collision theory has grown (Griem, 1974; Breene, 1961). These profiles are now included within the class using the Impact Approximation. Within this approximation the following assumptions are made: a) that all collisions are instantaneous, and b) that only binary collisions occur, that is the molecule collides with only one perturber at a time. The resulting line profile is not sensitive to the detailed collision physics and is therefore independent of the collision forces. The impact approximation confines the primary effects of changes in the collision environment to the line width parameter and the line shift. It should be noted that quantum mechanical treatment of the collision process made using the assumptions of the impact approximation do not change the resulting line profile; they do provide a better value for the line width and line shift parameters.

The Impact Theory domain can be best summarized by considering the collision time t_c versus the radiation time t_R. In general, the impact approximation requires

$$t_c \ll t_R \tag{2}$$

that is, the collision itself occurs during only a small interval during the radiation of a photon. When this condition is violated, the impact theory will not apply. Since $t_R = \Delta\nu^{-1}$ where $\Delta\nu$ is the frequency shift from line center, eventually for $\Delta\nu$ large enough, t_R will be less than t_c and we must consider the time evolution of the collision.

When this situation occurs the statistical approximation holds. The theory now must consider the collision with an ensemble of perturbers, occurring over a finite, that is extended interaction time. The specific form of the interaction potential becomes important in this description, as the line profile is predicted to have potential dependent frequency behavior:

$$1/\nu^{\frac{n+3}{n}} \tag{3}$$

where n is the exponent in the interaction potential, $E = r^{-n}$. In the present context, n varies from 3 to 6 spanning from dipole - dipole to dipole - induced dipole interactions. Thus, the profile frequency dependence varies

from -2 to -1.5 in the line wings (Townes & Schawlow, 1955).

The point at which the transition from impact to statistical broadening occurs is not well defined, depending on both temperature and pressure. Generally, it increases with temperature and decreases with pressure. Cold, low altitude conditions should maximize the effects of statistical broadening.

3. APPLICATION TO THE FAR INFRARED

In order to incorporate the results of the statistical broadening theory, a profile function must be selected and modified. In the context of the derivations of the Kinetic profile and the VanVleck&Weisskopf profile, it is not possible to introduce a modified interaction potential and proceed with their respective methods of solution. First, because their methods do not allow for more complicated potentials, and second, because so doing would not change the impact approximation which is a necessary part of their theories, we decided to heuristically modify a profile function to allow, but not force, the inclusion of statistical broadening effects into the profile expression.

The Kinetic Profile was chosen for this modification primarily for esthetic reasons; there is no reason that the VanVleck&Weisskopf could not also be employed.

The modification consists of allowing the far wings of the line profile, beyond some frequency $\Delta\nu_m$ from line center, to deviate from the essential Lorentzian behavior at line center. The cores of the H_2O lines have been demonstrated to be **Lorentzian to a high** accuracy (Liebe et al., 1969). The new profile, which we have named the Super Kinetic, is defined as

$$\phi_{sk}(\nu,\gamma) = \frac{NORM}{\pi\gamma}\left[\frac{(\nu_o^2-\nu^2)^2}{2\gamma\nu}+1\right]^{-1} \qquad |\nu-\nu_o|\leq\Delta\nu$$

$$= \chi\frac{NORM}{\pi\gamma}\left[\frac{(\nu_o^2-\nu^2)\eta}{2\gamma\nu}+1\right]^{-1} \qquad |\nu-\nu_o|>\Delta\nu \qquad (4)$$

where χ is defined such that

$$\phi_{sk}(|\nu-\nu_o|=\Delta\nu_m) = \lim_{\delta\to o}\phi_{sk}(|\nu-\nu_o|=\Delta\nu_m+\delta) \qquad (5)$$

to insure that ϕ_{sk} is continuous at $\nu-\nu_o=\Delta\nu_m$. NORM is a normalization factor defined by

$$\int_o^\infty \phi_{sk}(\nu)d\nu = 1 \qquad (6)$$

The normalization of the Kinetic Line Profile and Super Kinetic Profile was computed numerically for lines at different frequencies ν_o and was confirmed to be in agreement with eq. 6 to within ±0.1%. Explicitly, NORM is defined

$$NORM = \frac{\eta}{2}\ SIN\ \frac{\pi}{\eta} \qquad (7)$$

The modifications to the standard Kinetic Profile are the η exponent which no longer must have a value 2, but is limited by normalization constraints to the range

$$1.0<\eta<\infty \qquad (8)$$

and by the Statistical Broadening Theory to the range

$$1.5\leq\eta\leq 2 \qquad (9)$$

for potentials of interest here, and the crossover frequency $\Delta\nu_m$ from impact to statistical broadening. The range for $\Delta\nu_m$ is not as well determined as that for η.

The parameter η is controlled by the relative number densities of perturbers with different interaction potentials with respect to the active molecule, in this case H_2O. Thus, η should change with different buffer gases and different relative humidities. The frequency crossover $\Delta\nu_m$ should be most sensitive to temperature and pressure changes, increasing for higher temperatures and lower pressures.

4. ANALYSIS OF H_2O MILLIMETER ABSORPTION

Water vapor absorption is calculated theoretically using standard high resolution line by line techniques where the AFGL line parameters (McClatchy et al., 1973)) are used for characterizing the H_2O lines. This technique employing the usual line profile functions provides a fit to general H_2O experimental data shown in Fig. 1. The normal recourse in light of this result is to employ a "continuum" contribution, empirically determined, to force agreement with the experimental data. The source of this continuum is still a point of some controversy (see this conference proceedings).

Use of the Super Kinetic profile can change the result significantly. Because the application of a rigorous statistical broadening theory to the H_2O molecule is beyond the intent of this paper, we have fit the η and $\Delta\nu_m$ parameters to the data. The result is shown in Fig. 2. The values found for 760 torr, 298°K, 7.5 gm/m^3 H_2O absolute humidity were $\eta \simeq 1.88$, and $\Delta\nu_m \simeq 10$ halfwidths. There now appears to be no need for an H_2O millimeter continuum.

Though this result is encouraging, caution must be used. The absorption in the 10μ and 4μ windows due to H_2O should also be, if not explained, then the size of the discrepancy significantly reduced by this same mechanism. Such a result seems hopeful.

The H_2O millimeter absorption discrepancy has a ν^2 dependence. But due to the functional form of the line profiles in this frequency domain, this must be expected. Any increase in line attenuation will be reflected in the line wings below 20 wavenumbers (600 GHz) as a ν^2 dependent term, since all the valid line profiles go to zero at zero wavenumber ν^2. For this reason, a fit to experimental data for one set of physical conditions is not sufficient to test the hypothesis. Data are required on the detailed pressure and temperature dependence.

A preliminary confirmation of the pressure dependence was made by Aganbekyan et al. (Aganbekyan et al., 1971) in the submillimeter windows at 34.5, 27.8, and 22.2 wavenumbers. They found that in those windows where wing absorption predominates the absorption depends on pressure as

$$\kappa = p^{-1.9} \qquad (10)$$

for constant relative humidity. This is in agreement with our value of $\eta \simeq 1.88$.

The available temperature dependence data are more difficult to interpret and have not been completed.

5. CONCLUSIONS

The Super Kinetic profile does produce a significant improvement between experimental and theoretical H_2O millimeter absorption. The degree to which it explains the discrepancy must await a more complete application of the statistical broadening theory to the H_2O molecule and a subsequent comparison to experimental data. The present result should at least argue for the consideration of more complicated collision effects in the H_2O line formation problem.

REFERENCES

Aganbekyan, K. A., A. Yu. Zrazhevskiy, M. A. Kolosov, and A. V. Sokolov, 1971: Investigations of absorption as a function of air pressure at the wavelengths of 0.29, 0.36, and 0.45 mm. Radio Eng. Electron. Phys., 16, 1433-1437. [Russian version, Radiotek. Electron., 16, 1564-1568.]

Breene, R. G., 1961: The Shift and Shape of Spectral Lines. Pergamon Press, New York.

Burch, D. E., 1968: Absorption of infrared radiant energy by CO_2 and H_2O. III, Absorption by H_2O between 0.5 and 36 cm^{-1} (278 μ - 2 cm). J. Opt. Soc. Amer., 58, 1383-1394.

Frenkel, L. and D. Woods, 1966: The microwave absorption by H_2O vapor and its mixture with other gases between 100 and 300 Gc/s. Proc. IEEE, 54, 498-505.

Gebbie, H. A. and W. J. Burroughs, 1968: Observations of atmospheric absorption in the wavelength range 2 mm-300 μm. Nature, 217, 1241-1242.

Griem, H. R., 1974: Spectral Line Broadening by Plasmas. Academic Press, New York.

Gross, E. P., 1955: Shape of collision-broadened spectral lines. Phys. Rev., 97, 395-403.

Liebe, H. J., M. C. Thompson. and T. A. Dillon, 1969: Dispersion studies of the 22 GHz water vapor line shape. J. Quant. Spectrosc. Radiat. Transfer, 9, 31-47.

Liebe, H. J., 1979: private communication.

McClatchey, R. A., W. S. Benedict, S. A. Clough, D. E. Burch, R. F. Calfee, K. Fox, L. S. Rothman, and J. S. Garing, 1973: AFCRL Atmospheric Absorption Line Parameters Compilation. AFCRL-TR-0096.

Swihart, T. L., 1971: Basic Physics of Stellar Atmospheres. Pachart Publishing, Tucson.

Townes, C. H., and A. L. Schawlow, 1955: Microwave Spectroscopy. McGraw-Hill, New York.

VanVleck, J. H. and V. F. Weisskopf, 1945: On the shape of collision-broadened lines. Rev. Modern Phys., 17, 227-236.

Waters, J. W., 1976: Absorption and emission by atmospheric gases. In Methods of Experimental Physics, Vol. 12, Astrophysics, Part B, Radio Telescopes, Edited by M. L. Meeks, Academic Press, New York, 142-176.

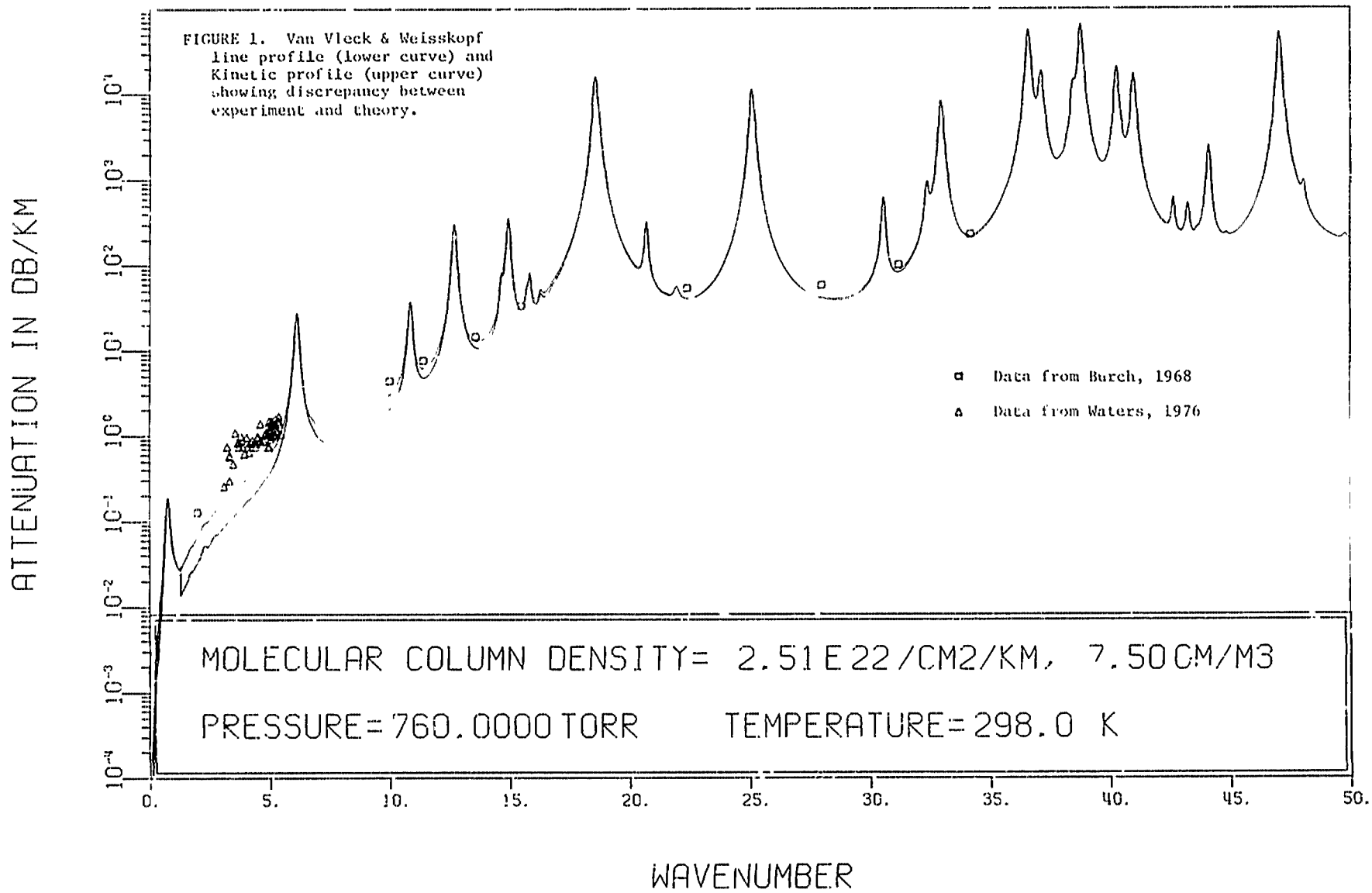

FIGURE 1. Van Vleck & Weisskopf line profile (lower curve) and Kinetic profile (upper curve) showing discrepancy between experiment and theory.

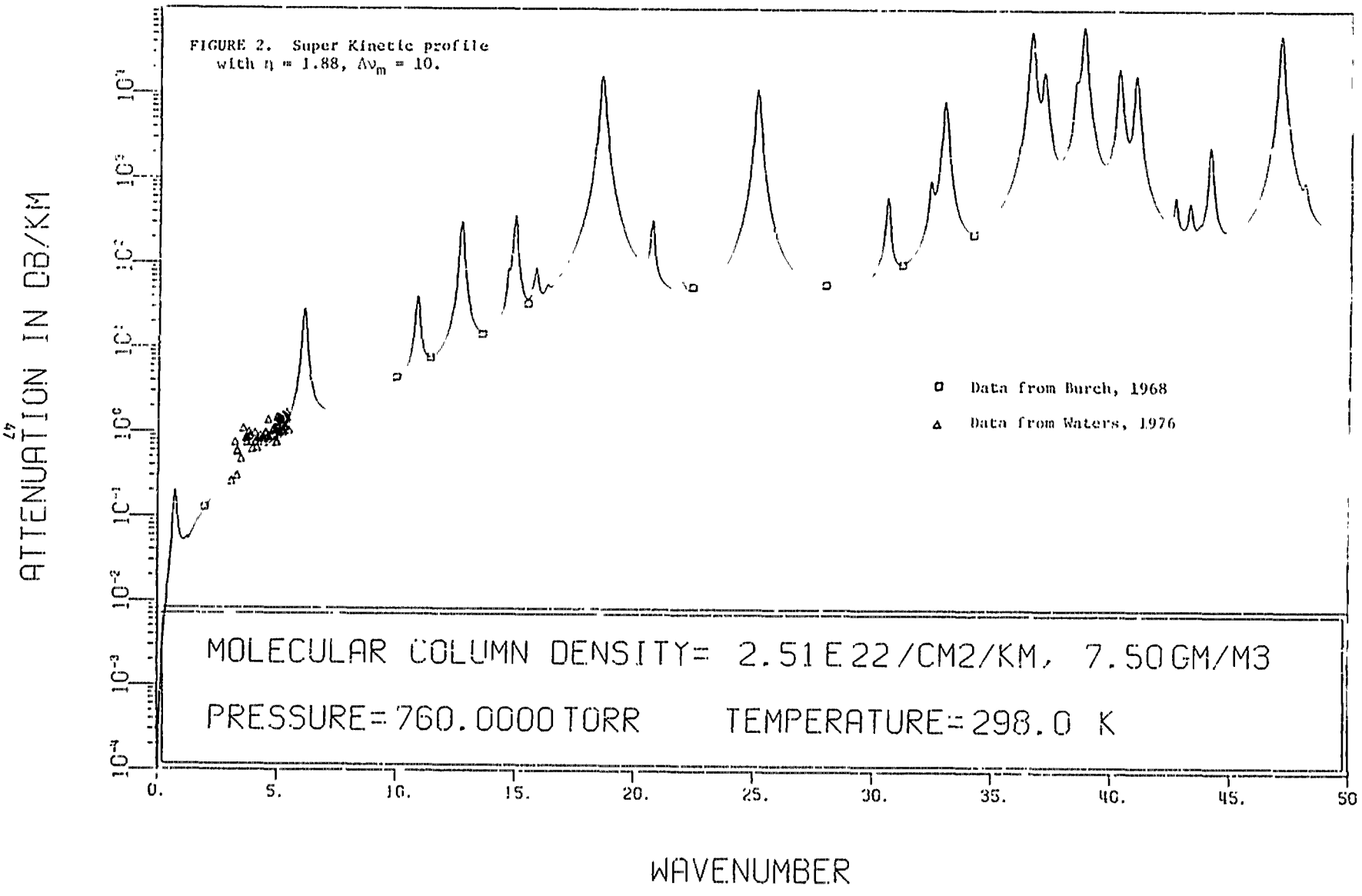

FIGURE 2. Super Kinetic profile with $\eta = 1.88$, $\Delta\nu_m = 10$.

SEASONAL ATMOSPHERIC EMISSION AT 94 GHz*

J. Hank Rainwater, J. J. Gallagher, P. B. Reinhart

Georgia Institute of Technology
Engineering Experiment Station
Atlanta, Georgia 30332

ABSTRACT

A novel beam-waveguide millimeter radiometer feeding a 10 foot parabolic dish has been used to measure seasonal atmospheric emissions at 94 GHz. The radiometer incorporates a beam waveguide in the RF section which allows Dicke switching and calibration to be accomplished at the focal points between the beam waveguide lenses. A unique directional waveguide filter, designed and built at Georgia Tech, using a single circularly polarized cavity is used to inject the LO into a Schottky barrier mixer. The radiometric antenna half-power beamwidth is under 0.2°, thus these measurements represent atmospheric variations occurring within small spatial elements. Measurements to date have been made during high humidity, summertime conditions and during less humid, winter sky conditions; the data show seasonal emission variations due to clouds and other atmospheric conditions. Ground based measurements at the zenith and celestial equator with varying data integration times have been made. Antenna temperatures of the solar radiosphere have also been measured at a variety of azimuthal angles and atmospheric conditions. Theoretical calculations incorporating state-of-the-art H_2O, O_2, and O_3 absorption line shape expressions, water vapor distribution, temperature and pressure profiles, have been performed and exhibit a disparity with experimental measurements.

The empirical measurements have been reduced into a variety of formats including power spectral density plots which aid understanding of the nature of atmospheric "clutter". Theoretical calculations are compared with the experimental measurements and differences analyzed.

1. INTRODUCTION

The nature of clutter in atmospheric emission, i.e., short term fluctuating components of emission, is not well understood nor characterized in the millimeter wave region. This program was established by DARPA to help establish a data base of atmospheric emission statistics which would allow realistic system planning, especially for down looking target detection radiometers. The measurements described herein were made with a millimeter wave radiometer (94 GHz) at Naval Research Laboratory (NRL) in Washington, D.C. Antenna temperatures of the sky for various atmospheric conditions were recorded and compared with theoretical calculations based on current meteorological conditions.

2. DESCRIPTION OF THE RADIOMETER SYSTEM

In August of 1978 construction of a Dicke switched radiometer began at Georgia Tech (GT) that would permit the NRL 10' dish to be operated in the prime focus mode. Because the prime focal length of the antenna is approximately 3', the radiometer front-end feed must diverge the radiation over a large angle (with appropriate edge illumination taper) in order to achieve the narrow antenna beamwidths desired for atmospheric observations. In order to fulfill these requirements, a novel beam waveguide radiometer front-end scheme was devised. The quasi-optical approach developed allows Dicke switching and calibration load imaging to be performed behind the 10' dish feed horn, thus eliminating the problems of switching a highly diverging beam.

Figure 1 shows the RF portion of the radiometer in block form. The beam waveguide consists of three lenses equally spaced at twice the focal length of a single lens. Goubau (1961) showed that a reiterative field having linear polarization, a Gaussian distributed radial amplitude and a uniform phase front would appear in the center plane of each lens when the lenses were of finite diameter and had a paraboloidal surface. The beam waveguide is excited by conical horns in WR-10 waveguide. The complete beam waveguide portion of the radiometer with three lenses and two horns has a total insertion loss of 2.8 dB referenced to the conical horn waveguide ports (see inset in Figure 1).

*This measurement program is funded by the Naval Research Laboratory under Contract No. N00173-78-C-0165 to the Georgia Institute of Technology.

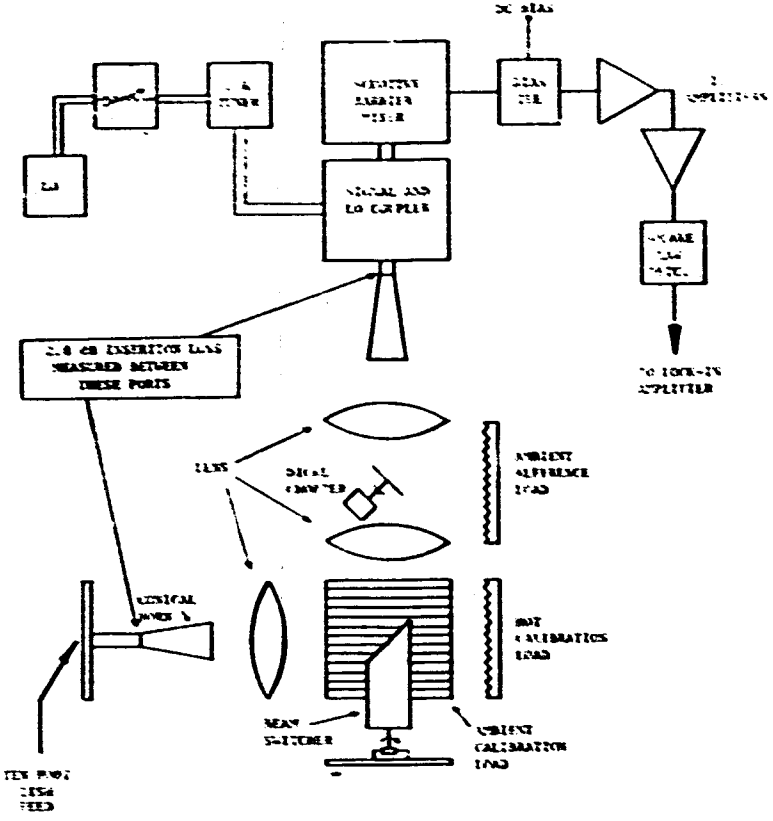

Figure 1. Radiometer RF Front-End

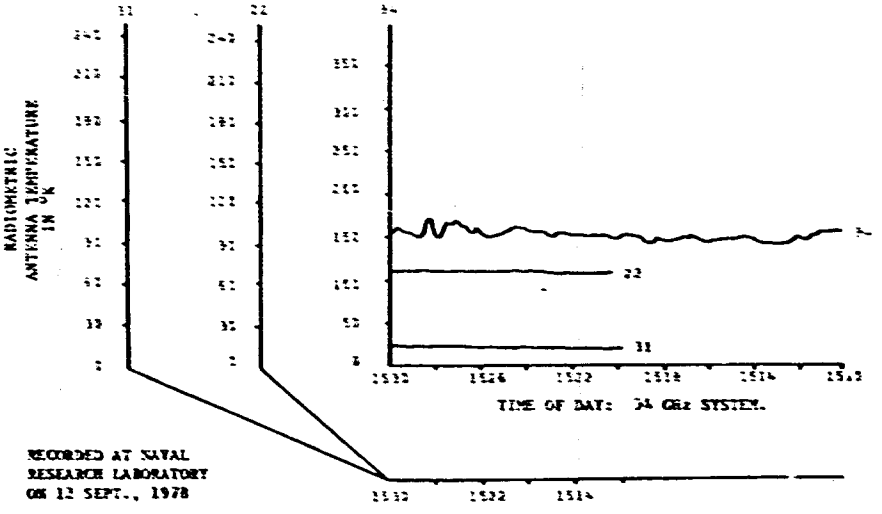

AVERAGE METEOROLOGICAL CONDITIONS AT ANTENNA SITE

AIR TEMP: 303.69°K WATER VAPOR: 20.53 g/m^3 PRESSURE: 1011.0 mb

Optically hazy with scattered cumulus clouds, no clouds over zenith during data run.

22, 31 GHz SYSTEM PARAMETERS		94 GHz SYSTEM PARAMETERS	
DSB HETERODYNE SYSTEM		DSB HETERODYNE SYSTEM	
LO FREQ.	22.234 GHz, 31.4 GHz	LO FREQ.	94.356 GHz
IF FREQ.	10-300 MHz	IF FREQ.	1.6 ± 0.7 GHz
POST DETECTION INTEGRATION CONSTANT	0.5 sec	POST DETECTION INTEGRATION CONSTANT	5.00 sec
ANTENNA TEMPERATURE NOISE ΔT_{MIN}	0.098°K	ANTENNA TEMPERATURE NOISE ΔT_{MIN}	1.11°K
ANTENNA BEAM HALF-WIDTH AT -20dB POWER POINTS	22 GHz, 10°		
	31 GHz, 9°		

Figure 2. Zenith Antenna Temperatures: 22,31,94 GHz On 12 Sept 78

Dicke switching is accomplished with a motor driven "bow-tie" chopper set at 45° to the beam waveguide between the first pair of lenses. The chopper alternately switches the radiometer beam between an ambient temperature reference load (black-body) and the beam switch reflector, viewed through the second lens, at a 40 Hz rate. With the beam switcher in the position shown in Figure 1, the radiometer is Dicke switched between the reference load and the medium viewed via the third beam waveguide lens and horn. The second conical horn feeds a circular waveguide horn which in turn illuminates the 10' parabolic dish (F/D = 0.33) from the prime focus.

Calibration of the radiometer is accomplished by rotating the beam switcher to view either an ambient temperature calibration load or a heated calibration load. When the ambient load is viewed the radiometer yields a zero output which can be compared to the output obtained when the hot load is viewed. All front end losses have been accounted for in the calibration procedure since each calibration load is viewed through a single lens, while the radiometrically observed medium is seen through two lenses, a conical horn and dish feeding horn, with respect to the Dicke reference load.

The double sideband RF information is down converted to an IF frequency (0.9 to 2.3 GHz) via a single ended Schottky barrier mixer fundamentally pumped by a reflex klystron at 94.556 GHz. The local oscillator is injected through a directional waveguide filter designed and built at Georgia Tech. This filter differs from the conventional two cavity structure in that only a single circularly polarized cavity is used. Because the cavity is polarized with two orthogonal, degenerate TE_{112} modes, nearly 100 percent of the incident power is coupled into the cavity. This results in a relatively low loss, reflection-less filter that can be constructed to provide 1.5 dB local oscillator signal loss and 0.5 dB RF signal loss near 100 GHz without difficulty.

The IF output of the radiometer is detected by a tunnel diode, operating in the square law range, and synchronously amplified and integrated by a lock-in amplifier. The lock-in amplifier (Ithaco 391A) has adjustable video gain and low pass filter bandwidth controls enabling the radiometer to operate over a large dynamic range. (For instance antenna temperatures of both the sky and the solar radiosphere can be measured accurately.) The integrated radiometer output voltage (proportional to antenna temperature) has been recorded both by chart recorders and magnetic FM tape recorders.

3. THEORETICAL STUDY

3.1 The Non-fluctuating Atmospheric Model

Atmospheric antenna temperatures may be calculated from model atmospheres based on the solution to the differential equation of radiative transfer originally developed by Chandrasekhar (1950). According to a method developed by McMillan et al. (1977), if the atmosphere can be vertically stratified into horizontal slabs, with constant values of pressure, temperature and water vapor density the antenna temperature of each slab as measured by a radiometer would be given by

$$T_{SLAB} = T(1 - e^{-\alpha \ell \sec\theta}) + T_o e^{-\alpha \ell \sec\theta} ,$$

where
- T_{SLAB} - antenna temperature of slab of thickness ℓ viewed at zenith angle θ.
- T - physical temperature of slab.
- α - atmospheric attenuation, inverse length units.
- T_o - antenna temperature that would be measured above the slab.

The parameter α is a function of the contributions of the millimeter and submillimeter H_2O and O_2 absorption line wings in the 94 GHz "window".[2] In the NRL program, 39 H_2O and 40 O_2 lines up to 1000 GHz were included in the computation of α.

The computer program which calculates the antenna temperature of the atmosphere according to summations of equation (1), divides a 50 km atmosphere into 500 slabs of equal thickness. The temperature, pressure and water vapor density of each slab are obtained from Air Force Geophysical Laboratory (formerly AFCRL) standard atmospheric tables. Ideally, radiosonde data on the measurement days in question would more accurately model the atmosphere; however, the data obtained from the National Weather Service arrived too late to be incorporated into the current theoretical calculations.

3.2 Studies of the Fluctuating Components in Emission

3.2.1 Introduction

The atmospheric model discussed in the previous section is fairly simplistic in its approach and thus leads to analytically tractable solutions. For instance, by neglecting scattering effects in layers of cloud and rain the radiative transfer equations yield simple integral expressions which can be evaluated numerically as in the non-fluctuating model. However, in order to more accurately model the atmosphere, clouds

and other inhomogeneous regions need to be included in the formulation of sky brightness temperatures. The authors are currently studying and searching the available literature on atmospheric modeling, especially in regard to the effect of inhomogeneous regions on short term fluctuations in the sky brightness.

Section 3.2.2 is an annotated bibliography of this on-going study. Most of the referenced literature treats the case of fluctuations at ground level along horizontal paths. The importance of wind velocity in moving inhomogeneous regions through the antenna beam is indicated in Reference 9. One phase of the experiments which are being performed provides for observations in the direction of the wind by moving the dish with and against the wind. This method was suggested by Dr. J. Hollinger of NRL.

Some papers have treated the effects of atmospheric radiation variations on the vertical measurement of fluctuations in antenna temperature [14, 15, 21, 22 and 24]. Reference 24 reports on calculations of power spectra in the submillimeter wavelength region in the range 6.5×10^{-5} - 1.6×10^{-2} Hz and 1 - 200 Hz and have indicated that no excess noise has been detected. These were reported for one site in the Italian Alps. More recently, fluctuation measurements have been reported by another Italian group, and their work is currently in preparation for public ion.

Reference 15 is primarily concerned with the power spectrum between 4×10^{-3} Hz and 0.25 Hz of emission and absorption near the 350 μm atmospheric window. These measurements were also made at a single location. Reference 14 deals with the fluctuating component in antenna noise temperature resulting from varying atmospheric absorption along the line-of-sight. Even in clear weather fluctuations have been observed. The frequency range of interest is the 1 - 10^{-2} Hz range. Operating frequencies of the radiometers were S GHz and 3 GHz. Reference 27 looked for long term fluctuations, but found no significant contributions for integration times up to 160 minutes.

3.2.2 Annotated Bibliography

1. L. Tsang, et al., "Theory for Microwave Thermal Emission from a Layer of Cloud or Rain", IEEE Trans. AP, Vol. AP-25, No. 5, pp. 650-657, Sept. 1977. -- Formulation of scattering effects of layers of clouds and rain on down looking radiometers. Derive radiative transfer equations accounting for polarization dependence and drop size distributions. Model clouds and solve resulting equations for brightness versus frequency up to 300 GHz.
2. G. G. Haroules, W. E. Brown, "A 60-GHz Multi-Frequency Radiometric Sensor for Detecting Clear Air Turbulence in the Troposphere", IEEE Trans. Aero. Elec. Sys., Vol. AES-5, No. 5, pp. 712-723, Sept. 1969. -- Model turbulence regions with respect to temperature anomalies.
3. A. M. Zavody, "Effect of Scattering by Rain on Radiometer Measurements at Millimeter Wavelengths", Proc. IEE , Vol. 121, No. 4, pp. 257-263, April 1974, -- Emission from rain due to scattering effects at 37, 72 and 110 GHz discussed. Correction term to antenna temperature for rain in beam area derived.
4. R. S. Lawrence, J. W. Strohbehn, "A Survey of Clear-Air Propagation Effects Relevant to Optical Communications", Proc. IEEE, Vol. 58, No. 10, pp. 1523-1545, Oct. 1970. -- Good treatment of how inhomogeneous regions are modeled in the optical region Large and small scale refractive variations treated.
5. J. W. Strohbehn, "Line-of-Sight Wave Propagation Through The Turbulent Atmosphere", Proc. IEEE, Vol. 56, No. 8, pp. 1301-1317, August 1968. -- A review of treatments involving random fluctuations from optical to millimeter wavelengths. Geometrical models of turbulent mediums presented.
6. A. Ishimaru, "Fluctuations of a Beam Wave Propagating Through a Locally Homogeneous Medium", Radio Science, Vol. 4, No. 4, pp. 245-305, April 1969, -- Spectral features of index of refraction and its effects on fluctuations.
7. H. J. Liebe, J. D. Hoppenen, "Variability of EHF Air Refractivity with Respect to Temperature, Pressure, and Frequency", IEEE Trans. AP, Vol. SP-25, No. 3, pp. 336-345, May 1977. -- Treat 40 to 140 GHz band for simulated atmosphere up to 40 km. Present graphs of refractivity vs. frequency, temperature and pressure. Model O_2 spectral contributions to refractivity variations.
8. C. B. Hogge, R. R. Butts, "Frequency Spectra for the Geometric Representation of Wavefront Distortions Due to Atmospheric Turbulence", IEEE Trans. AP-24, No. 2, pp. 144-154, March 1976. -- Frequency spectrum of fluctuations versus wind velocity and antenna aperture derived.
9. L. Shen, "Remote Probing of Atmosphere and Wind Velocity by Millimeter Waves", IEEE Trans. AP, Vol. AP-18, No. 4, pp. 493-497, July 1970. -- Effect of wind on C_n^2 discussed and modeled. Limitations concerning knowledge of path wind velocities discussed.

10. M. B. Kanevskii, "The Problem of the Influence of Absorption on Amplitude Fluctuations of Submillimeter Radio Waves in the Atmosphere", Scientific-Research Radio-Physics Institute, Vol. 15, No. 12, pp. 1939-1940, Dec. 1972. -- Show intensity dependence of amplitude fluctuations on wavelength due to large and small scale turbulence.

11. A. O. Izyumov, "Amplitude and Phase Fluctuations of a Plane Monochromatic Submillimeter Wave in a Near-Ground Layer of Moisture-Containing Turbulent Air", Radio Eng. and Elec. Phys., Vol. 13, No. 7, pp. 1009-1013, 1968. -- Increase in fluctuations in window regions compared to absorption line centers discussed.

12. A. O. Izyumov, "Frequency Spectrum of Amplitude Fluctuations of a Plane Electronagmatic Wave in Submillimeter Range Propagating in a Surface Layer of Turbulent Atmosphere", Radio Eng. and Elec. Phys., Vol. 14, No. 10, pp. 1609-1611, 1969. -- Presents frequency spectra for various sizes of inhomogeneities at 300 GHz. Treatment has bearing on 94 GHz modeling.

13. L. A. Hoffman, et al., "Propagation Observations at 3.2 Millimeters", Proc. IEEE, Vol. 54, No. 4, pp. 449-454, April 1966. -- Dry wind atmospheric effects on signal scintillation observed and discussed.

14. T. Orhaug, "The Effect of Atmospheric Radiation in the Microwave Region", Publ. of NRAO, Vol. 1, No. 14, pp. 215-250, Oct. 1962. -- Causes for fluctuating component of antenna temperature discussed. Variation formulated in terms of fluctuations in absorption coefficient.

15. T. C. L. G. Sollner, "Frequency Spectrum of Fluctuation in Submillimetre Sky Emission and Absorption", Astron. Astrophys., Vol. 55, pp. 361-368, 19 -- Dual beam astronomy investigation of variations in sky emission. Shows power spectra up to 1 Hz for 350 μ window region.

16. N. D. Mavrokoukoulakis et al, "Temporal Spectra of Atmospheric Amplitude Scintillations at 110 GHz and 36 GHz", IEEE Trans. AP, Vol. AP-26, No. 6, pp. 875-877, Nov. 1978. -- Results of propagation experiment over 4 km London path. Shows spectral density roll-off at 4.5 Hz at 110 GHz. Models atmosphere according to Ishimaru [see reference (6)] formulism. Good theoretical vs. experimental agreement.

17. R. S. Cole et al., "The Effect of the Outer Scale of Turbulence and Wavelength on Scintillation Fading at Millimeter Wavelengths", IEEE Trans. AP, Vol. AP-26, No. 5, pp. 712-715, Sept. 1978. -- Theoretical treatment of data from reference (16). Show how varying outer scale of turbulence with respect to Fresnel zones affect spectral densities.

18. K. L. Ho et al., "Wavelength Dependence of Scintillation Fading at 110 and 36 GHz", Elec. Lett., Vol. 13, No. 7, pp. 181-182, March 1977. -- Original British publication of work described in references (16) and (17).

19. N. D. Mavrokoukoulakis et al., "Observation of Millimeter-Wave Amplitude Scintillations In A Town Environment", Elect. Lett., Vol. 13, No. 14, pp. 391-392, July 1977. -- Time records of amplitude fluctuations observed over 4 km London path at 36, 110 GHz. Correlation of fading with wind and temperature changes noted.

20. R. W. Lee, "A Review of Line-of-Sight Propagation Studies of the Small-Scale Structure of the Atmosphere", Stanford Electronics Laboratories, May 1969. -- Describes methods of modeling small-scale effects and presents some experimental work on refractivity variations.

21. G. T. Wrixon and R. W. McMillan, "Measurements of Earth-Space Attenuation at 230 GHz", IEEE Trans. on Microwave Theory and Techniques, Vol. MTT-26, No. 6, p. 434, 1978. -- This paper is concerned mainly with observations in the 1.3 mm wavelength region but also describes the continuous fluctuations which have been observed on days of high overcast. These data should be further analyzed.

22. G. T. Wrixon, "Measurements of Atmospheric Attenuation on an Earth-Space Path at 90 GHz, Using a Sun Tracker", Bell System Tech. Journal, 50, No. 1, p. 103, 1971. -- Has also observed the same effects mentioned in Reference 22.

23. L. Lo, B. M. Fannin and A. W. Straiton, "Attenuation of 8.6 and 3.2 mm Radio Waves by Clouds", IEEE Transactions on Antennas and Propagation, AP-23, No. 6, p. 782, 1975. -- Mainly treats attenuation associated with variety of cloud conditions.

24. S. Corsi et al., "Atmospheric Noise in the Far Infrared (300-3000 μm)", IEEE Transactions on Microwave Theory and Techniques, MTT-22, No. 12, p. 1036, 1974.

25. N. A. Armand et al., "Fluctuations of Submillimeter Waves in a Turbulent Atmosphere", Radio Engineering and Electronics Physics, 13, No. 7, p. 1009, 1968. -- Basic theory of fluctuations in an absorbing medium; calculates the ratio of fluctuation variance in absorption to non-absorption fluctuation variance.
26. A. S. Gurvich, "Effects of Absorption on the Fluctuation in Signal Level During Atmospheric Propagation", Ibid., 13, No. 11, p. 1687, 1968. -- Paper covers essentially same ground as Reference 25 above from slightly different point of view.
27. F. I. Shimabukuro and E. E. Epstein, "Attenuation and Emission of Atmosphere at 3.3 mm", IEEE Transactions on Antennas and Propagation, AP-18, No. 4, p. 485, 1970. -- Looked for fluctuations from atmosphere for long integration times > 4 sec, observed no significant contributions.

4. EXPERIMENTAL MEASUREMENTS

4.1 Summer Measurements

During September of 1978 the first atmospheric observations at 94 GHz with the beam waveguide radiometer system were recorded. System installation began on September 8th and focusing of the antenna was completed by mid-day of September 12th. The bulk of the atmospheric observations made during the September field trip occurred on the 12th and 13th of September; unfortunately, a mixer failure during the late afternoon of September 13th precluded any further measurements. Included in the experimental records are measurements of cloud effects on both atmospheric and solar emissions in addition to zenith and celestial equatorial sky emissions. Antenna temperatures of the zenith sky at 22 and 31 GHz, provided by the dual-frequency NRL radiometer, are also presented where appropriate, along with the chronologically ordered 94 GHz data.

Figures 2 and 3 show zenith sky emissions at 22, 31, and 94 GHz measured during the partly cloudy afternoon of September 12th. Note the effects of clouds in Figure 3 as compared to Figure 2. Theoretical predictions of the zenith antenna temperatures (which do not account for clouds) based on the meteorological conditions stated in Figures 2 and 3 are 142.2°K and 147.56°K respectively. Figure 4 shows how cloud cover affects the emission received from the sun at 94 GHz on the same day, September 12th. Different solar drift scans from right to left in Figure 4 show the gradual attenuation of the sun by increasing cloudiness. The theoretical atmospheric model predicts a solar antenna temperature of 3663.4°K, based on a solar brightness temperature of 6500°K, a cloudless sky, and the antenna site meteorological conditions.

During the morning of September 13th, when the sky was completely overcast and the winds were calm, ground temperatures were considerably lower than the previous afternoon. Figures 5 and 6 show atmospheric emissions measured during this morning at two zenith angles, zero and at the celestial equator. Figures 7 and 8 present zenith sky emissions with short integration time periods. A theoretical calculation of the zenith sky emission based on the meteorological conditions of Figure 8 yielded an antenna temperature of 100.35°K.

The differences between the experimental and theoretical values of atmospheric antenna temperatures illustrate the inaccuracy of an atmospheric model which does not account for inhomogeneous features and non-standard variations in temperature, pressure and water vapor distributions. Table 1 is a summary of the comparisons of theoretical and experimental antenna temperatures which were described above. The experimental values representing atmospheric emission are on the average much larger than the theoretical, indicating that the real atmosphere is slightly more lossy than the atmospheric model predicts. In the case of the solar emission comparison, the higher theoretical value indicates that the atmospheric extinction predicted is lower than that actually encountered empirically (assuming the 6500°K brightness temperature of the sun is reasonable).

TABLE 1. EXPERIMENTAL VS. THEORETICAL ANTENNA TEMPERATURES IN DEGREES KELVIN (°K)

TYPE DATA	EXPERIMENTAL MIN	EXPERIMENTAL MAX	THEORETICAL	FIGURE NUMBER
Zenith Emission	144	173	142.2	2
Zenith Emission with Clouds	139	266	147.56	3
Zenith Emission	136	161	100.35	8
Solar Emission	2320	3182	3663.4	4

4.2 Winter Measurements

At this reporting date some of the March 1979 data have been reduced into both time records and power spectral density plots (PSD) of atmospheric antenna temperatures. Figure 9 shows the radiometer output and spectral density for the calibration run performed prior to the sky emissions

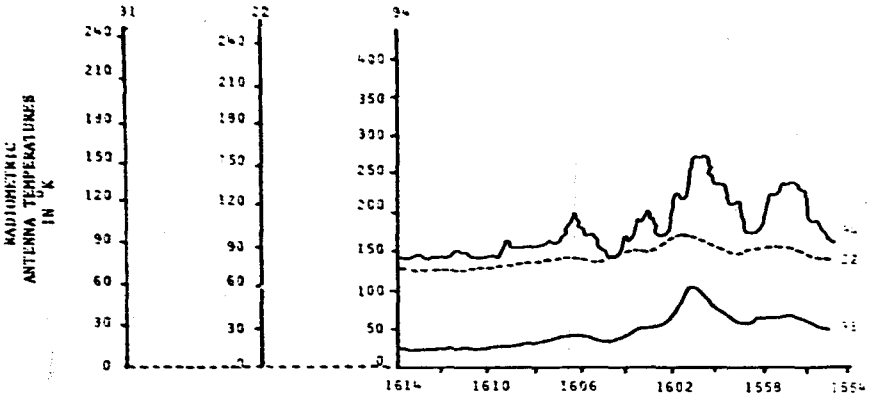

TIME OF DAY: 22, 31 and 94 GHz SYSTEMS

AVERAGE METEOROLOGICAL CONDITIONS AT ANTENNA SITE

AIR TEMP: 303.52°K WATER VAPOR: 21.75 g/m^3 PRESSURE: 1010.6 mb

Optically hazy with scattered cumulus clouds. clouds drifting over zenith during data run.

22, 31 GHz SYSTEM PARAMETERS

DSB HETERODYNE SYSTEM

LO FREQ. 22.234 GHz, 31.4 GHz
IF FREQ. 10-300 MHz

POST DETECTION INTEGRATION CONSTANT 0.5 sec

ANTENNA TEMPERATURE NOISE . . . . . ΔT_{MIN} 0.095°K

ANTENNA BEAM HALF-WIDTH AT -20dB POWER POINTS 22 GHz, 10°
31 GHz, 9°

94 GHz SYSTEM PARAMETERS

DSB HETERODYNE SYSTEM

LO FREQ. 94.556 GHz
IF FREQ. 1.6 ± 0.7 GHz

POST DETECTION INTEGRATION CONSTANT 5.00 sec

ANTENNA TEMPERATURE NOISE . . . . . ΔT_{MIN} 1.26°K

*22 and 31 GHz Antenna Temperatures plotted every 30 seconds such that time scales for 22, 31 and 94 GHz systems are coincident.

Figure 3. Zenith Antenna Temperatures : 22,31,94 GHz On 12 Sept 78

Figure 4. Attenuation Of Solar Radiation By Cumulus Cloud

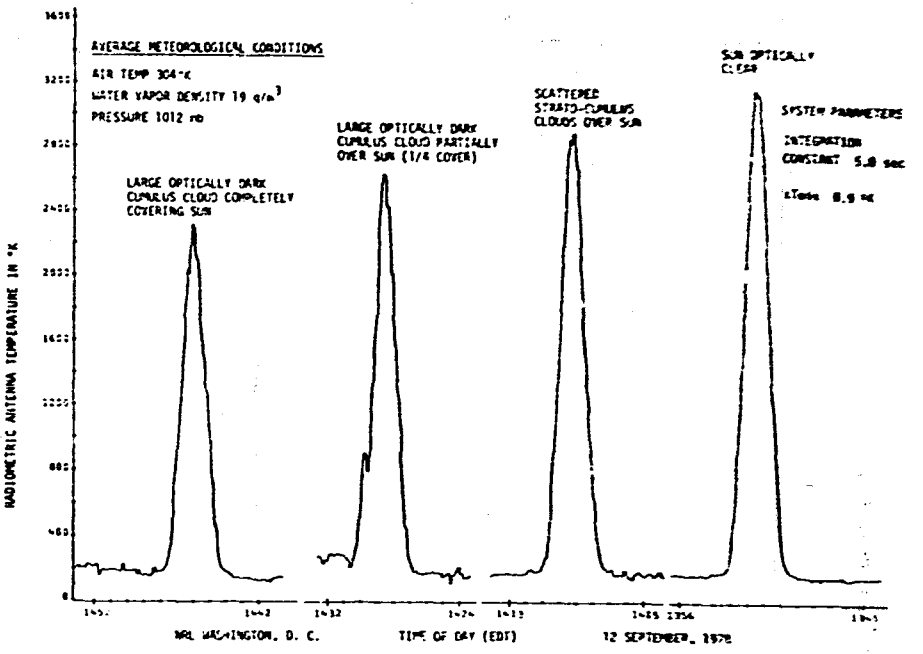

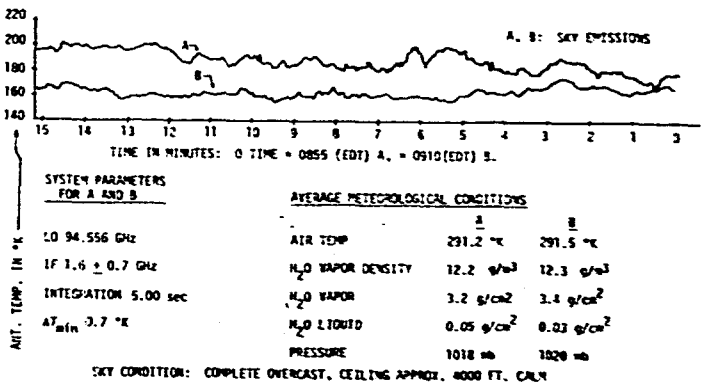

Figure 5. Emissions At Celestial Equator On 13 Sept 78

measured in Figure 10. Comparison of the PSD of Figure 9 with 10 shows the effect of system signal convolution in the frequency domain which must be accounted for before any atmospheric spectral feature can be determined. The large spikes in the antenna temperature records are a result of interfering electrical noise at the antenna site. For a more complete presentation and discussion of the winter measurement program results the reader is referred to Rainwater, et al. (1979).

5. CONCLUSIONS

To date the scale of atmospheric fluctuations has not been determined. The data have shown the need for an atmospheric model which will account for inhomogeneous regions such as clouds.

6. ACKNOWLEDGEMENTS

Without the technical assistance of the Electromagnetics Laboratory staff, the work reported herein would not have been possible. A. Contrada was responsible for the design, construction and modifications of all radiometer electronics and was most helpful during the field operations. J. M. Newton conceived the original idea of a beam waveguide feed and designed the LO directional filter. The helpful assistance of D. A. Duchesneau, D. O. Gallentine, V.T. Brady and W. W. King of Georgia Tech and J. P. Hollinger of NRL was also most appreciated.

REFERENCES

Chandrasekhar, S., 1950: Radiative Transfer. Oxford, Clarendon Press.

Goubau, G. and F. Schwering, 1961: On the guided propagation of electromagnetic wavebeams. IEEE Trans. Ant. Prop., AP-9, 248-256.

McMillan, R. W., J. J. Gallagher, and A. M. Cook, 1977: Calculations of antenna temperature, horizontal path attenuation and zenith attenuation due to water vapor in the frequency band 150-700 GH_z. IEEE Trans. MTT, MTT-25, 484-488.

Rainwater, J. H., J. J. Gallagher, and P. B. Reinhart, 1979: Millimeter Wave Atmospheric Radiometry Observations. Semi-Annual Report, Contract N00173-78-C-0165, Georgia Inst. Technology, May 1979.

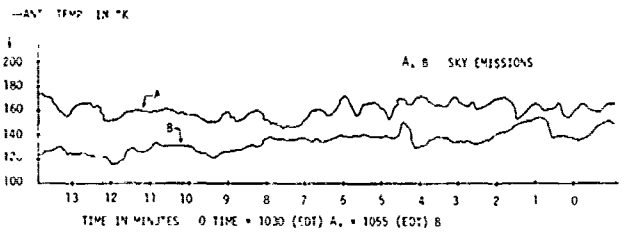

SYSTEM PARAMETERS FOR A AND B

LO 94.556 GHz
IF 1.6 ± 0.7 GHz
INTEGRATION 5.90 sec
ΔT_{min} 0.2 °K

AVERAGE METEOROLOGICAL CONDITIONS

	A	B
AIR TEMP	290.4 °K	290.9 °K
H_2O VAPOR DENSITY	12.0 g/m^3	12.0 g/m^3
H_2O VAPOR	3.5 g/cm^2	4.0 g/cm^2
H_2O LIQUID	0.01 g/cm^2	0.02 g/cm^2
PRESSURE	1020 mb	1020 mb

SKY CONDITION COMPLETE OVERCAST, CEILING APPROX 6000 FT
MODERATE BREEZE

Figure 6. Emissions At Zenith On 13 Sept 78

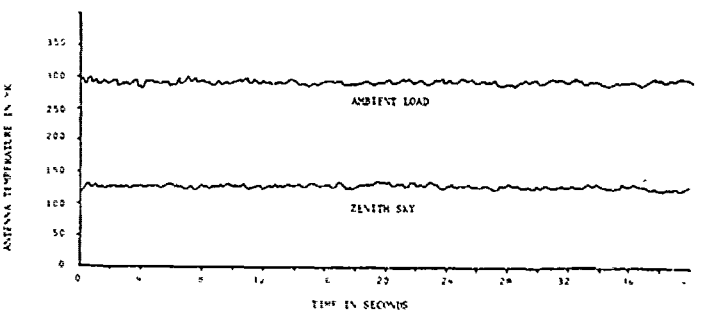

RECORDED AT NAVAL RESEARCH LABORATORY ON 13 SEPTEMBER 1978 AT 14.22 HOURS LOCAL

METEOROLOGICAL CONDITIONS AT ANTENNA SITE

AIR TEMPERATURE	291°K
WATER VAPOR	11.5 g/m^3
PRESSURE	1020.9 mb
SCATTERED STRATUS CLOUDS AT ZENITH	

94 GHz SYSTEM PARAMETERS

DSB RADIOMETRIC SYSTEM	
LO FREQ	94.556 GHz
IF FREQ	1.6 ± 0.7 GHz
POST DETECTION INTEGRATION CONSTANT	0.05 sec
ANTENNA TEMPERATURE NOISE ΔT_{MIN}	1.75°K

Figure 7. Emissions At Zenith On 13 Sept 78 -- Reduced Integration Constant

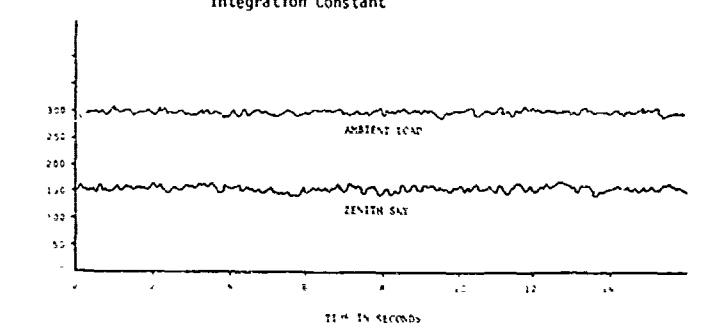

RECORDED AT NAVAL RESEARCH LABORATORY ON 13 SEPTEMBER 1978 AT 12.34 HOURS LOCAL

METEOROLOGICAL CONDITIONS AT ANTENNA SITE

AIR TEMPERATURE	291°K
WATER VAPOR	11.5 g/m^3
PRESSURE	920.9 mb
SCATTERED STRATUS CLOUDS AT ZENITH	

94 GHz SYSTEM PARAMETERS

DSB RADIOMETRIC SYSTEM	
LO FREQ	94.556 GHz
IF FREQ	1.6 ± 0.7 GHz
POST DETECTION INTEGRATION CONSTANT	0.016 sec
ANTENNA TEMPERATURE NOISE ΔT_{MIN}	5.8°K

Figure 8. Emissions At Zenith On 13 Sept 78 With 0.016 sec Integration Constant

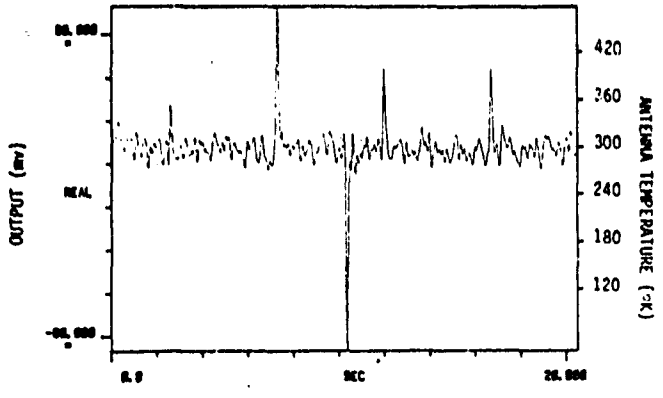

a. Time Record

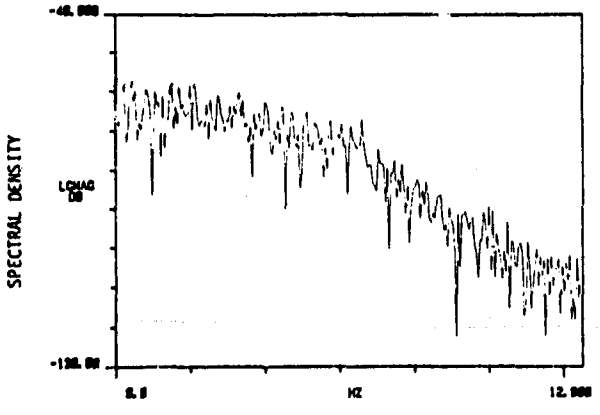

b. Spectral Density

Figure 9. Radiometer Output And Spectral Density At Ambient Load Calibration 13 March 1979. (Calibration No. 2, Applicable to Fig. 28-30)

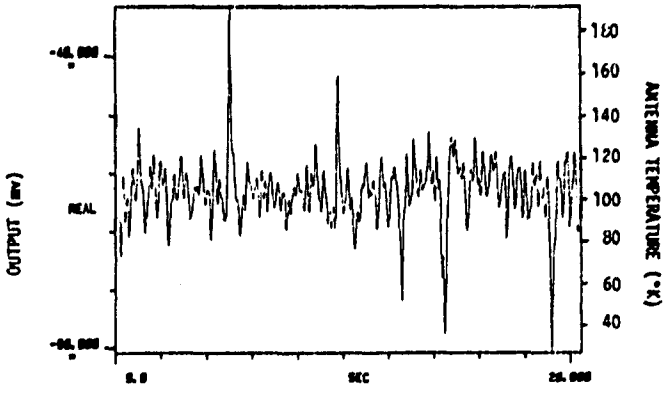

a. Time Record

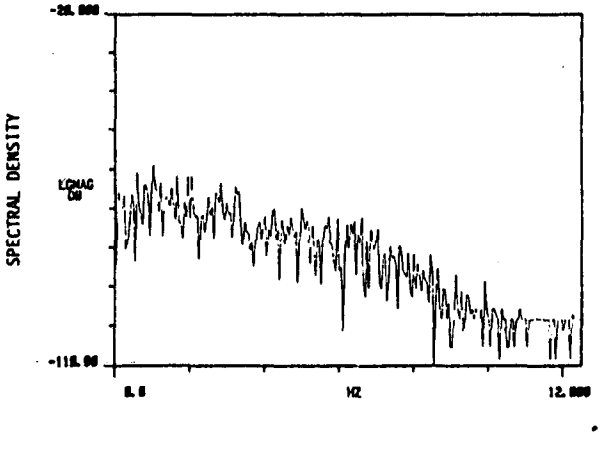

b. Spectral Density

Figure 10. Zenith Sky Emissions, Afternoon Of 13 March 1979. Air Temperature 290.35°K, Water Vapor Density 5.57 g/m^3, Pressure 1019 mb. Integration Constant 0.5 sec, ΔT_{MIN} = 6.46°K.

TWO PROBLEMS IN UNDERSTANDING THE ROLE OF WATER DIMERS IN ATMOSPHERIC ABSORPTION

R. A. Bohlander
Appleton Laboratory, Slough, England
Present address: Georgia Institute of Technology
Engineering Experiment Station
Atlanta, Georgia 30332

R. J. Emery and D. T. Llewellyn-Jones
Appleton Laboratory, Slough, England

G. G. Ginmestad
University of Colorado, Boulder, Colorado
Present adress: Michigan Technological University
Keweenaw Research Center, Houghton, Michigan 49931

H. A. Gebbie
Imperial College of Science and Technology
University of London, London, England

ABSTRACT

A model of the water dimer having a single linear hydrogen bond has been used to predict the pure rotation and rotation-vibration band absorption by this species. Using Fourier spectroscopy, we have looked for this in the difference between measured and predicted absorption by water molecules in the wavenumber ranges 8 to 40 cm^{-1} (240 to 1,400 GHz) and 300 to 600 cm^{-1}. However, the present model of dimer absorption does not satisfactorily account for the observed excess absorption by water vapor in the laboratory or by the atmosphere containing water vapor. The nature of the disagreement is different in laboratory and field studies. When equilibrium samples of water vapor are studied in the laboratory, the temperature dependence and over-all magnitude of observed excess absorption are in reasonable agreement with prediction for dimers, but the shape of the spectrum is very different. This suggests that the average molecular pair structure is different at normal temperatures from the ground state structure of dimers found by Dyke and others in 1977 in molecular beams. It is well-known that excess absorption will be found in the atmosphere when comparison is made with predictions for known constituents. Even if laboratory spectra of water vapor are used to improve the predictions, there is a residual observed. It is characterized mainly by more variability than can be attributed to dimers in equilibrium.

1. INTRODUCTION

The importance of absorption by water dimers in the atmosphere at near millimeter wavelengths has needed clarification. Viktorova and Zhevakin (1967, 1971, 1975) originally suggested that dimers might account for the observed excess of absorption in the gaps between water lines. A dimer is a pair of water molecules bound by a weak hydrogen bond; because of this, dimer concentrations depend on the water vapor density and the temperature. We have made a study of excess absorption by water vapor in the laboratory to find out two things: (1)whether present dimer models account for the excess over prediction for monomers, and (2) whether our laboratory findings can account for observed anomalies in atmospheric attenuation. A detailed account has been given in the thesis by Bohlander (1979), and further publications will follow.

2. THEORETICAL DIMER ABSORPTION

We have made theoretical calculations of the absorption spectrum of dimers from existing information about their structure. A number of theoretical chemists have made molecular orbital calculations in order to find the hydrogen bond energy and the most stable structure, shown in Figure 1. Dill et al. (1975) give a useful review, and more recent work is described by Matsuoka et al. (1976). These predictions were found to be consistent with high resolution measurements (Dyke et al., 1977) of the microwave transitions of dimers in molecular beams. We have, therefore, a fairly clear idea of the structure of dimer molecules when they are in the ground vibrational state.

Since it can be estimated that only four percent of the dimer population is in the ground vibrational state at normal temperatures, the question as to whether dimers retain approximately the lowest energy configuration at these temperatures is an important one. To shed light on this question a comparison has been made of observed excess absorption with a theoretical dimer spectrum calculated on the assumption that dimers undergo rigid rotation and small-amplitude harmonic vibration. This is not an unreasonable model to try since Thomas (1975) has found vibration bands of the hydrogen-bonded complex H_2O--HF which were easily

recognizable despite some anharmonicity.

It is also necessary to make an assumption about dimer concentrations. Although molecular beam measurements have given important structural information, they tell us nothing about equilibrium concentrations. These we have estimated in the usual way (see eg. Bolander et al. 1969) from experimental values of the second virial coefficient (Goff and Gratch, 1946). Typical calculated dimer concentrations are of the order of a part in 1000 of the monomer concentration. Uncertainties in the theory on which these calculations are based will be discussed later.

Figure 2a shows where dimers are expected to come in atmospheric composition. Ground level water vapor is shown with a possible variation from 2 to 50 parts in 1000. Dimer concentrations are proportional to the square of the water vapor density; their dependence on temperature is determined by the hydrogen bond energy, estimated to be 0.12eV. Although this would give a relatively steep temperature dependence, the variability of the equilibrium dimer concentration resulting from variations in water vapor density is more important in the atmosphere since water vapor density naturally varies by a greater percentage than does the temperature. The figure shows the range of dimer concentrations expected for the range of water vapor density shown, taking temperature to be at the dew point.

Although water dimers are expected to come seventh in the list of atmospheric constituents, they are expected to rank higher in importance as absorbers since they have a large dipole moment. A crude way to make a comparison is to look at expected integrated absorption coefficients for the range 0 to 30 cm^{-1} (900GHz), as shown in Figure 2b.

The theoretical spectrum of water dimers in the far infrared, shown in Figure 3a, is overlayed by the monomer pure rotation spectrum (Figure 3b). The dimer's expected pure rotation band comes at a low frequency because the dipole moment measured by Dyke et al. (1977) was found to be nearly parallel to the line between the heavy oxygen atoms. The inertial spectral constant for end-over-end transitions is about 0.2 cm^{-1}, and the peak of the band is at 16 cm^{-1} (480GHz). The rotational structure is not given in detail because the splitting parameters for inversion tunnelling are not well-known. Smoothed band contours are shown and are all that is needed for an interesting comparison with experimental data.

The remainder of the predicted absorption is assigned to six intermolecular vibration modes involving the hydrogen bond. We have calculated the normal intermolecular vibration frequencies for the dimer from recent molecular orbital studies of intermolecular potential energy (Matsuoka et al., 1976). Most of the modes involve partial rotation of the monomers within the dimer, and, since this causes large dipole moment oscillations, the predicted absorption intensity is large. Intensities were calculated with the assumption that the charge distribution remains fixed on the monomer units during vibrations.

3. OBSERVATIONS IN THE LABORATORY

The spectral ranges that are most accessible to experimental study are in the wings of the monomer pure rotation band and include the predicted dimer pure rotation band and the predicted bands for hydrogen bond bending. These were also perhaps the most interesting on theoretical grounds, as will be discussed later. We have studied water vapor without a foreign broadening gas since this would give the widest possible spectral ranges in which to search for dimer absorption.

Path lengths between 20 and 200 meters were needed to measure the absorption coefficients of water vapor in the gaps between lines; these were obtained chiefly with white-type folded-path optics. Wide-band radiation was taken from Mercury lamps or glow bar sources, and Helium-cooled bolometers or Golay cell detectors were used. Spectra were obtained by Fourier transform spectroscopy. Supplementary measurements of absorption were made with an HCN maser at a frequency of 29.7 cm^{-1} (891GHz).

A selection of observed spectra is given in Figure 4. They represent one minus the ratio of spectra obtained with a sample and with a vacuum in the absorption cell. The dashed curves show expected monomer absorption calculated with the Gross line shape formula and the line parameters given by McClatchey et al. (1973) and Benedict and Kaplan (1964). Due to the presence of numerous strong monomer lines, one can get only a fragmentary picture of the excess absorption's spectral shape, as shown for the near millimeter region in Figure 5. Horizontal bars show intervals of wavenumber in which excess absorption has been averaged. Some results of Burch (1968) and Burroughs et al.(1969) which are in good agreement are also shown. Preliminary results for which a large untuned cavity was used in place of the White cell are also shown in the low frequency region, where the use of White-type absorption cells can be troublesome.

The integral of the observed excess absorption is about the same as that predicted by the dimer model, but the shape of the spectrum is different. This is also true for the higher wavenumber range studied (Figure 6). Here observed excess absorption is represented by a smooth curve that fits our data and that of Burch et al. (1974) within the experimental uncertainty. As previously noted by Roberts et al.(1976), this seems to have the form of an exponential decrease with frequency in the range 300 to 600 cm^{-1}. Further discussion of the shape of excess absorption will be given, following consideration of the observed temperature dependence.

Typical results in the low and high frequency regions are given in Figure 7. The excess absorption data are plotted in this way to find the value of the energy E that characterizes the temperature dependence; this in turn can be compared with the estimated dimer energy of formation. The dotted lines show the temperature dependence of the predicted monomer component of the absorption. This is governed mainly by the Boltzmann distribution of the energy

levels from which nearby absorption transitions arise; the slope therefore switches sign from one side of the monomer pure rotation band to the other. The temperature dependence of the excess absorption is more nearly uniform. Values of E given in Figure 8 are near the dimer energy of formation estimated from the temperature dependence of the second virial coefficient (Bolander et al. 1969; Bohlander, 1979).

4. DISCUSSION

There are in general terms two possible ways of interpreting the discrepancy between the shape of observed excess absorption and that of predicted dimer absorption:

(1) Dimers at normal temperatures may have significantly different structures than they have at low temperatures, or
(2) The contributions by dimers to the excess absorption may be less important than possible contributions by unbound molecular pairs.

It is widely recognized that there is an important weakness in present models of molecular absorption--namely, in the line shape formulae, which are based on the assumption of instantaneous collisions. Water molecules interacting in unbound pairs can contribute absorption to the wings of monomer lines and may make a larger contribution than that predicted by present line shape formulae. Various authors, for example Zuev and Fomin (1978) and Brown and Snider (1979, in the present proceedings), have shown that modifications to line shape formulae could substantially reduce excess absorption for selected conditions. However, the formulae and the values of the free parameters which make them fit observed absorption have not as yet been tested to see if they are physically meaningful in terms of molecular interactions.

Present theories, by which dimer concentrations are calculated from values of the second virial coefficient, discount the importance of unbound pairs at atmospheric temperatures, but there are some simplifications made. For molecules with a spherically symmetric form of potential energy, Stogryn and Hirschfelder (1959) have shown that dimers are responsible for nearly all of the second virial coefficient when the dimer binding energy exceeds kT. In the case of water, the energy of dimer formation is more than 4kT, but it is not known whether the generalization of Stogryn and Hirschfelder can be extended to the case of molecules of low symmetry, such as water. Calculations of dimer concentrations may also be done from a knowledge of the intermolecular potential energy (Viktorova and Zhevakin 1971; Braun and Leidecker 1974; Lane 1975; Bohlander 1979). While reasonable agreement with experimental values of the second virial coefficient have been obtained thus far, much uncertainty remains about the reliability of the approximations. Therefore, the possibility of a significant contribution by unbound pairs to excess absorption cannot be ruled out.

It is significant that the predicted vibration and assigned to hydrogen bond bending in dimers has not been found in observed excess absorption. The tendency of a hydrogen bond to remain linear, as shown in Figure 1, is a common characteristic of hydrogen-bonded complexes and is manifested in the relatively high frequency of the bending motion. The absence of the mode suggests that the association of water molecules at normal temperatures does not usually involve a linear hydrogen bond. To explain the observed excess absorption spectrum, other ways of looking at dimer structure might be considered. An error in the theory of the most stable structure is ruled out by the molecular beam measurements cited earlier. Theoretical calculations have not identified any sufficiently stable alternative structures with higher energy. Thus it remains to consider the possible effects of large amplitude vibrations or of internal rotation. Further work is needed, for example, on the theoretical barriers to internal rotation.

It is appropriate to end this section by remarking that pairs of molecules bound in a weak and floppy way may be difficult to distinguish spectroscopically from pairs which are not quite bound. Prengel and Gornall (1976) have recently demonstrated some similarities in the way photons interact with unbound pairs and bound pairs of methane molecules.

5. COMPARISON WITH ATTENUATION BY THE ATMOSPHERE

Although we do not fully understand the spectrum of water vapor, it is important to ask whether laboratory measurements give us a better understanding of absorption by the atmosphere. Figure 9 gives a simplified representation of attenuation by the atmosphere as observed by Emery, Zavody and Gebbie (to be published). Transmission was measured in a folded path in the open atmosphere, and the path was then dessicated to obtain a calibration under conditions of low atmospheric attenuation. Water vapor is the only important known absorber for this wavelength range and for the path length and clear-air conditions studied. The solid line gives the water vapor absorption which is predicted for the case of pressure broadening by air when the Gross line shape formula is used, and the dashed line shows corrected values of the predicted absorption based on the laboratory measurements described above. The observations covered a range of temperature (280-290K) and of absolute humidity (6-11 g/m^3), and the data points shown in the figure are the result of an attempt to reduce all the observations to attenuation values representative of the mean conditions. This was done on the assumption that the observed excess absorption depended on water vapor density and on temperature in the same way that it did for laboratory measurements of water vapor. Only the value of the exponent E was left as a free parameter to be fit to the data. It turned out that the excess attenuation was poorly correlated with values of the water vapor density, and the measure of this variability shown was larger than the instrumental noise. Moreover, the temperature dependence appeared to be steeper than

that found in the laboratory. For these reasons, the large mean excess attenuation found in the above measurements of the atmosphere cannot be attributed to absorption by water vapor in equilibrium.

6. CONCLUSIONS

Although excess absorption observed in laboratory studies of water vapor in equilibrium is like the absorption expected from dimers as regards the over-all absorption level and its temperature dependence, present knowledge of dimer structure does not give a good prediction of the shape of the excess spectrum. Further theoretical attention should be given to whether internal rotation significantly affects the structure and spectrum of dimers at normal temperatures. It is not now known whether unbound molecular pairs can account for a significant part of the excess absorption found in the laboratory. Finally, an attempt has been made to understand atmospheric attenuation of near millimeter waves in terms of the absorption by water vapor in equilibrium, but it has not been possible to explain the mean level of observed attenuation in this way. Perhaps of greater significance is the unexplained variability in the atmospheric attenuation.

REFERENCES

Benedict, W. S. and L. D. Kaplan, 1964: Calculation of line widths in H_2O-H_2O and H_2O-O_2 collisions. J. Quant. Spectrosc. Radiative Transfer, 4, 453-469.

Bohlander, R. A., 1979: Ph.D. Thesis. Imperial College of Science and Technology, University of London.

Bolander, R. W., J. L. Kassner, and J. T. Zung, 1969: Semiempirical determination of the hydrogen bond energy for water clusters in the vapor phase. I. General theory and application to the dimer. J. Chem. Phys., 50, 4402-4407.

Braun, C. and H. Leidecker, 1974: Rotation and vibration spectra for the H_2O dimer: Theory and comparison with experimental data. J. Chem. Phys., 61, 3104-3113.

Brown, D. R. and D. E. Snider, 1979: H_2O near millimeter absorption: the effects of line shape variations. Proc. Workshop on Millimeter and Submillimeter Atmos. Prop. Applicable to Radar and Missile Systems. 20-22 March 1979, Redstone Arsenal, AL.

Burch, D. E., 1968: Absorption of infrared radiant energy by CO_2 and H_2O. III. Absorption by H_2O between 0.5 and 36 cm^{-1} (278 μ - 2 cm). J. Opt. Soc. Amer., 58, 1383-1394.

Burch, D. E., D. A. Gryvnak, and F. J. Gates, 1974: Continuum Absorption by H_2O between 330 and 825 cm^{-1}. Air Force Cambridge Research Laboratories Report AFCRL-TR-74-0377.

Burroughs, W. J., R. G. Jones, and H. A. Gebbie, 1969: A study of submillimetre atmospheric absorption using the HCN Maser. J. Quant. Spectrosc. Radiative Transfer, 9, 809-824.

Dill, J. D., L. C. Allen, W. C. Topp, and J. A. Pople, 1975: A systematic study of the nine hydrogen-bonded dimers involving NH_3, OH_2, and HF. J. Amer. Chem. Soc., 97, 7220-7226.

Dyke, T. R., K. M. Mack, and J. S. Muenter, 1977: The structure of water dimer from molecular beam electric resonance spectroscopy. J. Chem. Phys., 66, 498-510.

Emery, R. J., A. M. Zavody and H. A. Gebbie: to be published.

Goff, J. A. and S. Gratch, 1946: Low-pressure properties of water from -160 to 212 F. Trans. Amer. Soc. Heat. Vent. Eng., 52, 95-122.

Gryvnak, D. A., D. E. Burch, R. L. Alt, and D. K. Zgonc, 1976: Infrared Absorption by CH_4, H_2O, and CO_2. Air Force Geophysics Laboratory Report AFGL-TR-76-0246.

Lane, J. G., 1975: Comment on "Study of the structure of molecular complexes. IV. The Hartree-Fock potential for the water dimer and its application to the liquid state." J. Chem. Phys., 62, 1605-1606.

McClatchey, R. A., W. S. Benedict, S. A. Clough, D. E. Burch, R. F. Calfee, K. Fox, L. S. Rothmann, and J. S. Garing, 1973: AFCRL Atmospheric Absorption Line Parameters Compilation. Air Force Cambridge Research Laboratories Report AFCRL-TR-73-0096.

Matsuoka, O., E. Clementi, and M. Yoshimine, 1976: CI study of the water dimer potential surface. J. Chem. Phys., 64, 1351-1361.

Prengel, A. T. and W. S. Gornall, 1976: Raman scattering from colliding molecules and Van der Waals dimers ingasecus methane. Phys. Rev. A, 13, 253-262.

Roberts, R. E., J. E. A. Selby, and L. M. Biberman, 1976: Infrared continuum absorption by atmospheric water vapor in the 8-12-μm window. Appl. Optics, 15, 2085-2090.

Stogryn, D. E. and J. O. Hirschfelder, 1959: Contribution of bound metastable, and free molecules to the second virial coefficient and some properties of double molecules. J. Chem. Phys., 31, 1531-1545. [Errata, 1960, J. Chem. Phys., 33, 942-943.]

Thomas, R. K., 1975: Hydrogen bonding in the vapour phase between water and hydrogen fluoride: the infrared spectrum of the 1:1 complex. Proc. Roy. Soc. London, 344, 579-592.

Viktorova, A. A. and S. A. Zhevakin, 1967a: The water-vapor dimer and its spectrum. Sov. Phys.-Dokl., 11, 1059-1062.

Viktorova, A. A. and S. A. Zhevakin, 1967b: Absorption of microwaves in air by water-vapor dimers. Sov. Phys.,-Dokl. , 11, 1065-1068.

Viktorova, A. A. and S. A. Zhevakin, 1971a: Band spectrum of a dimer of water vapor. Sov. Phys.-Dokl., 15, 836-839.

Viktorova, A. A. and S. A. Zhevakin, 1971b: Microradiowave absorption by dimers of atmospheric water vapor. Sov. Phys.-Dokl., 15, 852-855.

Viktorova, A. A. and S. A. Zhevakin, 1975: The rotational spectrum of water vapor dimer. Izv. VUZ. Radiofiz., 18, 211-221.

Zuev, V.E., and V. V. Fomin, 1978: Symposium on Remote Soundings in the Atmosphere from Space. Innsbruck, Austria, 1-3 June 1978.

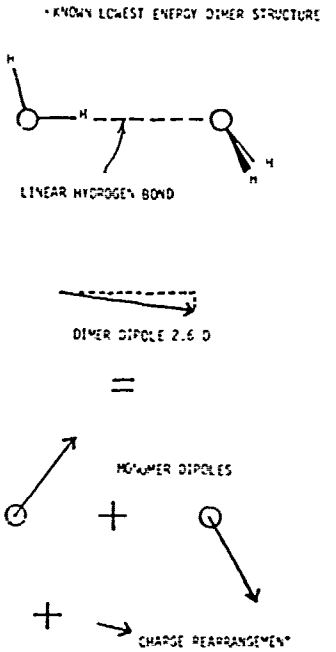

FIGURE 1

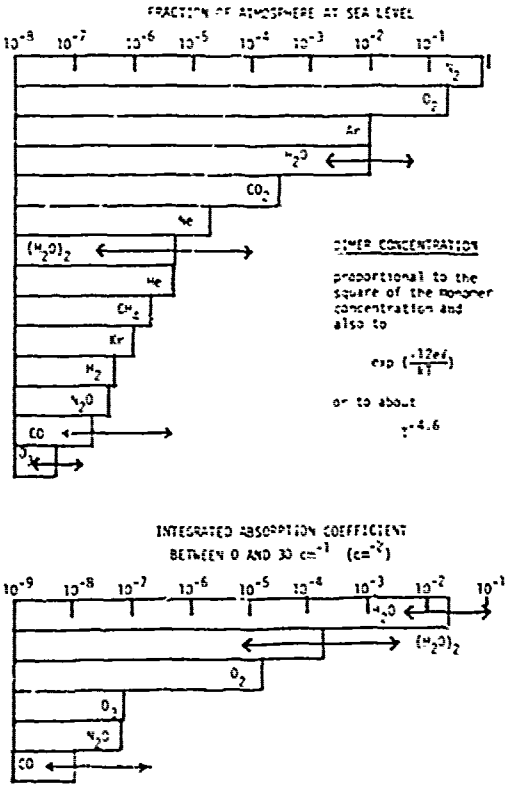

FIGURE 2

PREDICTIONS OF ABSORPTION BY WATER VAPOR

DENSITY 18 g/m^3 TEMPERATURE 296 K

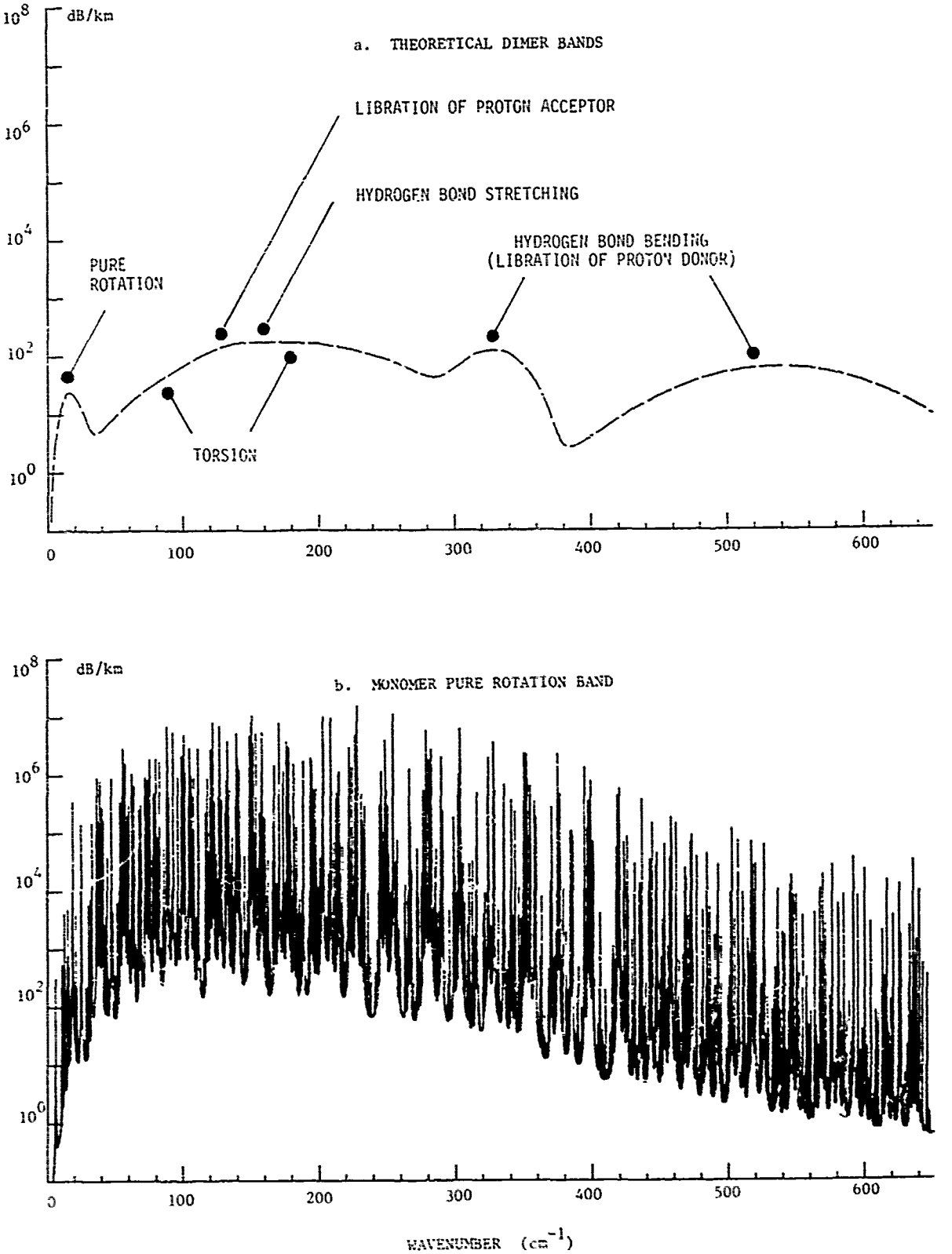

FIGURE 3

FIGURE 4

ABSORPTION SPECTRUM OF WATER VAPOR

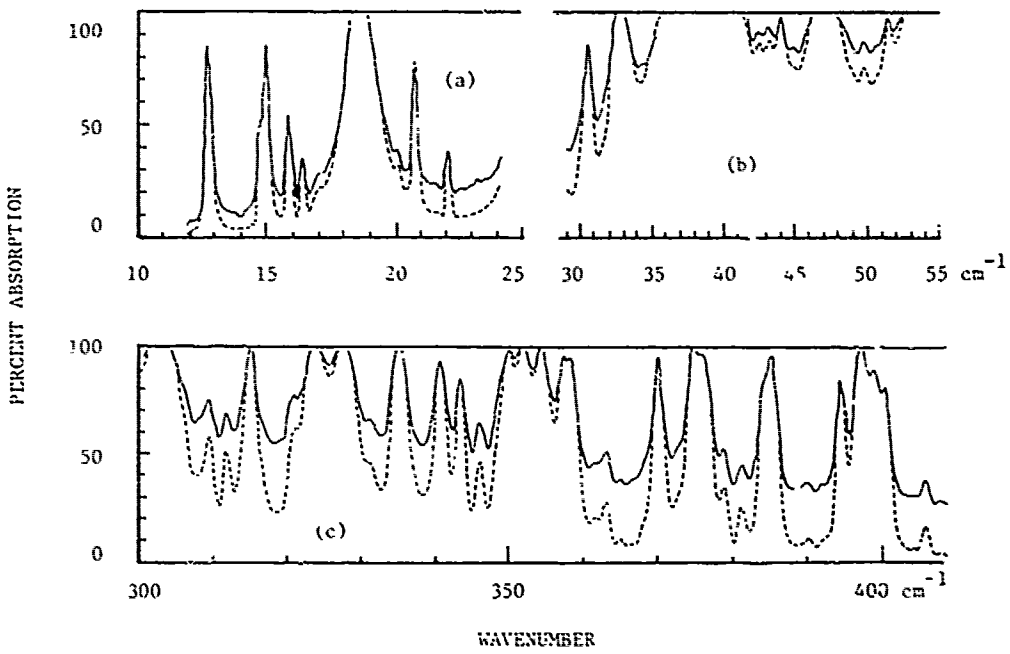

	WATER DENSITY $g\ m^{-3}$	TEMPERATURE K	PATH LENGTH m	RESOLUTION cm^{-1}	UNCERTAINTIES IN PERCENTAGE ABSORPTION
(a)	17	294	45	0.23	$\pm$1.25
(b)	15	294	103	0.5	$\pm$ 7 <40 cm^{-1} $\pm$ 1.6 >40 cm^{-1}
(c)	5.6	283	133	1.25	$\pm$2

FIGURE 5

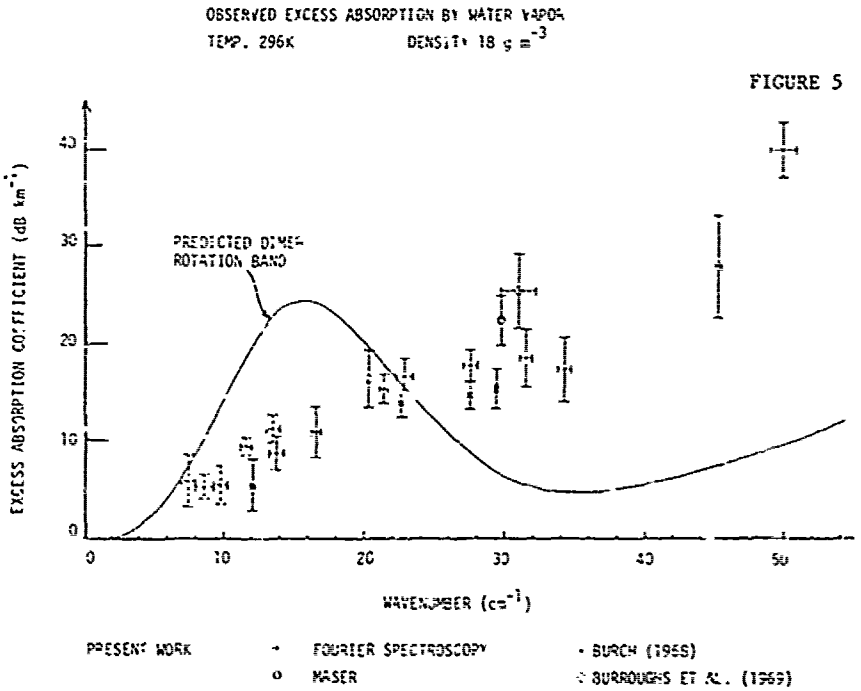

FIGURE 6

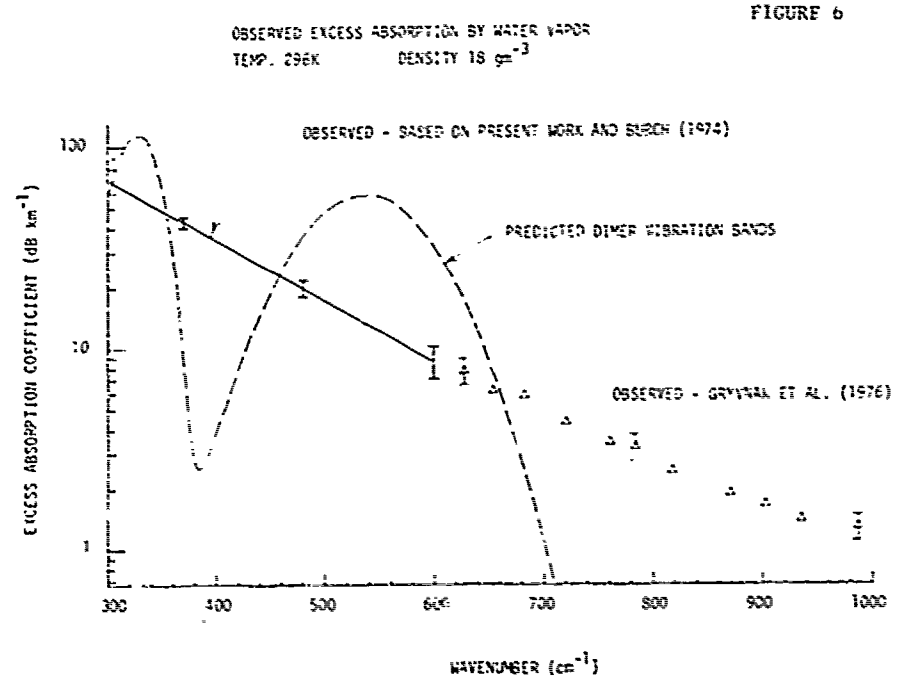

OBSERVED TEMPERATURE DEPENDENCE OF THE
EXCESS ABSORPTION COEFFICIENT K_e

FIGURE 7

K_e/ρ^2 assumed $\propto \exp[-F/(kT)]$, ρ = water vapor density

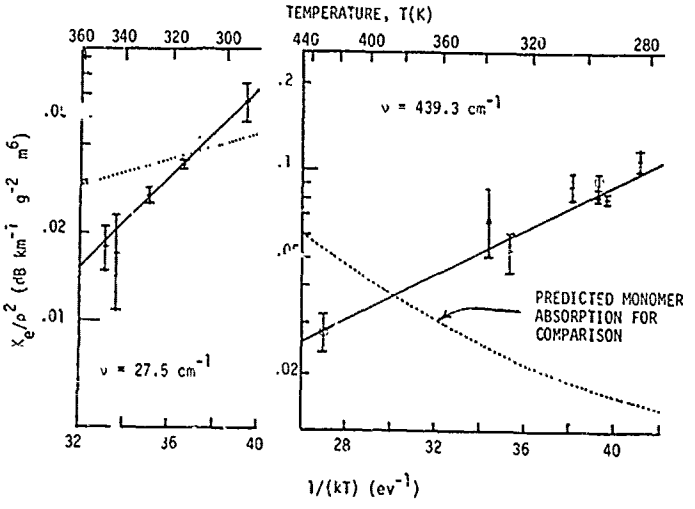

+ PRESENT WORK ○ BURCH ET AL. (1974) ▲ GRYVNAK ET AL. (1976)

ENERGY CHARACTERIZING OBSERVED TEMPERATURE DEPENDENCE
OF EXCESS ABSORPTION

FIGURE 8

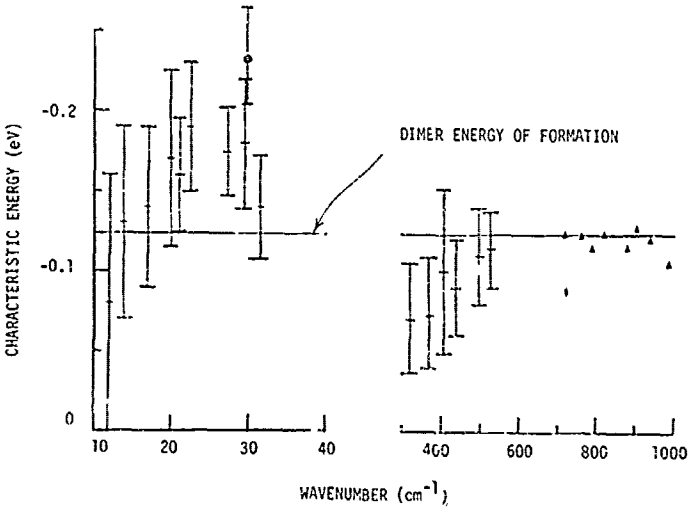

PRESENT WORK + FOURIER TRANSFORM SPECTROSCOPY

• MASER

GRYVNAK ET AL. (1976) ▲

OBSERVED ATTENUATION BY THE ATMOSPHERE IN CLEAR CONDITIONS

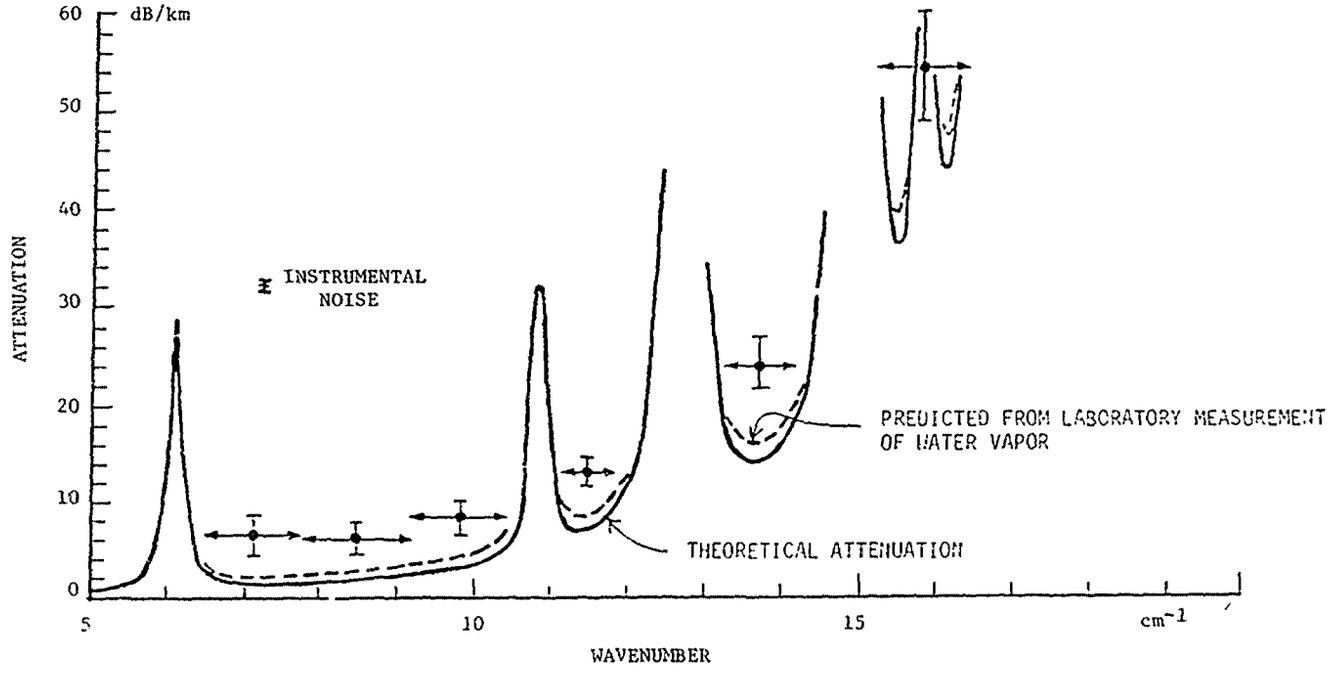

KEYS TO OBSERVATIONS BY EMERY, ZAVODY AND GEBBIE

1 STANDARD DEVIATION OF ATTENUATION

INTERVAL OF WAVENUMBER OVER WHICH ATTENUATION WAS AVERAGED.

FIGURE 9

A RADAR SYSTEM ENGINEER LOOKS AT CURRENT MILLIMETER-SUBMILLIMETER ATMOSPHERIC PROPAGATION AND RADARS

Stephen L. Johnston
US Army Missile Research and Development Command
Redstone Arsenal, Alabama

ABSTRACT

Numerous reviews have been made of theoretical atmospheric propagation characteristics in the millimeter and submillimeter regions. Additionally, extensive experimental atmospheric propagation measurements have been made in these regions. These have generally been made for purposes other than radar systems design. It would appear that the propagation community may not have a sufficient appreciation for the needs of the radar system design engineer. This paper will set forth the general atmospheric propagation requirements of a millimeter/submillimeter radar system design engineer. These requirements include much more than mere atmospheric absorption/attenuation.

1. INTRODUCTION

The reader should keep in mind the following IEEE radar definition: An electromagnetic device for detecting presence and location of objects. Object presence and distance (range) determined by transmission and return of electromagnetic energy; also, direction through use of movable or rotating directive antenna pattern.

This paper is brief and consists essentially of the information from the viewgraphs used in the presentation at the workshop and a bibliography. It is intended that a full paper which will include a limited review of presently existing mm/smm propagation data will be presented at the IEEE Electronics and Aerospace Systems Conference (EASCON-79), Arlington, VA., Oct 9-11, 1979 and will be published in the EASCON Conference Record.

The following are suggested radar applications from Skolnik (1970a,b):

Low-angle tracking*
"Secure" military radar*
Interference-free radar*
Cloud sensing radar*
High resolution radar*
Imaging radar
Ground mapping
Map matching
Space object identification
Lunar radar astronomy
Target characteristics
Weather radar
Clear-air turbulence sensor
Remote sensing of the environment
Surveillance
Target acquisition, recognition, identification
Missile guidance
Navigation
Obstacle detection
Clutter suppression
Fuzes
Harbor surveillance radar
Airport surface detection radar
Landing aids
Air traffic control beacons
Jet engine exhaust and cannon blast

*Applications in which Skolnik believed that submillimeter waves offer more advantage than microwave frequencies.

2. RADAR CHARACTERISTICS

The following are characteristics of a "typical" mm radar:

Maximum application range	3 km
Maximum PRF for unambiguous range	50 kHz (max)
Single scan correlation time	20 μs (min)
Pulse width	20 ns (min)
RF bandwidth	50 MHz (max)*
Antenna beamwidth	6-15 mrad (.5-1 deg)
Conical scan frequency	30-100 Hz
Angle of arrival measurement time	100 S (K_A band)
Average RF power output	.1-1W
Antenna diameter	.25-1 m
Radar size	Breadbox up
Power requirements	50 W

3. PROPAGATION EFFECTS

The following 19 radar features are influenced by propagation effects:

1. Maximum range.
2. Choice of detection thresholds.
3. Type of detector.
4. Detection logic.
5. Signal processing technique.
6. Search scan rate.
7. Antenna polarization.
8. Type of angle measurement: monopulse/conical scan.
9. Pulse width (RF bandwidth).
10. Conical scan frequency choice.
11. Doppler bandwidth.
12. Number of pulses intergrated.

*250 MHZ for spread spectrum or frequency agility.

13. False alarm rate.
14. Moving target indicator performance.
15. Receiver automatic gain control characteristics.
16. Angle tracking accuracy.
17. Range tracking accuracy.
18. Range gate width.
19. Choice of frequency.

Radar functions are also influenced by propagation effects. The function of detection is affected by atmospheric attenuation, fluctuation (scintillation), foliage attenuation backscatter, polarization variation, fade depths and durations. Angle measurement is influenced by angle of arrival variation due to meteorological causes, ducting, fluctuation (especially for conical scan), and depolarization. Special functions such as imaging depend upon characteristics affecting detection and upon spatial coherence.

The following propagation effects on radar/guidance were obtained from D. Howard in a private communication.

1. Multipath/forward scatter.
   a. Modeling sea/terrain.
   b. Experimental measurements:
      - angle errors
      - signal fading
2. Backscatter (theoretical and experimental).
   a. Rain.
   b. Sea.
   c. Terrain.
3. Ducting at mm waves.
4. Atmospheric/foliage attenuation.
   a. Attenuation in troposphere:
      - rain
      - fog
      - humid air
   b. Near ocean surface moisture layer.
   c. Foliage penetration.

Propagation data requirements for radar design are listed in alphabetic order.

Aerosol (dusts, etc.) characteristics:

Loss tangent
Refractive index

Angle of arrival variations:

Correlation interval
Power spectral density

Atmospheric attenuation:

Correlation interval
Fluctuation distribution
Power spectral density

Atmospheric backscatter

Foliage penetration

Phase variations

Polarization effects

Surface phenomena:

Bistatic clutter
Forward scatter
Nature of surface roughness
Decorrelation time
Power spectral content
Backscatter (monostatic)

4. ENVIRONMENTAL CONSTRAINTS

Environmental constraints for a microwave radar have been given by Barton (1977), where the items in parentheses refer to references listed in Barton (1977):

Line of sight:

Horizon range
Range-Height-angle charts (Blake)
Terrain masking (Geodetic Survey Maps)

Attenuation:

Clear atmosphere (Blake)
Rain, clouds, Snow (Gunn and East; Barton; Bean, Dutton, and Warner)

Clutter:

Weather (Gunn and East; Barton; Bean, Dutton, and Warner)

Land and sea (Moore; Skolnik; Nathanson; Barton)

Refraction:

Tropospheric bias (Barton)
Trophospheric fluctuation (Barton and Ward)
Ionsophere (Barton)
Ducting (Bean and Dutton)

Surface reflection:

Lobing (fading) (Blake)
Multipath error (Barton and Ward; Barton; Blake)

Diffraction:

Interference (ECM) model (arbitrary selection)

5. BIBLIOGRAPHY

Altshuler, E. E., et al., 1968: Atmospheric Effects on propagation at millimeter wavelengths. IEEE Spectrum, 5, No. 7, 83-90.

Barton, D. K., 1977: Philosophy of radar design. In Radar Technology (edited by E. Brookner), ARTECH House Books, Dedham, Massachusetts.

Barton, D. K., 1978: International Cumulative Index on Radar Systems. IEEE Publication Catalog No. JH 4675-5.

IEEE, 1976: IEEE Standard Letter Designation for "Radar Bands." IEEE Standard 521-1976, November 30, 1976.

IEEE, 1977a: IEEE Standard Radar Definitions. IEEE Standard 686-1977, November, 1977.

IEEE, 1977b: IEEE Standard Dictionary of Electrical and Electronic Terms. IEEE Standard 100-1977, IEEE Press, New York.

Johnston, S. L., 1977: Millimeter radar, Microwave J., 20, No. 11, 16ff.

Johnston, S. L., 1978: Some aspects of millimeter radar. Proc. Int. Conf. on Radar, Paris, 4-8 December 1978, 148-159.

Johnston, S. L., 1979: Radar systems for operation at short millimeter wavelengths. The Radio and Electron. Engr., 49, No. 8, (in press).

Skolnik, M. I., 1970a: Millimeter and submillimeter wave applications. Proc. Symp. Submillimeter Waves, Polytechic Press of the Polytechnic Inst. of Brooklyn, N. Y., 9-26.

Skolnik, M. I., 1970b: Millimeter and submillimeter wave applications. NRL Memorandum Rept. 2159, 12 August 1970, DDC No. AD 712055.

Sundaram, G. S., 1979: Millimeter waves - the much-awaited technological breakthrough. Int. Def. Rev., 2, 271-277.

MILLIMETRE WAVELENGTH RESEARCH AT THE APPLETON LABORATORY

Dr. Christopher J. Gibbins

S.R.C., Appleton Laboratory

Ditton Park, Slough, Berks

ABSTRACT

This paper describes various aspects of atmospheric research at millimetre wavelengths being carried out at the Appleton Laboratory. The work includes studies of rainfall attenuation, probing of strato-cumulus clouds and clear-sky measurements of atmospheric attenuation due to resonant absorption by oxygen and water vapour. The work spans a frequency range from 12 GHz to 220 GHz.

1. INTRODUCTION

The propagation of millimetre wavelength radio waves through the Earth's atmosphere is influenced by two factors, non-resonant absorption in condensed water, both in the form of precipitation and clouds, and resonant absorption by molecular oxygen and water vapour. In order, for example, to predict the performance of a communication link operating at millimetre wavelengths, it is necessary to specify and characterise the effects of both these types of attenuation.

The attenuation caused by rainfall increases monotonically with frequency up to about 100 GHz, above which it tends to become independent of frequency, except at low rainfall rates; it will generally be the major factor affecting the reliability of practical communication links operating in the frequency range up to 300 GHz. To plan such links, it is clearly desirable to have comprehensive information on the relationship between attenuation and rainfall characteristics, particularly those between attenuation over a link several kilometres long and rainfall measured at a single point, because it is in this form that most long-term rainfall records exist. Statistical information on the distribution of different levels of attenuation is also of great value.

Attenuation due to non-precipitating cloud is also important along slant paths, as, for example, in an Earth-to-satellite communication link.

At certain frequencies, the attenuation of radio waves by the atmosphere is very high, due to resonant absorption in molecules of oxygen and water vapour. Molecular oxygen has a spectrum comprising many rotational (fine structure) transitions near 60 GHz, which are pressure broadened to form a continuum absorption band from about 55 to 65 GHz, together with a single isolated transition at 119 GHz. The water-vapour spectrum is very complex, but in the millimeter wave region it is characterised by a weak absorption line at 22 GHz, a very strong absorption line at 183 GHz, and an absorption continuum caused by the pressure broadened wings of these and the many infra-red absorption lines. The resulting attenuation is variable, both in space and time due to variations in the distribution of water vapour molecules, and also because the absorption spectrum of water vapour is not fully understood.

Several groups at the Appleton Laboratory are currently studying the various interactions between electro-magnetic radiation at millimetre wavelength and the phenomena described above, using both line-of-sight transmission links and passive radiometry, coupled with measurements of meteorological parameters. This paper describes some of the results obtained.

2. ATTENUATION DUE TO RAIN

2.1 Attenuation - Rainfall Relationships

The attenuation due to rainfall depends primarily on two parameters, the distribution of size and density of the rain drops, and the rainfall rate. Large variations in drop-size distributions occur not only for different types of rain, but also during a single rainfall event. However, average distributions have been found applicable for three different types of rain - drizzle, widespread and thunderstorm (Joss et al., 1968), which relate the number of drops per unit volume per unit diameter to the rainfall rate. Simultaneous measurements of attenuation and rainfall rate will thus provide valuable information on the interaction between radio waves and rain drops.

Measurement of rainfall rate requires a rapid-response raingauge capable of yielding near-instantaneous rainfall rates up to 200 mm h^{-1}. Correlations of attenuation with

rainfall rate measured, for example, with a tipping-bucket raingauge with a slow response time will produce scatter in the data, as shown in Figure 1, where the attenuation on a 7.5 km long 36 GHz link is plotted against rainfall rate from raingauges with a response time of two minutes, spaced 1 km apart. To reduce this scatter, a rapid-response raingauge has been developed by Norbury and White (1971), with a response time of 10 seconds. The same data as shown in Figure 1, correlated with rainfall rate measured with this type of raingauge, is shown in Figure 2, demonstrating the considerable reduction in scatter when near-instantaneous rainfall rates are measured.

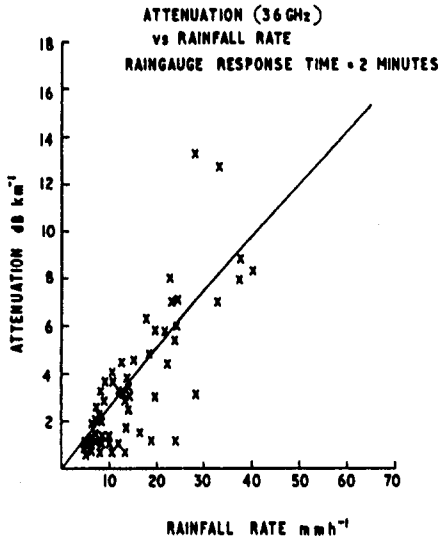

Figure 1 : Attenuation at 36 GHz versus rainfall rate measured with response time of 2 minutes.

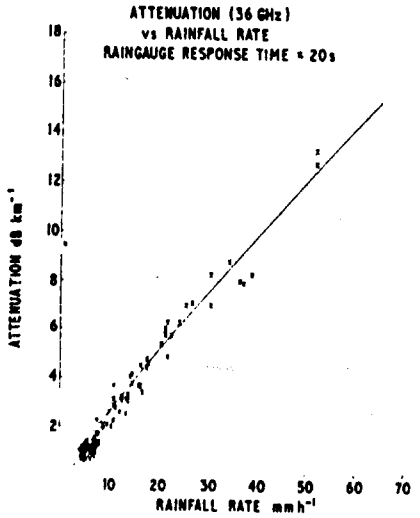

Figure 2 : Attenuation at 36 GHz versus rainfall rate measured with response time of 20 seconds.

Using four such raingauges, the attenuation over a 220 m path at 36 GHz and 110 GHz has been studied by Zavody and Harden (1976), in order to develop a model for predicting the performance of communication links operating at millimetre wavelengths, either from theory or by extrapolation from lower frequency data. Figures 3 and 4 show measured values of attenuation at 36 and 110 GHz, as a function of measured rainfall rates. The theoretical curves have been calculated for drop-size distributions of Laws and Parsons (1943) and Joss et al. (1968) for three types of rain, assuming vertical polarization, and oblate spheroidal drops falling with terminal velocity. At 36 GHz, the agreement between experiment and theory is good, and is better than using theoretical calculations assuming spherical drops. The effects of different drop-size distributions are small, and it is not possible to distinguish experimentally these differences.

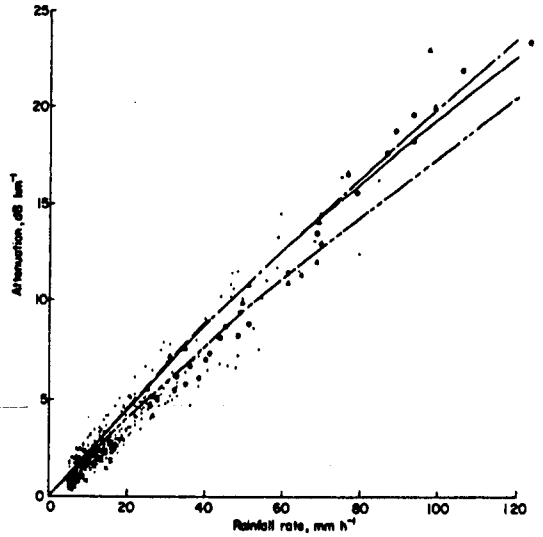

Figure 3 : Variations of attenuation at 36 GHz with rainfall rate.
Experimental values (10 s averages)
. miscellaneous events
X warm front event
▲ leading edge of Thundery shower
● trailing edge of thundery shower
Theoretical values for different drop size distributions:
_____ Laws and Parsons
- - - - - - "thunderstorm") Joss
- . - . - "widespread") et al.
- .. - .. - "drizzle")

At 110 GHz, however, the attenuation at a given rainfall rate is more dependent on drop sizes, as both experimental and theoretical values show in Figure 4. Data from two events have been distinguished to indicate this. Points denoted by crosses (X) are from an event when a weak warm front passed over the links, containing an unusually high proportion of small drops at rain rates exceeding 15 mm hr^{-1}. The triangles (▲) are data from the leading edge of a thundery shower, and the circles (●)

are from its trailing edge. The reduction in drop sizes from leading to trailing edges is common, and is confirmed by significantly higher attenuation, for a given rainfall rate, in the leading edge compared with the trailing edge.

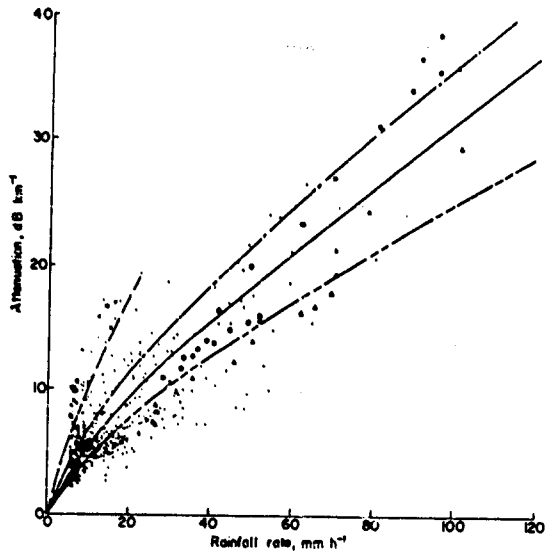

Figure 4 : Variation of attenuation at 110 GHz with rainfall rate. Key as in Figure 3.

A significant number of the data fall outside the limiting curves calculated from theory. The causes for this are thought to be that the actual drop-size distributions differed from those assumed, the drop velocities diverged from the still-air values or the sampling of rain was inadequate. At 110 GHz, small drops are important in the total attenuation, and such drops may be affected by up-draughts or down-draughts leading to errors in the drop-size distributions assumed.

Rainfall attenuation at 110 GHz has been studied by Harden, Llewellyn-Jones and Zavody (1975) using two simultaneous transmission links, one with a 2.65 km path, the other with a path of 215 m. Attenuation on the short link will often be caused by one part of a rain cell, and this can be considered to indicate "attenuation at a point". For events where the rain cell is moving along the link, some estimate can be made of how far spatial variations in rainfall intensity are retained as the cell moves along the path.

Figure 5 shows a comparison of attenuation, averaged over 36 seconds, observed on the 2.65 km path, with the corresponding attenuation derived from the short 215 m path, obtained by smoothing and shifting in time to obtain the best fit to a 45° straight line. The smoothing time of the short-link data is dependent on the speed with which the rain cell is moving along the link, and for the data shown in Figure 4, the smoothing time indicated by the best fit agreed well with that expected from the estimated wind speed. The results of such short and long link comparisons indicate that for cases when the wind direction is along the 2.65 km path, the structure of rain is substantially retained during its movement over that distance.

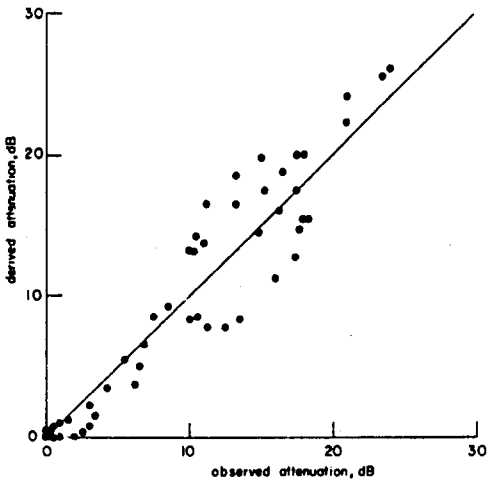

Figure 5 : Comparison of rainfall attenuation at 110 GHz observed on 2.65 km path with that derived from attenuation on 215 m path.

For south-east England, where significant attenuation is caused by rain from a variety of weather types Harden, Llewellyn-Jones and Zavody (1975) reasonably good agreement is found using the Laws and Parsons drop size distribution, assuming spheroidal drops, to predict values of attenuation at low frequencies. Above 100 GHz, however, variations are so great from one rain event to another, and during individual events, that other statistical distributions of drop sizes are needed to estimate the spread in attenuation levels from the mean.

2.2 Statistical Studies

The reliability of communication links, either horizontal or on an Earth-space path, is largely determined by the attenuation caused by rain and cloud, and statistics of this attenuation are important in system planning.

Studies using the horizontal links described in Section 2.1 have shown that the probability distribution of attenuation at 110 GHz on a 2.65 km path is essentially log-normal Harden, Llewellyn-Jones and Zavody, (1975), except at very high attenuation levels, where the sample of data becomes small. Further, the distribution of the duration of fades and the time between fades is also log-normal. Comparisons of measured statistical distributions of attenuation and those derived

from distributions of rainfall rates covering the same period have shown that drop-size distributions are important, but that in general good agreement is found.

Attenuation along slant paths at a number of frequencies has been studied using passive radiometric techniques. Statistical probability distributions of attenuation at 12, 19, 37 and 71 GHz have been obtained using sun-tracking Dicke-type radiometers Davies (1975). Figure 6 presents a summary of the excess attenuation caused by rain and cloud over all elevation angles from 0° to 62°. The 71 GHz data refer mainly to summer months, when large attenuations can occur due to thunderstorms. An estimated distribution for 71 GHz more appropriate to longer-term periods is also shown in Figure 6, obtained using concurrent measurements at 37 and 71 GHz, and normalising to the longer term distribution at 37 GHz. All these data were obtained using sun-tracking radiometers, and may thus be subject to any diurnal effects in rainfall distribution. However, a study was made of the meteorological conditions producing the most intense fades, and this showed that these events are equally likely to occur by day or by night. The data are thus regarded as representative of those which would be obtained by continuous monitoring.

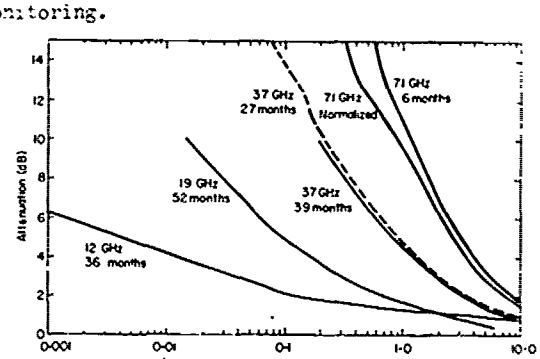

Attenuation Statistics from Sun-Tracking Radiometers at Slough

Figure 6 : Statistics of attenuation obtained with sun-tracking radiometers.

Statistical distributions of attenuation at 10 GHz have also been obtained by Gibbins (1974) using a zenith pointing radiometer measuring atmospheric emission to obtain attenuation data. These results showed that, in south-east England, a zenith attenuation of 10 dB is exceeded approximately 1% of the time.

3. THE EFFECTS OF CLOUDS

The additional contribution to attenuation which clouds can cause, compared with clear sky values, is of importance, for example, in radio astronomy and possibly in space communication systems. To study these effects, ground-based Dicke radiometers operating at several frequencies between 22 and 150 GHz have been used to measure emission noise at vertical incidence from various types of cloud. The additional attenuation caused by cloud was derived from these emission measurements. Figure 7 shows an example of data obtained at 22, 95 and 123 GHz, and indicates that the attenuation in clouds increases with frequency, and that appreciable attenuation can occur above 100 GHz in cumulo-nimbus cloud. Other types of cloud, however, such as stratocumulus or small fair-weather cumulus, produced an additional attenuation of no more than 1 dB even at 150 GHz.

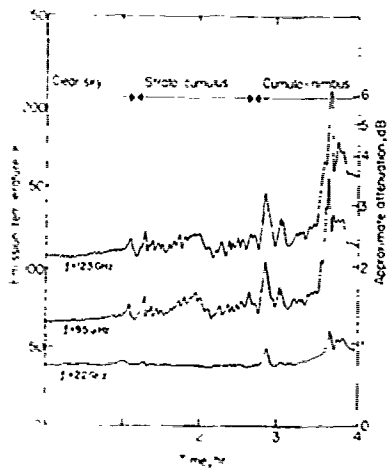

Figure 7 : Measurements of emission noise temperature at the zenith, showing the effects of clouds at different frequencies.

It has been shown, for example, by Westwater (1978), that ground-based microwave radiometry can be used to determine the liquid water content of clouds. There is considerable interest in determining the amount of liquid water in clouds, in order, for example, to predict in real-time, the transmission of millimetre wavelength and infra-red signals through the atmosphere, and also for basic meteorological studies of the formation and development of clouds.

A ground-based radiometer at 95 GHz has been used to obtain values for the total liquid water content of strato-cumulus clouds. Simultaneous with these measurements, the Meteorological Office has measured the size distribution of water droplets in the cloud, using a Knollenberg instrument suspended from a tethered balloon. By integrating this data through the clouds, values are obtained for the total liquid water content. Preliminary comparisons between the two techniques indicate good agreement between the passive ground-based radiometer and the in-situ measurements.

4. CLEAR SKY MEASUREMENTS OF ATMOSPHERIC ATTENUATION

4.1 Absorption due to Oxygen

Multi-frequency studies of the shape of the low-frequency wing of the 119 GHz oxygen line were made using Dicke radiometers which could be tuned manually over the frequency range 85 to 118 GHz. Full details of the experimental technique have been given by Gibbins, Gordon-Smith and Croom (1975).

Figure 8 shows some of the results in the form of zenith attenuation, obtained on clear-sky days, as a function of frequency. The data are for ground-level water-vapour densities of between 3 and 8 gm m^{-3}, and the solid curves are calculations assuming an exponential height distribution of water vapour, with a scale height of 2 km and ground level values of 5 and 10 gm m^{-3}.

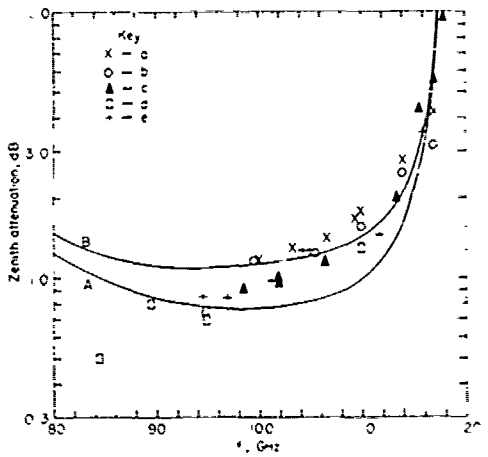

Figure 8 : Experimental values for total zenith attenuation, dB, deduced from emission temperature measurements, under different clear sky conditions. a) ground level H_2O 7.7 gm.m^{-3}; b) 7.7 gm.m^{-3}; c) 4.4 gm.m^{-3}; d) 4.7 gm.m^{-3}; e) 7.7 gm.m^{-3}; Continuous lines are theoretical calculations of attenuation for ground-level H_2O densities of A) 5 gm.m^{-3}; B) 10 gm.m^{-3}.

The data in Figure 8 have been used to study the shape and width of the oxygen line at 119 GHz. Two line shapes were used, that derived by Van Vleck and Weisskopf (1945) and that derived by Gross (1955) and Zhevakin and Naumov (1963). The half-width parameter $\Delta\nu$ for the 119 GHz oxygen line was allowed to vary in calculations using these two line shapes, with the value of $\Delta\nu$ for the 60 GHz oxygen lines obtained by Reber (1973). The best fit to the data was obtained with the Gross line shape, and a value $\Delta\nu$ = 2.20 MHz $torr^{-1}$ for the 119 GHz oxygen line in the atmosphere, compared with earlier laboratory measurements of 1.90 to 1.97 MHz $torr^{-1}$.

4.2 Absorption due to Water Vapour

The absorption at the zenith due to atmospheric water vapour has been studied at a number of frequencies between 22 GHz and 220 GHz, by measuring atmospheric emission on clear-sky days for a range of water-vapour densities. By plotting the derived values of attenuation against surface water-vapour density or the total precipitable water vapour obtained from radiosonde measurements, it is possible to separate the attenuation due to oxygen which is constant, from the variable component, which is normally attributed to water vapour. Some of the results have been reported previously Gibbins, Wrench and Croom, 1977).

The data obtained at 22 GHz are shown in Figure 9, where the measured zenith attenuation is plotted against total precipitable water vapour. The factor 0.95 in values of precipitable water vapour arises from the fact that the radiosonde used to provide this data is located about 50 miles from the Appleton Laboratory. Discussions with the Meteorological Office indicated this correction factor was required to apply the radiosonde data to the Slough site. The factor 1.05 is a correction factor for the side lobes of the horn antenna used in the 22 GHz radiometer.

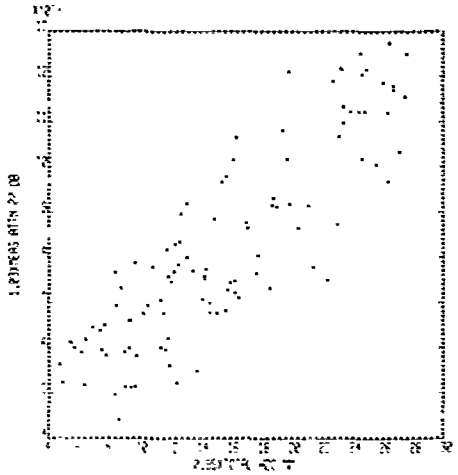

Figure 9 : Measurements of clear-sky zenith attenuation at 22 GHz, dB, versus total precipitable water vapour, mm. See text.

A least squares fit to this data yielded the relation, for the attenuation in dB at 22 GHz.

$$Y_{measured} = 0.28 \pm 0.02W + 0.10 \pm 0.03 \quad (1)$$

where W is the total precipitable water vapour in cm; the correlation coefficient was 0.82.

The experimental results have been compared with calculated values of attenuation obtained from a computer model, using the radiosonde data, and including 46 oxygen lines and 150 water-vapour lines between 22.2 and 6000 GHz. At 22 GHz, the calculated attenuation was

$$Y_{calculated} = 0.2 W + 0.08. \quad (2)$$

Comparison between these two relationships indicates that the constant term, due to oxygen, is in good agreement with theory, and the water-vapour attenuation is about two standard deviations higher than the theoretical value. This is not regarded as significant.

Similar analyses of data obtained at 95 GHz, 110 GHz, 123 GHz, and 150 GHz all indicated good agreement between experiment and theory for the constant oxygen component of attenuation. Except at 110 GHz, the correlations obtained in least squares fitting were good, being between 0.85 and 0.91. At 110 GHz, however, the correlation coefficient was only 0.39, and comparisons between experiment and theory are difficult because of the large scatter in the data; it is not known if the scatter is a real effect, and further work is in progress to determine this.

The measured water-vapour attenuations at the other frequencies, however, were all in excess of calculated values. At 95 GHz, the excess attenuation amounted to about 40%, and was 5 standard deviations above theory. At 123 GHz, an excess of 63% was measured (5σ difference), at 150 GHz the excess attenuation was 47% (3σ difference) and a limited amount of data at 220 GHz indicated an excess of 50 - 60%. Similar results were obtained when the attenuation data were correlated with surface water vapour densities.

The excess attenuation, i.e. the residuals, γ(measured) - γ(calculated), was examined to see if it bore any relation to relative humidity, to water vapour density ρ and to the square of water-vapour density, ρ^2. For relative humidity, only the data at 110 and 150 GHz exhibited a correlation coefficient significantly different from zero. Correlation between the excess attenuation and ρ and ρ^2 was weak at 22.2 and 150 GHz, but much stronger at 95 and 123 GHz. In no case, however, was it possible, because of the scatter in the data, to distinguish between a ρ or ρ^2 dependence.

The data above are still being analysed, but the conclusion is that there is clear evidence for excess attenuation due to atmospheric water vapour, compared with that expected from the simple water-vapour molecule, particularly at the higher frequencies. Such an effect has also been observed in the infra-red region e.g. Emery et al.,(1975), and has been attributed to absorption by water-vapour complexes, in particular, the dimeric molecule. Absorption by dimers would produce a square-law dependence of attenuation on water-vapour density, and there is some evidence in the present data for such a relationship, although it is not conclusive.

5. SUMMARY AND ACKNOWLEDGEMENTS

This paper has reviewed some of the work currently in progress at the Appleton Laboratory in the millimeter wavelength region. The work encompasses studies of rainfall attenuation, of particular relevance to the design of communication links operating at high frequencies, remote sensing studies of clouds, and measurements of the fundamental absorption by atmospheric molecules of oxygen and water vapour, aimed towards a greater understanding of the physics of the interaction between these molecules and electromagnetic radiation. It is clear from the work already done that there is still much to learn, in particular, about the characteristics of rainfall and also the behaviour of the water-vapour molecule.

The work described in this paper has been carried out by several groups at the Appleton Laboratory, and the author particularly acknowledges the contribution of the following: Dr. D. L. Croom, Dr. P. G. Davies, Mr. B. N. Harden, Dr. D. T. Llewellyn-Jones, Dr. J. A. Lane, Dr. J. R. Norbury, Dr. W. J. K. White, Mr. C. L. Wrench and Mr. A. M. Zavody. This work was carried out as part of the programme of the U.K. Science Research Council, Appleton Laboratory, and is published by permission of the Director.

REFERENCES

Davies, P. G., 1975: Attenuation by cloud and rain on Earth-Sun paths at 12 to 71 GHz. Electron. Lett., 11, 547-548.

Emery, R. J., P. Moffat, R. A. Bohlander, and H. A. Gebbie, 1975: Measurements of anomalous atmospheric absorption in the wavenumber range 4 cm^{-1} - 15 cm^{-1}. J. Atmos. Terr. Phys., 37, 587-594.

Gibbins, C. J., 1974: Tropospheric emission and attenuation statistics at 110 GHz. Electron. Lett., 10, 241-243.

Gibbins, C. J., A. C. Gordon-Smith, and D. L. Croom, 1975: Atmospheric emission measurement at 85-118 GHz. Planet. Space Sci., 23, 61-73.

Gibbins, C. J., C. L. Wrench, and D. L. Croom, 1977: Atmospheric emission measurements between 22 and 150 GHz. Proc. URSI Commission F, 28 Apr-6 May, La Baule, France, 19-21.

Gross, E. P., 1955: Shape of collision-broadened spectral lines. Phys. Rev., 97, 395-403.

Harden, B. N., D. T. Llewellyn-Jones, and A. M. Zavody, 1975: Investigations of attenuation by rainfall at 110 GHz in south-east England. Proc. Inst. Elect. Eng., 122, 600-604.

Joss, J., J. C. Thams, and A. Waldvogel, 1968: The variation of rain drop size distributions at Locarno. Proc. Int. Conf. Cloud Phys., Toronto, 369-373.

Laws, J. O. and D. A. Parsons, 1943: The relation of rain drop size to intensity. Trans. Amer. Geophys. Union, 24, 432-460.

Norbury, J. R. and W. J. White, 1971: A rapid-response rain gauge. J. Phys. E., Scientific Instruments, 4, 601-602.

Reber, F. E., 1972: Absorption of the 4-6 millimeter wavelength band in the atmosphere. J. Geophys. Res., 77, 3831-3845.

Van Vleck, J. H. and V. F. Weisskopf, 1945: On the shape of collision-broadened lines. Rev. Mod. Phys., 17, 227-236.

Westwater, E. R., 1978: The accuracy of water vapor and cloud liquid determination by dual frequency ground-based microwave radiometry. Radio Sci., 13, 677-685.

Zavody, A. M. and B. N. Harden, 1976: Attenuation/rain-rate relationship at 36 and 110 GHz. Electron. Lett., 12, 422-424.

Zhevakin, S. A. and A. P. Naumov, 1963: Absorption coefficient of water vapor for electromagnetic waves in the wavelength range 10μ-2 cm. IZV. VUZ. Radiofiz., 6, 674-694.

SUBMILLIMETER PROPAGATION THROUGH FOG

Dr. Dorathy Anne Stewart
US Army Missile Research and Development Command
Redstone Arsenal, Alabama

ABSTRACT

Submillimeter waves propagating through fog are attenuated by fog droplets and by water vapor. Extinction by fog droplets depends upon the wavelength of the energy, the complex index of refraction of the drops for that wavelength, and the drop-size distribution. A thorough literature survey of fog drop-size distributions throughout the world is discussed, and data from 36 references are summarized. A representative sample of data is used to compare propagation of 870 and 1250 μm with the infrared wavelength of 10.6 μm. At the submillimeter wavelengths attenuation by water vapor is usually larger than attenuation by fog droplets, but in the infrared droplets make the dominant contribution and the attenuation by water vapor is almost negligible.

1. INTRODUCTION

This paper compares attenuation of the submillimeter wavelength 870 μm with attenuation of 0.55 μm in the visible, 10.6 μm in the infrared and 1250 μm near 1 mm during fog. Fog exists when the atmosphere contains a suspended aggregate of very small water drops which reduce the horizontal visibility to one km or less near the surface. These conditions of low visibility are important to the Army because they occur frequently in Central Europe (Essenwanger, 1973). The graph in Fig. 1 shows the frequency distribution of fog in the early morning hours by season for ten stations in Germany. Fog occurs most frequently during fall and second most frequently during winter at most stations. Fulda has fog 25 per cent of the time during early morning hours in fall.

Fog is formed by a variety of meteorological processes. When the ground loses heat at night by radiational cooling through a clear atmosphere, radiation fog forms if the air cools enough to become supersaturated. Advection fog is fog which forms when warm, moist air moves across water or land which has a lower temperature. Frontal fog is associated with a frontal passage. It may be caused by rain falling into cooler air or by mixing of different air masses near the frontal zone. Some authors call the former an evaporation fog and the latter a mixing fog. An upslope fog is formed when air flows upward over rising terrain and cools adiabatically below the dew point. Steam fog, which is also called evaporation fog, is formed when cold air moves over a warmer body of water or when warm rain falls through a layer of colder air.

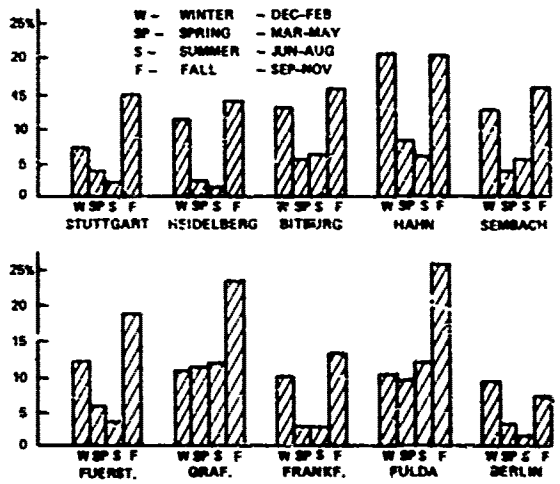

Fig. 1. Frequency of Visibility < 1 km at 0600 GMT.

2. COMPUTATIONAL PROCEDURE

When electromagnetic energy propagates through an atmosphere which contains particles, the extinction coefficient (which is also called the attenuation coefficient) is given by the following formula:

$$\sigma = \sum_i \pi r_i^2 \, (Q_{ext})_i N_i, \qquad (1)$$

where r_i is the radius of particles which have an extinction efficiency factor $(Q_{ext})_i$ (also called the relative extinction coefficient or the normalized extinction cross section). $(Q_{ext})_i$ is a dimensionless function of drop size, wavelength of electromagnetic energy, and complex index of refraction for the given wavelength and particle material. N_i is the number of particles per cubic unit of length of radius r_i. The extinction coefficient σ is in units of inverse length. If σ is in units of m^{-1}, the attenuation in dB/km may be obtained by multiplying by 4343.

All computations in this paper are based on the theory of Mie (1908), and the assumption is made that fog consists of spherical pure water drops. Fig. 2 is a conventional graph of Q_{ext} for 0.55 μm and 10.6 μm versus the parameter $\alpha = 2\pi r/\lambda$ where λ is the wavelength of electro-

magnetic energy. This conventional graph does not illustrate the effect of fog drop size on the relative extinction of different wavelengths as well as Fig. 3 where Q_{ext} is plotted against radius. One sees that for droplets with radii greater than 10 μm, energy of 10.6 μm is attenuated more than visible energy. Fog droplets cause much less attenuation for the submillimeter wavelength of 870 μm. Further details of the computation may be found in Stewart (1977).

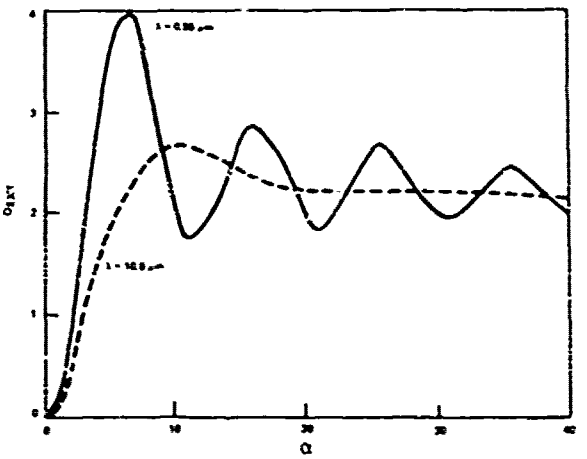

Fig. 2. Q_{ext} versus $\alpha(= 2\pi r/\lambda)$ for 0.55 and 10.6 μm.

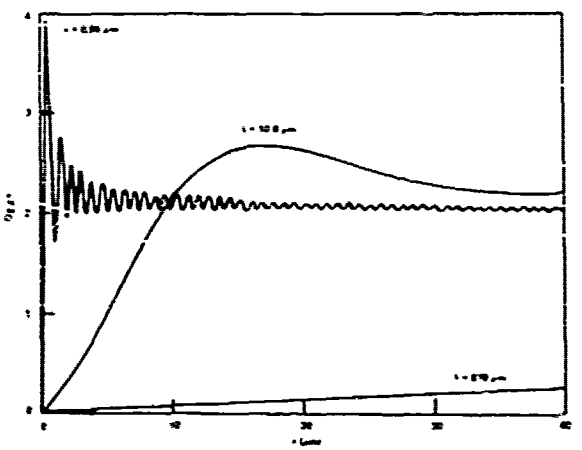

Fig. 3. Q_{ext} versus radius for 0.55, 10.6 and 870 μm.

3. DROP SIZES IN FOGS

Table 1 summarizes an extensive literature survey of measurements of drop sizes in fog near the surface of the earth. Limitations of space prevent a thorough discussion of each set of measurements.

Although some of the variations among the results of different investigators may be caused by biases in different methods of measurement, this cannot explain all the differences. Furthermore, difference in geographic location does not account for all differences. For example, all of May's (1961) measurements were taken from the same position at the side of a building on open Salisbury Plain in England, and the same measuring technique was used. In 9 of the 28 fogs which May studied the maximum droplet radius was greater than 53 μm, but in 11 fogs the maximum radius was less than 28 μm. One fog had a minimum radius of 8 μm, and another had a maximum radius of 7.5 μm. Three distributions had median radii less than 0.5 μm while one had a median radius of 15 μm. Grunow (1960) and Goodman (1977) showed that much of the variation in a given location can be explained by the origin of the air mass in which a fog forms. Mészaros (1965) and Jiusto (1964) concluded that on the average droplet radii in radiation fogs are smaller than those in advection fogs. Chisholm and Kruse (1974) made mesoscale measurements of visibility at L. G. Hanscom Field in Massachusetts, and they found that temporal and spatial variability was much greater in radiation fogs than in advection fogs.

The preceding discussion applies to observations near the surface. Very few observations exist for higher levels, but in one case Okita (1962) observed a liquid water content of 1.6 g/m^3 at a height of 50 m. Rogers et al. (1974) also found that average and maximum liquid water content increased with height, but at 42 m the largest measured liquid water content was only 0.4 g/m^3. Stalenhoef (1974) found that slant visibility from 40 m was normally less than horizontal visibility at 2 m. Pilié et al. (1975a, b) discovered that the broadest drop-size distributions occurred near the surface. Finnick et al. (1978) found significant vertical increases in concentration of droplets with radii greater than 4 μm up to an altitude of 150 m.

4. COMPUTED ATTENUATIONS

Attenuations in fogs were computed for the wavelengths 0.55, 10.6, 870, and 1250 μm. Drop-size distributions were taken from the following six articles: Eldridge (1966); Garland (1971); Garland et al. (1973); Kumai (1973); Pedersen and Todsen (1960); and Pilié et al. (1975b). The complex index of refraction of water for 0.55 μm was taken from Hale and Querry (1973), and the value for 10.6 μm was interpolated from a table in the same article. Davies et al. (1970) made measurements from which the index of refraction of water for 1250 μm could be computed, and interpolation from their data was necessary to obtain the value for 870 μm.

Figs. 4-7 illustrate some of the results of the computations. There is a great deal of scatter of the data in Fig. 4 which shows the relationship between attenuation of visible and infrared energy. An attenuation of 50 dB/km at 10.6 μm can be associated with visibilities considerably less than 100 m or over 300 m. The correlation of attenuations by fog droplets at 0.55 and 10.6 μm is only 0.61. Fig. 5 illustrates the relation of visible and 1250-μm attenuation, and the correlation between the two attenuations is only 0.49. Fig. 6 shows that 10.6-μm attenuation by fog droplets is more closely related to 1250-μm attenuation than to 0.55-μm attenuation. The correlation of the

Table 1. Summary of Measurements of Fog Droplet Radii Near The Surface

Source	Typical Radii (μm)	Maximum Radius (μm)	Miscellaneous Information
Arnulf et al. (1957)	2.5	15	France
Best (1951)	5 to 12	40	From earlier work by Hagemann
Cong and Dessens (1973)	8 to 10	22	Localized near plume from pulp mill
	4.5 to 5.2	17	Widespread through valley
Deloncle (1963)	< 1	10	Urban, near Paris
	< 0.75	8	Mountain top, France
Dickson et al. (1975)	3.4	118	Capistrano, California
Donaldson (1955)	10 to 25	100	Massachusetts
Eldridge (1961)	< 1	32	Massachusetts
Findeisen (1932)	1 to 4	60	Hamburg, Germany
Garland (1971)	< 1	40	Radiation fogs, all water
	10	70	Radiation fogs, ice crystals
	4	60	Advection fogs
Garland et al. (1977)	< 0.6	20	Radiation fogs
Gathman and Larson (1974)	3 to 9	64	Greenland Sea
Goodman (1977)	3.1		San Francisco, CA (2 mete.
Gorchakov (1972)	5.5 to 17.5		Russia
Grunow (1960)			Mt. Hohenpeissenberg, Germany
	1.5	7.5	Polar air
	4 to 7	12.5	Maritime air
	6 to 9	30	Continental air
Houghton and Radford (1938)	4 to 35	65	Typically advection fogs
Jiusto (1964)	5	17.5	Radiation
	10	32.5	Advection
Kozima et al. (1953)	2.5 to 7.5	55	Japan
Kumai (1973)	3.5 to 12.6	65	Point Barrow, Alaska; Advection
Kunkel (1971)	5 to 10	45	Otis Air Force Base
Low (1975)	9 to 13	21	Radiation fog; Ft. Rucker, AL
	4 to 13		Mixed radiation, advection; CA
Ludwig et al. (1974)	0.1	15	Radiation fog
Mack et al. (1973)	4 to 8	31	At sea
May (1961)	< 0.5 to 15	160	Salisbury Plain, England
Mészaros (1965)	< 0.4 to 10	43.8	Budapest, Hungary: Radiation
	2 to 13	101.5	Advection
Okita (1962)	6 to 17	60	Radiation fogs in Japan
Pedersen and Todsen (1960)	< 2	16	Oslo, Norway: Radiation
	2	25	Advection
Pilié et al. (1975)	3 to 12	31	Chemung River Valley, New York
Reinking (1975)	3	7.5	San Joaquin Valley, California
Roberts (1976)	0.2 to 1.1	8	Grafenwöhr, Germany
Rogers et al. (1974)	8	115	California Coast
Rozenberg (1974)	5		Thin
	50		Medium
Tag (1976)	8	23	Panama Canal Zone
Tampieri and Tomasi (1976)	8	22	Radiation fog, Otlay
Thompson et al. (1967)	10	34	Otis Air Force Base
Tverskoi (1965)	1.5	60	Radiation fog
	2	60	Evaporation fog
Webb (1956)	5 to 19	70	Washington, DC and Virginia

data in Fig. 6 is 0.9664. The correlation between 10.6-μm and 870-μm attenuations by fog droplets is 0.9668. Fig. 7 contains a plot of 870-μm attenuation versus 1250-μm attenuation, and the correlation between these attenuations is 0.9873.

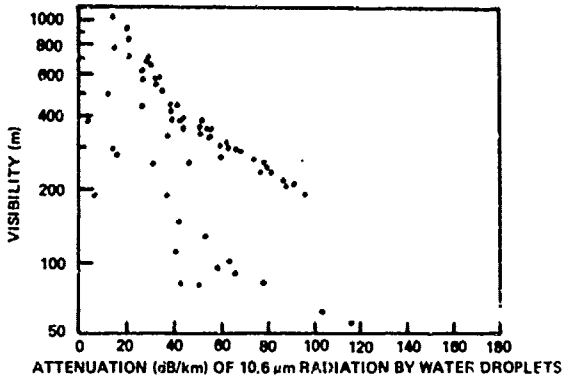

Fig. 4. Plot of Visibility Versus Attenuation at 10.6 μm.

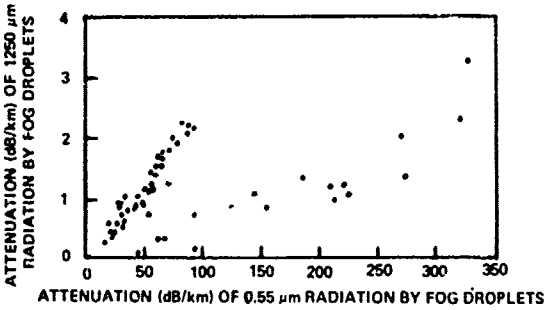

Fig. 5. Comparison of Attenuations of 1250-μm and 0.55-μm Wavelengths by Fog Droplets.

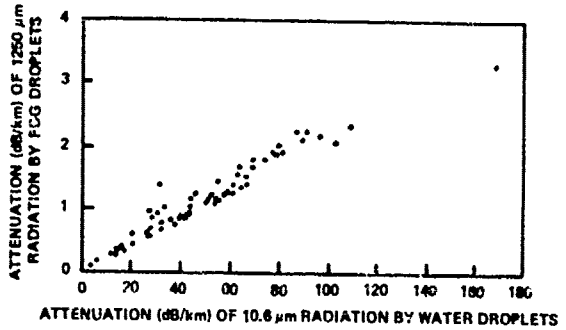

Fig. 6. Comparison of Attenuations of 1250-μm and 10.6-μm Wavelengths by Fog Droplets.

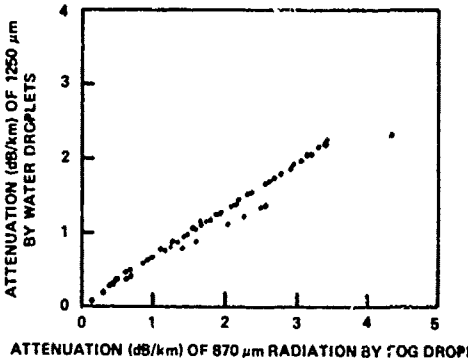

Fig. 7. Comparison of Attenuations of 1250-μm and 870-μm Wavelengths by Fog Droplets.

The data in Figs. 4-7 were examined individually to determine which fogs should be classified as radiation and non-radiation fogs. Average drop sizes are typically smaller in radiation than in non-radiation fogs. Mean attenuations of 10.6, 870, and 1250 μm by fog drops were estimated as a function of visibility for each type of fog.

Unfortunately, climacological fog observations are not classified according to type of fog. Therefore, Essenwanger and Stewart (1978) divided fog into categories on the basis of objective criteria suitable for computerized analysis of large data collections. Observations for several years from ten stations in Central Europe were examined. Finally, fog categories were combined so that each fog was classified as a fog caused primarily by radiational cooling or as a non-radiation fog. Although an individual fog may be a borderline case, these cases should balance out in a statistical sense.

Water vapor is another source of extinction of infrared and near-millimeter wavelengths. McCoy et al. (1969) gave a formula for computing attenuation of 10.6-μm radiant energy by water vapor. Webster (1973) developed a procedure for calculating attenuation by water vapor near 1 mm. Attenuation by water vapor depends primarily upon the amount of water vapor, somewhat upon the temperature, and slightly on the pressure.

Table 2 from Essenwanger and Stewart (1978) contains the mean attenuation by water vapor in German fogs at 0600 GMT as a function of season, wavelength, and type of fog. Attenuation by water vapor is almost negligible for 10.6 μm. Attenuation of 870 μm by water vapor is much larger than attenuation of fog drops. The least amount of water vapor occurs in winter during

Table 2. Mean Attenuation (dB/km) by Water Vapor in German Fogs at 0600 Greenwich Mean Time (from work with Dr. Oskar M. Essenwanger).

	Radiation Fog			Non-Radiation Fog		
	10.6 μm	870 μm	1250 μm	10.6 μm	870 μm	1250 μm
Winter	0.11	5.61	1.74	0.14	6.63	2.06
Spring	0.21	8.16	2.54	0.25	9.06	2.82
Summer	0.50	13.45	4.21	0.64	15.38	4.8[illegible]
Fall	0.29	9.82	3.06	0.32	10.26	3.20

radiation fog, and the mean attenuation of 870 μm under these conditions is 5.61 dB/km. Mean attenuation of 870 μm by water vapor in the summer during non-radiation fogs is 15.38 dB/km. Attenuation of 1250 μm by water vapor is less than one-third the attenuation of 870 μm.

The mean attenuations by water vapor in Table 2 were weighted according to the percentage of radiation and non-radiation fogs and added to a weighted mean attenuation by fog droplets to obtain Table 3 which summarizes expected mean attenuation in German fogs in the early morning. One sees that 1250 μm penetrates fog better than 10.6 μm and 870 μm in all seasons and for all visibilities. Transmission of 870 μm is comparable to or better than transmission of 10.6 μm except in the summer when water vapor content is high.

Table 3. Expected Mean Attenuation (dB/km) in German Fogs at 0600 Greenwich Mean Time (from work with Dr. O. Essenwanger).

Season	Wavelength (μm)	Visibility 1000m	400m	200m
Dec-Feb	10.6	10.5	26.1	52.0
	870	6.5	7.1	8.0
	1250	2.1	2.5	3.1
Mar-May	10.6	8.6	21.3	42.3
	870	8.7	9.2	9.9
	1250	2.8	3.1	3.6
Jun-Aug	10.6	8.4	20.3	40.1
	870	14.2	14.6	15.3
	1250	4.5	4.8	5.2
Sep-Nov	10.6	8.8	21.5	42.7
	870	10.3	10.7	11.5
	1250	3.3	3.6	4.0

Acknowledgment: The author thanks Dr. Oskar M. Essenwanger for encouragement in doing this work and appreciates his letting her use two tables from previous work which we did together.

REFERENCES

Arnulf, A., J. Bricard, E. Curé, and C. Véret, 1957: Transmission by haze and fog in the spectral region 0.35 to 10 microns. J. Opt. Soc. Amer., 47, 491-498.

Best, A. C., 1951: Drop-size distribution in cloud and fog. Quart. J. Roy. Meteor. Soc., 77, 418-426.

Chisholm, D. A. and H. Kruse, 1974: The Variability of Visibility in the Hanscom Mesonetwork: A Preliminary Assessment. Air Force Cambridge Research Laboratories Report AFCRL-TR-74-0265, Environmental Research Paper AFCRL-ERP-479, NTIS Catalog No. AD-784791, 32 pp.

Cong, L. P. and J. Dessens, 1973: Brouillards artificiels produits par émission industrielle de vapeur d'eau. J. Rech. Atmos., 7, 109-116.

Davies, M., G. W. F. Pardoe, J. Chamberlain, and H. A. Gebbie, 1970: Submillimetre- and millimetre-wave absorptions of some polar and non-polar liquids measured by Fourier transform spectroscopy. Trans. Faraday Soc., 66, Part 2, 273-292.

Deloncle, M., 1963a: Constitution des brouillards urbains. J. Rech. Atmos., 1, 107-111.

Deloncle, M., 1963b: Étude photoelectrique des aerosols volatils. Revue d'Optique Théorique et Instrumentale, 42, 157-196.

Dickson, D. H., R. B. Loveland, and W. H. Hatch, 1975: Atmospheric Waterdrop Size Distribution at Capistrano Test Site (CTS) from 16 April through 11 May 1974, Volumes I, II, III, IV, V, and VI. Report ECOM-DR 75-3.

Donaldson, R. J., 1955: Drop-size distribution, liquid water content, optical transmission, and radar reflectivity in fog and drizzle. Proc. Fifth Wea. Radar Conf., 12-15 Sep 1955, Asbury Park, New Jersey, 275-280.

Eldridge, R. G., 1961: A few fog drop-size distributions. J. Meteor., 18, 671-676.

Eldridge, R. G., 1966: Haze and fog aerosol distribution. J. Atmos. Sci., 23, 605-613.

Essenwanger, O. M., 1973a: On the duration of widespread fog and low ceiling in Central Europe and some aspects of predictability. US Army Missile Command, Technical Report RR-73-9, 58 pp.

Essenwanger, O.M., 1973b: On spatial distribution of visibility and clouds in Central Europe. US Army Missile Command, Technical Report RR-73-10, 63 pp.

Essenwanger, O. M. and D. A. Stewart, 1978: Fog and haze in Europe and their effects on performance of electro-optical systems. Paper presented at the Army Science Conference, West Point, New York, 20-22 June 1978.

Lindeisen, W., 1932: Messungen der Grösse und Anzahl der Nebeltropfen zum Studium der Koagulation Inhomogenen Nebels. Gerlands Beitraege zur Geophysik, 35, 295-340.

Garland, J. A., 1971: Some fog droplet size distributions obtained by an impaction method. Quart. J. Roy. Meteor. Soc., 97, 483-494.

Garland, J. A., J. R. Branson, and L. C. Cox, 1973: A study of the contribution of pollution to visibility in a radiation fog. Atmos. Environment, 7, 1079-1092.

Gathman, S. G. and R. E. Larson, 1974: Marine fog observations in the Arctic. Naval Research Laboratory Report 7693, NTIS Catalog Number AD-778999, 27 pp.

Goodman, J., 1977: The microstructure of California coastal fog and stratus. J. Appl. Meteor., 16, 1056-1067.

Gorchakov, G. I., A. A. Isakov, and L. N. Markina, 1972: Determination of the basic parameters of fog microstructure from the coronal indicatrix. Atmos. Oceanic Phys., 8, 50-53.

Grunow, J., 1960: The productiveness of fog precipitation in relation to the cloud droplet spectrum. Physics of Precipitation, Geophysical Monograph Number 5, published by the American Geophysical Union, pp. 110-117.

Hale, G. M. and M. R. Querry, 1973: Optical constants of water in the 200-nm to 200-μm wavelength region, Appl. Optics, 12, 555-563.

Houghton, H. G. and W. H. Radford, 1938: On the measurement of drop size and liquid water content in fogs and clouds. Papers Phys. Oceanogr. Meteor., 6, No. 4, 31 pp.

Jiusto, J. E., 1964: Investigation of warm fog properties and fog modification concepts. NASA Contract Report CR-72, Contract NASr-156, Cornell Aeronautical Laboratory, Buffalo, NY.

Kozima, K., T. Ono, and K. Yamaji, 1953: The size distribution of fog particles. Studies on Fogs, Hokkaido Univ., 303-309.

Kumai, M., 1973: Arctic fog droplet size distribution and its effect on light attenuation. J. Atmos. Sci., 30, 635-643.

Kunkel, B. A., 1971: Fog drop-size distributions measured with a laser hologram camera. J. Appl. Meteor., 10, 482-486.

Low, R. D. H., 1975: Microphysical evolution of fog. J. Rech. Atmos., 9, 23-32.

Ludwig, F. L., S. Schechter, R. C. Robbins, and J. H. Smith, 1974: Condensation nuclei and aerosol populations related to fog formation. Final Report II, SRI Project 6676, prepared under Army Contract DAHC04-67-C-0059, completed December 1973 and printed January 1974, 212 pp.

McCoy, J. H., D. B. Rensch, and R. K. Long, 1969: Water vapor continuum absorption of carbon dioxide laser radiation near 10 μ. Appl. Optics, 8, 1471-1478.

Mack, E. J., R. J. Pilié, W. C. Kocmond, 1973: An investigation of the microphysical and micrometeorological properties of sea fog. Calspan No. CJ-5237-M-1, 40 pp.

May, K. R., 1961: Fog-droplet sampling using a modified impactor technique. Quart. J. Roy. Meteor. Soc., 87, 535-548.

Mészaros, A., 1965: Concentration et distribution dimensionnelle des gouttelettes de brouillards atmosphériques. J. Rech. Atmos., 2, 53-64.

Mie, G., 1908: Beiträge zur Optik trüber Medien, speziell kolloidaler Metallösungen. Annalen der Physik, 25, fourth series, 377-445.

Okita, T., 1962: Observations of the vertical structure of a stratus cloud and radiation fogs in relation to the mechanism of drizzle formation. Tellus, 14, 310-322.

Pedersen, K. and M. Todsen, 1960: Some measurements of the microstructure of fog and stratus clouds in the Oslo-area. Geofysiske Publikasjoner, 21, No. 7, 1-16.

Pilié, R. J., E. J. Mack, W. C. Kocmond, C. W. Rogers, and W. J. Eadie, 1975a: The life cycle of valley fog, part I: micrometeorological characteristics. J. Appl. Meteor., 14, 347-363.

Pilié, R. J., E. J. Mack, W. C. Kocmond, W. J. Eadie, and C. W. Rogers, 1975b: The life cycle of valley fog, part II: fog microphysics. J. Appl. Meteor., 14, 364-374.

Pinnick, R. G., D. L. Hoihjelle, G. Fernandez, E. B. Stenmark, J. D. Lindberg, and G. B. Hoidale, 1978: Vertical structure in atmospheric fog and haze and its effects on visible and infrared extinction. J. Atmos. Sci., 35, 2020-2032.

Reinking, R. F., 1975: Project Foggy Cloud VII--Warm Fog Dispersal and Prevention (Preliminary Summary). Naval Weapons Center Technical Memorandum 2527, 30 pp.

Roberts, R. E., 1976: Atmospheric Transmission Modeling: Proposed Aerosol Methodology with Application to the Grafenwöhr Atmospheric Optics Data Base. Institute for Defense Analysis Paper P-1225, 24 pp.

Rogers, C. W., E. J. Mack, U. Katz, C. C. Easterbrook, and R. J. Pilié, 1974: The life cycle of California coastal fog onshore. Calspan Report No. CJ-5076-M-3 for Air Force Cambridge Research Laboratories AFCRL-TR-74-0419, 85 pp.

Rozenberg, V. I., 1974: Scattering and attenuation of electromagnetic radiation by atmospheric particles. NASA Technical Translation F-771 of a Russian Hydrometeorological Press Publication in Leningrad in 1972, 339 pp.

Stalenhoef, A. H. C., 1974: Slant visibility during fog related to wind speed, air temperature and stability. Arch. Meteor. Geophys. Bioklim., Ser. B., 22, 351-361.

Stewart, D. A., 1977: Infrared and submillimeter extinction by fog. US Army Missile R&D Command Technical Report TR-77-9, 51 pp.

Tag, P. M., 1976: A numerical simulation of warm fog dissipation by electrically enhanced coalescence: part I: An applied electric field. J. Appl. Meteor., 15, 282-291.

Tampieri, F., and C. Tomasi, 1976: Size distribution models of fog and cloud droplets in terms of the modified gamma function. Tellus, 28, 333-347.

Thompson, B. J., J. H. Ward, and W. R. Zinky, 1967: Application of hologram techniques for particle size analysis. Appl. Optics, 6, 519-526.

Tverskoi, P. N., 1965: Physics of the atmosphere. Translated from Russian for the National Aeronautics and Space Administration and the National Science Foundation, NASA TTF-288 TT65-50114, 314-343.

Webb, W. L., 1956: Particulate counts in natural clouds and fogs. J. Meteor., 13, 203-206.

Webster, D. W., 1973: Military potential of the extreme infrared: Technology and applications. Naval Weapons Center Report TP 5565. Catalogued under AD915347.

MICROWAVE EFFECTIVE EARTH RADIUS FACTOR VARIABILITY AT WIESBADEN AND BALBOA

Robert Rubio
US Army Atmospheric Sciences Laboratory
White Sands Missile Range, New Mexico

Don Hoock
Physical Science Laboratory
New Mexico State University
Las Cruces, New Mexico

ABSTRACT

This report describes the variability of the microwave (3-30 GHz) circuit design parameter, effective earth radius factor, at two sites which served as test cases: Balboa, Panama, and Wiesbaden, Germany. Median effective earth radius factors, K, derived from meteorological data for the first 100 m altitude at these two sites, were found to be 1.32 for Wiesbaden and 1.68 for Balboa. K factor variability at Balboa and Wiesbaden is illustrated with sets of equivalent earth profile curves enclosing 68.3, 95.4, 99.7, and 100 percent of the data and by K factor cumulative distribution functions bounded by respective 90 and 99 percent confidence limits. Effective earth radius factors were found to be highly variable, particularly at Balboa.

1. INTRODUCTION

A study designed to examine the variability of microwave effective earth radius factors has been performed for the sites of Wiesbaden, Germany, and Balboa, Panama, which served as test cases. Effective earth radius factors representative of a given geographical location are conventionally used in path profiling of microwave communication links to account for tropospheric refractivity gradients, which in turn are dependent on atmospheric relative humidity, temperature, and pressure magnitudes--three highly variable parameters. The unpredictable variability of these atmospheric parameters prompted this effort which presents the statistical data that delineate the range of effective earth radius values which occur in Wiesbaden and Balboa.

Specifically, this report describes the mathematical procedure used in interpreting meteorological data used to derive refractivity gradients, the statistical technique employed to derive effective earth curvature and its variability, and presents the results obtained. The original meteorological data for Wiesbaden and Balboa collected by Samson (1975) were obtained and processed. Processing of the meteorological data involved the determination of over 4700 refractivity gradients at each station. Since most line of sight (LOS) microwave transmitters, repeaters, and receivers employ high-gain directional antennas located within the first 100 m above ground level, all atmospheric refractivity gradients derived here are for that interval between the earth's surface and 100 m altitude. Effective earth radius, K, values were determined corresponding to the median value of the refractivity gradient at each station and to selected percentile deviations of the data from the median. Cumulative distribution functions of K and the 90 and 99 percent confidence limits for each K value were also determined.

2. METEOROLOGICAL AND REFRACTIVITY DATA

The primary sources of meteorological data, excluding surface observations, are those measurements of relative humidity, pressure, and temperature obtained with standard balloon-borne radiosondes in use throughout the world. Radiosonde observations of temperature, pressure, and relative humidity are reported at fixed atmospheric pressure levels termed "mandatory levels" and at "significant levels." Significant levels are those where an appreciable change in temperature or relative humidity as a function of altitude occurred before the balloon reached the next mandatory level. Consequently, mandatory levels differ in altitude because of differences in terrain elevation at each sounding station. Significant levels differ in altitude due to the variable temperature lapse rates encountered during the year. Normally the first mandatory level or significant level above the surface is at an altitude greater than 100 m. Therefore to calculate refractivity at 100 m altitude, and subsequently the refractivity gradient for that interval, an interpolation scheme had to be employed which utilizes the calculated refractivity values obtained from the meteorological measurements at the surface and at the lowest recorded level.

The expression for radio wave refractivity in the lower troposphere, for frequencies up to 30 GHz, is well established (Bean and Dutton, 1966) and is of the form:

$$N = 77.6 \frac{P}{T} + 3.73 \times 10^5 \frac{e}{T^2} , \qquad (1)$$

where P is the total atmospheric pressure in millibars, T is absolute temperature in degrees Kelvin, and e is the partial pressure of water vapor in millibars. N is in units of refractivity, related to the usual index of refraction n by $N = 10^6(n - 1)$. In equation 1, the quantity $77.6\ P/T$ is normally referred to as the "dry term," while the quantity $3.73 \times 10^5 e/T^2$ is called the "wet term." Accordingly, the refractivity may be expressed as

$$N = N_D + N_w , \qquad (2)$$

where

$$N_D = 77.6\ P/T , \qquad (3)$$

$$N_w = 3.73 \times 10^5 e/T^2 . \qquad (4)$$

Variations in refractivity as a function of altitude have been shown to follow an exponential function (Bean and Thayer, 1959) of the form

$$N_D = A_D e^{-B_D h} , \qquad (5)$$

$$N_w = A_w e^{-B_w h} . \qquad (6)$$

Since the assembled meteorological data allow one to calculate N_D and N_w at the earth's surface and at the first mandatory altitude of h_1, solutions for the parameters A_D, A_w, B_D, and B_w were obtained and substituted into equations 5 and 6. Subsequently equations 5 and 6 were summed to yield the following refractivity interpolation equation:

$$N(h) = N_D(h_o) \left[\frac{N_D(h_o)}{N_D(h_1)}\right]^{-\frac{h}{h_1}} + N_w(h_o) \left[\frac{N_w(h_o)}{N_w(h_1)}\right]^{-\frac{h}{h_1}} , \qquad (7)$$

where

$N(h)$ = Total refractivity at altitude h,

$N_D(h_o)$ = Dry term refractivity at earth's surface, h_o,

$N_D(h_1)$ = Dry term refractivity at altitude h_1 for which data is available,

$N_w(h_o)$ = Wet term refractivity at earth's surface, h_o,

$N_w(h_1)$ = Wet term refractivity at altitude h_1 for which data is available.

Each interpolation yielded a refractivity magnitude at an altitude of 100 m, which when subtracted from the refractivity magnitude obtained at the earth's surface, provided the desired refractivity gradient, $\Delta N/\Delta h$. For the locality of Balboa, Panama, 4917 refractivity gradients were computed with radiosonde measurements of the period from 1951 to 1956. During the sunrise atmospheric heating and sunset cooling time periods, refractivity gradients exhibit maximum variability and definite changes in absolute magnitude. Thus in an analysis of this type, it is desirable to have a meteorological sample of the sunrise and sunset periods included. However, of the total data set, only 380 samples were representative of near sunset or sunrise hours; the remainder of the data set consists of a balanced mixture of totally night or daytime meteorological data. For Wiesbaden, Germany, 4798 refractivity gradients were derived from data recorded during the period 1951 to 1957. All Wiesbaden meteorological data are from either daytime or night radiosonde measurements; no sunrise or sunset samples were available. Consequently, the variability results to be presented here are inherently conservative.

Ordinal listings of the 100-m refractivity gradients for Balboa and Wiesbaden were compiled and median refractivities of -64 units/km and -38 units/km, respectively, were obtained. Initial attempts to work with average refractivity gradients and deviations from the average value proved meaningless because the frequency distribution of the refractivity gradients was found to be non-Gaussian. Figures 1 and 2 are refractivity gradient histograms which approximate the frequency distributions at Balboa and Wiesbaden. These figures show that the distribution is non-Gaussian or at least that the sample was insufficient to approximate a Gaussian distribution. Therefore, a median value and percentile distributions about the median were employed to describe refractivity gradient spread. Annotated on the histograms are the median values and percentile deviations from the median obtained directly from the ordinal listing. The 34th and 47.5th percentile deviations denote how 68 and 95 percent of the data are distributed about the median. For Balboa, 95 percent of the gradient data is within -202 and -1 units/km; while for Wiesbaden, 95 percent of the gradients have values ranging from -86 to +16 units/km.

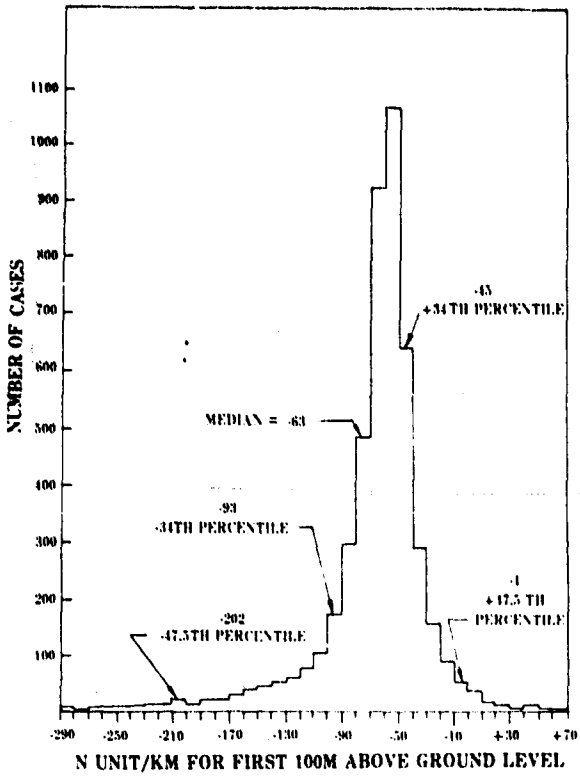

Figure 1. Balboa, Panama, refractivity gradient histogram.

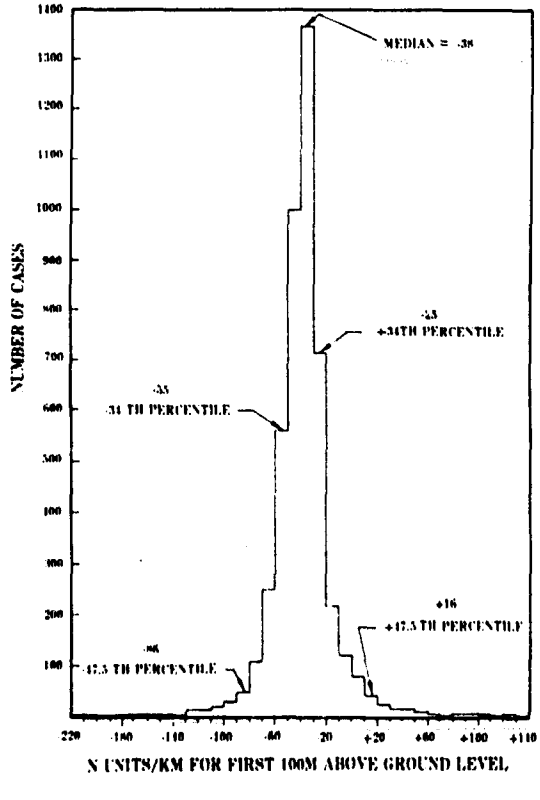

Figure 2. Wiesbaden, Germany, refractivity gradient histogram.

3. EFFECTIVE EARTH CURVATURES

Radio transmission path profiles drawn to aid in the design of microwave communications links must account for the earth's curvature and radio beam refractivity. Radio beam refraction is normally combined with the earth's curvature to define an effective earth radius usually designated as Kr, where r is the true earth radius and K is the atmospheric refraction dependent modification factor. Depiction of the earth with an effective earth radius of Kr allows the radio beam to be drawn as a straight line as shown in figures 3a and 3b. To facilitate path profile plotting, both curves may be transformed to a flat earth reference frame and a radio wave beam with curvature Kr as shown in figures 3c or 3d. Thus, variations in the K factor, induced by meteorological changes, may then be depicted by several plots representing the range of probable Kr magnitudes.

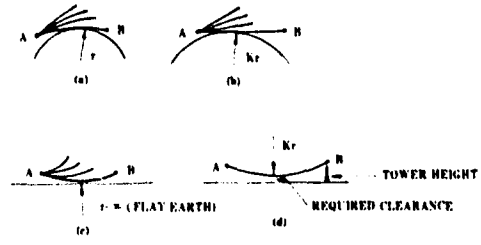

Figure 3. (a) and (b) consolidation of earth's curvature and radio beam atmospheric refractivity into an effective earth radius Kr, (c) and (d): inversion of consolidated curvatures for design purposes.

In this section the equations used to derive all the K factors, the median K, percentile deviations from the median K, and equivalent earth profile curves like those shown in figure 3d are described. Actual values and graphs for Balboa, Panama, and Wiesbaden, Germany, are obtained and a brief interpretation of their meaning is presented.

Conversion from refractivity gradients, $\Delta N/\Delta h$, to effective earth radius factors K is easily accomplished with the standard equation (Bean and Dutton, 1966, p. 14),

$$K \simeq \frac{157}{157 + \frac{\Delta N}{\Delta h}} \quad \frac{\text{units}}{\text{km}} , \qquad (8)$$

which is valid for radio waves originating at small angles with respect to the horizontal and when the magnitude of the atmosphere's index of refraction is near unity. Ground LOS microwave transmissions usually meet the above criteria. Calculation of an average K value for all data at a specific location proved meaningless because, as can be noted in equation 8, refractivity gradients of magnitudes near -157 yield extremely large values of K. Consequently, a few large K's (some equal to infinity) grossly distort the average K. Nonetheless large K's represent physically real conditions. In the case of

K equals infinity, the radio beam is traveling concentric to the earth's true surface. To overcome the above difficulty and properly include large values of K, medians and percentile deviations of data from the median were employed. These quantities were derived from the corresponding refractivity gradient median and percentile deviations with equation 8 expressed in the following manner:

$$K_M = \frac{157}{157 + \left(\frac{\Delta N}{\Delta h}\right)_M}, \qquad (9)$$

$$K_p = \frac{157}{157 + \left(\frac{\Delta N}{\Delta h}\right)_p}, \qquad (10)$$

where

K_M = median K,

K_p = K located at p^{th} percentile from median,

$\left(\frac{\Delta N}{\Delta h}\right)_M$ = Median $\Delta N/\Delta h$,

$\left(\frac{\Delta N}{\Delta h}\right)_p$ = p^{th} percentile value of $\Delta N/\Delta h$ obtained directly from ordinal listing

Equivalent earth profile curves, like those shown in figures 3c and 3d, were constructed by using the simple geometric relationship (Lenkurt Electric Co., Inc., 1970).

$$h = \frac{2}{3}\frac{d^2}{K}, \qquad (11)$$

where

h = height above path center,

d = horizontal distance from path center,

K = equivalent earth radius factor.

Graphs employing relationship shown in equation 11 will display the variability of radio beam refractivity for expected magnitudes of K.

Employing equation 9, median K values of 1.68 and 1.32 were calculated for Balboa and Wiesbaden, respectively. Note here that the Wiesbaden K value of 1.32 is in agreement with the K = 4/3 value conventionally used throughout the world; however, the Balboa median differs significantly from 4/3. Percentile deviations from the median equivalent to standard deviation percentage ranges commonly used in Gaussian distributions (σ, 2σ, etc.) were identified in the refractivity gradient ordinal listing and used in equation 10 to compute the corresponding K values. The median K values and the K's obtained for the 68.3th, 95.4th, 99.7th, and 100th percentile regions about the Balboa and Wiesbaden median, respectively, are tabulated in figures 4 and 5. Inspection of the K column in figures 4 and 5 reveals three ranges of the K magnitudes which are of interest: $0 < k < 1$, $1 \leq K < \infty$, and K negative.

These K data sets indicate, respectively, that the radio beam curves upward away from the earth, downward with a curvature less than the earth's, and downward with a curvature greater than the earth's. For Balboa, $0 < K < 1$ occurred about 2.5 percent of the time, $1 \leq K \leq \infty$ occurred about 93 percent of the time, and K negative occurred the remaining 4.5 percent. Note that the extreme K factors at Balboa for this 5-year period were +0.39 and -0.10. At Wiesbaden, $0 < K < 1$ occurred 4.6 percent of the time, $1 \leq K \leq \infty$ occurred 95.2 percent of the time, and K was negative the remaining 0.2 percent. The extreme K factors for Wiesbaden, +0.36 and -0.73, were not as severe as those found at Balboa.

Equivalent earth profile curves for each of the listed K values for Balboa and Wiesbaden are also included in figures 4 and 5. These sets of profiles were constructed with the use of equation 11 after the origin was chosen, quite arbitrarily, 275 ft above the abscissa which was designated as the flat earth surface. The coordinates (d,h) for a selected K of interest, identify the location of the radio terminals. Since the plots of figures 4 and 5 represent the percentile deviations from the median K values, these curves identify the expected variability of radio beam refraction along the path and particularly at the radio terminal. The plots labeled +4 and -4, accordingly, represent the maximum earth - beam divergence and maximum downward refractivity which might occur. Figures 4 and 5 show, again, that radio beam dispersion is greater at Balboa than at Wiesbaden. For example, if a transmission path of 32 miles is selected, the radio beam axis will remain within approximately +15 ft and -20 ft of the median K path 63.3 percent of the time and +60 ft and -55 ft 95.4 percent of the time at Wiesbaden, Germany, while at Balboa, Panama, the beam axis varies about the median K path +20 ft and -35 ft 63.3 percent of the time and +70 ft and -155 ft, 95.4 percent of the time. Radio beam variability for other transmission path distances can be readily estimated from these plots.

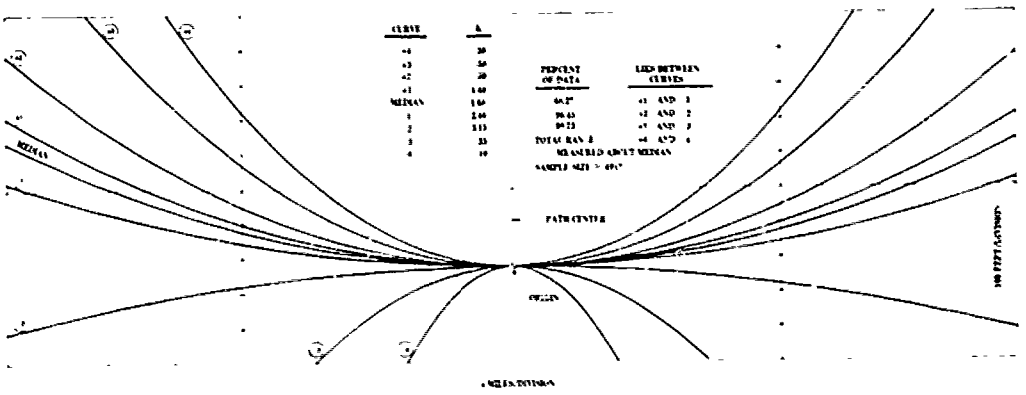

Figure 4. Profiles of combined earth and refractivity curvatures based on K median and percentile deviation values derived from Balboa, Panama, meteorological data.

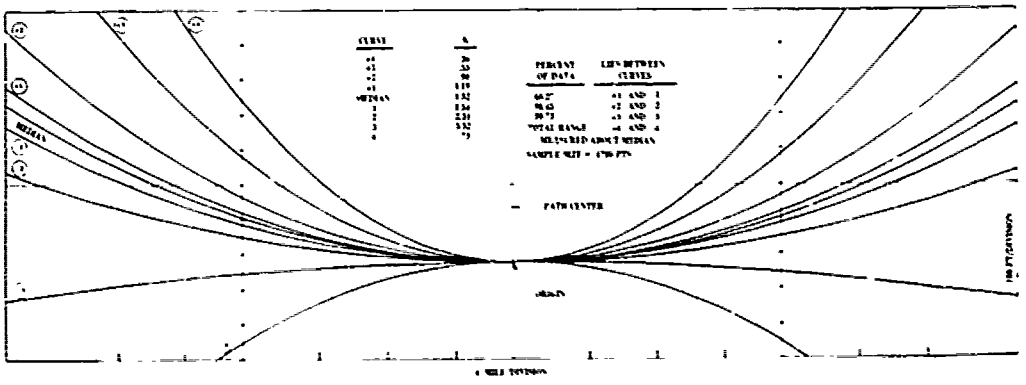

Figure 5. Profiles of combined earth and refractivity curvatures based on K median and percentile deviation values derived from Wiesbaden, Germany, meteorological data.

4. EFFECTIVE EARTH RADIUS FACTOR DISTRIBUTION FUNCTIONS

Cumulative distribution functions for the Balboa and Wiesbaden effective earth radius factors were constructed along with the derived 90 and 99 percent confidence interval for each function. K factor cumulative distributions were ordered from the smallest positive K value to infinity, abruptly changed to minus infinity, and then ordered towards the smallest negative K, all as a function of the percent of total cases. This arrangement is plotted in the center graphs of figures 6 and 7, and although it differs from the conventional smallest to largest number cumulative distributions, it does depict the degree and direction of actual radio beam bending without introducing physical discontinuities. Near-infinite K values occur a significant portion of the time. This arrangement also places the median K value near the graph center and relegates the rarer extreme refractivity cases to the plot edges. Figures 6 and 7 are not all-inclusive because the few extreme valued K factors encountered called for an unnecessarily large graph. Instead, these K factors and the respective cumulative percentages are listed in table 1.

By selection of a specific K_p magnitude from the cumulative distribution function, one can predict the percentage of time that radio beam bending will remain within a required criterion. However, each K_p percentile is a statistic based on a finite data sample. A small probability exists that the true distribution differs from the observed distribution. Thus confidence intervals were established to determine within which percentile limits the true K_p value would be located given a desired degree of confidence. This same K_p confidence interval defines the range within which K_p will occur for the stated confidence level. Two confidence levels of interest are 90 and 99 percent. The outermost plots of figures 6 and 7 are the 99 percent confidence limit boundaries, while the intermediate plots are the 90 percent confidence interval boundaries. The interval widths are based on the following nonparametric statistical technique (Conner, 1971).

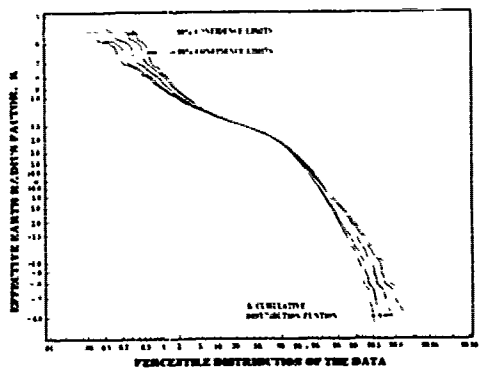

Figure 6. Effective earth radius factor cumulative distribution function and confidence intervals for Balboa, Panama.

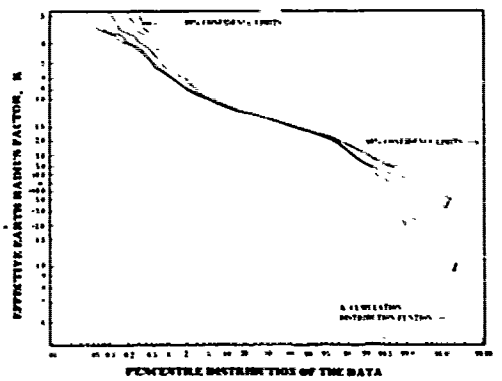

Figure 7. Effective earth radius factor cumulative distribution function and confidence intervals for Wiesbaden, Germany.

If $K_1\ K_2 \ldots K_n$ represent an ordered sample of independent random variables with

$$K_1 \leq K_2 \leq \ldots \leq K_r \leq \ldots \leq K_s \leq \ldots K_n$$

and $1 \leq r \leq s \leq n$; then the lower confidence limit is given by

$$r = np - W_{\alpha/2}\sqrt{np(1-p)}\ ; \qquad (12)$$

and the upper confidence limit is given by

$$s = np + W_{1-\alpha/2}\sqrt{np(1-p)}\ , \qquad (13)$$

where

n = total sample number,

p = data percentile value for which confidence interval is being established,

α = level of significance or 1 - confidence coefficient,

W = the $\alpha/2$ or $1 - \alpha/2$ percentile of a standard normal random variable.

TABLE 1. EXTREME EFFECTIVE EARTH RADIUS K FACTORS

Cumulative Percent*	K	Cumulative Percent*	K
	Balboa, Panama		
0.02	-0.10	99.87	0.58
0.04	-0.17	99.90	0.55
0.06	-0.18	99.92	0.55
0.08	-0.18	99.94	0.54
0.10	-0.25	99.96	0.48
0.12	-0.26	99.98	0.48
0.14	-0.33	100.00	0.39
0.16	-0.37		
0.18	-0.41		
0.20	-0.42		
0.22	-0.43		
0.24	-0.57		
	Wiesbaden, Germany		
0.02	-0.73	99.88	0.55
0.04	-0.75	99.90	0.55
0.06	-2.12	99.92	0.52
0.08	-3.20	99.94	0.50
0.10	-3.49	99.96	0.43
		99.98	0.40
		100.00	0.36

**Cumulative percentages are based on data listed here and that shown in figures 5 and 6.*

In accordance with the above definitions, K_s and K_r bound the K_p confidence interval for a stated $1 - \alpha$ confidence level.

Examination of the cumulative distribution curves in figures 6 and 7 again reveals a higher variability in effective earth radius factor at Balboa. At Wiesbaden, 99.86 percent of the effective earth radius factors encountered can be accounted for by considering the region $0.5 < K \leq \infty$ plus $-\infty \leq K < -2$, while at Balboa the larger numerical region of $0.55 < K \leq \infty$ plus $-\infty \leq K < 0.58$ must be considered to account for 99.$\overline{7}$ percent of the cases. The Balboa distribution function is also more widely dispersed towards negative K values. Wiesbaden data contain only a few negative K magnitudes, which means that there is an infrequent occurrence of severe downward radio beam refraction with curvatures greater than the earth's. Upward beam bending occurs approximately 2 percent of the time at both Balboa and Wiesbaden; this occurrence is demonstrated by that section of the cumulative distribution function where $0 < K < 1$. Table 1 indicates that the extreme downward refraction case for Wiesbaden, Germany, occurred at a K value of -0.73 which is less severe than the extreme Balboa case of K = -0.1. Table 1 also shows that extreme upward beam refraction encountered at Wiesbaden was for an effective earth radius factor of 0.36, while at Balboa the maximum upward refraction occurred at a comparable K

value of 0.39. All the extreme K values encountered represent refractivity conditions vastly different from those represented by the respective medians or the conventionally used K value of 4/3. The variability of K is high, particularly at Balboa, Panama.

The 99 percent confidence intervals ranged from a ΔK of less than 0.1 at the median to a ΔK of approximately 0.6 at K = -0.89 (last interval shown on figure 6 graph) for Balboa, and from a ΔK of approximately 0.1 at the median to a ΔK of about 4.3 at K = -2.0 for Wiesbaden. Since effective earth radius factor median changes less than 0.1 are considered negligible for present average microwave communications path lengths, a 99 percent level of confidence can be attached to the fact that the actual medians, both at Balboa and Wiesbaden, will remain ±0.05 K of the calculated median. In contrast, the confidence intervals at the fringe K values of -0.89 and -2.0 can be an appreciable percentage of the measured percentile. At Balboa, the negative section of the confidence interval at K = -0.89 is the larger one. The magnitude is +0.58 and is 35 percent of the absolute value of -0.89. Similarly at Wiesbaden the larger section of the confidence interval has a magnitude of approximately -3 or 150 percent of -2. The significance of these percentages is dependent on the circuit design criteria which define the necessity to keep the refractivity within certain bounds. Confidence intervals for the extreme K values at Wiesbaden are noted to be wider than those at Panama. The relative scarcity or infrequent occurrence of extreme K values at Wiesbaden caused the confidence interval to diverge. Equations 12 and 13 indicate that the width of the interval is dependent on the location of K_r and K_s percentile points. The locations of the K_r and K_s percentiles are dependent on the number of data points available in the K_p vicinity. Consequently, at Panama where the higher K variability places more data points at the fringe area, a smaller interval defines the 90 and 99 percent limits. At Wiesbaden a larger interval is required to retain the same confidence levels. Confidence intervals for the effective earth radius factor data listed in table 1 were not derived because the limited data sample in this data group rendered meaningless statistical results.

5. CONCLUSIONS

To better understand and quantitatively predict the degree of effective earth radius factor, K, variability, meteorological data were acquired from two distinct locations and used to derive the K factors, which served as test cases. Two areas of interest, Germany and Panama, were chosen as the sample sites. Specifically, atmospheric pressure, temperature, and relative humidity data from Balboa, Panama, and Wiesbaden, Germany, were converted to average refractivity gradients over the first 100 m altitude with the use of an interpolation scheme. Thereafter for each refractivity gradient, a corresponding effective earth radius factor was computed. The median refractivity gradients were determined to be -38 units/km for Wiesbaden and -64 units/km for Balboa. The refractivity gradient distribution was found to be non-Gaussian in both cases. Ninety-five percent of the Balboa refractivity gradients are contained within -202 units/km and -1 unit/km, while at Wiesbaden 95 percent of the data is within -86 units/km and +16 units/km. Median effective earth radius factors were found to be 1.32 for Wiesbaden and 1.68 for Balboa. Although the Wiesbaden K median is in general agreement with the current "standard" K = 4/3 magnitude, the Balboa K median is significantly different. Derived K factors enclosing 68.3, 95.4, 99.7, and 100 percent of the Balboa and Wiesbaden K data, listed in figures 4 and 5 along with the corresponding equivalent earth profiles curves, illustrate the high variability in microwave refraction at these two locations. At Wiesbaden radio beam upward refraction was found to occur 4.6 percent of the time, while downward beam bending occurred 95.4 percent. At Balboa upward refraction occurred only 2.5 percent of the time, while downward refraction occurred the other 97.5 percent of the time. Downward beam refraction is found to be more severe at Balboa. K factor cumulative distribution functions, shown in figures 6 and 7, also demonstrate the K variability at both locations. Boundaries defining the 90 and 99 percent confidence limits of the cumulative distributions established that both medians can be predicted to occur within K < 0.1 with a 99 percent level of confidence. Confidence intervals for extreme K values are considerably wider than 0.1 K. In general K was found to be highly variable at both Wiesbaden and Balboa.

REFERENCES

Bean, B. R., and E. J. Dutton, 1966: Radio Meteorology. US Government Printing Office, Washington, DC.

Bean, B. R., and G. D. Thayer, 1959: Models of the Atmospheric Index of Refraction. Proc. IRE, 47, No. 5, 740-755.

Conner, W. J., 1971: Practical Nonparametric Statistics. John Wiley & Sons, Inc., New York.

Lenkurt Electric Co., Inc., 1970: Engineering Considerations for Microwave Communications Systems. ,Report, Lenkurt Electric Co., Inc., San Carlos, California.

Samson, C. A., 1975: Refractivity Gradients in the Northern Hemisphere. Office of Telecommunications Report 75-59, Department of Commerce.

ATMOSPHERIC PROPAGATION OF SUBMILLIMETER WAVES: OBSERVED CORRELATIONS WITH FOG CONDITIONS AT 0.890 mm WAVELENGTH

G. A. Tanton, J. F. Osmundsen, R. L. Morgan, H. C. Meyer, and J. G. Castle, Jr.*

US Army Missile Command

Redstone Arsenal, Alabama

ABSTRACT

The present investigation is aimed at characterizing the propagation of submillimeter waves in the atmosphere for possible application in an all-weather radar. Preliminary experimental results for a 200 meter path close to ground level are presented. Atmospheric water vapor density, ρ, and dry bulb temperature, T, are correlated with the observed transmission ratio, R, where R is defined as the ratio of received intensity to the transmitted intensity of the 0.890 mm (330 GHz) radiation. The CO_2-pumped FIR laser source is described in some detail. The collection of data over many days shows an observed correlation of R with ρ as a linear increase in log R with temperature-dependent parameters over the range from 10 to 25 g/m^3, except for a cluster of some of the points near 17 g/m^3, where the transmission is significantly higher and essentially temperature-independent from 77 to 83°F. This apparent bimodal behavior is interpreted as further indication that the equilibrium values of ρ and T do not predict R. In addition to these observations at high visibility, we have observed some reduction in the transmission of 0.890 mm radiation during conditions of fog with visibility less than 100 meters.

1. INTRODUCTION

There is a military need for an all-weather target acquisition and recognition system that is compatible with requirements of small transmitting and receiving apertures and the ability to penetrate fogs and other target obscurants. Kruse (1974) and Hartman et al. (1976) have pointed out the advantages of working in the 0.74 - 1.3 mm atmospheric windows for all-weather radar applications. Wavelengths in these atmospheric windows are short enough to provide adequate resolution with small diameter apertures to recognize combat size targets but are long enough to be affected only slightly by fogs and aerosols.

It is now well known that the chief source of atmospheric absorption in the millimeter and SMMW region is the water molecule. The laboratory measurement of absorption due to pure water vapor and H_2O-N_2 mixture in the SMMW region is well documented in a number of recent reviews (Bastin (1966); Burch (1968); and Waters (1976)). It has been pointed out that the standard theoretical models of rotational line shapes do not predict the H_2O absorption in the window regions.

This paper reports experimental results pertaining to effects of atmospheric water vapor and temperature on propagation at 0.890 mm wavelength, in the window between the J' = 5 to J" = 4 line at 10.85 cm^{-1} and the J' = 4 to J" = 3 line at 12.68 cm^{-1}. The data were collected during the summer of 1978 at Redstone Arsenal, Alabama.

2. EXPERIMENTAL ARRANGEMENT

The FIR laser used is a dielectric waveguide laser designed and built in-house by W. L. Gamble and J. F. Osmundsen. The FIR laser cavity consists of two plane mirrors mounted coaxially with and at opposite ends of the glass tube waveguide, which measures 162.5 cm long, 4.8 cm OD, and 4.4 cm ID. The mirrors must be almost in contact with the waveguide to minimize radiation coupling losses from the waveguide to the mirrors and from the mirrors back into the waveguide.

The output coupler mirror is actually two mirrors in one. The substrate of this mirror must be transparent to FIR radiation, and thus it is a wafer of high resistivity intrinsic silicon and has a diameter of 50 mm and a thickness of 3 mm. First a 98% multilayer dielectric mirror to reflect the pump laser beam is evaporated onto this substrate. Then for reflection and output coupling of the FIR radiation, an optically thick annular shaped gold coating surrounding a central hole (1 cm diameter) is evaporated directly on top of the multilayer dielectric mirror.

The other mirror in the FIR laser is a gold-coated copper mirror having a 3 mm diameter central hole through which the pump laser beam is focused. This copper mirror is translated longitudinally for initial cavity tuning.

*Permanent address: Physics Department, University of Alabama in Huntsville, Huntsville, AL 35807

The entire FIR laser is supported in a cylindrical frame constructed of circular aluminum disk spacers and three Invar rods for thermal stability. The entire laser and frame fit into a vacuum chamber constructed from a section of industrial glass pipe 6 feet long and 7 inches in diameter. The end plate at the output end has a window of fused quartz which is transparent for the FIR laser beam, and the input end plate has a NaCℓ window which is transparent for the pump laser beam.

The pump laser is a flowing gas CO_2 laser. Its output is tuned from line to line with a Littrow-mounted, gold-coated-on-copper, diffraction grating blazed for a wavelength of 10.4 microns. This laser has a cavity length of 180 cm, and the output frequency is tunable $\pm$ 50 MHz from a line center by moving the output coupler with a PZT stack. A number of different reflectivity output couplers are used with this laser depending upon the CO_2 line required. The discharge tube is 160 cm long and has a diameter of 1 cm. The CO_2 partial pressure is 3 Torr, and the flow rate for the CO_2 alone is approximately 100 ml/min at STP. The nitrogen is at approximately the same pressure, and the helium is at approximately three times the CO_2 pressure. With new optics we have been able to achieve output powers of 45 Watts on the 10 P22 line and 20 Watts on the 9 P32 line.

In our present mode of operation, the CO_2 laser beam is chopped and then focused into the FIR laser with one 30-inch focal length lens. The effective f-number of the lens is such that the pump beam is able to travel the length of the FIR laser three or four times before it has expanded to the diameter of the waveguide. The output power of our FIR laser has not been accurately measured, but is approximately 100 microwatts average.

The SMMW transceiver uses a single transmit-receive mirror whose diameter is 35 cm. The FIR laser beam, after passing a beam splitter for monitoring output intensity, is expanded to 25 cm diameter by an off-axis collimating mirror system and is directed out of the laboratory through a 2 mil thick Teflon window to a 30 cm copper corner cube 100 meters downrange. Radiation reflected from this corner cube is collected by this same optical system. A fraction of the received thermal power is deflected by a second beam splitter and detected by a second Golay cell. Both detectors are coupled to lock-in amplifiers that derive a reference signal from the mechanical chopper positioned between the pump and FIR lasers.

Propagation data and meteorological data such as dry bulb temperature, wet bulb temperature, barometric pressure, wind speed and wind direction, and total solar radiation were sampled and recorded twice per second by computer-controlled instrumentation. Typical printouts list averages of all of these quantities for 200 consecutive readings or 100 second time spans.

3. EXPERIMENTAL RESULTS

It is apparently well known that the chief source of atmospheric absorption near one millimeter and throughout the SMMW region is rotational transitions of water molecules. All other constituent gases seem not to contribute significantly to the absorption. Both atmospheric water vapor density and temperature effect propagation.

Correlation between dry bulb temperature and water vapor density was usually quite high as plotted in Fig. 1 from data taken on a typical day; therefore, it was not possible to separate with confidence the independent effects of temperature and ρ on propagation on a single day basis. However, there were many days in which the relation between ρ and T was not single valued. The time evolution of ρ and T are shown for one such day in Fig. 2, where the cooling in the late afternoon and into the late evening of Day 229-78 produced the same ρ at two values of T.

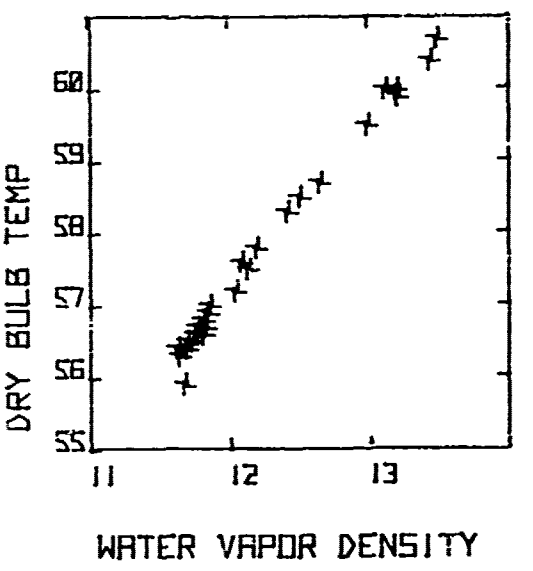

Fig. 1. Dry bulb temperature and simultaneous water vapor density as observed on the SMMW range at Redstone Arsenal, Alabama.
The units along the abscissa are g/m^3 and along the ordinate, degrees F. These data samples of the readings taken at 100 second intervals on one day, show the high correlation (CC = .995 and R.SQ = .991 to a straight line) usually observed during the daytime in the summer of 1978.

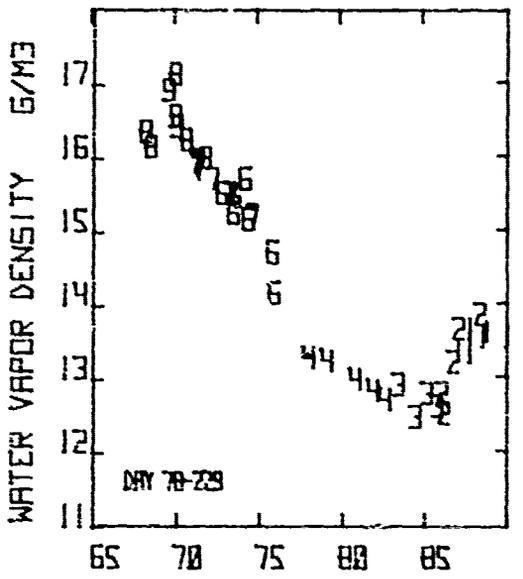

Fig. 2. Water vapor densities and the simultaneous dry bulb temperatures (°F) recorded on Day 229-78 on the SMMW range at Redstone Arsenal, Alabama from mid-afternoon through to late evening. The symbols represent fractional time of day as follows: 1 from 0.61 to 0.624 of 24 hours; 2 for .643 - .658; 3 for .689 - .705; 4 for .71 - .74; 6 for .79 - .825; 7 for .829 - .863; 8 for .864 - .913; and 9 for .914 - .926. The corresponding mean transmission values are shown in the next figure.

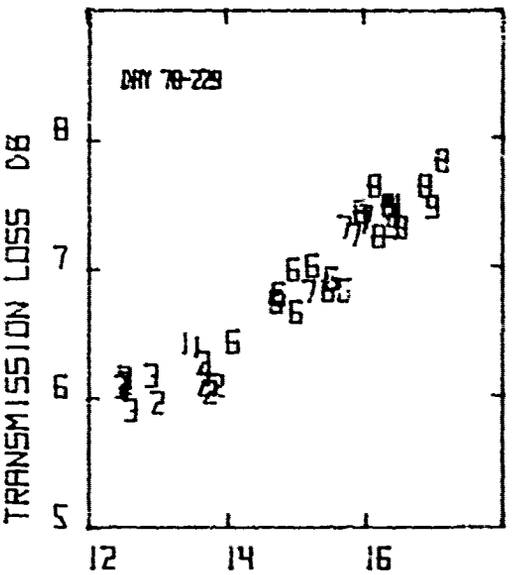

Fig. 3. Transmission loss (R) vs. the corresponding water vapor density (g/m^3) recorded on Day 229-78 thru sunset to late evening on the SMMW range at Redstone Arsenal, AL. The symbols represent approximate time of day as listed explicitly in the caption of Fig. 2. Each value of R was obtained from the 100 second average of the Golay cell outputs. The short term uncertainty in R is less than the size of the symbols displayed in the graph.

We find that the transmission values at 0.890 mm do not always reflect the equilibrium ρ and T values. For example, the time evolution of R, computed as the ratio of the average of 200 readings of the 15 Hz components of the Golay cell output on the same day as in Fig. 2, is shown in Fig. 3. The scatter in Fig. 3 is typical and appears to be wandering in R related to weather conditions other than mean ρ and T.

We therefore scanned the entire summer's data for values of 10 log R and ρ that were observed at selected temperatures of 77.0 ± .25°F, 79.0 ± .25°F, and 83.0 ± .25°F. The values observed at 77°F are plotted in Fig. 4. Similar behavior of log R vs. ρ was observed at the other two temperatures with the straight line having temperature dependent parameters but the lower group at 17 g/m^3 being temperature-independent. A bimodal description fits, with one type of behavior composed of log R,ρ data points that had r^2 fits > 0.9 to first-order linear equations with temperature-dependent coefficients for 77 < T ≤ 83°F and 10 < ρ < 25 g/m^3. The remaining data points consisted of temperature-independent values of log R clustered at ρ ~ 17 g/m^3.

Although one type of behavior appears to fit a first-order linear equation well, it should be pointed out that this way of describing the data does not take into consideration what physically happens at $\rho \sim 0$, but merely gives the fits of the measured points to a straight line in the region $\rho > 5$ g/m^3.

Table 1 summarizes the statistics of attenuation versus water vapor density at constant temperatures for those values of log R which fit linear equations of the form

$$\log R + C_1\rho + C_0 = 0 \quad . \qquad (1)$$

A dependence of R on T was obtained by interpolation of this equation and presented in Fig. 5. The temperature dependence of R expected from this interpolation is much larger at high or low values of the water vapor density than in the central range, as Fig. 5 shows. It is in the central range of ρ that interpolated values of R agree with those obtained from calculations plotted in Fig. 6 based on a Van Vleck/Weiskopf line shape. (Gamble et al. (1977)).

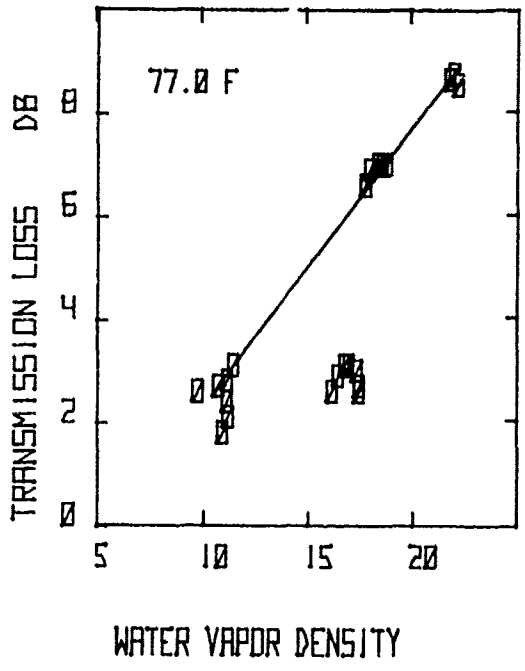

Fig. 4. Transmission loss vs. the corresponding water vapor density (g/m^3) observed at 77.0 ± .25°F and 0.890 mm wavelength during the summer of 1978 on the SMMW range at Redstone Arsenal, Alabama. The straight line through the data points has no sound theoretical basis.

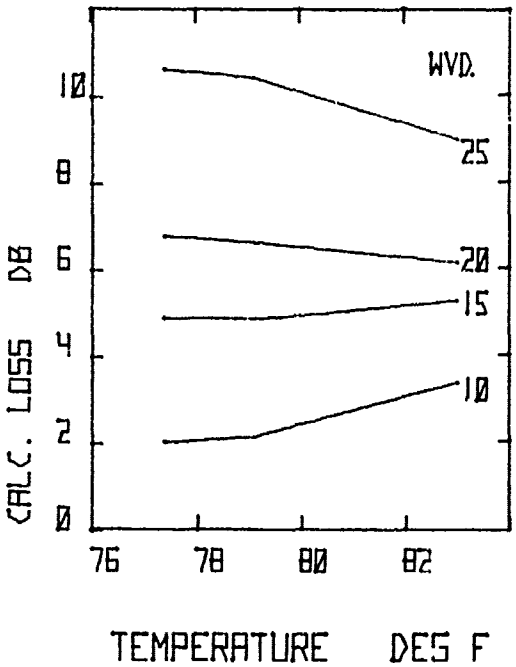

Fig. 5. SMMW loss calculated from Eq. (1) vs. temperature for values of water vapor density from 10 to 25 g/m^3. The loss values correspond to λ = 0.890 mm transmission data taken for the 200 meter round trip on the SMMW range at Redstone Arsenal, as displayed in Fig. 4.

TEMPERATURE (°F)	83	79	77
CORRELATION COEFFICIENT	0.96	0.99	0.99
r^2 FIT	0.92	0.99	0.98
SLOPE	0.37	0.55	0.58
INTERCEPT	-0.25	-3.36	-3.85

TABLE 1. Statistics of Attenuation vs. Water Vapor Density at Constant Temperatures.

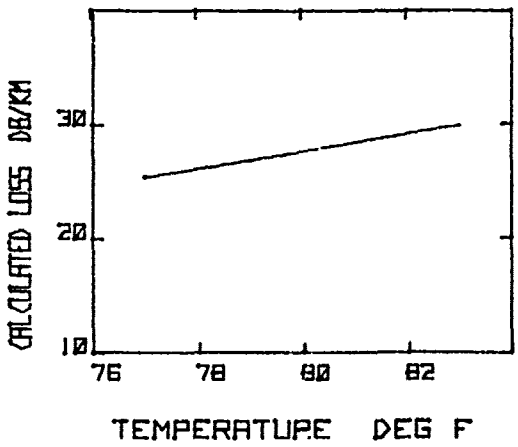

Fig. 6. Loss calculated for transmission thru a radiation fog in a standard atmosphere vs. temperature. The loss values were read from Tables 10-14 of Reference (Gamble et al. (1977)). The ordinate scale corresponds closely to the vertical scale in Fig. 5 and the horizontal scales are identical so that the slope can be compared between Figs. 5 and 6.

In addition to the clear air data described above, observations were made in fog. An example is shown in Fig. 7, where transmission loss is plotted against water vapor density on Day 271-78, a day on which fog with visibility no more than 300 feet persisted from dawn thru midmorning. The wander in R is much larger than the short-term fluctuations observed and appears to be due to weather conditions other than temperature and humidity. No significant attenuation due to this fog was detected.

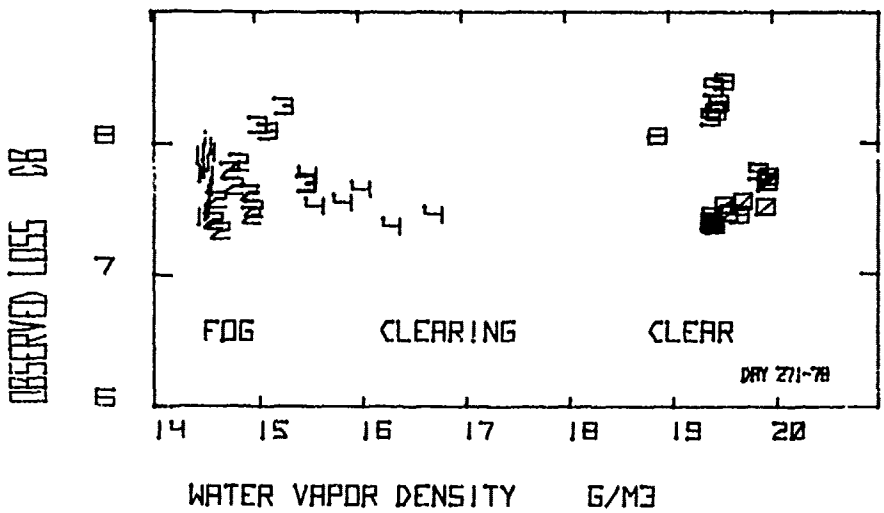

Fig. 7. Observed loss vs. water vapor density from near dawn thru midafternoon on Day 271-78 for transmission of 0.890 mm waves over the 200 meter path at Redstone Arsenal. The uncertainty due to short time fluctuations is represented by the height of the numerical symbols plotted. The symbols represent time of day as follows: #1 for .278 to .316 of 24 hours; #2 , .321 - .362; #3, .374 - .400; #4, .404 - .438; #8, .599 - .607; #9, .618 - .645; #0, .649 - .686. The visibility during 1, 2, 3, and most of 4 was 300 feet although the total solar radiation collected showed a strong increase. The visibility during periods 8 through 0 was greater than one-half mile.

4. CONCLUSIONS

In conclusion, there appears to be no significant attenuation of 0.89 mm radiation by a fog, even at visibilities of 300 feet. The bimodal values of R are due to parameters not quantified in this paper but are expected to involve atmospheric nonequilibrium. Using linear fits of R vs. ρ at constant temperatures between 77° and 83°F leads to a temperature dependence of R that agrees with expectations based on literature values except at the low and high ends of the water vapor density range (5 - 25 g/m^3).

More extensive measurements taken over a wide range of temperatures simultaneously with other parameters affecting atmospheric equilibrium are clearly needed for an understanding of attenuation in the 0.74 - 1.2 mm atmospheric window.

Acknowledgements: The authors wish to acknowledge Drs. Richard L. Hartman, John D. Stettler, William L. Gamble, and Dorathy A. Stewart of MICOM, and Dr. S. S. Mitra of the University of Rhode Island, for helpful discussions and suggestions.

REFERENCES

Bastin, J. A., 1966: Extreme infrared atmospheric absorption. Infrared Phys., 6, 209-221.

Burch, D. E., 1968: Absorption of infrared radiant energy by CO_2 and H_2O. III. Absorption by H_2O between 0.5 and 36 cm^{-1} (278 μ - 2 cm). J. Opt. Soc. Amer., 58, 1383-1394.

Gamble, W. L. and T. D. Hughes, 1977: Propagation of Millimeter and Submillimeter Waves. Technical Report TE-77-14, US Army MIRADCOM, 23 June 1977. Requests: Attention DRSMI-TI (R&D).

Hartman, R. L., W. L. Gamble, B. D. Guenther, and Paul W. Kruse, 1976: Submillimeter System for Imaging Through Inclement Weather. The Optical-Submillimeter Atmospheric Propagation Conference, Puerto Rico, 6-10 December 1976.

Kruse, Paul W., 1974: A System Enabling the Army to See Through Inclement Weather. US Army Scientific Advisory Panel Report.

Waters, J. W., 1976: Absorption and emission by atmospheric gases. In Methods of Experimental Physics, Vol 12, Astrophysics, Part B, Radio Telescopes, edited by M. L. Meeks, Academic Press, New York, 142-176.

A SHUTTLE PULSE TECHNIQUE FOR SIMULTANEOUS MEASUREMENT OF ATTENUATION AND BISTATIC SCATTER DUE TO PARTICULATES AT MILLIMETER WAVES

J. W. Mink

U. S. Army Research Office, Research Triangle Park, N. C. 27709

ABSTRACT

A shuttle-pulse technique for simultaneous measurement of the attenuation and bistatic scatter of millimeter waves is described. Measurements were obtained using a propagation path through rain of only a few meters; therefore, the rainfall statistics can be considered constant within the sample volume. A "total bistatic scatter coefficient" for rain is defined, and the technique of using a shuttle pulse for its measurement is discussed.

1. INTRODUCTION

A technique for simultaneous measurement of the attenuation and bistatic scatter of millimeter waves resulting from rainfall over short path lengths will be described in this paper. Measurements were made with a shuttle-pulse technique which utilizes a propagation path through rain of only a few meters. Absorption data [Medhurst, 1965; Godard, 1970; Mink, 1973] obtained from measurements over relatively long transmission paths, are in some disagreement with theoretical expectations. Results of this experiment for very short path lengths show a similar disagreement which indicates that the discrepancy between theory and experiment cannot be explained in terms of variations in the rainfall-rate and drop-size distribution along the path.

The total bistatic scatter coefficient per-unit-length defines an equivalent scatter area for all drops within the millimeter wave beam. From this quantity, the scattered signal level caused by rainfall may be determined.

The experimental setup used for the reported measurements is shown in Fig. 1. A short millimeter wave pulse (35 GHz) is injected into a wave beam resonator, where it shuttles back-and-forth between the two spherically shaped reflectors. After many round trips, if the resonator is properly designed, a Gaussian beam mode is established whose amplitude decays exponentially [Christian and Goubau, 1961]. When part of the path is intercepted by rain, the resulting increase in pulse attenuation per-round-trip is a measure of the rain attenuation. The bistatic scatter coefficient for rain can also be measured with this shuttle-pulse technique by placing a second receiving system at the desired scatter angle. The system is calibrated by placing a known scattering object in the beam.

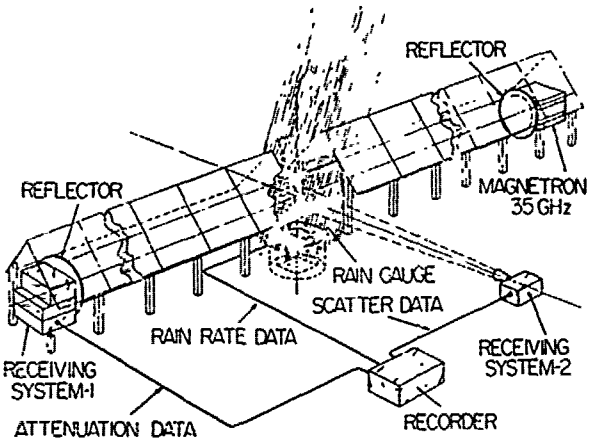

Figure 1. Overall view of measuring system.

2. DESIGN OF WAVE BEAM RESONATOR

The reflectors of the resonator have a diameter of 1 meter and a focal length of 28 meters; their mutual spacing is 25 meters. At the center of each reflector, there is a 1 x 1 cm coupling aperture which is used to inject and withdraw the vertically polarized millimeter wave signal. The 35 GHz magnetron, which was used as the signal source, supplies 70 ns pulses with a peak power of 10 kW. The measured loss of the cavity without rain is 0.1 dB per-round-trip; the theoretical diffraction and reflection loss of the reflectors is 0.048 dB per-round-trip [Goubau, 1968]. The additional loss of 0.052 dB is caused primarily by the coupling apertures.

3. MEASUREMENTS OF ATTENUATION CAUSED BY RAIN

The receiving system is a conventional crystal detector followed by a wideband video amplifier; the signal processing system, which compensates for power variations of the magnetron, follows the video amplifier. After the Gaussian mode has been established (see Figure 2), the pulse train is gated (using an FET switch) into an integrator circuit starting at time t_1. This pulse train is also gated into a second integrator circuit, which starts at a later time, t_2. The ratio between the outputs of these two circuits is then formed and

the resulting curves plotted by a strip chart recorder. This ratio is a function of the attenuation factor of the pulse train since the difference between the two switching times is constant. Calibration of the system is accomplished with an oscilloscope by measuring the decay of the pulse train for various losses.

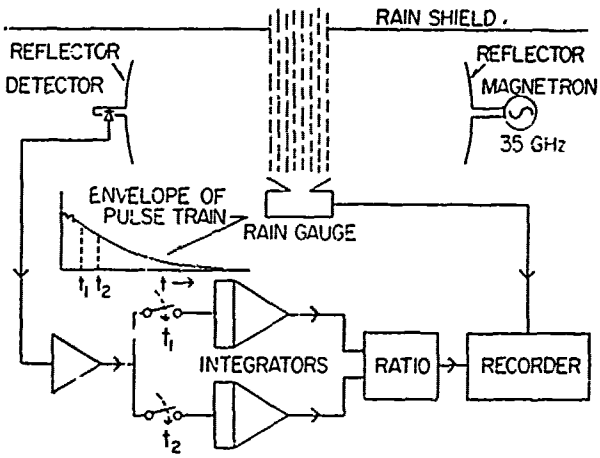

Figure 2. Rain-attenuation measuring system.

Since this measuring technique requires a path length through rain of only 5 meters or less, the remaining part of the beam path between the reflectors is covered by a roof. Only one rain gauge is required for measuring the precipitation rate within this short path. In order to obtain rain data at sufficiently short intervals, a special tipping bucket gauge was constructed [Mink and Forrest, 1974]. This gauge tips after each 5×10^{-3} mm of rainfall has collected; each bucket tip is recorded as a hack mark on the strip chart recording.

The data obtained during these experiments was evaluated in accordance with the empirical relation between attenuation and rainfall as proposed by Gunn and East [1954]:

$$L = AR^x, \qquad (1)$$

where L is the attenuation per kilometer and R is the rainfall rate in millimeters per hour. The parameters A and x were obtained by fitting the curve represented by equation (1) to the measured points with minimum square error. In order to obtain the most reliable data points, the measurements were evaluated for periods of relatively constant rain, i.e., constant attenuation. Data were taken for an average of 50 minutes during each shower. These data are represented by the dots in Fig. 3; the best fit curve to the data is shown in the form of a dashed line. For comparison, the theoretical attenuation results of Medhurst [1965] are plotted in the form of a solid line.

On the basis of the above data, which were obtained from measurements of rainfall samples uniform rate, one must conclude that there is no

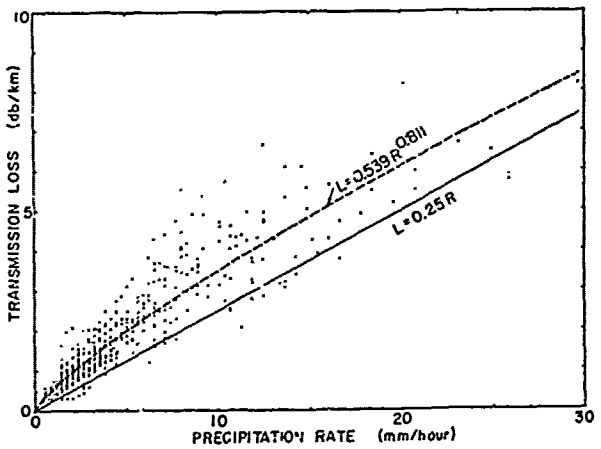

Figure 3. Comparison of experimental and theoretical rain attenuation data.

well-defined relationship between rainfall rate and millimeter wave absorption. This indicates that the rain statistics (i.e., drop size distribution, index of refraction, and terminal velocity) for a certain rainfall rate vary substantially.

4. MEASUREMENTS OF SIDE-SCATTER CAUSED BY RAIN

Since communication systems are being planned to operate in the millimeter wave length bands, a knowledge of the side-scatter (bistatic) characteristics of millimeter waves caused by rainfall becomes important. One vital aspect of bistatic scatter caused by rain, and a reason for this study, is that of security. If sufficient engergy is scattered by rain, the security of a millimeter wave relay system can be compromised by placing a receiver alongside of the path. Cross coupling between millimeter wave links is also a serious problem. Satellite systems are particularly subject to cross-coupling interference. In this section, the "total scatter coefficient" for rain s defined, and the shuttle-pulse technique used during this investigation for its measurement are discussed.

The received power scattered by a single drop as given by Cleverley [1973] is

$$P_r = \mathcal{P}_{(r)} \frac{\sigma_x}{4\pi d_r^2} A, \qquad (2)$$

where

$\mathcal{P}_{(r)} = |\bar{E} \times \bar{H}|$ at the drop;

σ_x = bistatic-scattering cross-section of the drop;

d_r = distance from the drop to the receiver; and

A = the area of the receiving aperture.

For calculation of the overall effect of raindrops on a Gaussian beam, a density function for rainfall is defined as follows [Kerr, 1951]

$$N_v = \int_{vol.} n dv, \tag{3}$$

where n is the number of drops per cubic meter, and N_v is the total number of drops within the scatter volume. Since the drops have a random distribution within the scattering volume, the scattered power from each drop [Kerr, 1951] must be added. The total received power then becomes:

$$P_T = \frac{A}{4\pi} \int_{vol.} \frac{n \mathcal{P}(r)\sigma_x}{d_r^2} dv . \tag{4}$$

Since evaluation of equation (4) is in general rather difficult, the following approximations will be used. The scatter volume is considered to be cylindrical in shape with its axis along the axis of the millimeter wave beam. This scatter volume is considered to be relatively small and far enough away from the receiver so that σ_x and d_r can be considered constant. Using these approximations, equation (4) when normalized per-unit-length becomes:

$$\frac{P_T}{L} = \frac{A}{4\pi d_r^2} SP , \tag{5}$$

where the total power incident upon the common scatter volume is

$$P = \int_{\substack{\text{incident} \\ \text{beam} \\ \text{area}}} \mathcal{P}(r) dr . \tag{6}$$

If one assumes that the path length through the common scatter volume is short enough so that attenuation may be neglected, the total side-scatter coefficient per-unit-length is

$$S = n\sigma_x . \tag{7}$$

Thus, if S is determined by measurements such as those described below, the side-scatter signal level may be determined. Of course, one must take into account the attenuation of the signal and the angular sensitivity of the receiver when determining the total received side-scatter signal for a long propagation path through the common scatter volume.

The experimental setup used for the rain side-scatter measurements is shown in Fig. 4. Since the resonator setup and the magnetron with its modulator are the same as previously described, only the equipment used for side-scatter measurements will be discussed here. Each time the shuttle pulse within the resonator passes through the portion of its path that is intercepted by rain, a portion of its energy is scattered. This scattered energy is detected by the side-scatter receiver. Thus for each round trip of the shuttle pulse, the output of the receiver is two pulses, one for each direction of travel of the shuttle pulse.

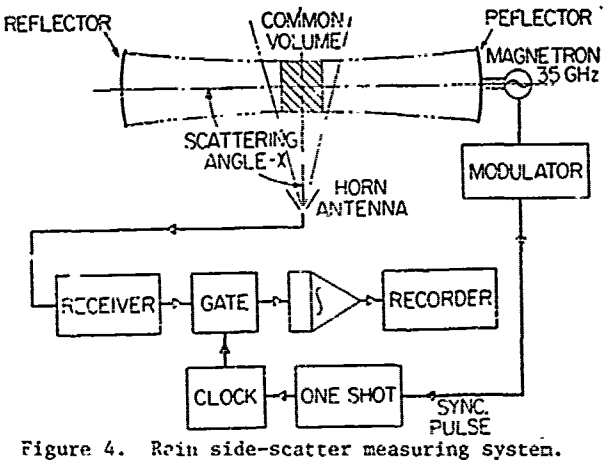

Figure 4. Rain side-scatter measuring system.

Side-scattered energy is collected over an aperture of 33 square centimeters, placed 12 meters from the common scattering volume, and positioned at the desired angle relative to the beam axis. A conventional millimeter wave superheterodyne receiving system was employed for this experiment. The receiver consisted of a balanced mixer, a 120 MHz post amplifier, and a video detector. Automatic frequency control was employed to keep the receiver properly tuned to the magnetron frequency.

Since the receiver gives an output for each passage of the shuttle pulse through the common scatter volume, the receiver output contains information about both the forward- and backward-scattering angles. To eliminate this ambiguity, the output of the receiver is gated with a synchronous gating circuit so that an output is generated only when the shuttle pulse passes through the common scattering volume in one direction. The pulse train thus generated is gated (using an FET switch) after the Gaussian mode has been established (see Fig. 2) into an integrator circuit. The output of this integrator circuit is plotted by a strip chart recorder. Calibration of the system is accomplished by measuring its response to a known scatter object (i.e., a thin wire) placed in the common scattering volume. The theory of calibration can be found in Appendix A.

Results of side-scatter measurements for a single scattering angle are indicated by the circles in Fig. 5. For comparison, theoretical points, based on Mie's scatter theory with Laws and Parson's drop distribution, are shown as crosses in Fig. 5 [Vogel, 1971]. As can be seen from this curve, the "total side-scatter coefficient" increases at a much faster rate than does the attenuation by rain. A similar result has been reported for radar backscatter as compared to attenuation caused by rain [Brinks, 1973]. Using the results of the measurements shown in Fig. 5 and equation (5), one finds for a receiving

aperture of 33 square centimeters placed 12 meters from the common scatter volume in the plane containing the beam axis and the magnetic field, that the power received is 60 db below the beam power for a moderate rainfall (~ 10 mm/hr).

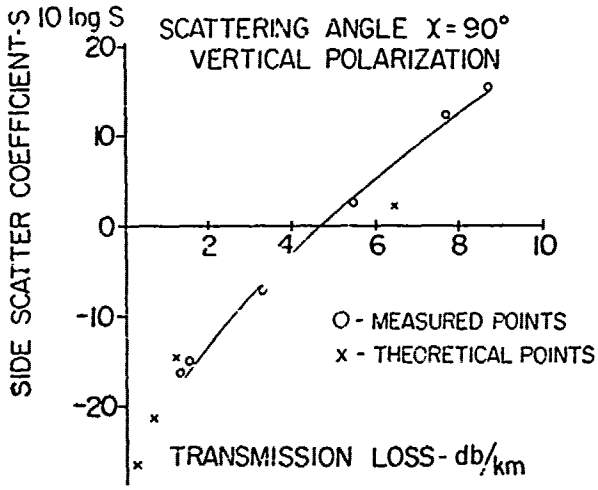

Figure 5. Measured data for rain side-scatter.

5. CONCLUSIONS AND RECOMMENDATIONS

A laboratory technique for simultaneously measuring the attenuation and bistatic scatter of millimeter waves has been demonstrated. Since this technique requires a path length through rain of only a few meters, the rain statistics for this path can be considered uniform. Since the quantity of data obtained from each rain event is substantial, it would be desirable to incorporate an automatic data processing unit into the system. This technique would reduce the data to usable form on a real-time basis. In addition, the dynamic range the rain-attenuation measuring systems may be increased by employing a superheterodyne receiver in place of the video detector. To achieve increased dynamic range, the times at which the pulse train is switched into the integrator circuits should also be under the control of the data processing system and the ratio of t_1 to t_2 should remain constant.

6. APPENDIX A
THEORY OF SIDE-SCATTER CALIBRATION

In order to calibrate the measuring system, it is necessary to determine the receiving system's response to an arbitrary lossless scattering object placed in the millimeter wave beam. In the signal processing system shown in Fig. 4, the pulse train detected by the side scatter receiver is gated (using an FET switch) into an integrator circuit starting at time t_1 after the Gaussian mode has been established, and ending after the pulse train has decayed. The output of the integrator circuit, which is recorded on a strip chart recorder, may be expressed as:

$$\frac{\mathcal{J}}{D} = \frac{AK(\tau)}{4\pi d_r^2} \frac{SP_o}{2\alpha} \exp(-2\alpha t_1), \qquad (A.1)$$

where

A = area of the receiving aperture;

$K(\tau)$ = a constant dependent upon the pulse width and spacing between pulses of the pulse train;

d_r = distance from the scattering object to the receiver, and

D = path length through rain.

When a known scattering object is placed in the millimeter wave beam, equation (A.1) becomes:

$$\mathcal{J}_o = \frac{AK(\tau)}{4\pi d_r^2} \frac{\sigma_o P_o}{2\alpha_o} \exp(-2\alpha_o t_1). \qquad (A.2)$$

The resulting signal is then used as the reference level for measurements of side-scatter due to rain. When using the same receiving aperture A and distance d_r for both calibration and measurement purposes, one obtains the ratio between equation (A.1) and (A.2). Thus

$$\frac{\mathcal{J}}{D\mathcal{J}_o} = \frac{S}{\sigma_o} \frac{\alpha_o}{\alpha} \exp(-2(\alpha-\alpha_o)t_1), \qquad (A.3)$$

where $\mathcal{J}/D\mathcal{J}_o$, α, and α_o are obtained from measurements of the received side-scatter energy and the attenuation of the millimeter wave beam. A more convenient form of equation (A.3) for evaluation purposes is:

$$10 \log S = 10 \log \frac{\mathcal{J}}{D\mathcal{J}_o} + 10 \log \sigma_o + 10 \log \frac{\alpha}{\alpha_o} + 8.68(\alpha-\alpha_o)t_1. \qquad (A.4)$$

When equation (A.4) is used to determine S, all parameters are known through measurements except σ_o. We will now show how σ_o can be obtained for a known scattering object such as a lossless wire. A thin wire was chosen for two reasons: (1) Its scatter characteristics can be obtained analytically and (2) In the case of a vertical wire, no supporting structures intercept the millimeter wave beam.

For a thin wire, long in terms of wave lengths, the current is filamentary and its distribution is proportional to the electric field intensity parallel to it [Johnson, 1965]. Since the wire is placed across a Gaussian beam [Goubau, 1963; 1968], the current distribution in this wire will be of the following form:

$$I(z) = I_o \exp(-\tfrac{1}{2}(\frac{z}{z_o})^2), \qquad (A.5)$$

where z is the mode parameter of the Gaussian beam. The radiated field of a current element along the z-axis is [Harrington, 1961]:

$$E_{(\theta)} = \frac{j\omega\mu I_o \exp(-jkr) \sin\theta}{4\pi r} \times \int_{-\ell/2}^{\ell/2} \exp(-\tfrac{1}{2}(\frac{z}{z_o})^2)\exp(jkz\cos\theta)\, dz. \quad (A.6)$$

The current maximum I_o may be determined by equating the total scattered power to the measured power lost from the millimeter wave beam, one obtains

$$\frac{P\, L_{db}^S}{4.34} = \sqrt{\frac{\mu}{\varepsilon}} \frac{I_o^2 k^2 z_o^2}{4} \times \int_0^{\pi} \sin^3\theta \exp(-k^2 z_o^2 \cos^2\theta) d\theta\,, \quad (A.7)$$

where P is the beam power and L_{db}^S is the loss in db caused by the scattering wire. For the parameters employed, $kz_o >> 1$; therefore equation (A.7) may be solved for I_o^2. Hence

$$I_o^2 = \frac{4P\, L_{db}^S}{3.34\, kz_o} \sqrt{\frac{\varepsilon}{\mu\pi}}\,. \quad (A.8)$$

One may now calculate the power received over an aperture. Thus

$$P_r = \frac{P L_{db}^S\, k\, z_o\, A}{8.68\sqrt{\pi}\, \pi d_r^2} \sin^2\theta \exp(-k^2 z_o^2 \cos^2\theta). \quad (A.9)$$

By comparing equation (A.9) with equation (A.2), we find that

$$\sigma_o = \frac{L_{db}^S\, k\, z_o}{2.17\sqrt{\pi}} \sin^2\theta \exp(-k^2 z_o^2 \cos^2\theta). \quad (A.10)$$

For the measurements performed in this experiment, the following parameters were used:

$\theta = \pi/2$

$k = 2\pi/\lambda = 7.33\ \text{cm}^{-1}$

$z_o = 17.9$ cm

$t_1 = 10^{-5}$ sec

$D = 1.21$ cm

Equation (A.10) then becomes

$$\sigma_o = 34.11\, L_{db}^S$$

and the measured increase of loss due to the wire passing through the millimeter wave beam is 0.06 db. Using the relation

$$\sigma_o = \frac{L_{db}\, c}{8.68\, d}\,,$$

the calibration equation then becomes in terms of measured parameters:

$$10 \log S = 3.12 + 10 \log \frac{1}{D f_o} + 10 \log \frac{L_{db/km}}{L_{O\ db/km}} + 3(L_{db/km} - L_{O\ db/km}). \quad (A.11)$$

The total side-scatter coefficient can now be determined from measurements using the scatter properties of a known scattering object as a reference.

REFERENCES

Brinks, W. J., 1973: A Discussion of Excessive Rainfall Attenuations at Millimeter Wavelengths. Report HDL-TM-73-14, Harry Diamond Laboratories, Washington. D. C.

Christian, J. R. and G. Goubau, 1961: Experimental studies on a beam waveguide for millimeter waves. IRE Trans. Antennas Propagat., AP-9(3), 256-263.

Cleverley, M. E., 1973: Observation of the small-scale structure of intense rain by the scattering of microwaves. Electron. Lett., 9(22), 535-536.

Godard, S. L., 1970: Propagation of centimeter and millimeter wavelengths through precipitation. IEEE Trans. Antennas Propagat., AP-18, 530-534.

Goubau, G., 1963: Optical relations for coherent wave beams. In Electromagnetic Theory and Antennas, edited by E.C. Jordan, Vol. 6, Part 2, Pergamon Press, Oxford, 907-918.

Goubau, G., 1968: Beam waveguides. In Advances in Microwaves, edited by L. Young, Vol. 3, Academic Press, New York, 67-126.

Gunn, K. L. S. and T. W. R. East, 1954: The microwave properties of precipitation particles. Quart. J. Roy. Meteor. Soc., 80, 522-545.

Harrington, R. F., 1961: Time-Harmonic Electromagnetic Fields. McGraw-Hill, New York, 81-82.

Johnson, C. C., 1965: Field and Wave Electrodynamics. McGraw-Hill, New York, 84-93.

Kerr, D. E., 1951: Propagation of Short Radio Waves. McGraw-Hill, New York, 588-620.

Medhurst, R. G., 1965: Rainfall attenuation of centimeter waves: Comparison of theory and measurement. IEEE Antennas Propagat., AP-13, 550-564.

Mink, J. W., 1973: Rain-attenuation measurements of millimetre waves over short paths. Electron. Lett., 9, 189-199.

Mink, J. W. and E. P. Forrest, 1974: A sensitive tipping-bucket rain gauge. Rev. Scientific Instruments, 45, 1268-1270.

Vogel, W., 1971: Scattering Intensity Plots and Transmission Coefficients for Millimeter-Wave Propagation through Rain. Technical Report AFAL-TR-71-345, Wright-Patterson Air Force Base, Ohio 45433.

MEASUREMENTS OF ATTENUATION DUE TO SIMULATED BATTLEFIELD DUST AT 94 AND 140 GHz*

J. J. Gallagher, R. W. McMillan, and R. C. Rogers

Georgia Institute of Technology
Engineering Experiment Station
Atlanta, Georgia 30332

Donald E. Snider

U. S. Army Atmospheric Sciences Laboratory
White Sands Missile Range, New Mexico

ABSTRACT

During the fall of 1978, a series of measurements, called DIRT I, of electromagnetic wave propagation through simulated battlefield dust were conducted at White Sands Missile Range. This paper gives an overview of the entire DIRT I tests as well as detailed results of those tests for millimeter wave (94 and 140 GHz) frequencies.

Attenuation measurements were made over an instrumented 2 km range. In the center of the range, explosive charges of different sizes were detonated, and the resulting signal level was compared to that existing before the explosive event. Measurements were also made of attenuation caused by artillery shells fired into the center of the range, and of that caused by burning diesel oil and rubber.

Both magnitude and duration of attenuation were found to vary with the amount of the explosive, sometimes reaching 30 dB and 20 seconds respectively. Copies of chart recorder tracings showing attenuation of both explosion products and oil smoke are presented. Oil smoke propagation measurements show scintillations of 3 to 5 dB.

1. INTRODUCTION

Battlefield obscurants such as dust and smoke from vehicle activity, burning wreckage, or explosion debris from artillery impacts can cause serious degradation in the performance of electro-optical (EO) weapon and surveillance systems. Individuals actively involved in the development of EO sensor systems realize that evaluating the performance of these systems under degraded atmospheric propagation conditions expected on the battlefield requires solutions to scientific and engineering problems of staggering difficulty. The extreme complexities of the natural atmosphere, the differing soil properties throughout the world, seasonal and meteorological variations, different types and different applications of military munitions, and the engineering details of EO systems themselves all combine to produce an endless list of problems to be solved. Some combination of empirical and theoretical investigations must be made to sort out these problems and to find solutions to the extent needed to permit an operationally adequate estimate of weapon system performance under realistic battlefield optical conditions. With this in mind the Dusty Infrared Test - 1 (DIRT I) was conceived as the beginning of a direct contribution toward the solution. The primary objectives of DIRT I were to provide a developmental test of some of the technology which must be brought to bear on the problems, such as lidars, soil analyses, FLIR images, aerosol samplers, transmissometers, and others together in a coordinated program to produce information of direct use to the EO sensor and obscuration modeling communities; to characterize the dust cloud produced by various amounts of high energy explosives; and to obtain data for the development of scaling laws. A detailed report on DIRT I has been prepared by the Atmospheric Sciences Laboratory [Lindberg, 1979].

In order to perform this first set of experiments, ASL assembled investigators from several organizations at the White Sands Missile Range to participate in the observations. Thus, for measuring aerosol particulate sizes, a large instrumented payload was suspended from a CH54 "Skycrane" helicopter and flown through the explosion cloud for direct sensing of the dust properties. Several measurements of the effects of the explosion dust on electro-magnetic transmissions were made. The Naval Research Laboratory performed bandpass filter and Fourier Transform Spectrometer transmission measurements; Stanford Research Institute provided lidar measurement support; and Georgia Tech performed millimeter wave transmission measurements. Excellent support was also provided by the U. S. Army Waterways Experiment Station (soil characterization and explosion crater data), the U. S. Army 3rd Armored Cavalry Regiment (155 - mm howitzer firings), the 14th Aviation Batallion, 273rd Transportation Company (CH54 helicopter support), the White Sands Missile Range Explosive Ordinance Demolition team (planning, installing and detonating the explosive arrays), and the U. S. Army Test and Evaluation Command elements at WSMR (gas sampling data, photography and general range support). The propagation measurements were performed by transmitting

*Lindberg (1979)

through TNT explosions, explosions from static 155 - mm rounds and live artillery firings. This presentation discusses the millimeter wave propagation tests.

2. DESCRIPTION OF TEST SITE

The DIRT I tests were conducted by ASL between 2 and 14 October 1978 in the southeast corner of White Sands Missile Range (WSMR), New Mexico. Figure 1 shows the orientation of the DIRT I test area and the locations of the test area and the major instrumentation and support sites. Figure 2 illustrates the detailed layout of the DIRT I site and location of experiments and equipment. The distance between the south site and north site was 2 kilometers. The test area, 100 by 300 meters was situated midway along the path and was the location of all detonations and artillery impacts. The path was cleared of vegetation to a width of approximately 20 meters.

3. DIRT I EVENTS

The simulated battlefield dust was generated by detonating TNT charges, static detonation of 155 mm projectiles and live firings of 155 mm howitzers. The detonation events were performed as indicated in Figures 3 through 8. Each event was designated as A - 1, A - 2, etc. through E - 10. Events A - 1 through D - 4 were detonations of charges of TNT laid as shown in Figures 3 through 6. The E - events (Figures 7 and 8) were static detonations of 155 - mm howitzer projectiles. The positions of the projectiles for the E - events are illustrated in Figure 9.

The F - events were live howitzer firing events with four 155 - millimeter howitzers firing at one point in the impact area. Event F - 1 consisted of firing one round from each of the four 155 - mm tubes simultaneously into the impact area. Events F - 2 and F - 3 were similar, except each tube delivered 3 rounds in a time interval of about 45 seconds for a total of 12 rounds. Events F - 4 through F - 7 were similar except that 8 rounds were fired. Three projectiles were fired for F - 8.

The last event in DIRT I was a fuel fire. For this test, four 55 - gallon steel drums were cut in half and laid in a trench perpendicular to the optical axis in the center of the test area. Thirty-eight liters of diesel fuel, two liters of motor oil, and one rubber tire were placed into each container. The mixture was ignited and produced great volumes of black smoke for the duration of the test, approximately 37 minutes. The payload was flown through the cloud 11 times at various heights above the ground while simultaneous transmission measurements were being made by ground-based sensors.

4. MILLIMETER WAVELENGTH TRANSMISSION MEASUREMENTS

A potentially severe problem in the use of millimeter waves in battlefield situations is the possible degradation of these systems caused by atmospheric propagation effects. Some fairly extensive studies and measurement programs have led to some understanding of the performance of millimeter systems in rain and fog, although much work remains to be done in this area, but little work has been done to characterize millimeter propagation through battlefield dust. This discussion gives the results of a series of experiments conducted during DIRT I by personnel of the Georgia Tech Engineering Experiment Station in October 1978 which attempt to fill this gap in knowledge about millimeter wave propagation.

During most of the experiments, simultaneous measurements were made at 94 - and 140 - gigahertz; however, a power supply failure caused the 140 - gigahertz receiver to become inoperative. Therefore, only 94 - gigahertz measurements were obtained during some of the events.

The simulated battlefield dust was generated by detonating TNT charges, static detonation of 155 - millimeter howitzer projectiles, and live firings of 155 - millimeter howitzers. In addition, an event was conducted on the final day which measured signal degradation caused by simulated burning vehicles. The aerosols generated during most of the above events were characterized by a helicopter - borne sensor package.

Block diagrams of the 94 - and 140 - gigahertz transmitter/receiver systems are shown in Figures 10 and 11 respectively. Both of these systems use CW klystrons that are chopped at a 1 - kilohertz rate for phase sensitive detection. Both also use superheterodyne receivers for good sensitivity.

The 94 - gigahertz transmitter uses an OKI 90V11 klystron which has a power output of about 80 milliwatts. The antenna is a horn/lens combination which has a beam width of 2 degrees. Part of the power is picked off with a directional coupler to monitor transmitter power and frequency through a wavemeter, detector, and oscilloscope. The klystron is 100 percent modulated with a 1 - kilohertz square wave applied to its reflector from the internal power supply modulator, whose output is also used to modulate the 140 - gigahertz tube, so that only one reference signal for phase sensitive detection need be transmitted. This signal is transmitted to the receiver over twisted pair lines by means of line drivers and receivers.

The 94 - gigahertz receiver uses a gallium arsenide Schottky barrier diode mixer pumped by a Varian VRB - 2113AB klystron local oscillator (LO). Signal and LO power are coupled into the mixer by a cylindrical coupling cavity. For most of the events, two Avantek 1 to 2 megahertz IF amplifiers were used, but for the first few events one Avantek 1 to 2 megahertz amplifier and one Watkins - Johnson 5 to 1000 - megahertz amplifier were used. Each of these amplifiers has a gain of 30 decibels, so that the IF gain was 60 decibels total. An identical amplifier arrangement was used on the 140 - gigahertz system; but after a power supply failure caused this system to be inoperative, both Avantek amplifiers were used with the 94 gigahertz receiver.

The output of the IF amplifier is fed into a zero-bias tunnel diode detector, which is the signal input for a lock-in amplifier. The output of this amplifier drives a strip chart recorder which shows the variations in signal as

a result of the explosions.

The 140 - gigahertz transmitter tube is an OKI KA1390 klystron with an out-put of about 40 milliwatts. A tunable Fabry - Perot interferometer was used to measure the frequency of this tube and a Sharpless wafer mixer-detector with a corrugated horn was used to monitor its power. This tube was modulated with the same signal used to modulate the 94 - gigahertz tube.

The 140 - gigahertz receiver consists of a gallium arsenide Schottky barrier diode harmonic mixer in a crossed waveguide mount. This mixer is pumped by an OKI 70V11A klystron which oscillates at 70 gigahertz. The IF amplifier arrangement is that discussed in the paragraph which treats the 94 - gigahertz receiver. The second detector, lock-in amplifier, and chart recorder are also used in the same way as discussed earlier for that receiver.

The measurements were calibrated both before and after the events. For the 94 - gigahertz system, a precision attenuator between the transmitter tube and the antenna was used. Generally, measurements were calibrated at 0 -, 3 -, 6 -, 9 -, and 12 - decibel levels. In comparing the results of event measurements to these calibrations, a curve was plotted which showed attenuation as a function of chart recorder displacement. The true attenuations due to the event could then be scaled from the curve. This method corrects for any nonlinearities or departures from square law in the superheterodyne receiver. A precision attenuator was not available for the 140 - gigahertz system, so it was calibrated by obtaining output readings for zero and infinite attenuation and scaling measured results linearly. This method assumes, of course, that the receiver is a true square law detector.

5. DISCUSSION OF EVENTS

The results of only a few events will be discussed here. The C - events were the large simulated barrages of 140 charges of 15 pounds each. Figure 12 shows the results obtained during event C - 1. Both 94 - and 140 - gigahertz channels exhibit attenuations of greater than 28 decibels. Recovery time of both systems was determined to be greater than 20 seconds. Note however that the 94 - gigahertz channel recovers to within 3 decibels of its original level in about 8 seconds, while the 140 - gigahertz channel requires about twice as long due to a large secondary minimum at about 12 seconds. Note also that the scintillation amplitude for both channels is smaller for this event. For this event, the system was operated with zero time constant. The dynamic range of the system amplifiers did not allow an exact determination of attenuation other than that it was greater than 28 decibels. The large minimum for 140 gigahertz in the region of 7 to 11 seconds was apparently a zero shift as the signal did not return to the original zero and no corresponding effects are observed on the 94 - gigahertz trace. Equipment problems prevented accurate measurements for the similar event, C - 2. It was estimated that, by changing scales on the lock - in and recorder, the attenuation at 94 gigahertz exceeded 35 decibels. No accurate rate time estimates could be made because of the equipment difficulties.

All events showed attenuation characteristic of the size of the explosion ranging from approximately 6dB maximum attenuation to 35 dB maximum attenuation. In all observations, recovery time for events B through E did not exceed 25 seconds.

The F - events are the remote howitzer firings and attenuation is strongly dependent on whether or not the rounds land on the road which is the millimeter wave transmission path. For example, the events corresponding to events F - 1 and F - 4 show no attenuation. However, the howitzer round did not land in the center of the test area. Figure 13 shows measurements made during event F - 2 of 12 October 1978. This firing consisted of three groups of four 155 - millimeter howitzer rounds. These three groups occur in the time range of 12 to 45 seconds. The peak at approximately 51 seconds is a single round that should have been included in the group at 43 seconds.

The measurements on 12 October through 14 October 1978 were overdriven and as a result gave nonlinear calibration. This can be seen from Figure 14 where it is evident that the greater power employed also resulted in a reduction of scintillation when explosions were not occurring. From Figure 14, the 0 - decibel level is the original level; but drift occured during the firing, resulting in a different baseline. This incident occured in several events during the last 3 days.

Note that on some rounds positive peaks were obtained which possibly corresponded to reflection of transmitter signal into the receiver antenna. Some of the attenuation peaks were on the order of 20 decibels. The recovery time cannot be ascertained accurately because of the spread of impact times, but recovery appears to be complete within 10 to 12 seconds after the last impact. Figure 15 shows the measurements of event F - 3 of 12 October 1978. The event was again three firings of four howitzer rounds. The first group which should have produced attenuation at 15 to 20 seconds did not record an effect, possibly as a result of the firing missing the test area. Figure 16 shows two groups at 35 to 40 seconds and 48 to 57 seconds; the amplitude of these groups is significantly reduced (3 to 4 decibels) relative to F - 2.

A second series of F events was run on 13 October 1978. Again during event F - 8 no attenuation was measured, probably as a result of the rounds missing the test area. Results obtained during event F - 5 are given in Figure 16. This recorder trace corresponds to two firings of four rounds each with peak attenuations of 10 decibels and approximately 6 decibels. For Figure 16, the chart recorder speed was set at 15 centimeters per minute, too slow to show very much detail. Recovery is within about 4 seconds for the first maximum. The second salvo of this event apparently did not land precisely in the line of sight because the maximum attenuation is 6 decibels and the recovery time is less than 1 second.

Event F - 6 of 13 October is shown in Figure 17. The maximum attenuation observed for this

event was approximately 6 decibels with recovery in 3 to 4 seconds. The chart recorder speed was increased to 1.25 centimeters per second to show more detail for this test. An interesting phenomenon occurs in both salvos of this event in which the attenuation actually goes negative. This may possibly be caused by multipath scattering from shell fragments.

The results obtained for event F - 7 are given in Figure 18. Maximum attenuation for both salvos was determined to be 9 and 8 decibels with recovery times of about 4 to 5 seconds. For this event, the absorption did not invert and was stronger than in event F - 6. The stronger absorptions of F - 7 are consistent with the impacts being more directly in the optical path than F - 6 with a corresponding reduction of scattering into the receiver.

On Saturday, 14 October 1978, a test was conducted in which diesel fuel, motor oil, and rubber, in the approximate ratios expected in a burning tank, were utilized to simulate a "burning hulk." The paper chart depicting 94 gigahertz transmission as a function of time (about 45 minutes) is published in **Lindberg (1979)**.

As might have been expected, the bulk average attenuation during this test was relatively small--on the order of 1 or 2 decibels. However, scintillations of up to 5 decibels peak were observed. The frequency spectrum of these scintillations appears higher than that observed for purely atmospheric scintillations, and the amplitude is also greater.

Unfortunately, the signal was not recorded on magnetic tape. Thus a power spectrum analysis cannot be readily performed. Such an analysis would be important in quantitatively determining the effects of these scintillations on millimeter wave systems.

6. CONCLUSIONS AND RECOMMENDATIONS

DIRT I has provided an opportunity for observing the effects of tactical size explosions on millimeter wave and electro-optical propagation. In many events, attenuations of 10 to 30 decibels were observed. Although damage suffered by equipment in transit caused some limitations and eventual failure of the 140 - gigahertz apparatus, generally significant data were obtained.

Several conclusions can be drawn from the measurements. As indicated, attenuation in most cases was large. The relatively short recovery time of the attenuated signal indicates that the attenuation was caused by the large pieces of soil blown in the air in the early stage of each event. The residual dust remaining in the air after the initial large particles have settled makes no significant contribution to the attenuation. This result is similar to the results obtained at millimeter wavelengths when propagating through dust raised by vehicles. The signal fluctuations in the majority of the events were large, and their origin has not been fully established. As indicated by the monitoring of the source amplitude stability and the receiver noise level when signal is blocked, the fluctuations probably do not receive a major contribution from the instrumentation. Some contribution could originate from atmospheric fluctuations. Quite probably, the majority of these fluctuations result from multipath effects.

The large beam widths (2 degrees) resulted in effects from vehicles, personnel, moving bushes, etc., being observable in the receiver system. A more narrow beam antenna system would minimize these effects. The fluctuations which were observed were of sufficient magnitude to obscure small attenuation effects. Frequency stability of the transmitter and local oscillator was sufficient to keep the signal within the amplifier bandwidth and thereby cause no fluctuations.

The scintillation during the burning of the diesel oil, motor oil, and rubber was large and exceeded the expected effect.

The signals obtained during the howitzer firings varied significantly for each event. The strength of the absorption depended on the position of the impact relative to the optical path of the system. The spread in absorption for each salvo resulted from the difference in time for the impact of each round. The positive signal response which was observed for some firings appeared to result when attenuation was not the greatest and probably when the impact area was not directly in the optical path. As a result, scattering of signal into the receiver by the fragments blown in the air may possibly have been the cause of signal increase.

DIRT I has provided a great deal of transmission data that were collected along nearly identical propagation paths. Detailed data reduction from all systems and careful consideration of possible extenuating circumstances, e. g., detector linearity, are not yet complete. However, quick-look data are sufficient to draw some tentative conclusions. An example is shown in Figure 18. In this figure the results from the 0.55- and the 10.35 - micrometer Naval Research Laboratory filter transmissometers, measurements of transmission obtained from the Atmospheric Sciences and Stanford Research Laboratories' lidars, and the Georgia Institute of Technology 94 - gigahertz transmissometer are intercompared for event F - 2. It is clear that for the visible and infrared wavelengths an artillery barrage can produce attenuation of 15 or 20 decibels for periods of several minutes and that, at least for a desert soil in New Mexico, the signal recovery is not significantly better for any particular visible or infrared wavelength. The attenuation at 94 - gigahertz was larger than anticipated but existed for a shorter period. Nevertheless even at this early stage in data examination, it is possible to conclude two things from data such as those in Figure 18. One is that a 155 - millimeter barrage can seriously obscure infrared propagation for periods of several minutes, and the second is that even a 94 - gigahertz signal can suffer attenuation greater than 10 decibels for periods of a few seconds.

7. ACKNOWLEDGEMENT

The authors wish to acknowledge the support of J. D. Lindberg, Test Director, T. Loveland, Deputy Test Director and B. W. Kennedy, Test Conductor and the assistance of R. Platt and D. Guillory, Georgia Tech students who helped in the measurement programs. This work was supported by the U. S. Army Atmospheric Science Laboratory through Army Research Office Contract

No. DAAG 29 - 77 - C - 0026.

REFERENCE

Lindberg, J. D., 1979: Measured Effects of Battlefield Dust and Smoke on Visible, Infrared, and Millimeter Wavelength Propagation; A Preliminary Report on Dusty Infrared Tests - I (DIRT I). ASL-TR-0021 (Atmospheric Sciences Laboratory, White Sands Missile Range, NM 88002), January 1979.

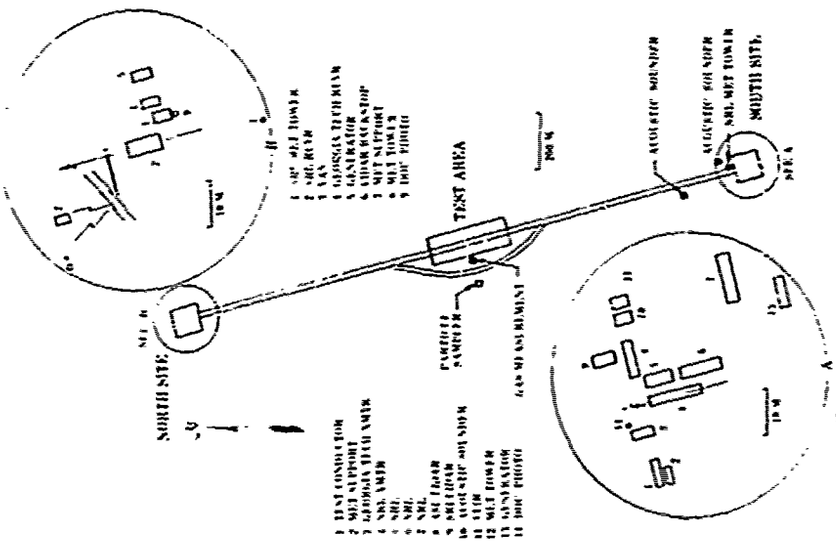

Figure 2. Detailed layout of DIRT I site showing locations of vans and experiments at each end. Path length from north to south is 2 km. Test area, where explosives were detonated and artillery shells impacted, is 100 by 300 m.

Figures 3 - 5 are below

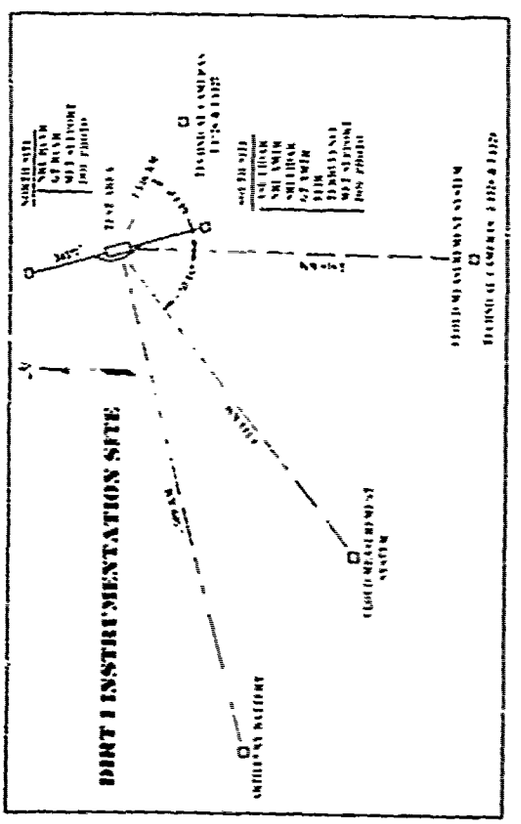

Figure 4. Plane view of DIRT I site showing primarily the instrumentation and support elements. General locations are to scale. White Sands Missile Range, New Mexico.

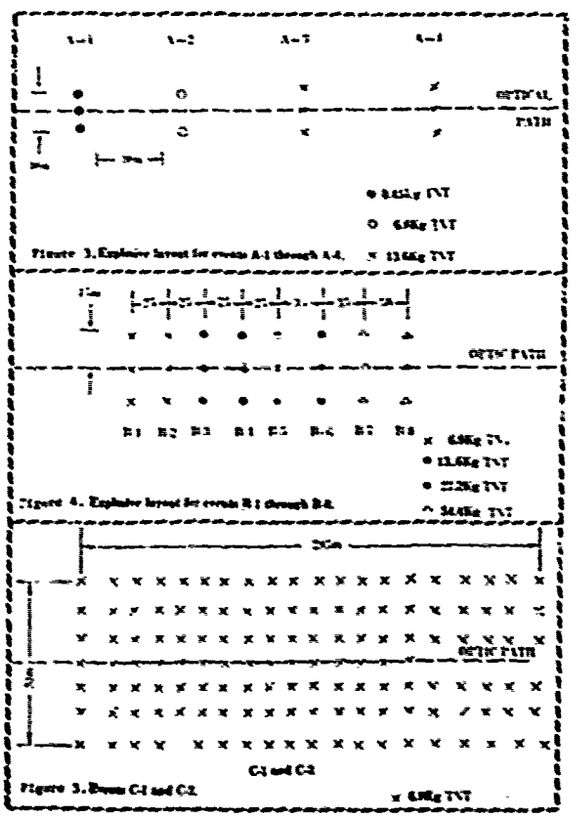

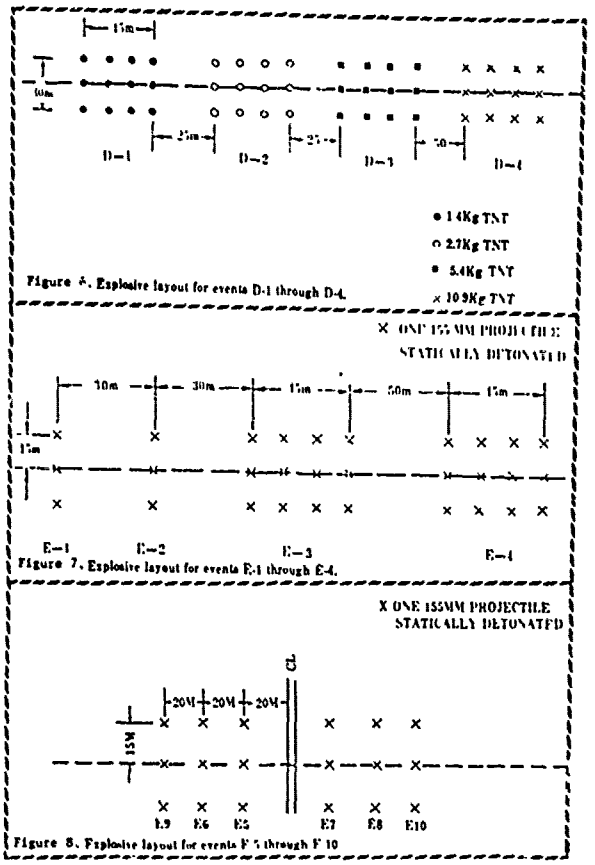

Figures 6 - 8 are above.

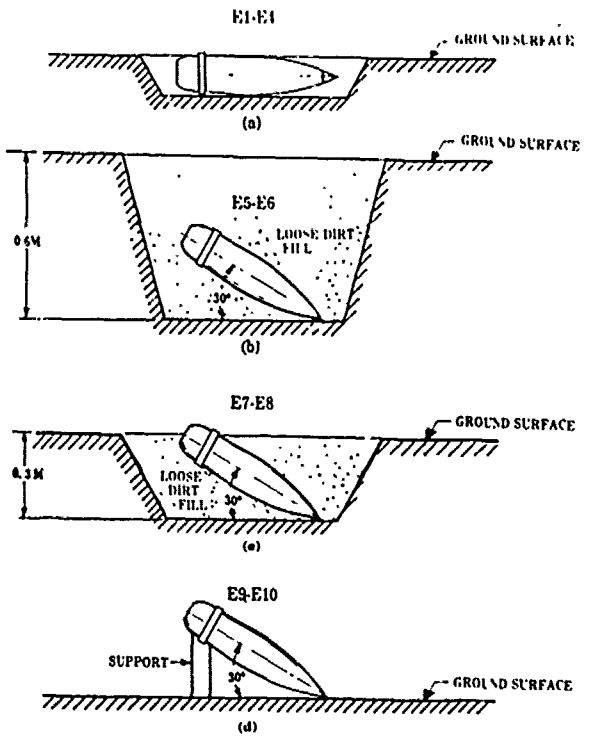

Figure 9. Altitude of 155 - mm projectiles in ground for events E - 1 through E - 10: (a) events E - 1 through E - 4, (b) E - 5 and E - 6, (c) E - 7 and E - 8, (d) E - 9 and E - 10.

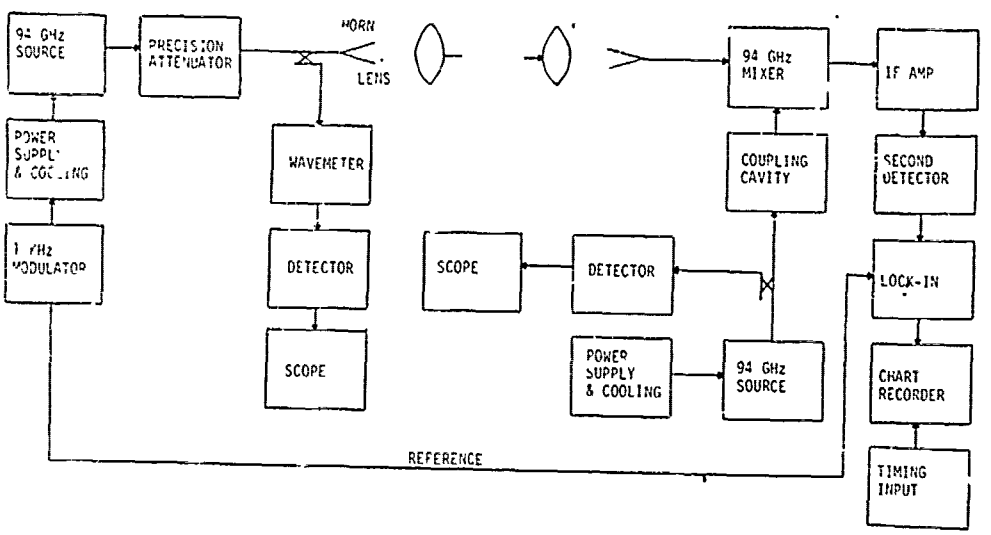

Figure 10. 94 gigahertz system block diagram.

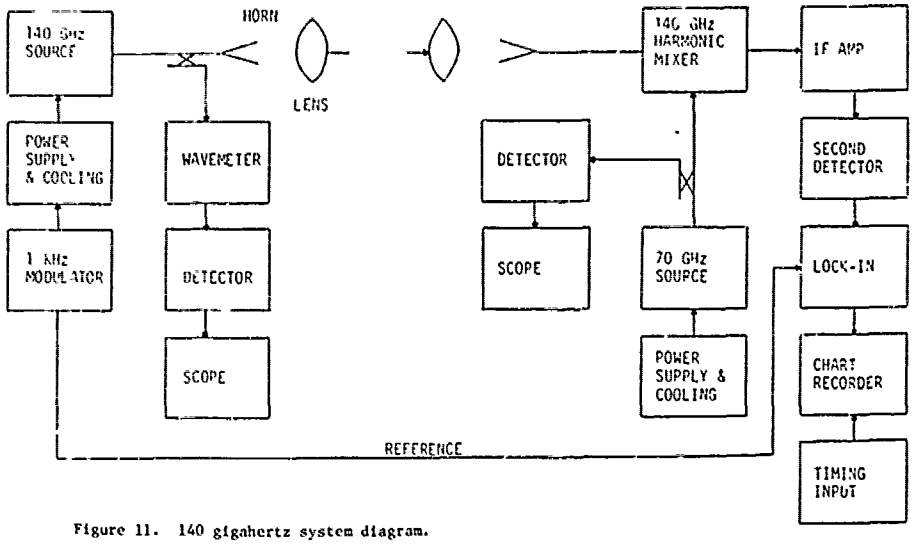

Figure 11. 140 gigahertz system diagram.

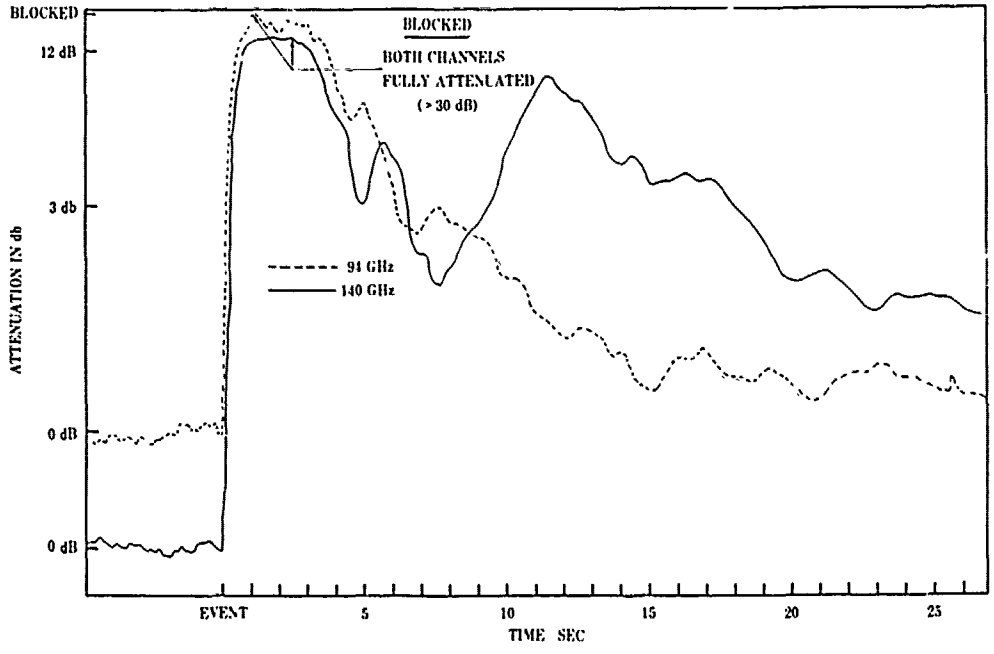

Figure 12. Measurements made during event C - 1, chart speed 1.25 cm/sec., time constant zero.

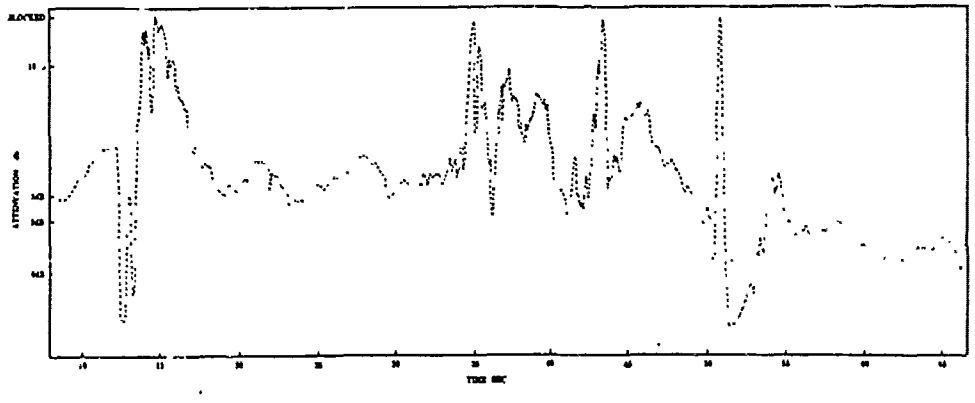

Figure 13. Event F - 2 of 12 October 1978. Three firings of four 155 - mm howitzers at 12 to 45 seconds. The spike at 51 seconds is the result of a late round from the group at 43.2 seconds. Chart speed was 1.25 cm/sec and time constant 40 msec.

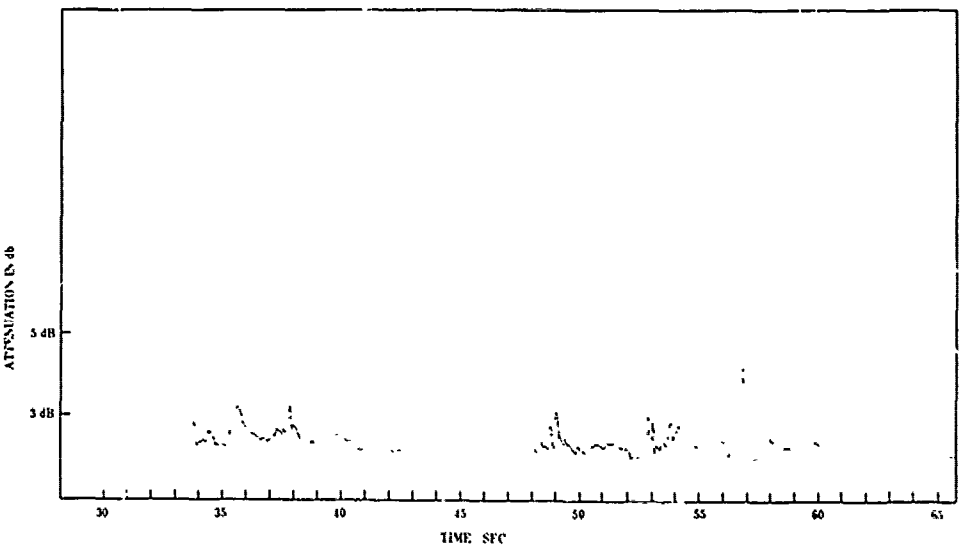

Figure 14: Measurement of attenuation made during event F - 3 of 12 October 1978. Chart speed 1.25 cm/sec, time constant 40 msec.

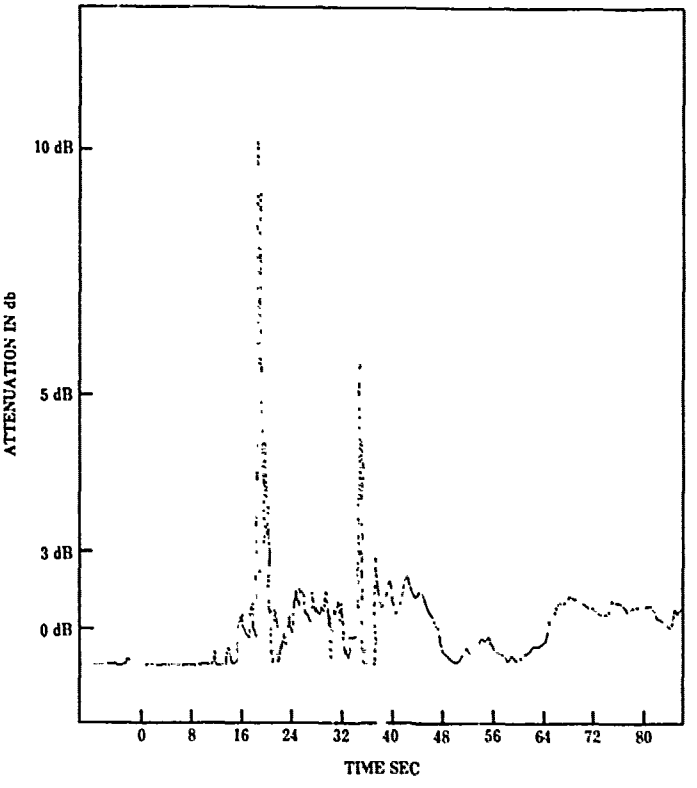

Figure 15. Attenuation measurement made at 94 GHz during event F - 5 of 13 October 1978. Chart speed 15 cm/min, time constant 40 msec.

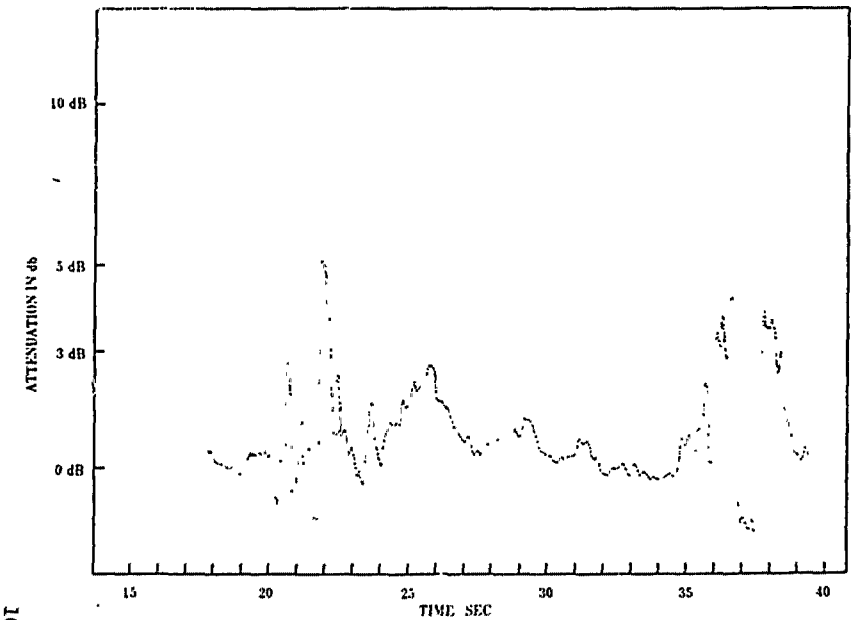

Figure 16. Attenuation measurements made at 94 GHz during event F - 7 of 13 October, 1978. Chart speed = 1.25 cm/sec, time constant = 40 msec.

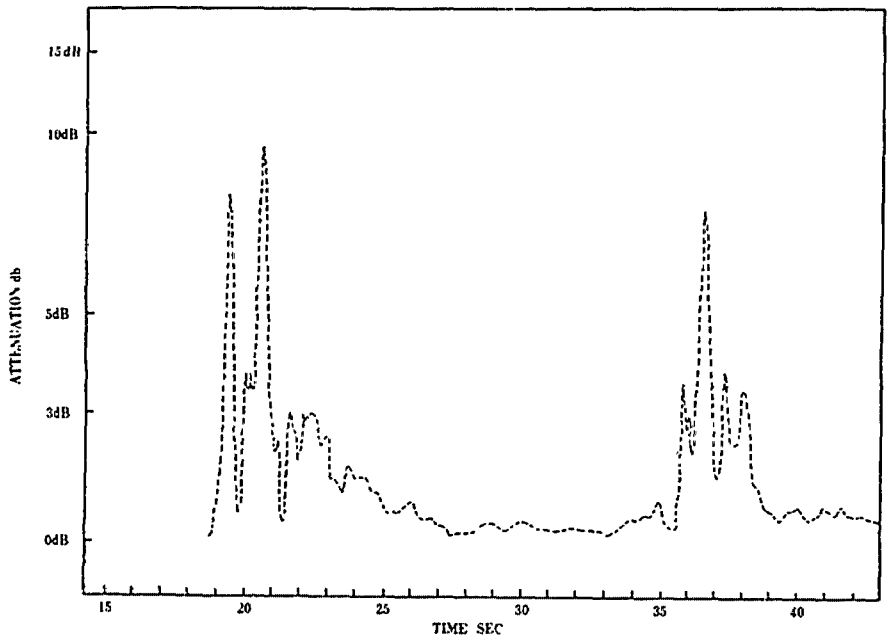

Figure 17. Attenuation measurements made at 94 GHz during event F - 7 of 13 October 1978. Chart speed 1.25 cm/sec, time constant 40 msec.

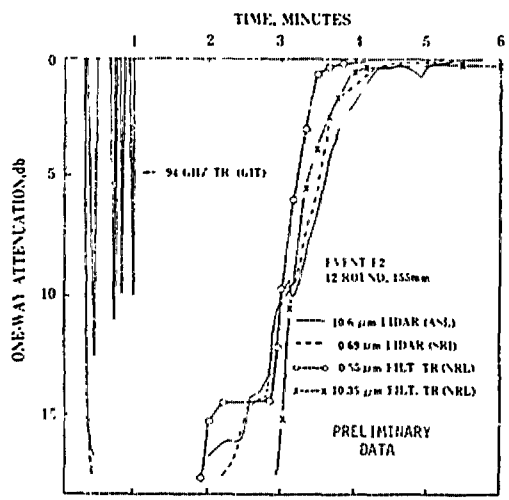

Figure 18. Intercomparison of attenuation at several wavelengths over the 2 km path for event F - 2.

RADAR SCATTERING PROPERTIES OF THE DUST CLOUD LOFTED BY THE MISERS BLUFF II HIGH EXPLOSIVE TEST

Edward E. Martin

Georgia Institute of Technology
Engineering Experiment Station
Atlanta, Georgia

ABSTRACT

An experiment was designed to measure the magnitude and wavelength dependence of the scattering cross-section and the total path attenuation of the dust clouds lofted by the MISERS BLUFF II high explosive test series. The radar instrumentation used to generate the data is described. A limited amount of data taken at frequencies of 10 GHz, 35 GHz, and 95 GHz have been reduced, and the results of a preliminary analysis covering a time span of 2 to 94 seconds after detonation is presented.

1. INTRODUCTION

An experiment was designed to measure the electromagnetic scattering and attenuation properties, over a frequency range of 10 GHz to 100 GHz, of the dust clouds lofted by the MISERS BLUFF II test series. The goal of the experiment was to supply information needed to develop a model which will allow prediction of the performance of millimeter wavelength radar systems operating through extensive dust cloud environments.

Under subcontract to SRI International, the Georgia Institute of Technology, Engineering Experiment Station modified four instrumentation radars and installed them on a modified AN/MPQ-18 antenna pedestal. The antennas were scaled in size and co-boresighted so that each 0.7 degree radar beam illuminated a common volume within the dust cloud.

The MISERS BLUFF II, Phase 2 test series was conducted by the Defense Nuclear Agency at the Planet Ranch test site located near Lake Havasu City, AZ. The second event of the test series consisted of the simultaneous detonation of six 120 ton stacks of ammonium nitrate and fuel oil (ANFO). A limited amount of data taken from this second event have been reduced.

2. RADAR AND DATA ACQUISITION SYSTEM

2.1 Radar System

Four instrumentation radars previously developed by the GIT/EES were used to gather the experimental data. The radars were reconfigured both electrically and mechanically to meet the weight and size limitations imposed by the antenna scanning system. Each antenna was horizontally polarized during transmission and was equipped with a dual mode coupler so that both the horizontally and vertically polarized components of the reflected wave could be simultaneously received in separate receiver channels.

The radars operated at frequencies of 9.4 GHz, 35 GHz, 70 GHz, and 95 GHz. A functional block diagram showing the general configuration of the four radars is shown in Figure 1. In the two higher frequency radars ferrite waveguide receiver protector switches replaced the TR tubes, klystron local oscillators replaced the solid state local oscillators, and single ended Schottky barrier diode mixers were used instead of balanced mixers. Parameters of the four radars are given in Table I. The radars were sequentially triggered at a 4 kHz rate to allow the eight i.f. signals to be multiplexed onto two data lines corresponding to the horizontal and vertical components of the reflected signal. Multiplexing was accomplished at the i.f. level to allow video detection in one set of logarithmic amplifiers.

2.2 Data Acquisition System

The data acquisition system was furnished by SRI and was time shared between the radar experiment and a multifrequency laser experiment. The two channels of radar data were sampled in two groups of 40 and 10 range bins. Each range bin corresponded to a range resolution of 37.5 meters. The first 40 range bins were set to begin sampling at a range of 4.1 km and were used to sample the video from the dust cloud. The second set of 10 range bins was set to sample the video from the bluff and mountain behind the blast area. The video samples from the two groups of range gates were digitized and stored in a buffer accumulator. The accumulator summed the digitized values from each range cell for 50 consecutive radar pulses before recording the values on the data tape. Each record on the data tape contained two sets of radar data; each set contained 400 words corresponding to the 50 range cells of sampled video from each of the eight radar channels. In addition to the radar and laser data, each record contained 65 header words defining the time and spatial parameters as well as status and antenna command information.

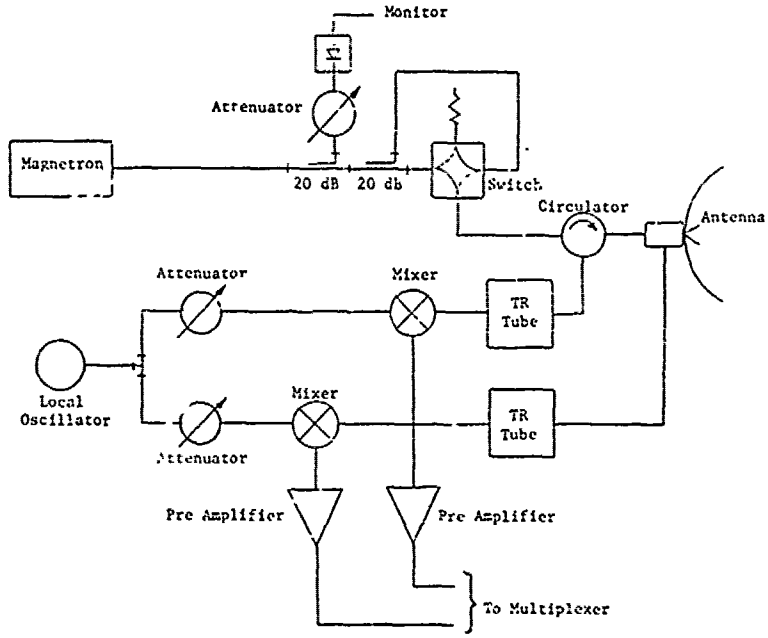

Figure 1. Functional diagram of instrumentation radars

TABLE I

Radar Parameters
MISERS BLUFF II - Event II

Parameter	Radar			
	1	2	3	4
Frequency (GHz)	9.375	35	69.7	94.5
Antenna				
Size (ft)	10	3	1.5	1.0
Beamwidth E-plane	0.78	0.70°	0.70°	0.70°
Beamwidth H-plane	0.70	.62°	.65°	0.66°
Isolation H/V (dB)	40	40	40	40
Gain (dB)	47	48	48	46
Polarization	Dual H/V	Dual H/V	Dual H/V	Dual H/V
Transmitter	Magnetron	Magnetron	Magnetron	EIO
Type	2J42	M5123	BL246	V1TB 2443
Power Output (kw)	6.2	5.9	0.8	0.8
Pulse Width	250 ns	250 ns	250 ns	250 ns
PRF (Hz)	1000	1000	1000	1000
Receiver				
Mixer	Balanced	Balanced	Single	Single
MDS (dBm)	-93	-90	-59	-62
Bandwidth (MHz)	12	12	80	80
Dynamic Range (dB)	70	70	50	70
Detection	Log	Log	Log	Log

3. EXPERIMENTAL PROCEDURES

This experiment was designed to measure the magnitude of the radar cross-section and the attenuation constants associated with the dust cloud at each of the four frequencies. The radars were located approximately 4.9 km from ground zero. A ridge approximately 10 m high and 0.8 km in front of ground zero obscured a direct view of the stacks of explosives. A mountain further in range ended in a near vertical bluff 200 meters beyond ground zero. A trihedral corner reflector was placed on the bluff to serve as a reference target for the attenuation measurements. A second trihedral corner reflector placed at the peak of the mountain served as a target for aligning the 4 radars to a common boresite and also as a secondary calibration reference.

A precision machined dihedral corner reflector, rotated 22.5 degrees from the vertical, was used to calibrate both the horizontally and vertically polarized channels of the radar prior

to detonation. After the radars were calibrated, samples of the signal returned from the corner reflectors located on the bluff and mountain were recorded on the data tape. The radars were then pointed immediately above ground zero and remained at that position until 8 seconds after detonation. At that time the radars were directed to the corner reflector located on the bluff to provide samples of the radar return for comparison to the pre-detonation values. The locations of the two corner reflectors are indicated in Figure 2. A television camera co-boresited with the radars was used for positioning the center of the scan sector. Figure 3 shows the television display 30 seconds after detonation. Twenty-six seconds after detonation the antenna was commanded to start a raster scan of the dust cloud. Both computer controlled raster scanning and manual positioning of the radar antennas were used throughout the remainder of the test.

Figure 2. Television display showing location of corner reflectors

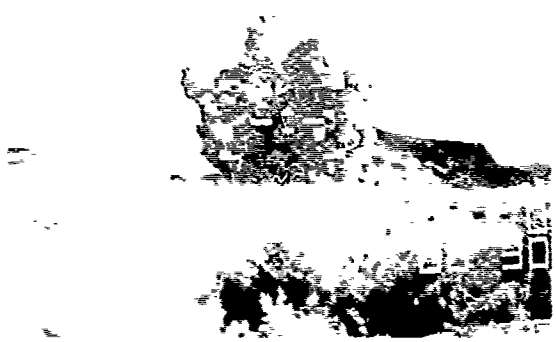

Figure 3. Television display showing the dust cloud 30 seconds after detonation

4. EXPERIMENTAL RESULTS

4.1 Volumetric Radar Cross-Section

Selected data over the time interval of 2 to 94 seconds after detonation have been reduced to plots and tabulations of volumetric radar cross-section. Values were not corrected for attenuation due to the dust cloud and were computed for a fixed range of 5 km. Figure 4 is a range profile of the 9.4 GHz and 35 GHz radar signal 10 seconds prior to detonation. Clearly visible are the radar returns from the ridge at 4.2 km and the bluff at 5.2 km. The signals beyond 5.8 km are side lobe returns from the mountain behind ground zero. Between the ridge and the bluff only the radar baseline noise is seen. Figure 5 shows the radar signals received two seconds after detonation at frequencies of 9.4 GHz and 35 GHz. A summary of the maximum radar cross-section values observed throughout the range extent of the dust cloud is given in Table II. Included in the table are the antenna pointing angles and the range at which the maximum signal occurred.

4.2 Frequency Dependence

The exponent of the frequency dependent term describing the radar cross-section must be determined before an adequate radar performance model can be developed. To lessen the offset of accumulated errors due to attenuation at ranges deep within the cloud, the frequency exponent was calculated only over the first six range cells. The calculated values of the exponents determined from the 9.4 GHz and the 35 GHz measurements are listed in Table III. From this table it is clear that the frequency exponent is a function of time in large artificially created dust clouds such as that generated by the MISERS BLUFF II test. This is seen in the model used by Burns and Bentley (1977) where the model was broken down into early, intermediate, and late time periods.

4.3 Attenuation

The corner reflector which was set upon the bluff as a reference for the attenuation measurements was knocked over by the shock wave resulting from the blast. However, over the time period of 0 to 6 seconds the antenna pointing angle varied less than 0.2 degrees. Based on the value of the signal returned from the bluff prior to detonation, the attenuations for the 9.4 GHz and 35 GHz radars were calculated. The justification for using the bluff as a reference is based on the fact that the signal from this area had previously appeared to be reasonably stationary in character when viewing the raw video. In addition the data which were recorded had effectively been smoothed by the summation of the signal from 50 consecutive radar pulses. The two-way attenuation calculated from these data indicate that at X-band less than 0.5 dB of attenuation would be expected. At 35 GHz the maximum calculated value was 12.2 dB. Additional analysis of the available data hopefully will allow a better definition of the attenuation function.

5. CONCLUSIONS

The data which have been analyzed represent only a small sample of the much larger data base which was generated during this experiment. While some trends may be indicated by the few samples, a much more thorough investigation of the total data base is needed.

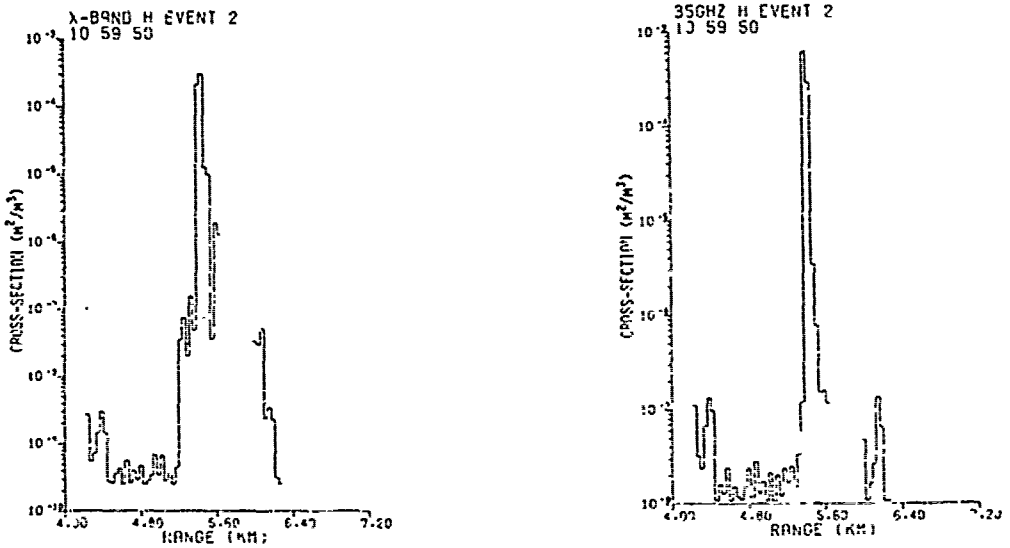

(a) 10 GHz radar (b) 35 GHz radar

Figure 4. Range profile showing characteristics of radar signal prior to detonation

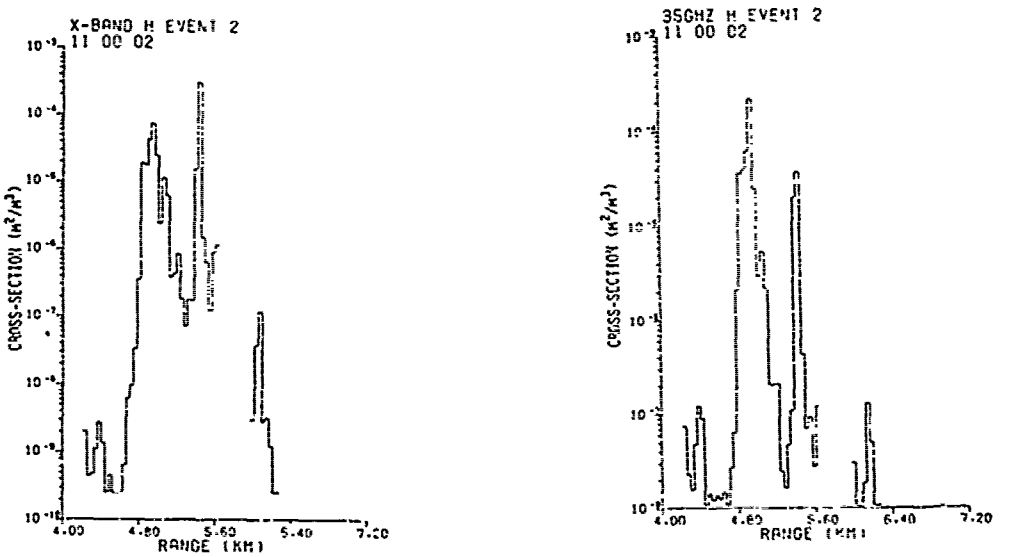

(a) 10 GHz radar (b) 35 GHz radar

Figure 5. Range profile showing characteristics of radar signal 2 seconds after detonation

TABLE II

PEAK RADAR CROSS-SECTION FOR MB-II, EVENT II

Time (sec) after T_o	Antenna Az	Antenna El	Range (meters)	Peak RCS m^2/m^3 9.4 GHz	35 GHz	95 GHz
-10	73.8	0.4		Pre Event Reference		
2	73.7	0.4	4950	7.3×10^{-5}	2.1×10^{-4}	2.7×10^{-4}
4	73.6	0.4	4950	4.4×10^{-5}	1.2×10^{-4}	1.9×10^{-4}
6	73.5	0.4	4988	2.0×10^{-5}	6.0×10^{-5}	2.2×10^{-4}
8	73.4	0.6	5025	3.3×10^{-6}	3.4×10^{-5}	2.0×10^{-4}
10	73.7	0.8	5025	9.0×10^{-7}	1.2×10^{-5}	-
12	72.7	0.9	5025	8.9×10^{-7}	6.7×10^{-6}	-
14	73.6	1.3	5025	1.5×10^{-7}	3.1×10^{-6}	-
16	73.0	1.4	5025	2.9×10^{-7}	6.7×10^{-6}	-
18	73.3	1.3	5025	1.9×10^{-7}	3.8×10^{-6}	-
20	73.1	1.5	5025	1.5×10^{-7}	3.6×10^{-6}	-
40	72.7	2.8	4988	5.9×10^{-8}	2.5×10^{-6}	-
42	71.6	1.8	4950	2.3×10^{-7}	1.1×10^{-5}	-
44	72.5	2.8	4963	1.9×10^{-7}	2.8×10^{-6}	-
94	73.4	11.2	5325	4.3×10^{-9}	1.9×10^{-7}	-

TABLE III

FREQUENCY DEPENDENCY FROM MB-II, EVENT II

(9.4 GHz and 35 GHz)

Time (sec)	Depth into Cloud (range cells) 1	2	3	4	5	6	Average
2	.49	1.37	.50	.51	.29	.82	.65
4	.92	(-).04	1.20	1.20	.82	.77	.81
6	2.40	1.29	1.73	2.01	1.60	1.37	1.73
14	2.04	1.69	2.11	2.53	2.97	2.31	2.28
40	2.72	2.52	3.17	3.02	2.86	2.87	2.86
44	2.09	2.89	2.79	2.66	2.70	2.42	2.58
94	3.01	3.12	2.03	1.44	1.54	2.92	2.34

REFERENCES

Burns, A. and P. Bentley, 1977: SHF/EHF Scattering Experiment for MISERS BLUFF. Technical Memorandum 1, SRI International, Project 6462.

CLOUDS—MODELS AND PROPAGATION EFFECTS

Dr. James H. Thompson
General Electric—TEMPO
Santa Barbara, California

ABSTRACT*

1. INTRODUCTION

In a nuclear battlefield environment, large extensive dust clouds are generated by low altitude and surface nuclear bursts. In a tactical battlefield environment a great number of small dust clouds are produced by munitions impacting the ground. Millimeter and submillimeter waves propagating through these dust clouds can suffer various degrading effects including absorption, scattering, decorrelation, and scintillations. Under contracts from the U.S. Army Atmospheric Sciences Laboratory and the Defense Nuclear Agency, General Electric—TEMPO has developed models describing the tactical, Thompson (22 November 1978), and the nuclear, Thompson (1 November 1978), dust clouds and the absorption and scattering propagation effects.

Is there sufficient dust in tactical and nuclear dust clouds to cause significant propagation effects for millimeter waves? A rough rule of thumb is 1 dB of total attenuation for each gram per square centimeter of path integrated dust mass for a 100-GHz (3 mm) wave. Some typical path integrated dust mass values are 10 to 20 gm cm^{-2} for tactical dust clouds at early times; for nuclear dust clouds the pedestal region has values of about 1 to 5 gm cm^{-2}; the stem fallback region can have 100's of gm cm^{-2} or larger; at late times the main cloud can have a few to a few tens of gm cm^{-2}. So the answer is yes; there are dust regions which can produce 5, 10, 20 dB or more attenuation for mm waves.

I would like to give a brief overview of dust clouds from the systems modeling standpoint. By systems modeling I am referring to computer codes which analytically model dust clouds and the propagation through these clouds. Examples of the systems codes are RANC, WEPH, and WOE which model propagation effects for radar, communications, and optical systems in a nuclear dust cloud environment. The Atmospheric Sciences Laboratory at White Sands Missile Range is in the process of developing the E-O SAEL code which will model propagation effects in a tactical battlefield dust environment. Systems models are by necessity simplified representations of the actual physical processes. The models are verified by comparing model predictions with experimental data taken in test events.

*Abstract is at the end of the paper.
Author did not comply with format.

2. DUST REGION MODELS

Figure 1 shows a sketch of the dust regions generated by a surface or near surface nuclear burst. The dust in the main cloud comes primarily from the crater ejecta. Additional dust can be transported up into the main cloud through the stem by the afterwinds. There is also dust in the stem and the extensive pedestal region surrounding the stem. The dust cloud generated by a tactical munition, such as a mortor or artillery shell, impacting the ground will have similar dust regions as the nuclear cloud. The tactical dust cloud will have a main cloud and a stem, but the pedestal region will be much smaller proportionally in height and extent. A large pedestal region is uniquely a nuclear effect. The differences between nuclear and tactical dust clouds are primarily that of scale—sizes in nuclear clouds are measured in kilometers while sizes in tactical clouds are measured in meters.

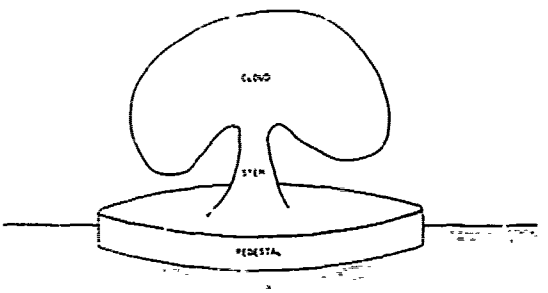

Figure 1. Nuclear dust regions.

2.1 Nuclear Dust Models

Figure 2 shows the model geometry for the main dust cloud for the nuclear case. The size distribution of the dust particles is divided into 8 size groups, ranging in diameter from 0.001 to 10 centimeters. The geometry of each size group is assumed to be cylindrical. The particles of each size group are assumed to be uniformly distributed within the volume of their cylinder. Initially all cylinders are the same size and are contained within the fireball. At late times each cylinder falls with the characteristic velocity of its size particles. Each

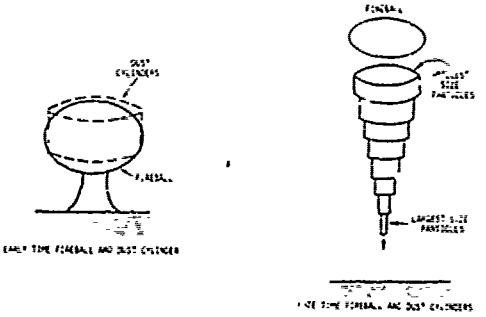

Figure 2. Model geometry for main nuclear cloud.

cylinder has the same radius as the fireball until the cylinder falls free of the fireball, then the cylinder radius remains constant. Figure 3 shows the model geometry for the nuclear stem and pedestal dust regions. Again cylindrical geometry is assumed. The dust particles are again divided into a number of size groups. Here the radii of each size group is taken to be the same, but the top of each size group falls with its own characteristic velocity. Model equations have been developed for the growth, rise, and fall of each region—cloud, stem, and pedestal— as well as for the dust loading of each region. Interested readers are referred to the reports for the detailed descriptions and equations.

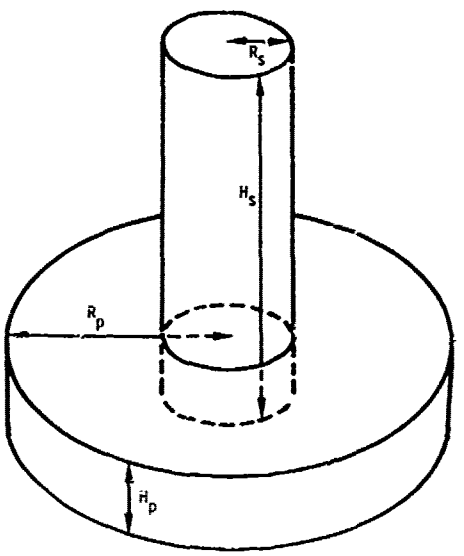

Figure 3. Pedestal and stem geometry for nuclear dust.

2.2 Munitions Dust Models

Figure 4 shows a sketch of the munition dust cloud formation and development. We ignore the extremely fast formation processes and assume an initial cloud is formed instantaneously at burst time. The dust particle size distribution is divided into a fairly large number (20 to 50) of individual size

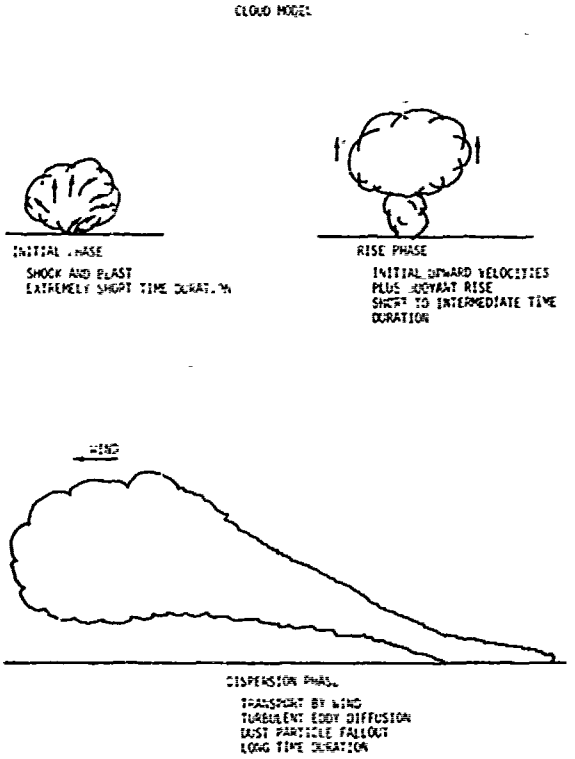

Figure 4. Munition dust cloud development.

groups. The geometry of each size group is taken to be spheroidal, rather than cylindrical as in the nuclear case. Also the mass distribution within each group is no longer assumed to be uniform, but is taken to be Gaussian along each of the three spheroidal axes. All size groups are assumed to occupy the same volume of the initial cloud at time zero. We model the rise, expansion, wind transport, and diffusion of each size group separately. The lightest particles will rise, expand, transport, and diffuse at the fastest rates, while the heavier particles will lag behind and fall out. Figure 5 shows a sketch of the size groups in the dust cloud. Again interested readers are referred to the reports for details and equations.

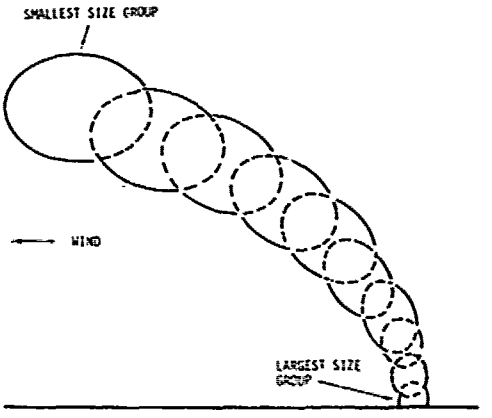

Figure 5. Size groups in dust cloud.

3. SIZE DISTRIBUTIONS

The two most common probability distributions used to describe particulates (whether dust, smoke, haze, fog, rain, or debris) are the power law and the log-normal distribution. For dust particles a hybrid distribution is also used; the hybrid uses a log-normal distribution for the smaller sized particles joined to a power law distribution for the larger sized particles. Under conditions of heavy dust aerosol loading, there appear to be two distinct size modes present, Patterson (1977). The small particle mode is termed mode A, is log-normally distributed, and is thought to be due to the breaking up of loose soil aggregates by the sandblasting process due to wind erosion. For explosively formed clouds, the blast and cratering processes can also be expected to break up the soil aggregates. The larger mode, mode B, has the hybrid distribution and is due to the soil aggregates themselves. Figure 6 shows the two-mode size probability distributions.

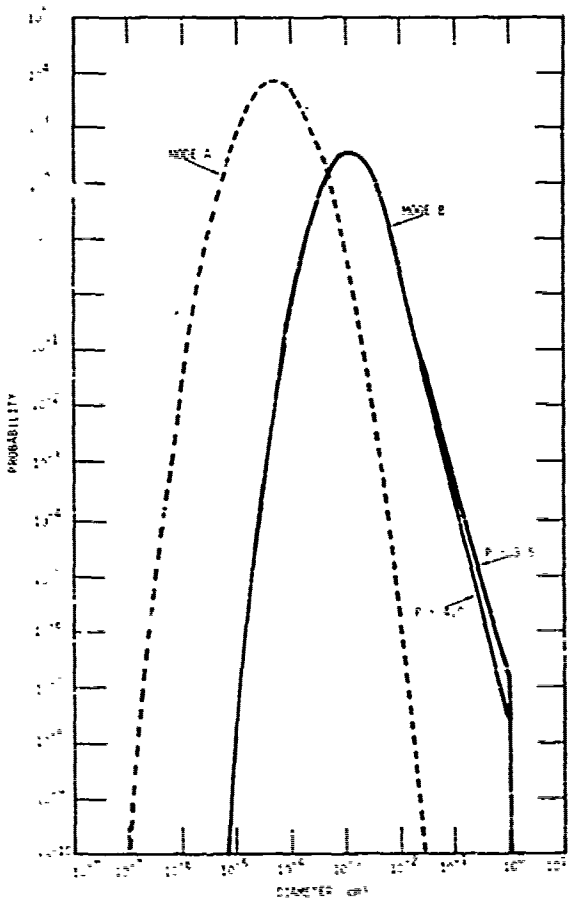

Figure 6. Particle size probability distributions.

4. MIE CALCULATIONS

For a given propagation path through a dust region, the models determine the total amount of dust mass penetrated and the size distribution of the dust particles. We use an exact Mie calculation to calculate the absorption, scattering, and extinction coefficients for the dust particles. Our standard Mie calculation for spherical particles is a new improved version; the computer routine is compact, fast running, and accurate for any combination of wavelengths and particle sizes. Since dust particles are, in general, irregular and nonspherical, several researchers have suggested modifying the standard Mie calculations to correct for the nonsphericity. Chylek (1976) has shown that a simple modification to the standard Mie solutions yields scattering pattern results for nonspherical particles which are in good agreement with experimental data. The modification eliminates the effects of the surface waves that are present in scattering by nonspherical particles. An option has been provided in the computer routines to use the Chylek method. Figure 7 shows an example of some scattering and total (scattering plus absorption) cross sections for spherical particles with a power law size distribution for a variety of frequencies and power law exponents.

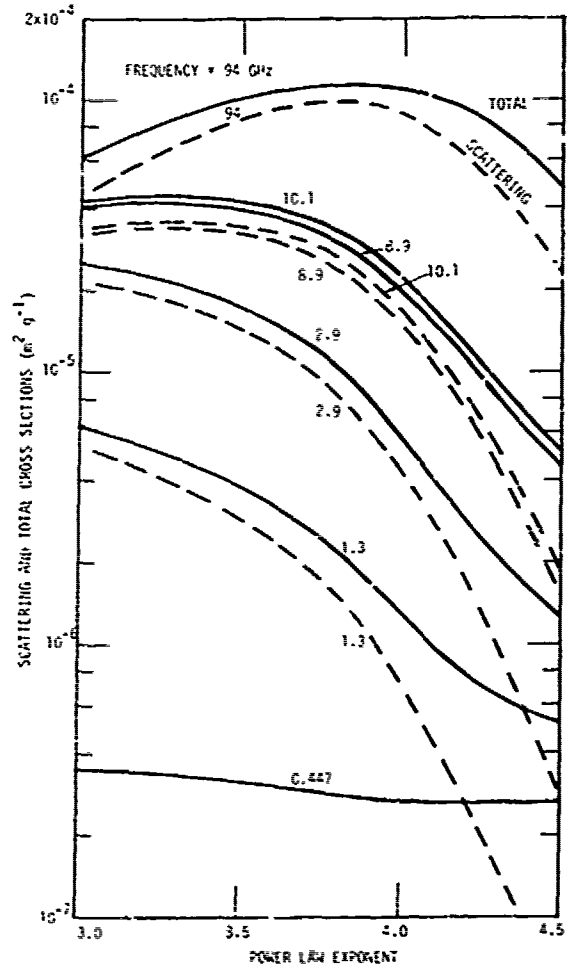

Figure 7. Scattering and total cross sections for dust particles from dry sandy soil having a power law size distribution.

REFERENCES

Chylek, P., G. W. Grams, R. G. Pinnick, 1976: Light Scattering by Irregular Randomly Oriented Particles. Science, 193, 480-482.

Patterson, E. M., D. A. Gillette, 1977: Commonalities in Measured Size Distributions for Aerosols Having a Soil-Derived Component. J. Geophys. Res., 82, No. 15, 2074-2082.

Thompson, J. H., 1978: Dust Cloud Modeling and Propagation Effects for Radar and Communications Codes. DNA-4697T (GE78TMP-81), General Electric-TEMPO, 1 November 1978.

Thompson, J. H., 1978: Models for Munition Dust Clouds. GE78TMP-99, General Electric-TEMPO, 22 November 1978.

ABSTRACT

In a nuclear battlefield environment, large extensive dust clouds are generated by low altitude and surface nuclear bursts. In a tactical battlefield environment, a great number of small dust clouds are produced by munitions impacting the ground. Millimeter and submillimeter waves propagating through these dust clouds can suffer various degrading effects including absorption, scattering, decorrelation and scintillations.

Under contracts from the U. S. Army Atmospheric Sciences Laboratory and the Defense Nuclear Agency, General Electric-TEMPO has developed models describing the tactical and nuclear dust clouds and the absorption and scattering propagation effects. A new efficient exact Mie cross section code has been developed. This code calculates the Mie absorption and scattering cross sections and scattering pattern for both individual particles and for distributions of particles. Utilizing the Mie parameters, analytic algorithms have been developed to calculate the absorption, single and multiple scattering effects. Sample calculations of dust cloud models and propagation effects are presented and compared with the exact theoretical or experimental data.

MILLIMETER WAVE ATTENUATION IN MOIST AIR*
- A REVIEW -

Hans J. Liebe

National Telecommunications and Information Administration
Institute for Telecommunication Sciences

Boulder, Colorado 80303

ABSTRACT

Considerable attention is currently being given to EHF (30-300 GHz) systems, in part due to their ability to penetrate most adverse atmospheric conditions (dust, smoke, clouds, fog, light rain). To assess the "all-weather" capabilities of such systems requires accurate predictions of the propagation effects under varying conditions of weather, height, location, etc. This complex task involves molecular absorption from oxygen, water vapor, and several trace gases (O_3, CO, etc.) and absorption and scattering loss from particulates[1,2]. Most applications will operate in the four spectral windows of the EHF region. Observations in clear air by laboratory[3-17] and field[18-21] experiments have found in these windows the existence of anomalous water vapor absorption (AWA). Anomalous implies that no reliable model exists to predict the effects of AWA. In particular, it was found that AWA increases in a complicated manner with humidity.

This paper reviews the AWA problem before the background of the known molecular absorption characteristics and discusses possibilities to gain a better understanding of the underlying physical phenomena.

1. INTRODUCTION

The number of millimeter wave systems operating through the atmosphere in the EHF band (30-300 GHz) is growing rapidly. The mostly tactical applications are short-range (1-5 km) for wideband communications and for sensors with high spatial resolution. Active (radar) and passive (radiometer) seekers can "look" through dust, fog, clouds, and light rain thus g them an advantage over infrared and electro-optical devices. The performance of these systems is most seriously affected by the transparency of the atmosphere; hence, most of them operate in four EHF window ranges (Fig. 1). Transparency is tightly coupled to the effects of moist weather. Propagation limitations in range or elevation angle increase with the amount of wate. vapor present in the path; i.e., as the conditions change from clear and dry to cloudy and wet.

1.1 EHF Refractivity and Propagation Factors

The refractivity N is a convenient macroscopic measure of the somewhat complicated interaction between millimeter waves and the molecules that comprise the atmosphere. Scattering is neglected since the air mass is assumed to be calm and clear. The spectroscopic base for the microwave N-value (frequency $\nu < 20$ GHz) of air requires only three parameters to relate the propagation effects of the medium to three meteorological variables: dry air pressure p, temperature T, and water vapor density ρ. Laboratory measurements under well-controlled p-T-ρ conditions have been the most reliable source for these parameters[3]. The EHF range (ν = 20 to 300 GHz) requires more than 200 additional spectroscopic parameters to express the properties of molecular absorption lines in a p-T-ρ scheme.[4-7]

The "microwave" refractivity of moist air is real, frequency independent and given by

$$N_0 = (2.589p + 5.76\rho)t + 0.331\rho \quad (\text{ppm}). \qquad (1)$$

Water vapor density ρ and partial vapor pressure p_w are related as follows:

$$\rho = 7.219\, p_w\, t \quad (g/m^3) \quad , \qquad (2)$$

where the temperature parameter is $t = 300/T(^0K)$ and the pressure units (p, p_w) are kPa (10 mb).

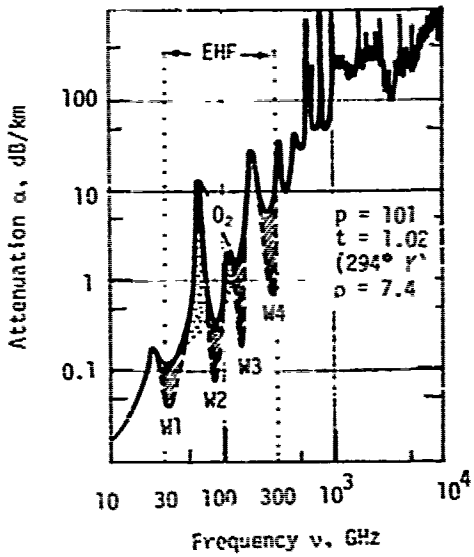

Figure 1. Molecular absorption in air at sea level from 10 GHz to 10 THz. Calculation is based on the AFGL[8,9] and ITS[6,7] data bases. The approximate variability due to water vapor (shaded area) is shown for the EHF window ranges:

	ν, GHz	α, dB/km
W1	24-46	<0.1
W2	72-110	<0.4
W3	126-160	<2
W4	200-260	<5

*Editors' Note: Author did not follow the requested procedure for quotation of references.

The "EHF" refractivity N of moist air is complex, highly frequency dependent, and can be expressed as

$$N = N_0 + \Sigma_i (S\,F')_i + N'_W + j\left[\Sigma_i (S\,F'')_i + N''_W\right] \text{ (ppm)}. \quad (3)$$

The molecular spectra are of two kinds:

(a) The line spectra of absorption (amplitude attenuation) SF" and dispersive refraction (nonlinear phase shift) SF' with a strength S in units of kHz and shape factors F' and F" in units of GHz^{-1}; the sums range over all spectral lines identified to make EHF contributions. The calculation of (3) takes into account 36 O_2 lines, 6 H_2O lines, and, if needed, includes a data base for trace gas spectra (>100 O_3, 2 CO, 64 N_2O lines) which are generally weak.[48]

(b) Nonresonant water vapor spectrum N'_W and N''_W due to wing terms of very strong infrared lines plus additional contributions not fully understood.

The power attenuation and phase delay ra .. the standard propagation factors, are simply

$$\alpha = 0.1820\nu \text{ Im } N \quad \text{(dB/km)}\ , \quad (4)$$

$$\varphi = 0.0209\nu \text{ Re } N \quad \text{(radians/km)}\ , \quad (5)$$

where Im stands for "imaginary part of" and Re for "real part of", and the frequency ν is in GHz.

2. MOLECULAR ABSORPTION

The molecular absorption (Eqs. 3, 4) of moist air has two main contributors in water vapor and oxygen,

$$\alpha = \alpha_1 (H_2O) + \alpha_2 (O_2) \quad . \quad (6)$$

Water vapor absorption has three significant terms,

$$\alpha_1 = \alpha_\ell + (\alpha_f + \alpha_x) \quad \text{(dB/km)}\ , \quad (7)$$

whereby

α_ℓ = 22 GHz and 183 GHz lines;

α_f = far wings of lines extending beyond 300 GHz up to 13 THz;

α_x = anomalous water vapor absorption (AWA).

The calculation scheme for the spectral line contributions, α_ℓ and α_2 has been verified by accurate laboratory measurements.[47-52] The water vapor continuum absorption,

$$\alpha_w = \alpha_f + \alpha_x \quad \text{(dB/km)}\ , \quad (7a)$$

determines the transparency in the four EHF window ranges (Fig. 1). At present, this contribution cannot be modeled reliably with the usual p-t-ρ scheme for clear air.

2.1 Molecular Absorption Peaks

Predicted results for α when based on available range or height profiles of p, t, ρ are in good agreement with observations in the vicinity of the absorption peaks. The spectral line properties (center frequency ν_0, strength S, shape F) of the major absorbers O_2 and H_2O have been established by extensive series of accurate laboratory measurements. The weaker water vapor continuum (Eq. 7a) is not critical around the center frequencies. Examples for the EHF spectrum of oxygen are depicted in Figure 2.

2.2 EHF Transmission Windows

Atmospheric windows are the valleys between absorption peaks (see Figure 1) of molecular resonances at 22 GHz (H_2O), 60 GHz (O_2), 119 GHz (O_2), 183 GHz (H_2O), 325 GHz (H_2O). It is generally accepted that the window transparencies in moist air are determined by a water vapor continuum spectrum which is, however, the least understood since it is difficult to measure quantitatively. In almost all cases, measured attenuation values with supportive environmental data are higher than predictions based upon known line shape theory. So far, it has not been possible to uniquely identify the absorption mechanism responsible for the AWA contribution.

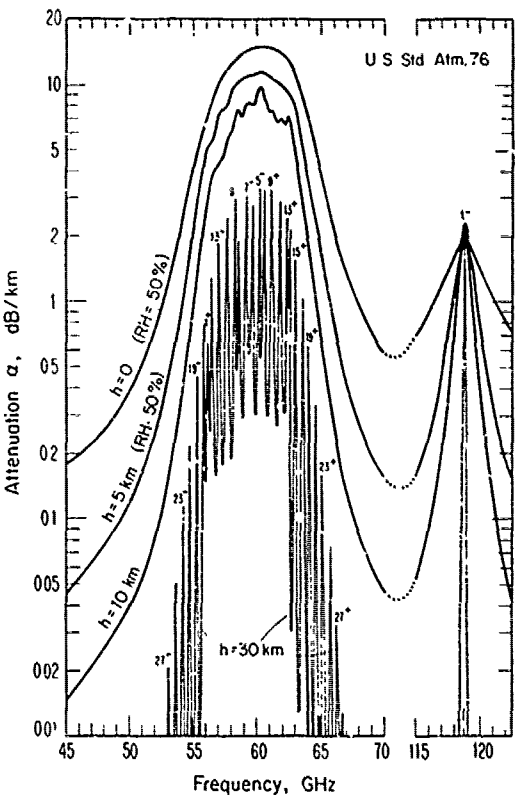

Figure 2. Peak attenuation rates α due to oxygen resonances ($\approx \alpha_2$) in the 45 to 122 GHz range at various altitudes h.[48]

The continuum absorption $\alpha_w = \alpha_f + \alpha_x$ is estimated for predictive modeling by empirical expressions derived from fitting a few available data points. We adopted a formulation introduced by Gaut and Reifenstein[52] and cast it for use in (3) into the form [48]

$$N''_w \approx 2.6 \cdot 10^{-7}\ p\ t^{2.1} \rho\ \nu \qquad \text{(ppm)} \qquad (8)$$

and

$$N'_w \approx 3.6 \cdot 10^{-5}\ t^{0.2}\ \rho\ \nu^{0.1} \ . \qquad \text{(ppm)} \qquad (9)$$

It seems that the water vapor density ρ is the single, most important parameter in determining the propagation limitations within the four EHF windows.

2.3 Physical Properties of Atmospheric Water Vapor

To understand and predict EHF continuum spectra, one has to know more about atmospheric water vapor density ρ than a number. Surface densities ρ_0 vary[54] typically between 0.1 (dry, winter, polar) and 40 g/m^3 (wet, summer, tropical). The maximum density, the saturation point ρ_s, is approximated by

(a) (b)

$$\rho \leq \rho_s \doteq 17.39\ t^6\ 10^{(10-9.834t)} \approx 25\ t^{-17} \ (g/m^3). \qquad (12)$$

The saturation density defines relative humidity,

$$RH \equiv (\rho/\rho_s)\ 100 \approx 4\ \rho t^{17} \qquad (\%) \ , \qquad (13)$$

and limits the partial water vapor pressure roughly (eq. 12b) to

$$p_w \lessapprox 3.5\ t^{-18} \qquad \text{(kPa)} \ . \qquad (14)$$

The humidity condition RH = 100% is a delicate balance point for phase changes (evaporation, condensation, precipitation). The density ρ_s changes over a wide range with temperature:

T	t	t^{-17}	ρ_s(true)+	ρ_s(12a)	ρ_s(12b)
°K			g/m^3		
333.3	0.9	6.00	130.35	130.4	150
300	1	1	25.50	25.5	25
*273.16	1.098	0.203	4.850	4.84	5
250	1.2	0.045	0.822	0.822	1

*Triple Point. +Smithonian Hydrometric Table

Molecular absorption generally is assumed to be proportional to the molecular number density M. The ideal gas law predicts for water vapor

$$M_i = 3.346 \cdot 10^{16}\ \rho \qquad (1/cm^3) \ . \qquad (15)$$

Water vapor is an imperfect gas. From calorimetric measurements it is known that there are slightly more H_2O molecules per unit volume than predicted by (15). The gas law is corrected to

$$M_w = [(1/M_i) + B(t)]^{-1} \qquad (1/cm^3) \qquad (16)$$

by introducing the second virial coefficient B. Very few values have been reported for atmospheric temperatures:[53]

t	0.96	1.04	1.18
B(cm^3)	-2.3	-1.6	-0.93×10^{-21} .

Based on these data, even at saturation the deviation

$$\delta = (M_w/M_i) - 1 \qquad (17)$$

turns out to be small:

T	t	B	ρ_s		δ, %
333	0.9	-2.8×10^{-21}	130	+	1.23
300	1	-1.9×10^{-21}	25.5	+	0.16
250	1.2	-0.9×10^{-21}	0.82	+	0.0025.

Up to this point, moist air was treated as a molecular p-t-ρ parameter system in thermodynamic equilibrium. Such simple description reflects the experimentally accessible properties of molecules and is only valid in calm air as long as the t-ρ combinations keep the air well (RH < 60%) below saturation. The optical property "clear" is generally associated with the full humidity range, RH < 100% and, in effect, only implies that any suspended particles are invisible. The microphysics of clouds[55,57] tells us that there are many invisible aerosol particles in natural air. They are smaller in size than about 0.2 μm dia and are at that size already made up by $\approx 10^8$ H_2O molecules.

Clarifications for inadequacies in the treatment of the EHF continuum spectrum (Eqs. 7 to 9) lie in understanding the variability of a multiphase atmospheric system consisting of H_2O and other molecules, of suspended foreign particles, and of aerosols that spontaneously reach visible sizes (> 0.2 μm dia) when RH exceeds 100 percent.

On the macroscopic scale one knows that:[55,57]

(a) Condensation nuclei in the form of foreign particles (size < 0.01 μm dia) are amply (> 10^2 cm^{-3}) suspended.

(b) Increases in RH above 70 percent foster "condensation" and, on the other hand, decreases cause "evaporation" of H_2O molecules from around the nuclei.

(c) The smallest stable droplet has a size of of ≈ 0.05 μm dia (10^6 molecules).

(d) The RH varies sharply with temperature (Eqs. 13, 2, 12b),

$$RH \approx 28\ p_w\ t^{18} \leq 100 \quad (\%) \ . \qquad (18)$$

(e) The condensation process (e.g., aerosol growth rate) avalanches when RH > 100. Visible sizes are reached within milliseconds and are noticed as haze (0.1 - 1 μm dia), fog (1 - 40 μm), mist (40 - 100 μm), drizzle (0.1 - 0.5 mm), or rain (0.5 - 8 mm) when t < 1.1.

(f) Suspended droplets are called aerosol and distinguished in two classes: permanent, mostly invisible (0.01 to 0.4 μm dia) and temporary, visible (0.4 to 100 μm dia). Gravity causes droplets to fall out when a critical size is exceeded (range of size/fall velocity: 0.1/0.5 to 6/10 mm/ms^{-1}).

(g) Invisible liquid-like droplets might exhibit the dielectric bulk properties of water reduced by their mass fraction v,

$$N''_{LW} = 7.09 \cdot 10^5\ [K(\sqrt{D^2 + 1} - 1)]^{1/2}\ v \ (ppm) \ , \qquad (19)$$

yielding (Eqs. 19, 4),

ν	K	D	v	α
GHz				dB/km
30	25	1.2	10^{-7}	1.4
300	8	1.0	10^{-7}	7.0 .

K and D are dielectric constant and loss tangent, respectively, of pure water at 20° C (for dielectric properties of ice see Ref. 4).

(h) A drop in temperature by 10 degrees decreases the water vapor density of saturated air by 50 percent.

(i) Substantial amounts of energy are released during condensation which were stored in the random motion of H_2O molecules (latent heat of vaporization is on the order of 0.5 kcal g/g).

(j) As a consequence of (i) the medium is perturbed in its thermodynamic equilibrium. The condensation process provides "fuel" for adverse weather. Depending upon the suddenness, the amount of cooling, and the water vapor supply, more or less violent updrafts (such as cumulonimbus clouds in thunderstorms) feed a turbulent air motion. Small aerosols are lofted onto the upper region of a forming cloud while the larger, heavier ones remain suspended at lower levels. The small aerosols carry a positive charge, the lower levels take on a negative charge. The charge separation generates high electric field strengths and lightning discharges occur when a value of about 30 MV/m is reached.

On the microscopic scale one suspects (mostly based on anomalous behaviors of the water vapor continuum spectra at EHF and infrared windows):[13,21,42,46]

(k) Water polymers or clusters $(H_2O)_n$ are formed and kept together by intermolecular hydrogen bonds.*

(l) The dimer (n=2) is the most prevalent cluster size monotonically decreasing with higher n.

(m) In case ionization takes place (e.g., natural radiation, high electric field strength, etc.), ion hydrates or ion-induced neutral clusters are generated with sizes ranging from n = 2 to 30 and peaking around n ≈ 12. A cluster of size n = 12 has an approximate diameter of 10^{-3} μm.

In the simple picture sketched by facts and hypotheses (a) to (m), one finds various arguments to explain anomalous behavior of water vapor-related absorption. The fundamentals of clear, moist air behavior must be expanded beyond a simple p-t-ρ relationship.

2.4 Anomalous Water Vapor Absorption (AWA)

AWA is defined as the component of absorption that cannot be attributed to the established molecular spectroscopic data base. The distinction between α_f ("normal") and α_v ("anomalous"), however, is not well defined. The line shape choice (VanVleck-Weisskopf, Rosenkranz, Gross) for features outside the frequency range of interest causes substantial differences in the magnitude of the EHF continuum (α_f).[47] The AFGL compilation[49] lists 38,350 H_2O lines from 20 GHz to 331 THz ordered in seven bands[44] with some line absorption strengths exceeding the one at 22 GHz by factors of 10^6(!). We found that rotational lines of up to 13 THz make contributions (> 0.002 dB/km) to the EHF continuum when applying the Gross shape. A fit to these results (see Fig. 3) yields approximately[47]

$$\alpha_f \approx b\ pt^{2.5}\ \rho\ \nu^{2.3} \qquad (dB/km) \ , \qquad (20)$$

about the same functional form adopted for the formulation (8), except for the scale factor, $b = 6.0 \cdot 10^{-9}$.

Experimental EHF attenuation data obeying (20) in the window ranges should be considered a low frequency-wing-effect of the H_2O rotational spectrum. In the wing exercise (model 2 in Fig. 3), shape functions are (mis-)used to calculate intensities on the order of 10^{-8} of the peak value (ν_o) occurring several thousand halfwidths below ν_o. Line shape theory is certainly not able to truly describe the real microscopic situation to such a degree of significance.

*The electron-rich end of O in the polar molecule H_2O attracts an electron-poor H end of a neighbour H_2O. The intermolecular bond has only 5 to 10 percent the strength of a covalent O-H bond but accounts for most of water's unique properties.

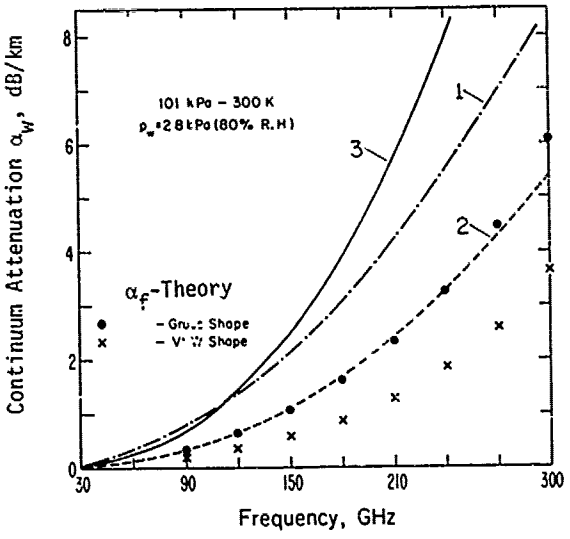

Figure 3. Example (p = 101, t = 1, ρ = 20) of EHF continuum water vapor attenuation calculated by various methods -

Model 1: Empirical fit (equations 8 and 4).
Model 2: Best theoretical fit based on the summation of 1836 stronger H_2O lines (200 GHz - 31 THz).[47]
Model 3: Empirical fit to ITS laboratory data (Eq. 27).[12]

AWA is redefined as the component α_x that does not obey the physical dependencies expressed in (20). A review of reported data is given in Table 1.

Table 1. AWA Evidence

Results	References Field Data	Lab Data
agree with theory	31	
are larger than theory predicts	20,21,23,24,25, 28,32,34,36	1,11,8
are proportional to ρ	23,24,25,33 37,41,52	1
increase with ρ^x (x > 1)	19,22,29,30, 34,36,39	7,9,10,12, 13,17
exhibit strong t^y law (y > 2)	21,22,39	5,12,13

There is ample evidence of AWA. The discrepancies are not small; i.e., the ratio α_x/α_f was found to be as large as 10. Laboratory[1-17] and field[18-41] experiments have contributed to gather AWA evidence and interpret its meaning. The work was not limited to the near millimeter wave range (10-1000 GHz) but included studies of infrared clear air window absorption as well.[5,6,17,42] Several hypotheses have been brought forward to explain these somewhat confusing experimental facts (Table 2).

So far, no unified AWA treatment exists that has a physical basis. Recommendations have been expressed for research, in particular for hard data from controlled experimental studies.

Table 2. AWA Hypotheses

AWA is due to	References
1) a special height distribution of $p_w(h)$	29
2) pressure-induced, forbidden transitions	5
3) far-wing line shape errors	46
4) a bulk dipole moment (Eq. 19)	8, 46
5) a dimer $(H_2O)_2$ spectrum	9, 13, 20, 23, 30, 32
6) molecular polymer (H_2O clusters) spectra	6, 17, 21, 42

3. FIELD MEASUREMENTS

EHF window absorption was measured over short horizontal paths[21,26,27,30,39] and to outer space through the total air mass. Some of the latter results are depicted in Figure 4. As expected, window absorption increases with water vapor density ρ. A more realistic parameter for transparency predictions is the total precipitable water w in a radio path,

$$w = \int \rho ds \approx 2.5\ \rho_0 \quad (mm) \ , \qquad (21)$$

where ds is the path differential (km). Unit of w stems from the fact that 1 g H_2O is equivalent 1 cm^3. In lieu of in situ height profiles[5c] (e.g., radiosonde data) or direct measurements of w, it is common to use the measured surface density ρ_0 and to assume for the height profile,

$$\rho(h) = \rho_0 \exp(-h/2\ km) \ . \qquad (22)$$

The scatter of the points (10 to 30%) in Figure 4 is an indication of the difficulties involved with cumulative absorption measurements conducted either directly (using sun emission as the source) or deduced from sky emission data (elevation scans). The correlation to surface-based meteorological variables is sometimes poor due to the unspecified wide range of "weather" along the path. Another shortcoming is that most of the data are for low humidities (RH < 60%) where anomalous absorption behavior is not pronounced.

Cumulative data obtained through a total air mass are difficult to interpret in terms of underlying physical principles. The water vapor continuum spectrum is present when ρ is prominent; say ρ > 0.1 g/m^3, which restricts the altitude range to be considered to h ≈ 0 to 8 km. Tropospheric water vapor is highly variable both in space and time. Simultaneous measurements of cumulative attenuation

$$A = \int \alpha\ (s)\ ds \qquad (dB) \qquad (23)$$

and p(s), t(s), ρ(s) are difficult to accomplish. The measurement range for A is approximately between 0.1 and 25 dB. Reported window data for ν = 15 to 230 GHz (see examples in Fig. 4) fit roughly the expression

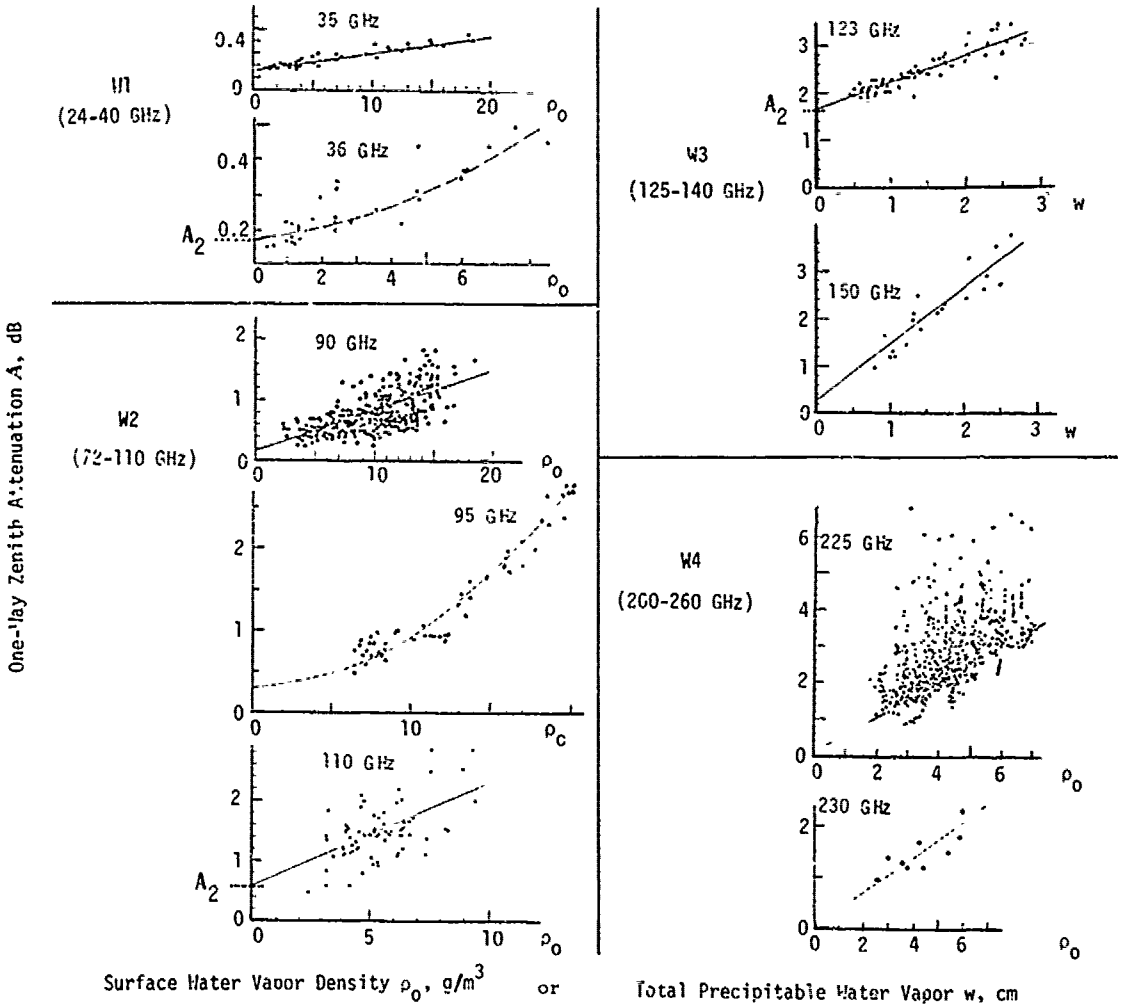

Figure 4. Reported zenith attenuation in clear air as a function of water vapor density at 35 GHz[52], 36 GHz[19], 90 GHz[52], 95 GHz[29], 110 GHz[24], 123 and 150 GHz[25], 225 GHz[53], 230 GHz[41].

$$A_W = \int \alpha_W dh \approx 0.013\ \rho_0 (\nu/30)^{1.8} \quad \text{(dB)} \qquad (24)$$

when $\rho_0 < 30$ g/m^3. The frequency dependence is close to ν^2 as assumed for equation (20).

An important variable of radio slant paths is the elevation angle θ. Careful measurements in clear air yielded:[18]

ν	$A_W(\theta=90°)$	$A_W^t(\theta=0°)/A_W$	A_2	A_2^t/A_2
GHz	dB		dB	
15	0.003 ρ_0	173	0.046	68
35	0.010 ρ_0	142	0.168	53

The dry term A_2 follows the secant law,

$$A_2(\theta) = A_2(90°) \,/\, \sin\theta \quad , \qquad (25)$$

to low (>2°) angles; the wet term increases below about 10° more rapidly.

The AWA contribution is identified by fitting an expression of the form

$$\alpha_x = a\ \rho^x\ t^y\ \nu^z, \qquad (26)$$

where $a = \alpha_x/\alpha_f > 0$, $x > 1$, and $y > 2.5$ (Eq. 20).

In field data it is difficult to recognize such dependencies. In several cases,[19,29,33,18] a ρ^2 term improved the otherwise linear ρ_0 fit to measured A_W - values (Eq. 24). Comparing measured attenuations in the 230 GHz range with calculated values based upon on-site radiosonde observations yielded, a = 3 to 9.[32]

Similar observations were made for the attenuation rates α of more homogeneous horizontal paths. For example, a short (≈ 200 m) path operated at 182.9 GHz exhibited a pronounced difference between clear and cloudy sky conditions; i.e., (3.9 vs. 4.2)ρ dB/km, which could be reconciled when a temperature term with y = 10 was assumed. This is about three times the t-dependence for the 183 GHz line.[39] At higher water vapor densities, the relationship between α and ρ became nonlinear. Data in the 210 to 510 GHz range taken for ρ = 4 to 11 and t = 1.1 to 1.03, clearly showed an AWA contribution with x = 2 and y = 16 to 30(!).[21]

At the onset of condensation, part of the air's humidity (molecules, clusters, aerosols) transforms into visible droplets that attenuate differently from Eq. (6), i.e. via scattering loss.[49] For example, warm fog (10° C, ρ = 1) attenuates about 0.4/3 dB/km at 95/300 GHz; ice fog (-30° C, ρ = ?) attenuates less (0.02 dB/km at 97 GHz).[16] For equal density, droplets attenuate more than ice spheres.[4]

4. LABORATORY MEASUREMENTS

Laboratory measurements play an important role in verifying modeling schemes for EHF properties of moist air. Generally, all the spectroscopic parameters (> 200) entering into equation (3) should be deduced from absolute intensity measurements under well controlled ν-p-t-ρ conditions. By a judicious choice of the experimental variables it is possible to investigate most parameters separately (e.g., α_f and α_w).

Numerous spectroscopic studies of water vapor have been performed[1-3,5-15,17] and H_2O is recognized to be a difficult test gas (ad- and de-sorption problems on surfaces). The evidence for AWA from these efforts is summarized in Table 3. No systematic study of AWA in the EHF windows (Fig. 1) has been reported. The evidence was not limited to absorption (e.g., Fig. 6), but also showed in refraction (Fig. 5) and refractive dispersion.[7,12] The results of Figure 6 are fitted by the expression,

$$\alpha = \alpha_x + \alpha_f = a\,\rho^2\,t^{10}\,\nu^{2.6} + b\,\rho t^{1.5}\,\nu^2 \quad (dB/km), \qquad (27)$$

where $a \approx 1.9 \cdot 10^{-8}$ and $b \approx 1.1 \cdot 10^{-6}$. The AWA component identified by (26) appears clearly and the far-wing term somewhat resembles (20). In light of other references, AWA looks as follows:

Eq. 26 AWA	Eq. 20 Wing Th.	Eq. 27 Exp.	Ref. 13 Exp.	Ref. 21 Exp.	Dimer Model	Aerosol Model
a	0	3.3	> 0	> 0	> 0	> 0
x (ρ)	1	2	2	2	2	2
y (t)	2.5	10	6 + 14	16 to 30	6	17
z (ν)	2.3	2.6				1

For simplicity's sake, we have reduced the different exponential temperature functions to a power law t^y. This is not based upon any particular theoretical model but is meant to be practical. The squared (x = 2) pressure dependence identifies AWA as a density-induced effect. The strong t dependence of AWA can be absorbed by making RH a variable. For example, the anomalous component α_x reported for moist nitrogen at 213 GHz[13] can be approximated by

$$\alpha_x \approx 0.016\ \rho\ RH \qquad (dB/km) \qquad (28)$$

The author believes that a systematic EHF study of α_w (t, ρ, p, ν) under controlled laboratory conditions will provide clues as to the number, kinds, and mass fraction (Eq. 19) of H_2O clusters in moist air. Additional variables such as air conductivity (ion activity),[42] condensation nuclei distributions, visibility, etc. might have to be considered.

Table 3. Laboratory Studies of Absorption in Moist Air

Frequency	AWA (Eq. 26) a	ρ^x x	t^y y	Water Vapor Density ρ	T Temperature	Path Length Free Path	Resonator Q	Reference
GHz				g/m^3	°K	m	x 10^3	
18-31	3-5	1+2		0-40	318	(Q-box)	> 800	1
22	>0	2		0-50	312		45	14
22, 24	>0	1+2		0-20	297	(30)	16	7
30, 60	>0	1+2	12	0-35	280-325	(>100)	200	12
117-120		>1		0-25	≈295	150		36
170-300	>0	2		0-20	≈295		30	8
183				0.5-5	243-323	150		10
180-420	>0			(0.18 cm)	293, 328	20-80		20
213	>0	2	>10	0-60	270-320	(40)	(Q-box)	13
210-300	>0	2	>10	3-6	273-333	28		9
450-960	>0			1	295	2		15
890, 965	>0	1+2		0-35	293,323	10-60		9
14-27T	>0	1+2	>10	2-20	293-313	500		2
21-38T	>0	1	≈5.5	14	296-388	1185		5
75-86T	>0	1+2		14	298	21		17

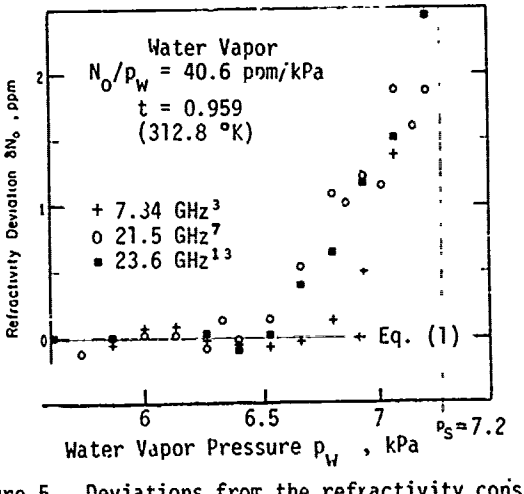

Figure 5. Deviations from the refractivity constant N_o/p_w when approaching saturation.[11,12,14]

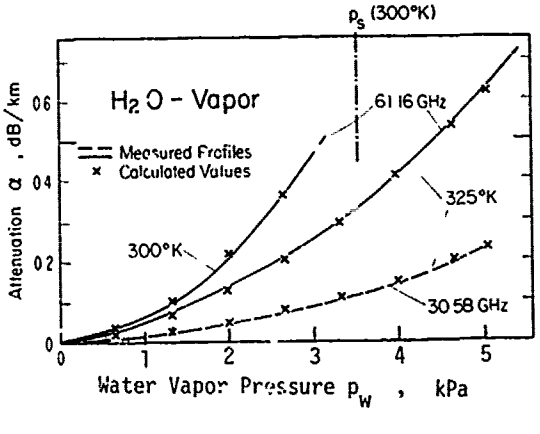

Figure 6. Water vapor attenuation measured in the laboratory as a function of vapor pressure.[12] x indicates the fit to Eq. (27).

5. RADIO PATH MODELING

Modeling implies that it is possible to predict the mean of EHF propagation effects and the limits of their variability (e.g., see examples in Fig. 4) from more readily available variables (p, t, ρ). At this point, all molecular absorption spectra have been reduced to a calculation scheme,[45,48,50,51] which serves as a tool to generate for horizontal paths the rates α and φ (Eq. 4, 5); for earth-to-space paths, the cumulative values A (Eq. 23) and ϕ; and for receiver sites, the atmospheric noise temperature T_R.

A standard example for cumulative values is the one-way zenith response through the U. S. Std. Atmosphere 76. Figure 7 gives attenuation results for three $\rho(h)$ profiles assuming RH = 5, 50, 100% in each of 26 height layers between h = 0 and 8 km. The comparison in Table 4 with measurements yields reasonably good agreement considering the various assumptions entering the calculation. This is mainly due to the unreasonable, but convenient assumption that water vapor is saturated at all levels between h=0 and 8 km; and that the model (8) has a scale factor about three times the value for b in (20).

Table 4. Comparison of Measured and Predicted Zenith Attenuation (see Figure 7)

ν	Ref.	Dry Air Meas. A_2	Dry Air Model A(5%)	Moist Air Measurement A_w/ρ	Moist Air Measurement A_w+A_2*	Moist Air Model A(100%)
GHz		dB	dB	dB/g/m^3	dB	dB
15	52	0.055	0.05	0.004	0.12	0.11
22.235	25	0.11	0.11	0.048	0.83	0.91
35	18	0.168	0.17	0.010	0.32	0.39
36	19	0.16	0.18	0.032	0.64	0.41
95	25	0.41	0.30	0.09	1.76	1.48
150	25	0.3	0.26	0.30	4.8	3.62
225	33	--	0.45	0.54	8.1	7.64

* ρ = 15, RH ≈ 100%

6. CONCLUSIONS

The role that water vapor (ρ, RH, w) plays in atmospheric millimeter wave propagation was traced by means of data from field, laboratory, and modeling studies. In particular, the transmissivity of the four EHF window ranges is not simply related to the amount of water vapor in the radio path. A continuum spectrum of water vapor is mostly responsible for window absorption and was found to consist of a normal (α_f) and an anomalous (α_x) "AWA" component. The normal component has a p^2-t-ρ dependence (Eq. 20), which is well-established as a low-frequency wing effect of the rotational H_2O spectrum. The anomalous component is little understood. In a few available experimental results, AWA displays an unexpected magnitude (up to 10 α_f) and variability with respect to t and ρ, which can cause serious uncertainties in the prediction of EHF window transmission through clear air under conditions of high humidity (RH > 90%) and/or low temperatures (< 280° K).

A parametric study of absolute attenuation rates for moist air in the EHF window ranges remains a challenging research topic, especially when laboratory simulations of high humidities (RH > 90%) are attempted. The systematic investigation of AWA might reveal the various stages and time scales which H_2O molecules undergo close to saturation until they become barely visible as a molecule ensemble (aerosol) of 10^8. Some research in this direction has already led to the formulation of DIMER[9,13,21,23,32,53] and CLUSTER[6,42] hypotheses. The former cannot explain all measured anomalies[21] and the latter has not yet been cast into a form of easy-to-measure additional variables. We conclude that, before AWA can be elucidated beyond empirical relationships, further work is needed to support or eliminate conjectures presently "clouding" the problem.

Work was partially supported by the U. S. Army Research Office (ARO 30-79).

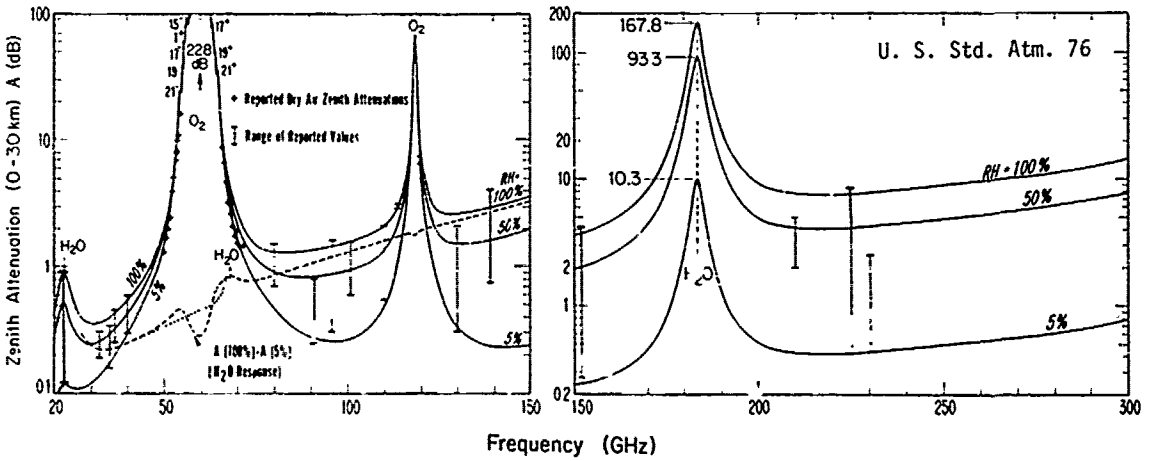

Figure 7. Predicted EHF zenith attenuation for dry (RH = 5%), moderate (50%), and humid (100%) conditions.[48] Reported values are in references[20,22-24,26,28,29,34-36,38,40] and Figure 4.

REFERENCES

(* indicates a representative review of sub-heading topic)

a) Laboratory Measurements

1. Becker, E. G. and S. H. Autler, 1946: Water vapor absorption of EM radiation in the cm range. Phys. Rev., 70 (5,6), 300-307.

2. Bignell, K. J., 1970: The water-vapour infra-red continuum. Quart. J. Royal Meteor. Soc., 96, 390-403.

*3. Boudouris, G., 1963: On the index of refraction of air, the absorption and dispersion of centimeter waves by gases. J. Res. NBS, 67D (6),631-684 (and 183 references therein).

4. Bryant, D. L. and J. J. Auchterlonie,1979: Measurement of the extinction cross-sections of dry and wet ice spheres at 35 GHz. Electron. Lett., 15 (2), 52-53.

5. Burch, D., D. Gryvnak, and J. Pembrook, Jr., 1971: Continuous Absorption in the 8-14 μm Range by Atmospheric Gases. Philco-Ford Report F19 628-69-C-0263.

6. Carlon, H. R., 1979: Variations in emission spectra from warm water fogs: Evidence for clusters in the vapor phase. Infrared Phys., 19, 49-64.

7. Dillon, T. A. and H. J. Liebe, 1971: Dispersion studies of the 22 GHz water vapor line shape. J. Quant. Spectrosc. Radiat. Transfer, 11, 1803-1817.

8. Frenkel, L. and D. Woods, 1966: The microwave absorption of H_2O vapor and its mixtures with other gases between 100 and 300 GHz. Proc. IEEE, 54 (4), 498-505.

9. Harries, J. E., W. J. Burrougns, and H. A. Gebbie, 1969: MM wavelength spectroscopic observations of water dimer in the vapour phase. J. Quant. Spectrosc. Radiat. Transfer, 9, 799-807.

10. Hemmi, C. G. and A. W. Straiton, 1969: Pressure broadening of the 1.63 mm water vapor absorption line. Radio Sc ., 4 (1), 9-15.

11. Liebe, H. J., 1966: Untersuchungen an Gasmischungen, Wasserdampf-Luft, mit einem digitalen Mikrowellen-Refraktometer. Ph.D. Thesis, Techn. University, W-Berlin, Electr. Eng. Dept. (D 83), 1964; also NTZ Communications J. 19, 79-83.

12. Liebe, H. J., 1975: Studies of Oxygen and Water Vapor Microwave Spectra under Simulated Atmospheric Conditions. OT Rpt. 75-65, June 1975, (U. S. Government Printing Office).

13. Llewellyn-Jones, D. T., R. J. Knight, and H. A. Gebbie, 1978: Absorption by water vapour at 7.1 cm-1 and its temperature dependence. Nature, 274 (5674), 876-878.

14. Mrowinski, D., 1970: Refraktion und Absorption in atmosphaerischen Gasen in der Umgebung der 22 GHz H_2O Linie. Ph.D. Thesis, Techn. University, W-Berlin, Electr. Eng. Dept., 1969; also Z. Angew. Phys., 29 (5), 323-330, 1970.

15. Sheppard, A. P., K. H. Breeden, and A. McSweeney, 1970: High resolution sub-mm measurements of atmospheric water vapor absorption. Proc. Sym. on Sub-mm Waves, Polytechn. Inst. Brooklyn, 445-453.

16. Straiton, A. W., B. M. Fannin, and J. W. Perry, 1974: Measurements of index of refraction and signal loss due to an ice fog medium at 97 GHz using a Fabry-Perot reasonator. IEEE Trans., AP-22 (4), 613-616.

17. White, K. O., W. R. Watkins, and L. R. Bruce, 1978 : Water Vapor Continuum Absorption in the 3.5 to 4 μm Region. U.S. Army Atm. Sciences Laboratory Report ASL-TR-0004, March 1978; and Report ASL-TR-0017, September 1978.

b) Field Measurements

18. Altshuler, E. E., M. A Gallop, and L. E. Telford, 1978: Atmospheric attenuation statistics at 15 and 35 GHz for very low elevation angles. Radio Sci., 13 (5), 839-852.

19. Crawford, A. B. and D. C. Hogg, 1971: Measurement of atmospheric attenuation at mm. Bell Sys. Tech. J., 35 (6), 907-916, 1956, also D. Hogg, Progress in Radio Science 1966-69, Vol. 2, URSI 1971.

20. Emery, R. J., P. Moffat, R. Bohlander, H.G. Gebbie, 1975: Measurement of anomalous atmospheric absorption in the 4 to 15 cm-1 range. J. Atmos. Terrestr. Phys., 37, 587-594.

21. Emery, R. J., A. M. Zavody and H. A. Gebbie, 1979: Measurements of atmospheric absorption in the range 4-17 cm-1 and its temperature dependence. J. Atmos. Terr. Phys., 1979.

22. Fogarty, W. G., 1975: Total atmospheric absorption at 22.2 GHz. IEEE Trans., AP-23 (3) 441-444.

23. Gibbins, C. J., A. C. Gordon-Smith, and H. A. Gebbie, 1973: Anomalous absorption in the atmosphere for 2.7 mm radiation. Nature, 243, 397.

24. Gibbins, C. J., A. C. Gordon-Smith, and D.L. Croom, 1975: Atmospheric emission measurements at 85 to 118 GHz. Planet. Space Sci., 23, 61-73.

25. Gibbins, C. J., C. L. Wrench, and D. L. Croom, 1976: Atmospheric emission measurements between 22 and 150 GHz. Proc. URSI Comm. F. Sym., Labaule, France, 19-21.

26. Gimmestad, G. G. and H. A. Gebbie, 1976: Atmospheric absorption in the range 12 to 31 cm^{-1} measures in a horizontal path. J. Atmos. Terr. Phys., 38, 325-328.

27. Gimmestad, G. G., R. H. Ware, R. A. Bohlander, and H. A. Gebbie, 1977: Observations of anomalous submillimeter atmospheric spectra. Astroph. J., 218, 311-313.

28. Goldsmith, P. F., R. L. Plambeck, and R. Y. Chiao, 1974: Measurements of atmospheric attenuation at 1.3 and 0.87 mm. IEEE Trans., MTT 22 (12), 1115-1116.

29. Lo, L. I., B. M. Fannin, and A. W. Straiton, 1975: Attenuation of 8.6 and 3.2 mm radio waves by clouds. IEEE Trans., AP-23 (6), 782-786.

30. Malyshenko, Y. I., 1969: Measurement of absorption coefficient of water vapor in the transparency window at 1.3 mm. Rad. Eng. & Electr. Phys., 14 (3), 447-448, (Engl. Transl.).

31. Mather, J. C., M. W. Werner, and P. L. Richards, 1971: A search for spectral features in the sub-mm background radiation. Astrophys. J., 170, L59-65.

32. Moffat, P. H., R. A. Bohlander, W. R. Macrae, H. A. Gebbie, 1977: Atmospheric absorption between 4 and 30 cm-1 measured above Mauna Kea. Nature, 269, 676-677.

33. Plambeck, R. L., 1978: Measurements of atmospheric attenuation near 225 GHz: Correlation with surface water vapor density. IEEE Trans., AP-26, 737-738.

34. Ryadov, V. Y., N. I. Furashov, and G. A. Sharonov, 1964: Measurement of atmospheric transparency to 0.87 mm waves. Rad. Eng. & Electr. Phys., 11, 773-778.

*35. Thompson, III, W. I., 1971: Atmospheric Transmission Handbook. NASA Tech. Rept. No. DOT-TSC-NASA-71-6 (Chapter 9 and 140 references therein).

36. Tolbert, C. W., L. C. Krause, and A. W. Straiton, 1964: Attenuation of the earth's atmosphere between 100 and 140 GHz. J. Geophys. Res., 69 (7), 1349-1357.

37. Ulaby, F. T. and A. W. Straiton, 1969: Atmospheric attenuation studies in the 183-325 GHz region. IEEE Trans., AP-17 (3), 337-342.

38. Ulaby, F. T., 1973: Absorption in the 220 GHz atmospheric window. IEEE Trans., AP-21 (2), 266-269.

39. Whaley, T. W., 1969: Characterization of free space propagation near the 183 GHz H_2O line. Ph.D. Thesis, U. of Texas, Electr. Eng. Dept., 1968, also IEEE Trans., AP-17 (5), 682-684, 1969.

40. Wrixon, G. T., 1971: Measurements of atmospheric attenuation on an earth-space path at 90 GHz using a sun tracker. Bell Sys. Tech. J., 50 (1), 103-114.

41. Wrixon, G. T. and R. W. McMillan, 1978: Measurements of earth-space attenuation at 230 GHz. IEEE Trans., MTT-26 (6), 434-439.

c) Theory, Predictions, Modelling

*42. Carlon, H. R., 1979: Infrared Absorption by Water Clusters. U.S. Army Armament Research and Development Command, Aberdeen P.G., MA 21010, Technical Report ARCSL-TR-79013, March 1979 (and 33 references therein).

43. Deirmendjian, D., 1975: Far infrared and sub-mm scattering, II: Attenuation by clouds and rain. The Rand Corp., Rept R-1718-PR, Feb. 1975; also J. Appl. Meteor., 14 (8), 1584-1593.

44. Derr, V. E., and R. F. Calfee, 1977: Spectral Transmission of Water Vapor from 1 to 1200 cm-1 at Low Concentration and Low Pressure. NOAA Tech. Memo ERL WPL-24, July 1977.

45. Hall, J. T.., 1970: Atmospheric effects on sub-mm radiation. Proc. Sym. on Sub-mm Waves, Polytechn. Inst., Brooklyn, 455-465.

*46. Lam, K. S., 1977: Application of pressure-broadening theory to the calculation of atmospheric oxygen and water vapor microwave absorption. J. Quant. Spectrosc. Radiat. Transfer, 17, 351-383 (and 68 references therein).

47. Liebe, H. J. and G. G. Gimmestad, 1978: Calculation of clear air EHF refractivity, Radio Sci., 13 (2), 245-251.

48. Liebe, H. J. and R. K. Rosich, 1978: Modelling of EHF propagation in clear air. Proc. IEEE Conf. Space Instrum. for Atm. Observation, El Paso, 4/1-15, April 1979; also AGARD CP 238-II, 45/1-18, 1978

49. McClatchey, R. A., W. S. Benedict, S. A. Clough, D. E. Burch, R. F. Calfee, K. Fox, L. S. Rothman, and J. S. Garing, 1978: AFCRL Atmospheric absorption line parameters compilation, AFCRL Environm. Research Paper No. 434, 1973; Appl. Optics, 15, 2616-2617, 1976; 17, 507, 1978.

50. McMillan, R. W., J. J. Gallagher, and A.M. Cook, 1977: Calculation of antenna temperature, horizontal path attenuation, and zenith attenuation due to water vapor in the band 150-700 GHz. IEEE Trans., MTT-25 (6), 484-488.

51. Ulaby, F. T. and A. W. Straiton, 1970: Atmospheric absorption of radio waves between 150 and 350 GHz. IEEE Trans., AP-18 (4), 479-485.

52. Waters, J. R., 1976: Absorption and emission by atmospheric gases. (Chapter 2.3 in Methods of Experimental Physics, Vol. 12B; editor, M. L. Meeks), N.Y., Academic Press.

d) Atmospheric Water Vapor Properties

53. Bohlander, R. A. and H. A. Gebbie, 1975: Molecular complexity of water vapour and the speed of sound. Nature, 253 (5492), 523-525.

54. Hall, M. P., 1977: Variability of atmospheric water-vapor concentration and its implications for microwave-radio-link planning. Electron. Lett., 13 (21), 650-652.

*55. Haenel, G., 1976: The properties of atmospheric aerosol particles as a function of the relative humidity. Advances in Geophysics, Vol. 19, Academic Press, 74-189.

56. Harries, J. E., 1977: The distribution of water vapor in the stratosphere. Rev. Geophys. & Space Phys., 14 (4), 465-475.

*57. Pruppacher, H. R. and J. D. Klett, 1978: Microphysics of clouds and precipitation. D. Reidel Publ. Comp., Dordrecht, Boston, London, 1978 (and about 1350 references therein).

ATMOSPHERIC TURBULENCE EFFECTS ON MILLIMETER WAVE PROPAGATION*

R. W. McMillan and J. C. Wiltse

Georgia Institute of Technology, Engineering Experiment Station
Atlanta, Georgia 30332

D. E. Snider

Atmospheric Sciences Laboratory, White Sands Missile Range
New Mexico 88002

ABSTRACT

The effects of atmospheric turbulence on the propagation of optical signals have been thoroughly analyzed by other workers, and good agreement with experiment has generally been obtained. In the case of millimeter microwave radiation, however, less work has been done, and theory predicts a strong dependence of the scintillation amplitude and angle of arrival variations on the humidity structure parameter C_ρ in addition to the temperature structure parameter C_T. This paper extends the work of several Russian authors to the point of calculating both intensity and angle of arrival fluctuations in the atmospheric windows at 94 and 140 GHz. The calculated results for intensity are compared to experiment for both frequencies, and the angle of arrival calculations for 140 GHz are compared to the experimental work of other authors. Reasonably good agreement is obtained in both cases.

1. INTRODUCTION

Scintillation of electromagnetic energy traversing the turbulent atmosphere is caused by refractive index inhomogeneities in the path that cause phase shifts, giving rise to selective reinforcement or degradation of the energy across the beam. The resulting energy distribution is log normal [7], characterized by a variance σ_ξ^2 that is a function of the degree of atmospheric turbulence. These inhomogeneities also cause angle of arrival fluctuations, depolarization, frequency shift, and thermal blooming; although the latter three effects are thought to be of minor importance in the NMMW spectral region.

Most of the original work on atmospheric turbulence was done in Russia by Chernov [3] and Tatarski [7], who treated mainly optical fluctuations and neglected the effects of absorption on the fluctuation intensity. This approach has worked well for optical wavelengths, as attested by the large number of turbulence papers which show reasonable agreement between theory and experiment. More recently, several other Russian workers have examined the problem of millimeter and submillimeter wave fluctuations; which requires that absorption by atmospheric constituents, mainly water vapor, be considered. This approach was apparently first taken by Izyumov [5] who solved the wave equation using a complex index of refraction to account for absorption and thus obtained expressions for amplitude and phase fluctuations valid for NMMW propagation. This work was refined by Gurvich [4] and by Armand, Izyumov and Sokolov [2], who obtained the reasonably tractable expressions used for calculations in this paper.

2. MILLIMETER WAVE TURBULENCE THEORY

2.1 Intensity Fluctuations

The method used for determining the magnitudes of the amplitude and phase variations of an electromagnetic wave propagating through the turbulent atmosphere consists of solving the scalar wave equation

$$\nabla^2 \psi + k^2 N^2 \psi = 0 \,, \tag{1}$$

under the conditions

$$\begin{aligned} n &= n_0 + \mu \\ m &= m_0 + \nu \end{aligned} \tag{2}$$

where ψ is the wave function, k is the wave number, and N is the index of refraction. To account for index fluctuations, the form of this index is taken to be that of Equation (2), where n and m are the real and imaginary parts of the refractive index, n_0 and m_0 are the mean values of these parts, and μ and ν are the fluctuating parts.

Equation (1) is solved by the method of smooth perturbations which is discussed in detail in Tatarski [7]. The results of solving this equation are the autocorrelation functions R_χ and R_ξ of the fluctuations of

*Editor's Note: Author did not follow the requested procedure for quotation of references.

the amplitude and phase of the wave, as given below:

$$\begin{pmatrix} R_\chi(a,L) \\ R_\phi(a,L) \end{pmatrix} = 2\pi^2 k^2 L \int_0^\infty J_0(qa) \left\{ \phi_\mu(q) \left(1 \mp \frac{k}{q^2 L} \sin \frac{q^2 L}{k} \right) \right.$$

$$\left. \mp \frac{4\nu}{q^2 L} \phi_{\mu\nu}(q) \sin^2 \frac{q^2 L}{2k} + \phi_\nu(q) \left(1 \pm \frac{k}{q^2 L} \sin \frac{q^2 L}{k} \right) \right\} q\,dq. \quad (3)$$

where the upper sign gives amplitude fluctuations and the lower sign gives phase fluctuations. Previously undefined parameters appearing in these equations are:

- a = correlation distance
- L = transmission path length
- q = wavenumber, the integrations are carried out over all wavenumbers
- J_0 = Bessel function of the first kind of order zero
- $\phi_\mu, \phi_{\mu\nu}, \phi_\nu$ = spectra of fluctuations of real and imaginary parts of index and their cross correlation.

Armand et al. [2] state that these spectra are related to the spectra of the temperature and humidity fluctuations by the relations

$$\begin{aligned} \phi_\mu(q) &= \left(\frac{\partial\mu}{\partial T}\right)^2 \phi_T(q) + \left(\frac{\partial\mu}{\partial\rho}\right)^2 \phi_\rho(q) \\ \phi_\nu(q) &= \left(\frac{\partial\nu}{\partial T}\right)^2 \phi_T(q) + \left(\frac{\partial\nu}{\partial\rho}\right)^2 \phi_\rho(q) \\ \phi_{\mu\nu}(q) &= \left(\frac{\partial\mu}{\partial T}\right)\left(\frac{\partial\nu}{\partial T}\right) \phi_T(q) + \left(\frac{\partial\mu}{\partial\rho}\right)\left(\frac{\partial\nu}{\partial\rho}\right) \phi_\rho(q). \end{aligned} \quad (4)$$

where ρ is absolute humidity and T is absolute temperature.

Values of μ and ν suitable for use in Equation (4) have been given by Gurvich [4], who states that:

$$\begin{aligned} \mu &= \left(K_1 \frac{P}{T} + K_2 \frac{e}{T} + K_3(\lambda) \frac{e}{T^2} \right) \times 10^{-6} \\ \nu &= \gamma(P_0, T_0, e_0) \frac{e}{e_0} \frac{T_0^2}{T^2} \frac{P}{P_0} \frac{\lambda}{2\pi} \times 10^{-6} \quad . \end{aligned} \quad (5)$$

where previously undefined parameters are defined below.

- K_1 = 78°K/mb
- K_2 = 72°K/mb
- K_3 = 3.7×10^5 (°K)^2/mb (only weakly dependent on λ)
- P = atmospheric pressure in mb
- e = partial pressure of water vapor in mb
- λ = wavelength of transmitted radiation
- γ = absorption coefficient in neper/km, 1 neper = 4.34 dB
- e_0, P_0, T_0 = stationary values of e, P, T.

The forms of the spectral distributions of fluctuations of temperature and humidity $\phi_T(q)$ and $\phi_\rho(q)$ are taken from Gurvich [4], who gives

$$\phi(q) = \frac{5}{36} \left(\frac{2}{\pi}\right)^{2/3} L_0^{11/3} \frac{\Gamma(5/6)}{\Gamma(2/3)} C^2 (1 + q^2 L_0^2)^{-11/6} \quad (6)$$

The factor C may be either C_T or C_ρ which are the temperature and humidity structure parameters, respectively. However, it will be seen that the integrals corresponding to Equation (3) for angle of arrival calculations do not converge when Equation (6) is used. For this reason a Gaussian "tail" of the form [2]

$$\phi(q) = \frac{5}{36} \left(\frac{2}{\pi}\right)^{2/3} L_0^{11/3} \frac{\Gamma(5/6)}{\Gamma(2/3)} C^2 e^{-q^2 L_0^2/4} \quad (7)$$

was added to ensure convergence. Since Equation (7) is also a legitimate choice for the fluctuation spectrum, no loss of rigor is inherent in this approach.

Now consider again Equation (3). The log amplitude variance of the fluctuations is related to the autocorrelation function $R_\phi(a,L)$ by the equation

$$\sigma_\chi^2 = R_\chi(0,L) \quad .$$

Since $J_0(0) = 1$, the Bessel functions in Equation (3) vanish and the log amplitude variance may be written as

$$\begin{aligned} \sigma_\chi^2 &= \frac{5}{18} \pi^{2/3} L_0^{11/3} \pi^{1/2} k^2 L \frac{\Gamma(5/6)}{\Gamma(2/3)} \\ &\cdot \left\{ I_1 \left[\left(\frac{\partial\mu}{\partial T}\right)^2 C_T^2 + \left(\frac{\partial\mu}{\partial\rho}\right)^2 C_\rho^2 \right] - 4 I_2 \left[\left(\frac{\partial\mu}{\partial T}\right)\left(\frac{\partial\nu}{\partial T}\right) C_T^2 \right. \right. \\ &\left. \left. + \left(\frac{\partial\mu}{\partial\rho}\right)\left(\frac{\partial\nu}{\partial\rho}\right) C_\rho^2 \right] + I_3 \left[\left(\frac{\partial\nu}{\partial T}\right)^2 C_T^2 + \left(\frac{\partial\nu}{\partial\rho}\right)^2 C_\rho^2 \right] \right\} . \end{aligned} \quad (8)$$

where the I's are the integrals

$$\begin{aligned} I_1 &= \int_0^\infty \frac{1}{(1 + q^2 L_0^2)^{11/6}} \left(1 - \frac{k}{q^2 L} \sin \frac{q^2 L}{k} \right) q\,dq \\ I_2 &= \int_0^\infty \frac{1}{(1 + q^2 L_0^2)^{11/6}} \cdot \frac{k}{q^2 L} \sin^2 \frac{q^2 L}{2k} \, q\,dq \\ I_3 &= \int_0^\infty \frac{1}{(1 + q^2 L_0^2)^{11/6}} \left(1 + \frac{k}{q^2 L} \sin \frac{q^2 L}{k} \right) q\,dq \quad . \end{aligned} \quad (9)$$

and where Equations (3), (4), and (6) are used. These integrations may be performed numerically using parameters measured in field experiments to obtain results for comparison. These comparisons will be discussed in a later section.

It should be noted that these results are obtained subject to the inequality $L \ll L_0^4/\lambda^3$,

where ℓ_0 is inner scale dimension and λ is wavelength. This criterion may not be well met for the longer millimeter waves, but the results discussed in Section 3 indicate that this limitation is not severe.

2.2 Angle of Arrival Fluctuations

The angle of arrival of an electromagnetic wave may be defined as the normal to the wavefront at any point. Fluctuations in angle of arrival are caused by refractive index inhomogeneities that cause phase shifts resulting in constructive and destructive interference across the wavefront of the beam, causing the localized angle of the wavefront normal to change relative to the line of sight to the transmitter.

Using the above definition, Strohbehn and Clifford [6] have derived an expression for the angle of arrival of an electromagnetic wave in turbulence based on the phase correlation function $R_\phi(a,L)$ given by the lower signs of Equation (3). Consider a wavefront propagating in the direction $\hat{n}$ which is nominally in the x-direction. The angles with the x-axis and with the x-y plane are θ and ϕ respectively. Now consider the placement of two receivers in the plane $x = L$. The angle α is the angle which the line between these receivers makes with the y-axis, and a is the distance between them. Using this geometry, Strohbehn and Clifford show in a very straightforward way that the correlation functions between these two receivers for angle fluctuations of θ and ϵ are, respectively

$$R_\theta(a,L) = -\frac{1}{k^2} R_\phi''(a,L)\cos^2\alpha - \frac{1}{k^2 a} R_\phi'(a,L)\sin^2\alpha \quad .$$
$$R_\gamma(a,L) = -\frac{1}{k^2} R_\phi''(a,L)\sin^2\alpha - \frac{1}{k^2 a} R_\phi'(a,L)\cos^2\alpha \quad . \qquad (10)$$

where the primes denote diffrentiation with respect to a. The only a-dependent term in the expression for $R_\phi(a,L)$ is the Bessel function $J_0(qa)$. Using the rules for differentiation of Bessel functions and assuming a point receiver which implies that a = 0 gives

$$R_\theta(0,L) = \sigma_\theta^2 = R_\theta(0,L) + R_\gamma(0,L) = -\frac{1}{k^2} R_\phi''(0,L) \quad . \qquad (11)$$

Substituting this result into Equation (3) gives

$$R_\theta(0,L) = \pi^2 L \int_0^\infty \left[\Phi_n(q)\left(1 + \frac{k}{q^2 L}\sin\frac{q^2 L}{k}\right) + \frac{\delta k}{q^2 L}\Phi_{nn}(q)\sin^2\frac{q^2 L}{2k} + \Phi_n(q)\left(1 - \frac{k}{q^2 L}\sin\frac{q^2 L}{k}\right)\right] q^3 dq \quad . \qquad (12)$$

Using this result, essentially all that must be done in evaluating the angle of arrival variance is to perform the integrals of Equations (9) with q replaced by q^3, as a result of the differentiation with respect to a. These integrals will be evaluated numerically and compared to measured results of other authors in the next section.

3. COMPARISON OF MEASURED AND CALCULATED RESULTS

In the fall of 1978, millimeter wave propagation measurements were made at both 94 and 140 GHz at White Sands Missile Range, New Mexico over a 2 km path. The index of refraction structure parameter C_n was also measured, together with other pertinent meteorological parameters. Strong intensity fluctuations were observed at both frequencies during these tests. A typical calibration run showing fluctuations at 94 GHz is shown in Figure 1.

Unfortunately, equipment was not available during these tests for measurement of the absolute humidity structure parameter C_ρ, so that it was necessary to assume a value for this important quantity before comparisons between theory and experiment could be made. The value assumed was $C_\rho = 1.45 \times 10^{-4}$ $m^{-1/3}$ g/m^3 which was chosen to give good agreement with the level of fluctuation measured during the initial series of propagation measurements at 94 GHz. It will be seen that this choice gives only fair agreement for the other 94 GHz measurements but good agreement for the 140 GHz measurements. Table I summarizes the parameters used in calculations of intensity and angle of arrival fluctuations at both 94 and 140 GHz. The values of C_T used in these calculations were obtained from the measured values of C_n^2 by using the equation

$$C_T = \frac{C_n^2 T^2}{79P} \times 10^{-6} \quad . \qquad (13)$$

Using the parameters defined above, and the approach discussed in the last section, peak-to-peak intensity fluctuations as a function of C_T were calculated for both 94 and 140 GHz. These results are shown in Figures 2 and 3 respectively in which the circles represent measured data and the solid curve shows calculated results. Similarly, angle of arrival fluctuations were calculated, and the results are shown in Figure 4. Since these fluctuations were not measured, the calculations for 140 GHz are compared to the results of Andreyev et al. [1], who measured 150 GHz fluctuations over a 5 km path, and obtained peak-to-peak levels of 0.49 mrad. This value compares favorably with the range of 0.34 to 0.53 mrad shown in Figure 4. Unfortunately, the conditions under which these measurements were made are not specified. Furthermore, no 94 GHz data are available, although Figure 4 shows that the frequency dependence is not strong.

TABLE 1

Values of Parameters Used in Calculations

PARAMETER	VALUE
P	1013 mb
e	10.7 mb
λ	3.19, 2.14 mm
γ	0.092 neper/km (94 GHz) 0.346 neper/km (140 GHz)
T	289°K
e_o	9.45 mb
P_o	1013 mb
T_o	293°K
C_ρ	1.45×10^{-4} g/m^3 . m$^{-1/3}$

4. CONCLUSIONS

To briefly review the approach, the scalar wave equation was solved under the conditions in which both real and imaginary parts of the index of refraction are fluctuating. Atmospheric parameters measured during the White Sands propagation tests were then substituted into the solutions to these equations to obtain calculated results for both intensity and angle of arrival fluctuations. Finally, the calculated fluctuation intensity results were compared to the measured results, and the calculated angle of arrival errors were compared to those measured by Andreyev, et al. [1]. Based on these comparisons, it is concluded that millimeter and submillimeter wave turbulence theory is substantially correct, and is able to give useful answers for systems calculations. At the same time, it is conceded that the data base for these comparisons is small, and results should be used with caution until a broader base is obtained. Intensity fluctuations are not considered likely to greatly affect millimeter wave systems except at the extreme limits of performance, but angle of arrival variations are of the same order of size as the required angular accuracy of many systems, and are therefore expected to be of some significance.

REFERENCES

1. Andreyev, G. A., V. A. Golunov, A. T. Ismailov, A. A. Parshikov, B. A. Rozanov, and A. A. Tanyigin, 1977: Intensity and angle of arrival fluctuations of millimetric radiowaves in turbulent atmosphere. Joint Anglo-Soviet Seminar on Atmospheric Propagation at Millimetre and Submillimetre Wavelengths, Institute of Radioengineering and Electronics, Moscow, November 1977.
2. Armand, N. A., A. O. Izyumov, and A. V. Sokolov, 1971: Fluctuations of submillimeter waves in a turbulent atmosphere. Radio Eng. Elect. Phys., 16, No. 8, 1257-1266.
3. Chernov, L. A., 1960: Wave Propagation in a Random Medium. McGraw-Hill Book Co., New York, Chapter 5.
4. Gurvich, A. S., 1968: Effect of absorption on the fluctuation in signal level during atmospheric propagation. Radio Eng. Elect. Phys., 13, No. 11, 1687-1694.
5. Izyumov, A. O., 1968: Amplitude and phase fluctuations of a plane monochromatic submillimeter wave in a near-ground layer of moisture-containing turbulent air. Radio Eng. Elect. Phys., 13, No. 7, 1009-1013.
6. Strohbehn, J. W. and S. F. Clifford, 1967: Polarization and angle of arrival fluctuations for a plane wave propagated through a turbulent medium. IEEE Trans. Ant. Prop., AP-15, 416-421.
7. Tatarskii, V. I., 1961: Wave Propagation in a Turbulent Medium. McGraw-Hill Book Co., New York, Chapter 7.

Acknowledgment: This work was supported by the US Army Atmospheric Sciences Laboratory and by Bateile Columbus Laboratories under Contract No. DAAG29-76-D-0100.

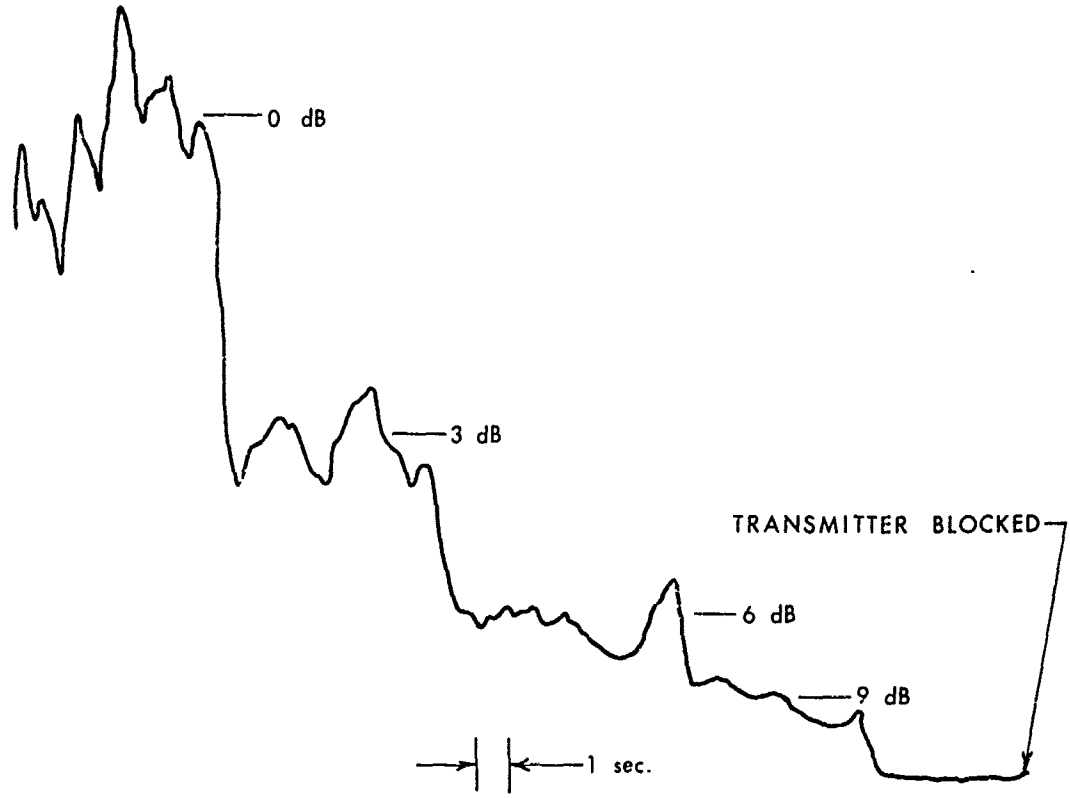

Figure 1. Fluctuations Measured During a Typical Calibration Run. Note the Absence of Fluctuations with the Transmitter Blocked.

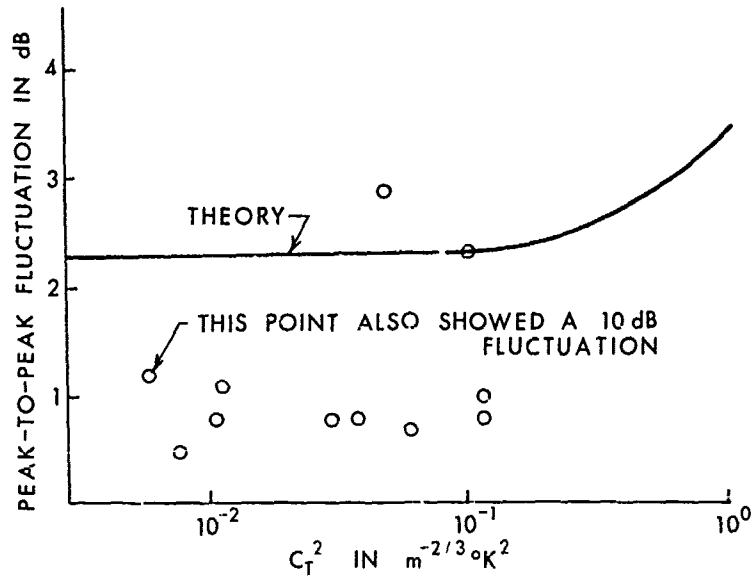

Figure 2. Peak-to-Peak Intensity Fluctuations vs. C_T^2 at 94 GHz. Values of Parameters Used for Calculation Are as Follows: L_0=1.5m, T=288.8k, ρ=8.5g/m^3, and C_ρ=1.45x10^{-4}m$^{-1/3}$g/m^3. Measured Results Are Shown as Circles.

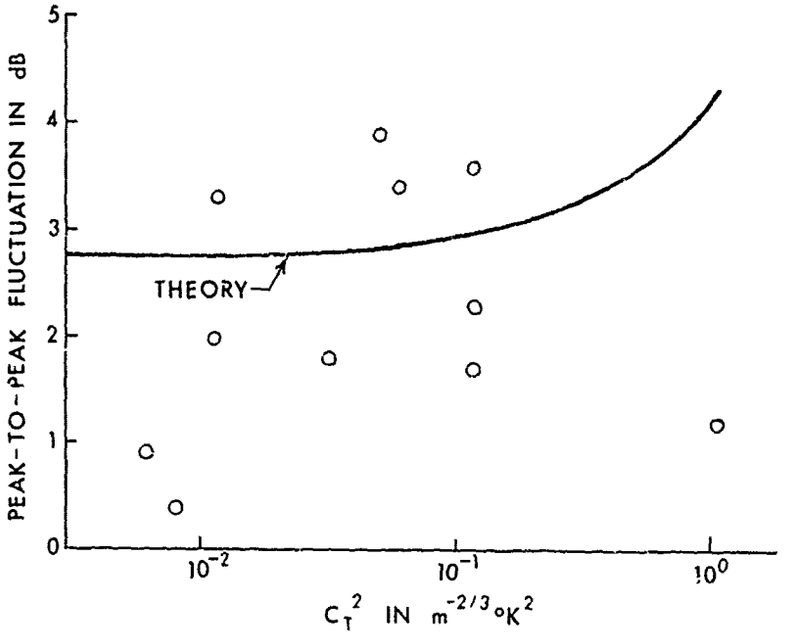

Figure 3. Peak-to-Peak Intensity Fluctuations vs. C_T^2 at 140 GHz, Parameters Used for Calculations are the Same as for Figure 2. Measured Results are Shown as Circles.

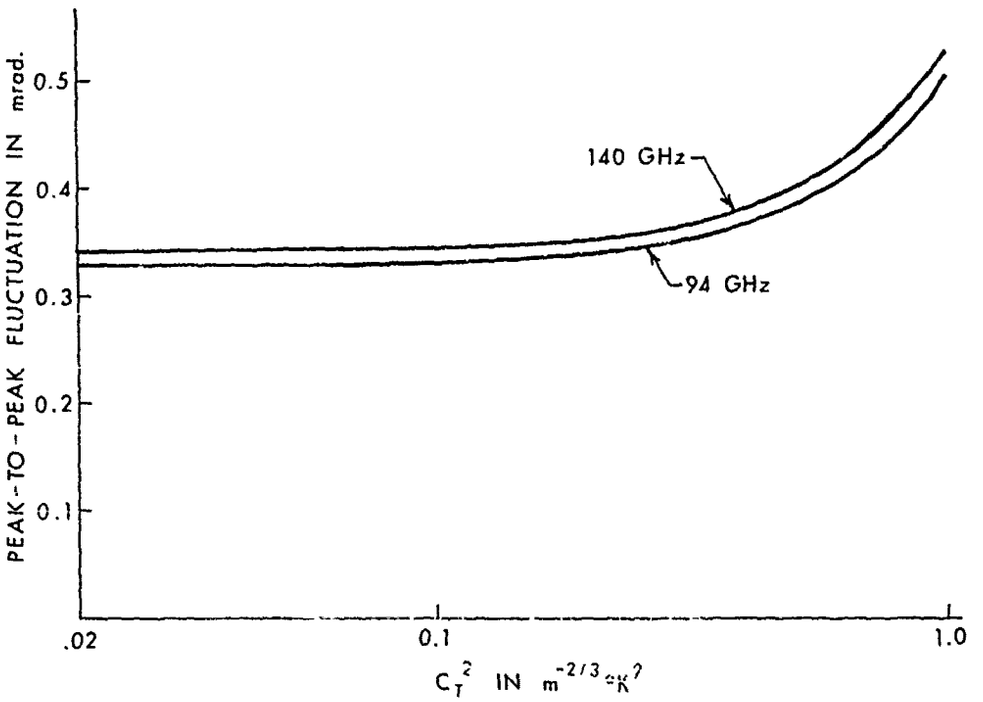

Figure 4. Calculated Angle of Arrival Fluctuations vs. C_T^2. The Conditions are the same as those used for Figures 2 and 3.

GAIN DEGRADATION AND AMPLITUDE SCINTILLATION DUE TO TROPOSPHERIC TURBULENCE

Dr. David M. Theobold

Lockheed Missiles & Space Company, Inc.

Sunnyvale, California

ABSTRACT

Mean signal levels well below those predicted by standard techniques on low elevation earth-space microwave links have been observed and reported previously. Additionally, amplitude fluctuations under clear air conditions accompany these reduced signal levels and increase significantly as elevation angle decreases. It is shown that a simple physical model is adequate for the prediction of the long term statistics of both reduced signal levels and increased peak-to-peak fluctuations.

It is hypothesized that a plane wave propagating through the troposphere is perturbed by the two coupled statistical processes of angle of arrival and amplitude fluctuation. This perturbed plane wave is then received by a finite aperture antenna having a Gaussian power pattern. The average realized gain is then calculated accounting for the angle of arrival fluctuations. The resulting average gain degradation, when combined with the usual atmospheric gas absorption, adequately predicts the reduced long term signal levels observed at low elevation angles on earth-space paths at 2, 7.3, and 30 GHz. The expected value of the variance of the received signal amplitude fluctuations is calculated by combining the amplitude and angle of arrival statistics of the incident wave with the receiver characteristics. This model predicts the average variance of signals observed under clear air conditions at low elevation angles on earth-space paths at 2, 7.3, 20, and 30 GHz.

Design curves based on this model for gain degradation, realizable gain, and amplitude fluctuation as a function of antenna aperture size, frequency, and either terrestrial path length or earth-space path elevation angle are presented.

1. INTRODUCTION

Millimeter waves propagating through the turbulent troposphere are subject to refractive effects caused by macroscopic and fine scale characteristics. Macroscopic characteristics of the atmosphere are thought of on time scales on the order of minutes and longer and on spatial scales of several kilometers and larger. They result in phenomena such as:

- o Average apparent angle of arrival changes
- o Ducting and atmospheric multipath fading
- o Diurnal and seasonal propagation variation
- o Changes in average propagation velocity

Fine scale characteristics of the atmosphere are considered to be on time scales shorter than a minute and on spatial scales shorter than a kilometer. They result in phenomena such as:

- o Amplitude fluctuations (scintillation fading)
- o Angle of arrival fluctuations (local fluctuation in wavefront normal)
- o Phase fluctuations
- o Phase delay variations
- o Gain degradation

The effect of fine scale characteristics on a communications link from the standpoint of received signal amplitude fluctuation and gain degradation has been modelled and is available for link design purposes.

2. AMPLITUDE FLUCTUATION

The phenomena of amplitude and angle-of-arrival fluctuations combine to form received signal amplitude fluctuations. The theory of wave propagation and scattering in random media allows a combination of the turbulence-induced effects to be performed in the context of weak fluctuation along a line-of-sight path. The work of Akira Ishimaru (1978), which defines coherent and incoherent field components as a plane wave propagates through a random medium, provides a method of combining amplitude and angle of arrival effects into a model of received signal amplitude fluctuation. Energy is transferred from a coherent component, which fluctuates in amplitude and is deterministic in angle of arrival, into an

incoherent component, which is deterministic in amplitude and fluctuater in angle of arrival. A model utilizing this concept of incident plane wave decomposition (Figure 1) has been proposed by Theobold and Hodge (1978).

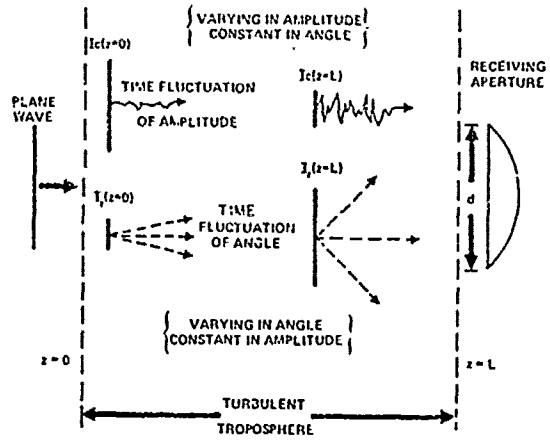

Figure 1. Decomposition into coherent and incoherent components.

The assumption of weak turbulence, i.e., log-amplitude variance $\sigma^2_x < 0.5$, is invoked for a plane wave incident on a region of turbulence, propagating a distance L (km) and impinging on a circular aperture of diameter d (meters). The antenna is assumed to have a Gaussian pattern function with half-power beamwidth B (degrees). If V is received signal amplitude, an expression for signal variance relative to average power is

$$S^2 = 10 \log_{10} \frac{\langle V^2 \rangle - \langle V \rangle^2}{\langle V \rangle^2}$$

$$S^2 = 10 \log_{10} \frac{I_c \sigma_1^2 + \frac{I_i B^2}{8 \ln(2) \sigma_2^2 + B^2} - I_i \left(\frac{B^2}{4 \ln(2) \sigma_2^2 + B^2} \right)^2}{I_c + I_i \left(\frac{B^2}{4 \ln(2) \sigma_2^2 + B^2} \right)^2}$$

where

$I_i = 1 - \exp(-L/L_o)$

$I_c = (1 - I_c) / (1 + \sigma_1^2)$

σ_1^2 = amplitude variance

σ_2^2 = angle-of-arrival variance (deg^2)

L = path length

L_o = a function of density and cross-section of scattering along the path.

Measurements at the Ohio State University (O.S.U.) of the ATS-6 2, 20, and 30 GHz beacons as the satellite underwent synchronous orbit transition were used to derive empirical constants for this model with an effective turbulence height, h, of 6 km and path length

$$L = \left[h^2 + 2 r_c h + (r_c \sin\theta)^2 \right]^{1/2} - r_c \sin\theta$$

assumed. The constants are

$L_o = 180$ km

$\sigma_1^2 = 2.6 \times 10^{-7} \, f(GHz)^{7/12} \, L(km)^{11/6}$

$\sigma_2^2 = 5.67 \times 10^{-6} \, L(km)^{1.56} \, d(m)^{-1/3}$.

A plot of the variance measure S^2, expressed in dB, is shown in Figure 2 for four representative frequencies for a 4.6 m diameter aperture. S^2 is plotted as a function

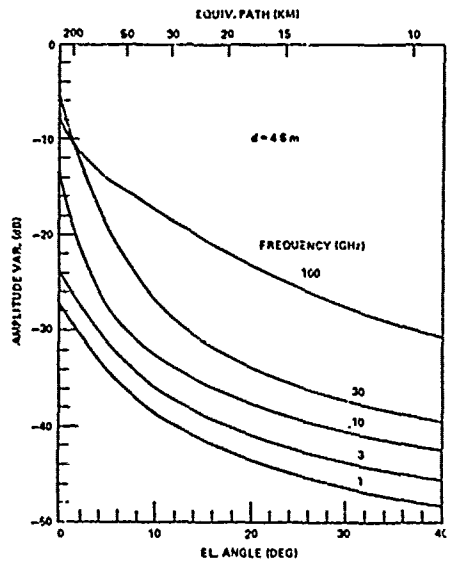

Figure 2. Amplitude Variance for a 4.6 m Diameter Aperture.

of elevation angle and equivalent path length for a 6 km high region of turbulence. Figure 2 represents the average S^2 as derived from the O.S.U. empirical constants. However, since both σ_1^2, and σ_2^2 may be represented in closed form as a function of the atmospheric structure constant C_n^2, instantaneous, diurnal, or seasonal values for S^2 may be found from this model given an estimate of the appropriate C_n^2.

The empirical constants which were found from observed data are applicable for the prediction of average turbulence-induced propagation effects in a temperate climate, during the warmer seasons of the year, and under non-precipitating clear-air conditions.

3. RECEIVED SIGNAL GAIN DEGRADATION

Wavefront tilt or angle of arrival variation results in time-averaged gain degradation; and phase incoherence across an aperture results in instantaneous gain loss, excluding the atmospheric gas loss.

The model of Section 2 for received signal amplitude variance has also been used to derive an expression for gain reduction, R, defined by

$$R = 10 \log_{10} \frac{\langle V \rangle^2}{\langle V \rangle^2_{\text{no angle fluctuation}}}$$

$$R = 10 \log_{10} \frac{I_c + I_i \left(\frac{B^2}{4 \ln(2) \sigma_\theta^2 + B^2} \right)^2}{I_c + I_i}$$

where the constants are the same as those defined for the variance expression, S^2. This value for R may then be combined with atmospheric gas loss in order to obtain an estimate of average received signal level for an earth-space path. Figure 3 presents an example of predicted signal levels for 2, 7.3, and 30 GHz for antenna beamwidths of 1.8°, 0.3°, and 0.15°, respectively. Also

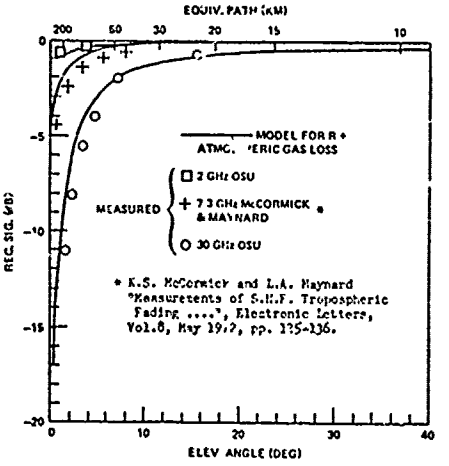

Figure 3. Predicted and Measured Signal Level as a Function of Elevation Angle.

included are measured signal levels, relative to zenith, from the ATS-6 and 30 GHz and TACSATCOM 7.3 GHz beacons as the satellites were moving in elevation angle.

4 DESIGN INFORMATION

The estimates of gain reduction and signal variance parameters, R and S^2, have been presented. These quantities may be incorporated into distribution functions which are of the form used in link design. They represent the long term average fade statistics due to clear air amplitude and angle of arrival fluctuations.

For a log-normal distribution of turbulence induced amplitude fading, the long term median is R (dB) and one standard deviation, σ_v(dB), from the median may be easily shown to be $\sigma_v(\text{dB}) = 20 \log_{10} e \times 10^{-S^2/20}$.

The effects of amplitude and angle-of-arrival fluctuation are, of course, most prominent for very long path lengths and/or very narrow beamwidths. One may estimate whether or not gain degradation need be considered in a path design if elevation angle (or equivalent path length) and antenna beamwidth are known. Figure 4 presents regimes where gain degradation must be considered.

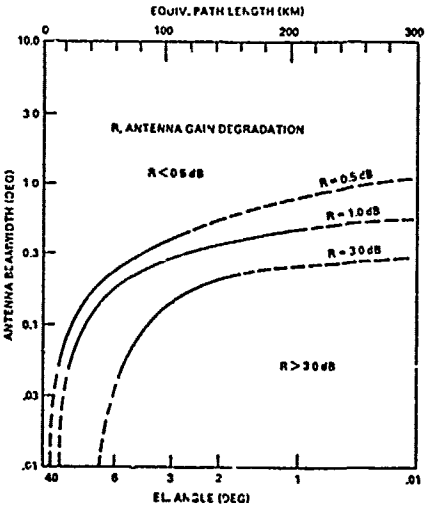

Figure 4. Gain Degradation Regimes as a Function of Beamwidth and Elevation Angle.

Realized gain, that is, expected gain less gain degradation, is plotted as a function of antenna beamwidth (for any frequency) or equivalent aperture diameter at 30 GHz in Figure 5. All equivalent aperture diameters are presented for an antenna aperture efficiency of 0.6. The curve representing zero path length L is simply the common gain approximation $G = 41253/B^2$, where B is in degrees. Realized gain curves for path lengths of 50 to 300 km are plotted using the previous model. Equivalent earth-space path elevation angles assuming a 6 km high homogeneous atmosphere are presented in parentheses. Notice

that gain degradation due to turbulence-induced

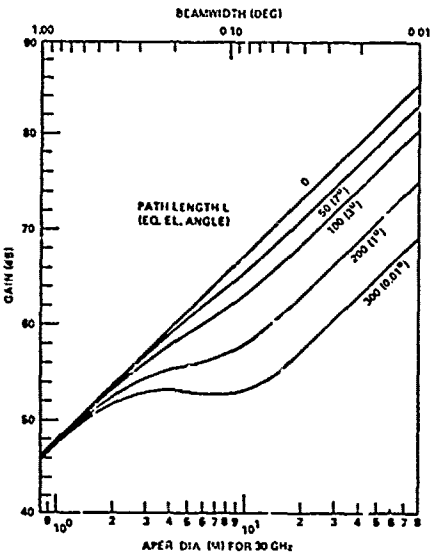

Figure 5. Realized Gain.

fluctuation is negligible for beamwidths wider than about 0.7^{o} for all path lengths. Degradation effects then gradually increase as beamwidth narrows from 0.7^{o} to 0.05^{o} and at any particular beamwidth are approximately directly proportional, in dB, to path length. As beamwidth narrows beyond 0.05^{o}, a saturation effect occurs and the degradation becomes constant for any one path length.

REFERENCES

Ishimaru, A., 1978: Wave Propagation and Scattering in Random Media, Vol. 2. Academic Press, New York.

McCormick, K. S. and L. A. Maynard, 1972: Measurements of S.H.F. tropospheric fading along earth-space paths at low elevation angles. Electron. Lett., 8, 274-276.

Theobold, D. M. and D. B. Hodge, 1978: Gain Degradation and Amplitude Scintillation due to Tropospheric Turbulence. The Ohio State University ElectroScience Lab. Tech. Rept. 784299-6. Prepared under NASA contract NAS5-22575.

EXPERIMENTAL SUBMILLIMETER LASER SYSTEM AND ITS APPLICATION TO ABSORPTION MEASUREMENTS IN BATTLEFIELD GASES AND WATER VAPOR

Brent L. Bean* and Kenneth O. White

Atmospheric Sciences Laboratory

White Sands Missile Range, New Mexico

ABSTRACT

A submillimeter laser spectrometer has been constructed for use in measuring the absorption of various atmospheric gases. A description is given of the basic laser design, its operation, overall stability, and the frequencies available in the 5 cm^{-1} to 100 cm^{-1} region. The use of the laser source with various spectrophones is discussed and evaluated. In particular, these discussions address applying this system to absorption measurements of water vapor for the determination of temperature and pressure dependencies, line shape information, and dimer/cluster contributions, as well as the absorption of battlefield gases including explosion products such as formaldehyde and hydrogen cyanide. Theoretical predictions of the absorption of typical battlefield gases are presented.

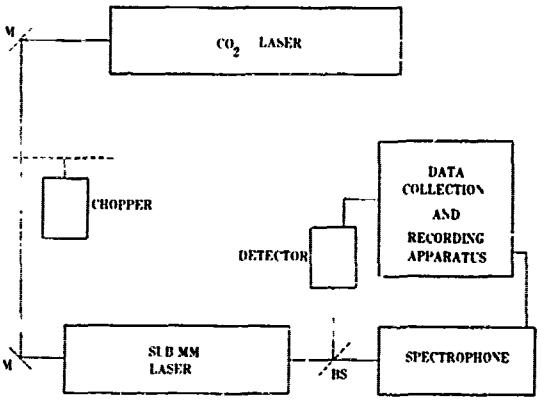

FIGURE 1. Block diagram of the experimental apparatus.

1. INTRODUCTION

The atmospheric window in the submillimeter region of the spectrum has stimulated an interest in the exact nature of the absorption there. Several explanations have been proposed to account for the difference between the theoretical and experimental values for the continuum absorption of water vapor in that region, including dimers, water clusters, and far wing line shapes (Burch, 1968; Gebbie et al., 1971). The experiment described here has been designed to provide useful information in order to determine the exact nature of the water vapor absorption and also to investigate the absorption of other gases that are generated in a battlefield environment.

2. LASER SYSTEM

2.1 CO_2 Laser

The basic experimental apparatus is shown in the diagram in Fig. 1. The CO_2 laser output is used to optically pump the SUB MM laser media. The SUB MM output is directed to a detector and a spectrophone. The signals from those two devices are fed into the data collection apparatus. The CO_2 laser is a commercial device that produces 25-40 Watts on most of the pertinent output lines. It is equipped with a piezoelectric drive on one mirror in order to fine tune the CO_2 emission. If a detector is placed between the chopper and SUB MM laser, the signal can be used as part of a feedback loop to stabilize and maximize the CO_2 output. However, the SUB MM output can often be improved by tuning the CO_2 laser away from the emission line center in order to maximize the absorption in the SUB MM laser medium. If the signal from the detector monitoring the SUB MM output is directed into the feedback system, then the CO_2 laser is maintained for optimum SUB MM lasing.

2.2 SUB MM Laser

A drawing representing the SUB MM laser is shown in Fig. 2. It consists of a vacuum chamber with a NaCl input window set at Brewster's angle and a crystal quartz output window. The cavity consists of a cylindrical metallic or dielectric waveguide with a gold coated copper mirror at the input end and a coated Si mirror for the output coupler. The input mirror has a 3-4 mm diameter hole to pass the CO_2 pump beam and the Si substrate is

*Science Applications, Incorporated White Sands, New Mexico

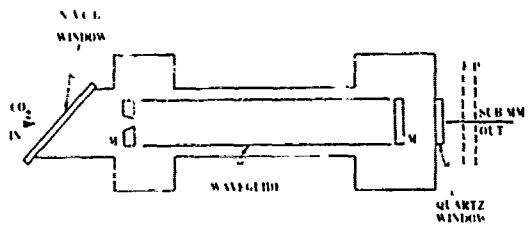

FIGURE 2. Diagram of the SUB MM laser and the Fabry-Perot interferometer (F-P).

coated with a gold annular ring with a 6-8 mm diameter hole to pass the SUB MM output. The hole is covered by a dielectric coating which is greater than 98% reflective for the CO_2 radiation. Thus the output coupler is highly reflective for the pump radiation but only partially reflective for the SUB MM over its central portion. The CO_2 beam is focussed by a long focal length lens which enables the radiation to make two or more passes before it strikes the walls of the waveguide; a feature which is important for efficient pumping. The output mirror is mounted on a translation stage in order to tune the laser to resonance for the desired frequency, (Hodges et al., 1977). The Fabry-Perot interferometer at the output end is constructed to accept various sets of metal mesh reflectors for optimum operation over the SUB MM range (Fenk and Genzel, 1962). It is used to measure the wavelength of the laser emission and to act as a filter when two or more frequencies are emitted simultaneously.

Figure 3 shows the water vapor absorption curve with vertical bars along the abscissa indicating the location of reported SUB MM

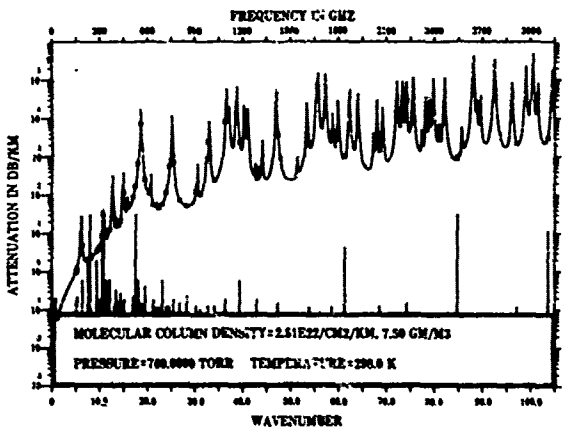

FIGURE 3. Water vapor absorption curve. The X marks on the curve indicate the position of the SUB MM laser lines shown by the vertical lines.

laser lines with the length being proportional to the output power. The maximum power for the strong laser lines is on the order of several mWatts. These laser lines are among the strongest listed for methanol, methyl chloride, methyl iodide, formic acid, methyl bromide, 1,1 difluoroethylene, and methanol-d CH_3OD. This figure illustrates that there is good spectral coverage with these few laser media especially in the low frequency region.

3. SPECTROPHONE

Using a spectrophone as the device to measure the absorption offers some distinct advantages over the use of a long, bulky transmission cell (Kreuzer, 1971). The relatively small size of the spectrophone makes it much easier to change the parameters for temperature and pressure measurements. Another advantage is that the signal which is obtained from the spectrophone is proportional to the absorption coefficient even for weak or strong absorptions, in which cases measurements are very difficult using transmission cells.

Figure 4 illustrates the general features of a spectrophone (Bruce, 1976). A collimated beam enters through the Brewster's angle window and propagates along the axis of the spectrophone. The acoustic traps near the ends are to help eliminate noise originating at the windows. The entire volume is filled with the sample gas which, when it absorbs the radiation, decays by non-radiative processes causing an increase in temperature and, consequently pressure. The pressure increase is sensed by the microphone which produces a signal proportional to the absorption coefficient. The spectrophone can be calibrated to yield absolute values by using a gas with known absorption coefficients. These devices may be constructed with enough sensitivity to measure an absorption coefficient of 10^{-3} km^{-1} per watt of input radiation.

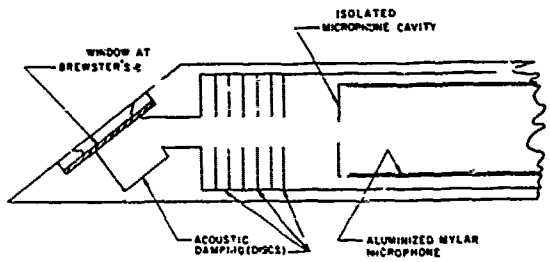

FIGURE 4. Diagram of a spectrophone. This design uses a cylindrical microphone to sense the pressure change.

Figure 5 is a diagram of another type of spectrophone (Schleusener et al., 1975). Two identical chambers are sandwiched between the

three windows. If an absorbing sample is placed in one chamber a differential pressure will be detected. This type works well for absorption measurements of particulates since identical pellets can be made with only one containing the sample. The pellets are constructed from relatively highly transparent material with the sample deposited on or imbedded into one of them. When these pellets are put into the two chambers, only the absorbtion due to the particulates contributes to the signal since all other effects are common to both sides. The spectrophone has the desirable feature of measuring only the absorption of particulates since the scattering does not contribute to the signal.

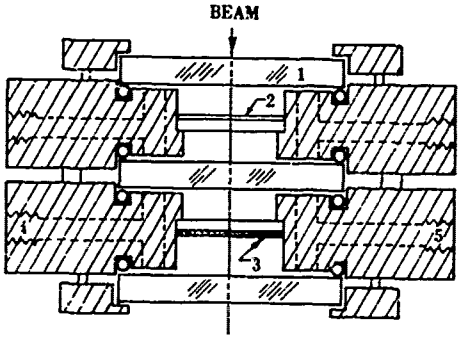

1. WINDOW
2. BLANK PELLET
3. SAMPLE PELLET
4. GAS FILLING AND EVACUATION PORT
5. PRESSURE SENSOR PORT

FIGURE 5, Diagram of a spectrophone which utilizes a differential pressure device to measure the signal

4. BATTLEFIELD GAS

In addition to water vapor and particulates in a battlefield situation, there are also gases that are generated due to explosives, burning vegetation, and other causes that may affect SUB MM propagation (Cook, 1958 and Leslie, 1979). Table 1 gives a partial list of gases produced under various battlefield conditions that may have significant effects on the SUB MM region either because of high concentrations or strong absorptions. All of these explosives are made from carbon, oxygen, nitrogen, hydrogen molecules so the resulting gases are also composed of those four elements.

It is difficult ot determine the value of the absorption coefficient for the gases because the amounts produced are not well known. Table II shows some peak absorption coefficients in km^{-1}/ppm. These must be multiplied by parts per million to yield a useful absorption coefficient for calculation purposes. A typical barage of explosives could be expected to yield 9 ppm of CO, 3.7 ppm of CH_3OH, 3.3 ppm of HCN, and .4 ppm of CH_2O contained in a 1 km by 1 km by 60 m volume (Leslie, 1979).

TABLE I. List of gases generated under various battlefield conditions. The explosives are those commonly used by U.S. and foreign military forces when large quanities are needed.

ORIGIN	GASES PRODUCED
Explosives (TNT, RDX, Amatol, and Composition B)	Carbon monoxide -CO Methanol $-CH_3OH$ Hydrogen cyanide-HCN Formaldehyde $-CH_2O$
Burning Foliage	Carbon monoxide -CO Methanol $-CH_3CH$
Vehicle Exhaust, Artillery Propellants Buring Fuel, etc.	Carbon monoxide -CO Hydrogen cyanide-HCN Butadiene $-C_4H_6$
Shock Heated Air	Ozone $-O_3$ Nitrogen oxides $-NO_x$

Even though there is uncertainty concerning the exact amounts of the above gases that are produced in a typical battlefield environment, it appears that the absorption values are high enough to warrant further studies.

TABLE II. List of peak absorption coefficients for several lines in the SUB MM region.

CO		CH_3OH	
$\gamma(cm^{-1})$	$\alpha(km^{-1}/ppm)$	$\gamma(cm^{-1})$	$\alpha(km^{-1}/ppm)$
7.69	3.1×10^{-4}	4.84	.04
15.38	2.1×10^{-3}	5.60	.01
23.06	6.1×10^{-3}	5.67	.02
30.75	1.1×10^{-2}	6.10	.10
34.59	1.3×10^{-2}	6.62	.10

CH_2O		HCN	
$\gamma(cm^{-1})$	$\alpha(km^{-1}/ppm)$	$\gamma(cm^{-1})$	$\alpha(km^{-1}/ppm)$
4.70	.03	5.91	.076
5.02	.04	11.83	.61
7.29	.46	17.74	2.1
9.39	.68	23.65	4.9
9.72	1.60	32.52	12.7

REFERENCES

Bruce, C., 1976: Development of Spectrophones for CW and Pulsed Radiation Sources. U. S. Army Electronics Command Research and Development Technical Report, ECOM-5802.

Burch, D. E., 1968: Absorption of Infrared Radiant Energy by CO_2 and H_2O. III. Absorption by H_2O between 0.5 and 36 cm^{-1} (278μm - 2 cm). J. Opt. Soc. Am., 58, 1383-1394.

Cook, M. A., 1958: The Science of High Explosives. Reinhold Publishing Corp.

Cebbie, H. A., R. A. Bohlander, and G. W. F. Pardoe, 1971: Submillimeter Wave Absorption Anomalies in the Lower Atmosphere and the Existence of Water Dimers. Nature, 230, 521-522.

Hodges, D. T., F. B. Foote, and R. D. Reel, 1977: High-Power Operation and Scaling Behavior of CW Optically Pumped FIR Waveguide Lasers. IEEE J. Quant. Elect., QE-13, 491-494.

Kreuzer, L. B., 1971: Ultralow Gas Concentration Infrared Absorption Spectroscopy. J. Appl. Phys., 42, 2934-2943.

Leslie, D. H., 1979: Submillimeter Wavelength Absorption due to Battlefield Gas. To be published by Science Applications, Inc., 15 Research Drive, Ann Arbor, Michigan 48103. Report No. SAI-79-004-AA.

Renk, K. F., and L. Genzel, 1962: Interference Filters and Fabry-Perot Interferometers for the Far Infrared Appl. Opt., 1, 643-648.

Schleusener, S. A., J. D. Lindberg, and K. O. White, 1975: Differential Spectrophone Measurements of the Absorption of Laser Energy by Atmospheric Dust. Appl. Opt., 14, 2564-2565.

ATMOSPHERIC INFLUENCES ON PASSIVE MILLIMETER-WAVE SEEKERS: MEASUREMENTS, MODELING, AND SYSTEMS APPLICATIONS

Dr. Kenneth P. Bechis
The Analytic Sciences Corporation
Reading, Massachusetts

ABSTRACT

The overall effectiveness of millimeter-wave radiometry in passive missile guidance and target detection systems is influenced principally by atmospheric effects on signal propagation and on the contrast brightness temperatures between targets and their surroundings. The attenuating effects of clouds, rain and other aerosols, along with atmospheric molecular resonant absorption lines, must be considered in predicting the effectiveness of both up- or down-looking mm-wave radiometric systems. This paper presents measurements of various sky brightness temperatures and attenuations through clear sky, various cloud covers, and precipitation (made with the University of Massachusetts 13.7-m mm-wave radio telescope). This paper also describes a very flexible mathematical model and FORTRAN program (at The Analytic Sciences Corporation (TASC)) capable of predicting the performance of a passive up- or down-looking radiometer at any altitude, zenith or nadir angle, in any weather environment, and for any postulated target.

Possible system applications include airborne all-weather seekers for passive detection of ground targets; long-range passive ground or ship-board detection of approaching low-altitude aircraft or missiles; or, high-altitude all-weather wide field-of-view passive detection of lower-altitude aircraft or missiles. Specific examples will be presented.

1. INTRODUCTION

The first part of this paper describes various atmospheric attenuation measurements and techniques at the University of Massachusetts (Amherst) Radio Astronomy Observatory. Computer codes developed for these measurements are also described. The second part of the paper depicts how these computer codes, as well as additional corroborating measurements made at the University of Massachusetts, have been incorporated at TASC into much larger system-modeling codes for various passive millimeter-wave seeker guidance systems.

It is hoped that the users of millimeter-wave atmospheric attenuation computer models realize that, no matter how complex the coding is, no matter how many naturally-occurring atmospheric molecular resonance lines are included (even all 6000 or so H_2O lines between 1.35 cm and 3 μm), these models will never predict exactly the propagation conditions on any particular day. The clear-sky programs model an ideal, static, homogeneous (in azimuth for a set elevation angle) atmosphere. Systems planners should realize that at a certain frequency, the exact attentuation along one line-of-sight may be up to 30% different from that along another line of sight, at a different azimuth but the same elevation angle, even in clear sky and at times when the human eye and/or a visible-light transmissometer would detect no difference between the two paths. The atmosphere is locally inhomogeneous, and there may be, for example, "invisible clouds" -- volumes of air where the water-vapor content is locally enhanced, but not so much as to produce a visibly-opaque cloud.

A final prefatory note, regarding the so-called "anomalous absorption" reported by some observers at ~110 GHz in excess of theoretical attenuation predictions. This phenomenon, reported to be prominent during cold weather or high humidity, and often varying significantly on a day-to-day basis, has been attributed to an as yet unknown effect of water vapor, water dimers, or some other molecules. It should be noted that no one in the radio astronomy community has ever commented on, let alone measured, anomalous absorption. However, millimeter-wavelength radio astronomers are acutely aware of the inhomogeneities of the atmosphere, particularly in terms of upper air flow (laminar or turbulent) and pockets of water vapor, as well as the low-frequency (~10^{-5} Hz) atmospheric waves in the vicinity of the tropopause (in part a creation of the global atmospheric heat circulation from the equator toward the poles). Unintentional placement of the 118-GHz O_2 absorption line in the image sideband of a mixer receiver having 110 GHz in the signal sideband may result in higher than expected sky brightness temperatures (and therefore attenuations)... this may be misinterpreted as "anomalous absorption". In addition, the

common visual problem of atmospheric seeing -- as manifested in the twinkling of stars, especially on cold, clear winter nights, has an analogous effect at millimeter wavelengths as well as a common cause -- again, turbulence and non-laminar airflow. One final point is that all millimeter-wave radio telescopes use very-high-gain antennas. Many antennas used solely for atmospheric attenuation measurements have undetermined and possibly poor main-beam-efficiencies, particularly at high frequencies. The additional effect of ground radiation entering undesirably large sidelobes or backlobes could be misinterpreted as anomalously higher atmospheric absorption.

2. THE UNIVERSITY OF MASSACHUSETTS RADIO TELESCOPE

The University of Massachusetts 45-foot (13.7-m) millimeter-wave radio telescope is located on a peninsula extending into the million-square-acre Quabbin Reservoir, which is itself in a remote, wooded, restricted area of Western Massachusetts. The mm-wave antenna is enclosed in a 60-foot diameter radome made of ESSCOLAM, and having a transmission-loss (one-way) of about 1 db. The internal radome temperature is maintained at about 278°K or the outside ambient air temperature, whichever is higher.

The millimeter-wave antenna has Cassegrain optics, and an azimuth/elevation mounting. All pointing, as well as data acquisition, reduction, and radome environment control, is interfaced through a MODCOMP IV computer.

The main reflecting surface consists of 72 separate panels, each of which was molded to high tolerances, and mounted and adjusted separately, using panel-mounted targets and a high-accuracy theodolite. The rms surface accuracy is 110 μm, allowing operating frequencies up to 300 GHz (though the present radome material is not optimized for transmission at that frequency). At 115 GHz, the aperture efficiency is about 50%, the beam efficiency is about 80%, and the half-power beamwidth is about 44" (8×10^{-2} mrad).

3. OPACITIES AND SKY BRIGHTNESS TEMPERATURE MEASUREMENTS

In general, the physical processes responsible for atmospheric attenuation in the millimeter-wave region are fairly well understood. Worthy of further study, for the clear-sky conditions for example, is the range of net attenuation values observed at a given frequency at different times or azimuths for the same apparent ambient temperature, barometric pressure, relative humidity, visual transmissivity, etc.

In calibrating measurements of weak, interstellar molecular spectral-line emission, radio astronomers need to know the concurrent atmospheric opacity at a particular elevation angle. For clear sky observations (and assuming azimuthal symmetry for the atmosphere), the total atmospheric opacity at any elevation angle above ~5° is given by $\tau_{TOTAL} = \tau_o A$, where τ_o is the zenith opacity and A is the number of airmasses* (= cosecant of elevation angle) associated with that elevation angle.

The University of Massachusetts Radio Telescope has a completely computer-controlled procedure known as "Skydip" that computes τ_o after performing an internal receiver-constant calibration, taking sky brightness temperature measurements at eight different elevation angles (or airmasses) from 12.6° to 65.4°, and fitting a curve through the data points. The antenna temperature observed with the telescope pointed at blank sky is made up of contributions due to system noise, self-absorbed radome emission coming into all lobes, ground radiation entering sidelobes not pointed at the sky, and attenuated by the radome, and self-absorbed atmospheric emission into sidelobes looking at sky, also attenuated by the radome. Thus, (assuming equal gain in the signal and image sidebands), the basic equation showing the contributions of all these effects to the observed temperature, T_{obs}, is:

$$T_{obs} = T_{sys} + T_{rad}(1 - e^{-\tau_{rad}}) + (1-\eta)T_{amb}e^{-\tau_{rad}} + \eta\, T_{atm}e^{-\tau_{rad}}(1-e^{-\tau_o A}) \qquad (1)$$

where

T_{sys} = system temperature (DSB)

T_{rad} = radome temperature

τ_{rad} = radome opacity (taking account of both space frame blockage and membrane attenuation)

η = telescope efficiency for all sidelobes which look at sky ($\geq \eta_{main\ beam}$)

T_{amb} = ambient (ground) temperature

*In the astronomical community, the term "airmass" commonly and unambiguously refers to the total distance within the atmosphere of a given line of sight from the ground to space, as normalized to the atmospheric path length along a line of sight to the zenith. For example, for observations at the zenith, the airmass is 1. For observations at an elevation angle of 30°, the airmass is 2, implying that twice as much atmosphere is encountered along that path than along a path through the zenith.

T_{atm} = mean atmospheric temperature (including contributions from both O_2 and uncondensed H_2O)

τ_o = zenith opacity

A = airmass (= secant of zenith angle).

A number of assumptions must be made in fitting the observed data to this equation. The radome opacity τ_{rad} and the telescope efficiency η are both functions of frequency. Since η is a measure of the fraction of the total antenna beam which sees sky rather than ground, it will also be a function of elevation. Even T_{rad}, the effective radome temperature, may not be constant over the radome.

The parameters T_{rad}, η, and τ_{rad} are inputs to the data-reduction program. The values $T_{rad} = 278°K$, $\eta = 0.9$, $\tau_{rad} = 0.22$ are currently being used. Values determined by the computer program for T_{atm} (and to a lesser degree for τ_o) are, of course, influenced by the values assumed for these parameters.

Treating the radome and ground emission as independent of airmass produces an equation of the form:

$$T_{obs} = T_{srg} + \eta\, e^{-\tau_{rad}}\, T_{atm}(1 - e^{-\tau_o A}), \quad (2)$$

where T_{srg} includes the terms in Eq. (1) for system noise, radome emission, and ground radiation. The Skydip data-reduction program thus fits the data to an equation of the form:

$$Y = a + b\, e^{cX}, \quad (3)$$

where

$a = T_{srg} + \eta\, T_{atm}\, e^{-\tau_{rad}}$

$b = T_{atm}\, \eta\, e^{-\tau_{rad}}$

$c = \tau_o$

$Y = T_{obs}$

$X = A$

By expanding the exponential in Eq. (2), we can write

$$T_{obs} = T_{srg} + (\eta\, e^{-\tau_{rad}}\, T_{atm}\, \tau_o)\, A \quad (4)$$

$$+ (-1/2\, \eta\, e^{-\tau_{rad}}\, T_{atm}\, \tau_o^2)\, A^2 + \ldots$$

It is clear that when $\tau_o A$ is small, the noise in the data may make it impossible to derive the coefficient of the quadratic or higher terms in this expansion. In such cases, T_{atm} and τ_o cannot both be determined from the data; a value for T_{atm} must be assumed in order to find τ_o. In the fit to Eq. (3), the computer program gives the option of trying to determine T_{atm} or of choosing to hold it fixed.

In order to determine if curvature is present in the data, a quadratic least squares curve of the form of Eq. (4) is first fit to the data-set requested by the operator. The resulting coefficient of the quadratic term,

$$C = -1/2\, \eta\, e^{-\tau_{rad}}\, T_{atm}\, \tau_o^2,$$

is compared with its standard deviation (ΔC); if C is positive (curvature in the wrong direction) or $|C| \leq 2\,\Delta C$, it is assumed that the required curvature in the data is not present. A fit holding T_{atm} fixed at the value input by the operator is then attempted. The coefficients determined by both quadratic and exponential fits are evaluated using the "input" values for T_{atm}, η, τ_{rad}, T_{rad}, and T_{amb} to produce two sets of values for T_{sys} and τ_o, which are output on the screen. The best fit for a particular data-set can be determined by examining the chi-squared parameter for each fit and the plots of the fitted curves with the data.

Figure 1 shows the raw data plotted for a Skydip at 86 GHz. TOBS corresponds in Kelvins to the sky brightness temperature plus the receiver noise temperature (in other words, the total system noise temperature). For this measurement, the total zenith opacity τ_o was computed to be 0.112 nepers or 0.49 dB. This corresponds to a total zenith transmittance of ~ 0.89.

Radio astronomers, as well as system planners considering passive mm-wave systems for target detection, must take into account not only the variations in clear-sky atmospheric attenuation as a function of temperature, pressure, and relative humidity, but also the variation resulting from non-precipitating clouds. Figure 2 shows observed rapid changes in total attentuation, as indicated by the brightness temperature variations caused by strato-cumulus clouds passing through the beam of the UMass radio telescope as it tracked a celestial source. A periodicity (indicated by hatch marks along the time axis) corresponding to the motion of the each cloud "wave" across the beam is clearly seen. A contrast-temperature-measuring ground-based passive mmw system would be rendered virtually useless with such a sky background, unless possibly some kind of polarization-switching were used.

The Skydip program can use an initial "guess" of the τ_o to aid its data-fitting program. Another computer code OPACMP (for Opacity Computation) exists at UMass which can

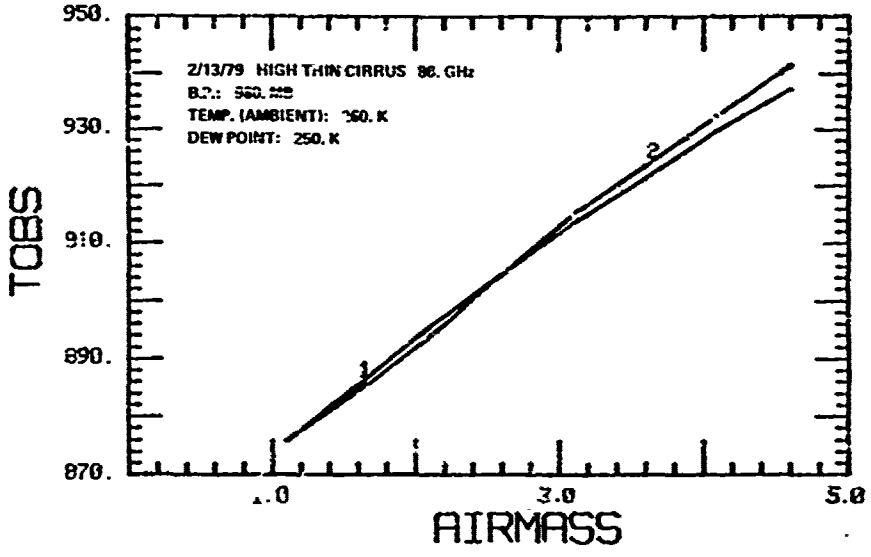

Figure 1 Tota' brightness temperature variations (elevation-dependent) sensed during SKYDIP by UMass 13.7-m mmw antenna

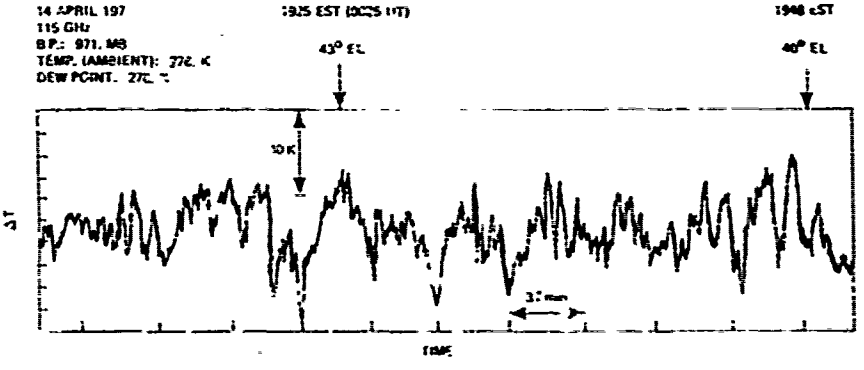

Figure 2 Short-time-scale sky brightness temperature variations; waves of strato-cumulus clouds passing through antenna beam

predict τ_o at a given frequency from meteorological information, given a mathematical description of the atmospheric absorption-line shapes. These predictions have often been identical to those derived later by the Skydip measurements.

4. MILLIMETER-WAVE SYSTEM MODELING AT TASC

The OPACMP computer code has been expanded in scope at the TASC facilities, and renamed RADENS (Radiometer Environmental Simulation). Table 1 summarizes the Input/Output parameters of RADENS. A typical system-modeling scenario that would use RADENS is described below.

A low-altitude submunition is guided over a battlefield area by a passive millimeter-wave seeker measuring ground contrast temperatures. A metallic object such as a tank would generally appear cooler than the surrounding terrain (i.e., have a negative contrast temperature), and would thus be sensed as a "target" by the millimeter-wave seeker. The contrast is reduced, or even eliminated, however, by such factors as the propagation loss along the slant path from the seeker to the target, as well as the sky radiation reflected by the metal target. Additional contrast reduction results from the presence of any clouds and/or precipitation along the line of sight to the target.

Using the initial environmental conditions as well as the instantaneous altitude, range, and depression angle of the radiometer seeker relative to the ground and the target, RADENS will compute the attenuation that a given contrast-temperature on the ground will experience. In addition, it will also compute the down-welling sky brightness temperature (also weather-dependent) which is reflected from the metallic target back up along the radiometer's line of sight, reducing the negative contrast temperature due to the target alone.

In a scenario similar to that presented above, the millimeter-wave seeker will likely use some scanning technique for initial target acquisition. With a conical-scan antenna, target position relative to the missile's flight path is determined as a function of phase angle on the antenna scan. In addition, the angular size subtended by the target in the beam also must be considered. Thus, a target possessing the same radiometric contrast temperature with the surrounding ground will produce different antenna temperatures, as sensed by the radiometer, depending upon the amount of the beam solid angle it fills.

The conical scan scenario is shown in Figure 3. The total power output of a radiometer sensing contrast temperatures via a conical-scan antenna (possessing the indicated antenna pattern to the 3 dB level) is shown in the right half of the figure. At time t=0, the target is at a greater range and subtends a smaller amount of the antenna beam. Hence the duration of the 360° scan that it is within the beam (the width of the negative-going trace) is less than at time t=1, when its range has decreased.

Such a passive-track model has also been computer-coded at TASC. This program, coupled with the RADENS output, has allowed very complete predictions of many millimeter-wave sensing scenarios, in a wide variety of possible adverse weather conditions.

5. SUMMARY

The University of Massachusetts Millimeter-Wave Radio Telescope has the capability of making accurate, rapid measurements of sky brightness temperatures and opacities. Existing software allows complete data reduction in minutes. The Analytic Sciences Corporation has the capability to construct extensive models of passive millimeter-wave guidance or target detection systems, taking into account not only imaging geometry and scene composition but also all possible atmospheric propagation effects.

INPUTS	"RADENS"	OUTPUTS
FREQUENCY (20 - 300 GHz)		
RADIOMETER ALTITUDE (AGL)		
GROUND ELEVATION (ASL)		SEPARATE ATTENUATIONS DUE TO 0_2
GROUND AIR TEMPERATURE		H_20 - VAPOR
GROUND BAROMETRIC PRESSURE		H_20 - CONDENSED
GROUND RELATIVE HUMIDITY		⇒ TOTAL ATMOSPHERIC ATTENUATION (ZENITH)
PRECIPITATION MODEL		TOTAL PATH LOSS (DB) BETWEEN AIRBORNE RADIOMETER AND GROUND AT ANY DEPRESSION ANGLE
(CLEAR SKY; CLOUDS/FOG; CLOUDS AND RAIN)		
CLOUD BASE ALTITUDE (AGL)		TOTAL SKY BRIGHTNESS TEMPERATURE (INCIDENT ON GROUND) FROM ANY ZENITH ANGLE
CLOUD TOP ALTITUDE (AGL)		
CLOUD H_20 CONTENT		
SURFACE RAIN RATE		

Table 1 Computer-modeling of atmospheric effects: RADENS Program (Radiometer Environmental Simulation) I/O parameters

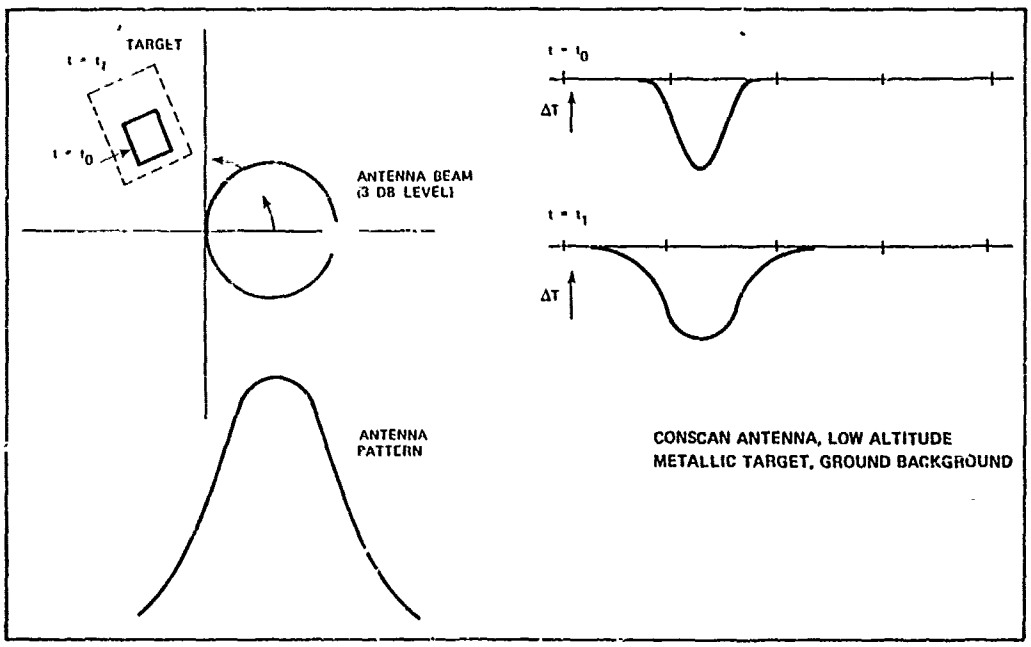

Figure 3 Passive-track modeling of contrast-temperature seeker using a conscan antenna to observe a rectangular metallic target at decreasing range

ANOMALOUSLY INTENSE SHORT COHERENT PULSE GENERATION BY SWEPT-GAIN SUPERRADIANCE

C. M. Bowden, D. W. Howgate, and J. J. Ehrlich

US Army Missile Research and Development Command

Redstone Arsenal, Alabama 35809

ABSTRACT

Short, intense pulses were generated in the FIR and millimeter regions by CO_2 pulse excitation of CH_3F gas in a long cell configuration without mirrors. The pulse evolution was observed over the pressure range from 0.05 torr to .3 torr and for cell lengths ranging from 6 m to 10 m. Using $C^{12}H_3F$ as the active material, FIR pulses at λ = 496 μm were obtained, whereas the use of $C^{13}H_3F$ produced pulses at λ = 1.2 mm. At the high pressures (homogeneous regime) pulses of temporal duration less than T_2 were observed.

1. EXPERIMENT

The experimental arrangement is shown in Figure 1. A TEA CO_2 laser was operated on the P(20) (λ = 9.55 μm) line to give a single longitudinal and transverse mode by using a low pressure CW CO_2 gain cell. Smooth 200 nsec pulses are produced of about 150 mJ total energy. These pulses are subsequently chopped using an optical breakdown switch which utilizes UV-triggered AC breakdown of clean N_2. The resulting CO_2 pulse is about 65 nsec duration and is cut off on its trailing side in less than 0.1 nsec. This pulse is passed through a $C^{12}H_3F$ cell, 6 m in length along the cell axis. The area of the IR beam is approximately 2 cm^2. The resulting FIR pulses at 496 μm were monitored in both the forward and backward directions by a low temperature phosphorous doped silicon detector which operated near 2°K. At the output end of the $C^{12}H_3F$ cell the IR pump pulse which emerges and the FIR pulse generated were monitored simultaneously by using a beam splitter which reflects nearly 100% of the IR and transmits about 50% of the FIR. These pulses were displayed in the same time frame on an oscilloscope, whereby the relative temporal positions of the two pulses were easily determined. Further details of the experimental apparatus are given in references Ehrlich et al. (1978) and Rosenberger et al. (1977). The relevant energy level diagram for CH_3F for the transition involved in the experiment is presented in Figure 2. Since it was possible to couple to two k-level transitions (approximately 45 MHz apart) by tuning the pump cavity, we tuned to the one corresponding to the highest gain, i.e., k = 2. Results of this experiment were reported earlier by Ehrlich et al. (1978) and Rosenberger et al. (1978).

If $C^{13}H_3F$ is used in the same configuration discussed above, and if the P(32) line at λ = 9.63 μm is selected for the CO_2 pump pulse, millimeter wavelength pulses are generated at λ = 1.222 millimeters. Results of this work will be published shortly, Ehrlich et al. (to be published).

REFERENCES

Ehrlich, J. J., C. M. Bowden, D. W. Howgate, S. H. Lehnigk, A. T. Rosenberger, and T. A. DeTemple, 1978: Swept-gain superradiance in CO_2-pumped CH_3F. Coherence and Quantum Optics IV, p. 923.

Ehrlich, J. J., T. A. DeTemple, S. Lee, C. M. Bowden, and D. W. Howgate, to be published.

Rosenberger, A. T., S. J. Petuchowski, and T. A. DeTemple, 1977: Experiments in FIR superradiance. Cooperative Effects in Matter and Radiation, edited by C. M. Bowden, D. W. Howgate, and H. R. Robl, Plenum Press, New York, pp. 15-35.

Rosenberger, A. T., T. A. DeTemple, C. M. Bowden, and C. C. Sung, 1978: Proceedings of the 10th International Quantum Electronics Conference 1978, Atlanta, GA, 29 May - 1 June 1978.

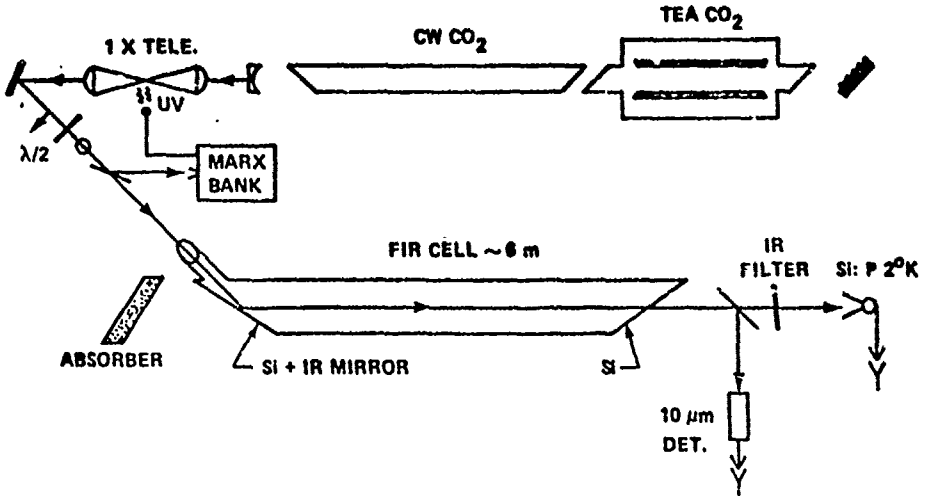

(Printed by permission of Plenum Press)

Figure 1. Experimental Arrangement

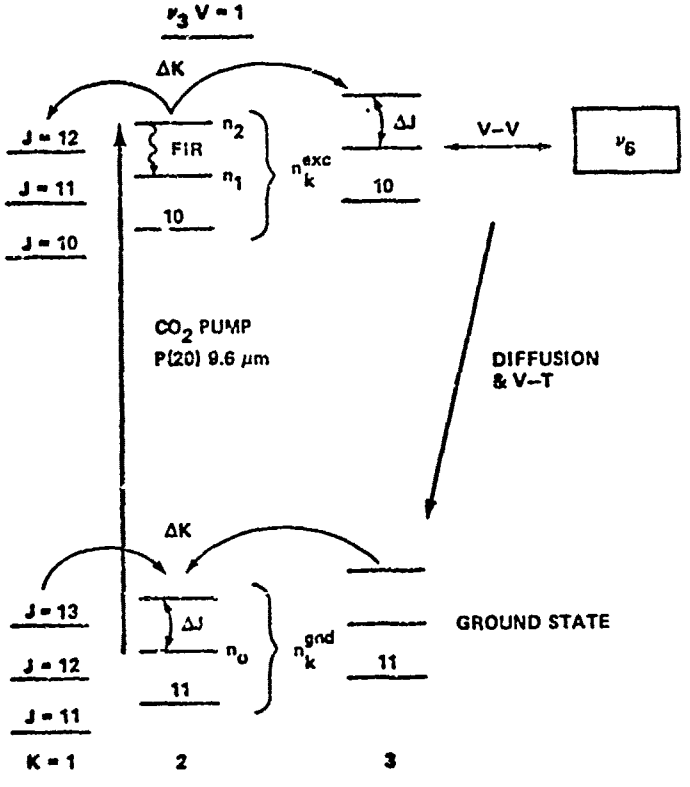

(Printed by permission of Plenum Press)

Figure 2. CH_3F Energy Levels Relevant to the Experiment

A MOBILE FACILITY FOR TARGET/BACKGROUND CHARACTERIZATION AT NEAR-MILLIMETER WAVELENGTHS

Edward Dudley
Harry Diamond Laboratories
Adelphi, Maryland

ABSTRACT

This paper describes the functions and use of a near-millimeter wave mobile measurement facility (NMMW/MMF) that will be used to characterize targets and backgrounds in clear air and in degraded environments (fog, rain, snow, smoke, and chaff). The facility will be capable of making simultaneous measurements at 94, 140, and 220 GHz.

1. INTRODUCTION

From time to time, interest in near-millimeter wave (90 to 1000 GHz) research and development has risen, only to wane again when researchers are confronted with the difficulties of developing high power sources and low noise receivers. Recently, however, military interest has been renewed because, in contrast to most electro-optical systems, near-millimeter wave systems are expected to be operational in spite of most adverse atmospheric conditions, either natural or man induced, that might be encountered on the modern battlefield. At the same time, near-millimeter wave radiation should provide better resolution than one could expect from longer wavelength radiation, such as microwaves.

One concrete result of this military interest is a near-millimeter wave mobile measurement facility (NMMW/MMF) being developed by Harry Diamond Laboratories (HDL). The facility is being designed and constructed by the Engineering Experiment Station of the Georgia Institute of Technology under contract with HDL. When complete this facility will be capable of measuring reflections from targets, backscatter from rain and other hydrometeors, background clutter, and attenuation in an environment that contains fog, rain, snow, smoke or chaff, or combinations of these. These measurements will be made with monochromatic sources operating at frequencies of 94, 140, and 220 GHz.

The concept of the NMMW/MMF arose from the recommendations of a study panel--made up of representatives of the government, universities, and industry--which convened in 1977 to assess the state of NMMW technology and its potential for application to military systems. This panel recommended a program to complete the NMMW data base needed for design of NMMW systems. One of their explicit recommendations was for the construction of a mobile measurement facility, to be used Army wide, for taking near-millimeter wave radar-type data at various test sites. Funds were made available to HDL to develop the facility and a contract was subsequently let for detailed design and construction of the NMMW/MMF.

The panel also recommended that provisions be made for simultaneous meteorological measurements to characterize the environment during the near-millimeter wave measurements. The responsibility for this task fell to the Atmospheric Sciences Laboratory (ASL), which is now developing a separate mobile meteorological facility that will be fully compatible with the MMF.

Throughout the development period, a coordination group, made up of potential users of the data that these two facilities will provide, met periodically to advise on the functional design.

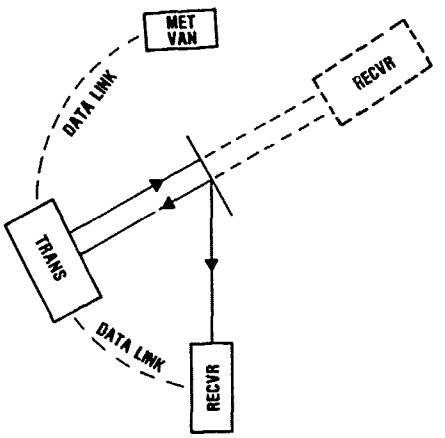

Fig. 1. Block Diagram of the MMF.

2. SYSTEM DESCRIPTION

Fig. 1 is a block diagram of the NMMW/MMF. The facility is housed in two trailers; one designated as a transmitter trailer, is approximately 40 by 10 ft, and the second is a receiver trailer, 30 by 8 ft. The trailers are heated and air conditioned. Parts of the facility that are not shown are three 30-kVA generators, one for the receiver trailer and two for the transmitter trailer where lighting, heating, and air conditioning together will be connected to a separate generator. Also shown in Fig. 1 is the meteorological van presently under development at ASL. It is planned that the meteorological van will be an integral part of any test on which the MMF is used.

The facility, as shown in figure 1, can be used for backscatter or target return measurements by means of transmitters and receivers in the transmitter trailer, for bistatic target return measurements by means of separate receivers in the receiver trailer, or one-way measurements with the receiver trailer down range. There will be data and voice links from receiver to transmitter trailer, and a data link between meteorological van and transmitter trailer.

Table I lists the more important equipment in both trailers. The equipment in the transmitter trailer includes transmitters at 94, 140, and 220 GHz, the receivers at the same frequencies. This trailer will also contain data acquisition and processing equipment, that is, a minicomputer, which will also be used for optimum positioning of the antennas by means of electrically controlled gimbals.

The receiver trailer will have receivers that operate at 94, 140, and 220 GHz. The 2-ft diameter dish-type antennas will also be computer controlled by means of gimbals identical to those in the transmitter van. The receiver trailer will contain a data collection and transmission system. Each of the trailers will have storage space, and space will be provided in the receiver trailer for paperwork and mechanical and electrical repairs.

Table II lists the functions of the data acquisition, processing, and control system in more detail. Provision is made for real-time data acquisition, analog readouts and recordings, and near real-time CRT display. Data will be recorded on nine-track tape. In addition, hard copy can be produced. The system can receive and process data from the receiver trailer and transmitter trailer, and also from ASL's meteorological van. The latter will have a data processing system that will be fully compatible with the system on the MMF; the two systems will be able to interchange data and serve as backups for each other.

Table I. MOBILE MEASUREMENT FACILITY EQUIPMENT

A. "Transmitter" trailer	B. "Receiver" trailer
1. Transmitters (94, 140, 220 GHz)	1. Receivers (94, 140, 220 GHz)
2. Receivers	2. Data collection and transmission
3. Data acquisition, processing and control	3. Controlled antenna mounts
4. Controlled antenna mounts	

C. Three power generators

Table II. DATA ACQUISITION, PROCESSING AND CONTROL SYSTEM

1. Real-time data acquisition
2. Analog readouts and recordings
3. Near real-time CRT display
4. Nine-track data file
5. Hard copy
6. Data communications (Transmitter to receiver, transmitter to meteorological facility)

All of this equipment will allow measurements to be made in clear air, rain, fog, snow, chaff, dust, or dirt. Measurements that will be made with the system include attenuation and backscatter from rain or snow or other atmospheric particles. There will be enough height adjustment of the antennas, approximately 20 cm, to distinguish the effects of multipath. Radar cross sections of targets and ground clutter, and target scintillation can be measured in both the bistatic and monostatic modes.

Table III shows the system performance requirements given in terms of the range to target or receiver for which a signal is required that is clearly discernible above background noise at 27 C in rain falling at 12 mm per hour. Additional performance specifications for the MMF are listed in Table IV. A data sampling rate of 1 kHz will provide for rapid update of any measurements that are made. For backscatter measurements, there will be 10 contiguous range gates of approximately 15 m each, positionable as a unit anywhere along a 1-km path. The antennas will be rotatable through 90 deg for measuring polarization effects. Altogether, the measurement apparatus will have a 60-dB dynamic range; that is, the facility will be able to measure a signal that is 60 dB down from the signal received under nominal best-case conditions.

Table III. PERFORMANCE SPECIFICATIONS

	27 C Rain at 12 mm/hr RANGE (km)		
Frequency	One-way	Backscatter	Target return (σ = 1m^2)
94 GHz	1.5	1.0	1.0
140	1.5	1.0	1.0
220	1.5	0.5	0.5

Table IV. PERFORMANCE SPECIFICATIONS

1. Height adjustment for multipath
2. 1000-Hz data sampling rate
3. 10 range gates
4. Polarization rotation of 90 deg
5. 60-dB dynamic range

3. SCHEDULE

The time table for the project completion follows. At this writing, the design is complete, except for minor changes that will be made as the construction progresses. The trailers have been refurbished; heating and air conditioning have been checked and repaired, as have the generators; and all equipment that requires a long lead time for delivery has been ordered. We expect the MMF to be fully operational by October, 1980. Follow-on additions and improvements will include a Fourier transform spectrometer for broadband measurements from 94 to 400 GHz, equipment to render the sources coherent for more sophisticated measurements, and equipment to convert electrical power requirements from 60 to 50 Hz for European operation.

NEAR MILLIMETER WAVE MOBILE MEASUREMENT FACILITY (NMMW/MMF)

James J. Gallagher, Wayne M. Penn and Lucien C. Bomar

Georgia Institute of Technology
Engineering Experiment Station
Atlanta, Georgia 30332

ABSTRACT

The Near Millimeter Wave Mobile Measurement Facility (NMMW/MMF) will provide the means for performing measurements in the near millimeter wavelength region at various locations where there are weather conditions of interest or where smoke tests may be conducted. The MMF will consist of two vans and will contain transmitters, backscatter receivers and one-way video link receivers at 3.2 mm, 2.1 mm, and 1.3 mm wavelengths. In addition, broadband coverage (~ 3 mm-0.7 mm) will be simultaneously performed with a Fourier Transform Spectrometer (FTS). The MMF will be accompanied by the ASL meteorological van and its data collection and processing system will interface with that of the ASL van.

The design of the entire MMF has been established, the performance of the NMMW systems analyzed, and the measurement capability of the facility determined. The capabilities of the MMF include attenuation measurements (one-way transmission and temporal fluctuations - short term at ~ 200 Hz or greater rate), backscatter from rain/other hydrometeors, multipath effects, clutter, target scintillation, doppler spectral characteristics and bistatic operation. The data processing system will permit on-site calculation of effects on the near millimeter wave signals. This paper will present a discussion of the project status, provisions made for additions to the MMF and the schedule for completion and availability of the facility for measurements.

1. INTRODUCTION

Recent investigations indicate that the near-millimeter wavelength (NMMW) region offers considerable military advantage over the microwave and optical spectral regions during periods of heavy fog or employment of smokes by the enemy. The particular regions of interest lie in the transmission windows at wavelengths 3.2 mm, 2.2 mm, 1.3 mm and 880 μm. No facility exists for the comparison of atmospheric propagation measurements at these wavelengths with measurements at optical and microwave wavelengths. It is necessary that the measurements be performed simultaneously at several wavelengths. In order to perform such measurements at several locations of interest or during planned smoke tests, an enormous investment in experimental apparatus is required. The alternative approach is to instrument a near millimeter wave Mobile Measurement Facility (MMF) which will enable the measurements to be made at various locations where there are weather conditions of interest or where smoke tests may be conducted. During the first period of this program, the design plan has been established, calculations performed on transmitter power requirements, costing of apparatus obtained to provide an overall budget estimate, milestones and schedules have been set. In order to design the facility properly, the measurements capability of the apparatus has been planned.

In this paper, a discussion of the utilization and capability of the MMF will be given. The goals and several characteristics of the system were presented in the previous paper (Dudley,1979).

The MMF will consist of two vans and will contain transmitters, backscatter superheterodyne receivers and one-way video link receivers at 3.2 mm, 2.1 mm, and 1.3 mm wavelengths. In addition, broadband coverage (~ 3 mm - 0.7 mm) will be simultaneously performed with a Fourier Transform Spectrometer (FTS). The NMMW/MMF will be accompanied by the ASL meteorological van and its data collection and processing system will interface with that of the ASL van (Snider, 1979).

2. RANGE CALCULATIONS

The power requirements for the transmitter sources are determined by the range capability under severe atmospheric conditions. Calculations have been performed assuming performance parameters for the systems to be employed. Estimates of required transmitter power are given for the near-millimeter wavelength regions which will be covered in the initial measurements, i.e. 94 GHz, 140 GHz and 220 GHz.

2.1 One-Way Transmission Link

For propagation between the two vans, the transmitter power and receiver sensitivity requirements are relatively easy to meet. The one-way link equation governing this operation for a heterodyne system is

$$P_T = \frac{S}{N}\left(\frac{4\pi R}{G_A \lambda}\right)^2 kTBN_F L_{RF} \, e^{\alpha R/4.34} \qquad (1)$$

and for a video system is

$$P_T = \frac{S}{N}\left(\frac{4\pi R}{G_A \lambda}\right)^2 (NEP)\, B^{\frac{1}{2}}\, L_{RF}\, e^{\alpha R/4.34} \qquad (2)$$

where

P_T = REQUIRED TRANSMITTER POWER (WATTS)

$\frac{S}{N}$ = SIGNAL-TO-NOISE RATIO, TYPICAL 10/1

R = RANGE IN KM

G_A = GAIN OF ONE ANTENNA (ANTENNAS ASSUMED TO BE SAME SIZE)

λ = WAVELENGTH IN KM ($\lambda = 3\times10^5/\nu$, ν - FREQUENCY)

$kT = 4.14 \times 10^{-21}$ JOULES FOR 300^0K

B = BANDWIDTH, TYPICALLY 10^7 Hz

N_F = NOISE FIGURE, EXPRESSED AS A FACTOR, I.E. 3DB = 2

L_{RF} = RF SYSTEM LOSSES, AS A FACTOR > 1

α = ABSORPTION COEFFICIENT IN DB/KM

$NEP = 10^{-11}$ WATTS, THE NOISE EQUIVALENT POWER ASSUMED FOR A SCHOTTKY BARRIER DIODE

$B^{\frac{1}{2}} = 3162.28\ Hz^{\frac{1}{2}}$

The calculations have been performed for both heterodyne and video receiver systems. The values for the parameters used are given in Table 1. The factor L_{RF} for the RF system loss, appears in the numerator as a factor >1 so that if the system has an internal loss of 3 dB, then $L_{RF} = 2$. For all the calculations, the bandwidth B of the system is assumed to be 10^7 Hz with the understanding that the pulse width will be on the order of 100 ns. The NEP, noise equivalent power, is assumed to be 10^{-11} watts/$Hz^{1/2}$ for a Schottky Barrier diode. Values of 10^{-12} watts/$Hz^{1/2}$ have been obtained for point contact diodes, so that 10^{-11} watts/$Hz^{1/2}$ is a reasonable value for a Schottky Barrier diode, which is expected to be more sensitive (video case as well as heterodyne case) than a silicon point contact diode. The values listed in Table 1 for RF losses, L_{RF}, have been achieved in the laboratory but will quite probably exceed these values in the field. Circulators and switching devices will contribute significantly to losses at the higher frequencies.

The antenna gains which are employed in the calculations are for an antenna diameter of 0.6 m and an antenna efficiency of 50%. If difficulty is encountered in the pointing and alignment of the antennas at high frequency, a smaller receiver antenna could be employed. An antenna of only 0.3 m diameter would increase the power required for the transmitter by a factor of 4. The results of the one-way propagation are given in Table 2 for rain rates of 4 mm/hr and 12.5 mm/hr. It is seen from Table 2 that, for R = 1 km, at all frequencies, the video systems are sufficiently sensitive to detect, on a single pulse basis, transmitter power well below the available power at each frequency. Actually, if the NMMW/MMF were to be employed for one-way transmission only, IMPATTS would provide sufficient power as transmitters. Further sensitivity can be obtained by integration. Thus, for a single pulse observation or for integrated operation, sufficient power is available with Extended Interaction Oscillators (EIO's) to perform one-way transmission at rain rates in excess of 12.5 mm/hr. at 1 km range. The interest in signal fluctuations requires S/N >10, and it is observed from Table 2 that sufficient dynamic range exists for single pulse or short term signal averaging. The output power quoted by Varian for EIO's is shown in Table 3. For one-way operation at 1.5 km, Table 4 shows the required power for video operation at 12.5 mm/hr and includes 340 GHz for the parameters of Table 1 but with NEP ($W/Hz^{1/2}$) = 10^{-10} and L_{RF} = 10. One-way transmission does not present a problem at ranges to 1.5 km for all NMMW frequencies to be included in the facility.

2.2 Rain Backscatter

For the case of rain backscatter, the problem becomes more severe. In this case, only heterodyne operation is applicable and the range under severe weather conditions will be limited to 0.5 - 1 km.

The transmitter power required for rain backscatter is given by

$$P_T = \frac{\left(\frac{S}{N} N_F kTB\right)(4\pi)^3 R^4 e^{2\alpha R} L_{RF}}{2\lambda^2 G_A^2 \sigma_B} \qquad (3)$$

Eq. (4) gives the backscatter cross-section as expressed in terms of the backscatter coefficient which can be thought of as the cross-section/unit scattering volume (m^2/m^3):

$$\sigma_B = \eta \frac{\pi}{8} R^2 \theta_B^2\, C\tau_P \qquad (4)$$

where

η = BACKSCATTER COEFFICIENT (m^2/m^3)

θ_B = BEAM DIAMETER IN RADIANS

C = VELOCITY OF LIGHT (3×10^5 KM/SEC)

τ_P = PULSE WIDTH (SEC)

The remaining parameters in (3) and (4) are defined in section 2.1. As in section 2.1, no integration is included. Table 5 gives parameter values for backscatter calculation at 94, 140, and 220 GHz. Power requirements for rain

TABLE 1

PARAMETER VALUES USED FOR ONE-WAY HETERODYNE SYSTEM

	94 GHz	140 GHz	220 GHz
N_F	10	20	60
L_{RF}	2	3.3	4
λ(KM)	3.2×10^{-6}	2.14×10^{-6}	1.36×10^{-6}
G_A	1.78×10^{5}	3.88×10^{5}	9.6×10^{5}
α(4MM/HR)	3.9	7.3	11.3
α(12.5MM/HR)	7.6	12.3	16.3
B(HZ)	10^7	10^7	10^7
$\frac{S}{N}$	10	10	10
R(KM)	0.5, 1.0	0.5, 1.0	0.5, 1.0
kT(JOULES)	4.14×10^{-21}	4.14×10^{-21}	4.14×10^{-21}

TABLE 2.

ONE-WAY PROPAGATION RESULTS

FREQ (GHz)	DETECTION	RAIN RATE(MM/HR)	POWER REQUIRED IN WATTS R = 0.5 KM	POWER REQUIRED IN WATTS R = 1 KM
94	HETERODYNE	4	1.58×10^{-9}	9.90×10^{-9}
		12.5	2.41×10^{-9}	2.32×10^{-8}
	VIDEO	4	1.21×10^{-4}	7.56×10^{-4}
		12.5	1.85×10^{-4}	1.77×10^{-3}
140	HETERODYNE	4	3.63×10^{-9}	3.36×10^{-8}
		12.5	6.45×10^{-9}	1.06×10^{-7}
	VIDEO	4	1.38×10^{-4}	1.28×10^{-3}
		12.5	2.46×10^{-4}	4.06×10^{-3}
220	HETERODYNE	4	8.46×10^{-9}	1.24×10^{-7}
		12.5	1.50×10^{-8}	3.94×10^{-7}
	VIDEO	4	1.08×10^{-4}	1.58×10^{-3}
		12.5	1.91×10^{-4}	5.01×10^{-3}

TABLE 3.

VARIAN EXTENDED INTERACTION OSCILLATORS

FREQ (GHz)	PEAK POWER OUTPUT (W)	DUTY	DELIVERY
35	1,000	0.0005	140 DARO
94	1,000	0.0005	120 DARO
140	200	0.0005	180 DARO
220 ± 10	60	0.0005	180-220 DARO
340	20	0.0005	300 DARO

DUTY CYCLE IS BASED UPON REQUEST FOR OSCILLATORS WITH 50-100 NS PULSE WIDTHS AND PRF CAPABILITY OF 10^3Hz.

TABLE 4.

POWER REQUIREMENT AT R = 1.5 KM
ONE-WAY TRANSMISSION
RAIN RATE = 12.5 MM/HR

FREQUENCY (GHz)	TRANSMITTER POWER (P_T IN WATTS)
94	9.58×10^{-3}
140	3.77×10^{-2}
220	7.37×10^{-2}
340	9.91

PARAMETERS OF TABLE 1 APPLY.
FOR 340 GHz, L_{RF} = 10, NEP = 10^{-10} W/Hz$^{1/2}$ AND α = 21 DB/KM.

TABLE 5.

PARAMETER VALUES FOR BACKSCATTER CALCULATION

PARAMETER	94 GHz	140 GHz	220 GHz
N_F	10	20	60
L_{RF}	2	3.3	4
$\lambda (10^{-6}$ KM)	3.2	2.14	1.36
$G_A (10^5)$	1.78	3.88	9.6
α 4 MM/HR	3.9	7.3	11.3
12.5 MM/HR	7.6	12.3	16.3
η 4 MM/HR	1.9×10^{-1} KM^2/KM^3	2.2×10^{-1}	9.5×10^{-2}
12.5 MM/HR	4×10^{-1}	4.2×10^{-1}	1.9×10^{-1}
RANGE (KM)	0.5, 1.0	0.5, 1.0	0.5, 1.0
Θ_B (RAD.)	5.9×10^{-3}	4.0×10^{-3}	2.4×10^{-3}
kT (JOULES) AT T=300°K	4.14×10^{-21}	4.14×10^{-21}	4.14×10^{-21}

TABLE 6.

POWER REQUIREMENTS FOR RAIN BACKSCATTER
MEASUREMENTS - HETERODYNE DETECTION

SINGLE PULSE

FREQUENCY (GHz)	RAIN RATE (MM/HR)	POWER REQUIRED (WATTS) R = 0.5 KM	R = 1.0 KM
94	4	0.2	1.96
	12.5	0.22	5.13
140	4	1.28	27.46
	12.5	2.12	144.04
220	4	30.36	1641.05
	12.5	48.04	8218.06

TABLE 7.

REQUIRED TRANSMITTER POWER FOR
TARGET RETURN, σ_T = 1 M^2, SINGLE PULSE
HETERODYNE RECEPTION

FREQUENCY (GHz)	RAIN RATE (MM/HR)	REQUIRED POWER (WATTS) R = 0.5 KM	R = 1.0 KM
94	4	3.89×10^{-3}	0.15
	12.5	9.12×10^{-3}	0.84
140	4	1.32×10^{-2}	1.14
	12.5	4.18×10^{-2}	11.40
220	4	4.48×10^{-2}	10.6
	12.5	1.56×10^{-1}	105.7

backscatter measurements at the three frequencies of primary interest are shown in Table 6. At R = 1 km, the required power for 220 GHz exceeds the quoted power listed in Table 3, and would require coherent integration or incoherent integration of approximately 1000 and 2 x 10^4 pulses respectively for 4 mm/hr and 12.5 mm/hr. In addition, integration would be required at 340 GHz to observe rain backscatter.

2.3 Target Return

The NMMW/MMF will have the capability of measuring not only atmospheric effects but target and terrain effects. Target return for a target cross-section σ_T = 1 m^2 has been calculated for the three frequencies of major interest. The relation for single pulse target return is given by

$$P_T = \frac{(4\pi)^3 R^4 \left(\frac{S}{N}\ kTBN_F\right) L_{RF} e^{2\alpha R/4.34}}{2 G_A^2 \lambda^2 \sigma_T} \qquad (5)$$

where all parameters are given in section 2.1 and σ_T is the target cross-section (m^2), assumed to be 1 m^2 for calculations. Table 7 gives the results for the required power.

From the calculations of this section, it is seen that the transmitter power required for the NMMW/MMF dictates the use of EIO's and, at the higher frequencies (220 GHz and 340 GHz), substantial integration is necessary. At 35 GHz, a frequency of secondary interest, the power requirements can be met by IMPATT or amplified Gunn oscillators.

3. MMF CHARACTERISTICS

3.1 Spectral Range for MMF

On the basis of projected military applications, the frequencies or spectral regions of interest are the following: 94 GHz, 140 GHz and 220 GHz employing monochromatic sources, and 3-13 cm^{-1} (90-390 GHz) continuous coverage with a Fourier Transform Spectrometer (FTS).

In addition, the MMF will be capable of operation at other wavelengths if a user wishes to provide the propagation apparatus. Thus, space would be available to include 8 mm, 0.88 mm, 10.6 μm or 1.06 μm for comparative propagation measurements.

3.2 Operational Range

The operational range for the NMMW/MMF is set by the requirements of observing the atmospheric, target and terrain characteristics under severe atmospheric conditions and by the limitations imposed by the availability of meteorological apparatus. The greater the range, the greater the amount (and therefore the cost) of met gear. The ranges over which observations will be made are:

Point-to-Point:	0.5 - 1.5 km
Signal Return;	0.5 - 1.0 km

The monochromatic systems to be employed will be capable of operating to approximately 3 km for the one-way link but will not have meteorological control over the entire path-length. The FTS apparatus will be limited to approximately 0.5 - 0.75 km range.

3.3 Operating Environmental Conditions

The NMMW/MMF will be employed for operation during rain, fog, snow and smoke conditions. The expected conditions will include temperature extremes from approximately -20°F to +120°F and exterior conditions of high humidity, rain, dust, and sun load typical of summertime desert environment. Rain rates will include 4 mm/hr and 12.5 mm/hr. It is expected that rates >12.5 mm/hr will occur for shorter periods of time during operation. The severity of conditions during fog or snow will not exceed the system capability.

3.4 Measurement Capability

The NMMW/MMF will have the capability not only for atmospheric measurements but also for the important function of determining target and terrain characteristics in the spectral regions of interest. At frequencies above 100 GHz, practically no information exists on the characteristics of targets and terrain. Table 8 lists the measurement capability of the facility in order of priority. Attenuation measurements under all environmental conditions are listed as the items of highest priority. In addition to the straight attenuation effects, temporal fluctuations of signals as a function of environmental conditions provide information important to military systems. At BRL, short term fluctuations have been observed in measurements at 94 GHz and 140 GHz. The FTS measurements at Appleton Laboratory indicate large spectral fluctuations in fog, varying in time with fog intensity. Correlation of these two effects is important, and a capability for measuring temporal fluctuations at a rate of at least 200 Hz must be built into the monochromatic systems. Actually single pulse measuring capability is being provided. The terrain/target characteristics are accounted for by the other measurements.

3.5 Mobile Measurement Units

The NMMW/MMF will consist of three vans capable of being moved to a location for measurements of interest. One van, to be provided by ASL, will provide meteorological support. Two large vans will serve as a transmit van and a receive van. The larger of the two will serve as the Transmit Van and will contain the facilities shown in Figure 1.

Table 8.

MEASUREMENT CAPABILITY OF NMMW/MMF

1. Attenuation
   (a) One-way transmission
   (b) Temporal fluctuations - short term at ~ 200 Hz rate
2. Backscatter - rain/other hydrometeors
3. Multipath effects
4. Target cross-sections
5. Clutter
6. Target scintillation
7. Doppler spectrum - clutter, targets
8. Bistatic operation capability

The smaller van will serve as the Receive Van with the apparatus also shown in Figure 1. The large van has three doors on one side, two of which will be employed as propagation ports. The smaller van has a rear double door and a side wall door.

An artist concept (Figure 2) shows the two vans with the configuration in which the NMMW apparatus will be operated. The transmitter van will have transmitter and backscatter receiver for the three frequencies, 94 GHz, 140 GHz and 220 GHz, and, at the rear of the van, a Fourier Transform Spectrometer and its source. The FTS will be operated with a roof retroreflector so that source and spectrometer can be controlled from the one van. The transmitter and backscatter receiver for each frequency have individual antennas and can be separated for bistatic operation. The transmitters are, as indicated above, Extended Interaction Oscillators. Hard tube modulators are being constructed rather than line modulators for improved pulse shape. It is planned to use these sources eventually in coherent operation.

The interiors of the vans are shown in the diagram of Figure 1. The position of the FTS, Antenna Bays and computer are shown in the transmitter van. The NMMW monochromatic systems are mounted in bays with the apparatus adjustable in height for multipath measurements. Each NMMW system is mounted in a gimbal mount for vertical/horizontal angular adjustments. The gimbals will be computer controlled for periodic checks on antenna alignment.

The receiver van has the NMMW equipment bay at the rear of the van. A small electronic shop and a machine shop are located in the receiver van for repairs in the field.

3.6 MMF Data Acquisition System

The MMF data acquisition system will be based upon an H-P 1000 Model 45 computer. The Model 45 provides the high precision processing speeds needed for the MMF. The computer has a disk operating system with a graphics console. The input data is derived from three microwave sources (94 GHz, 140 GHz, and 220 GHz) plus a fast scan Fourier Transform Spectrometer. Each microwave system produces three types of information. Initially the transmitted pulse is sampled, then the one-way link propagation information is provided, and finally a backscatter gated receiver generates a possible 128 range cells of data per pulse. The one way link data is brought back real time by a multiplexed digital wire or microwave (X-band) link. Antenna control is also provided over the two way data link along with a voice channel. The three microwave data sources are digitized and recorded in real time during the experiment. Analog data handling is also provided simultaneously with the experiment along with real time data presentations to personnel. Typical data rates are on the order of 37 Kbytes a second using ten range gates per wavelength. The final data file is stored on 9-track tape.

Figure 3 shows an outline of the manner in which the computer data acquisition system is employed, and Figure 4 presents a diagram of the 140 GHz NMMW system with transmitter, video receiver and backscatter receiver. The data processor requirements are given in Table 9. The range gating capabilities have been designed to provide at least ten contiguous gates, approximately 30 meters in length, positionable as a unit anywhere up to the maximum range of interest. Actually, up to 128 gates can be provided with this system for each pulse.

4. CONCLUSIONS

The system described in this paper will provide a capability to perform important measurements at any sites of military interest. In addition to the systems described above, provision has been made to be able to include any additional systems of interest. The Mobile Measurement Facility is scheduled to be completed by September, 1980.

REFERENCES

Dudley, E. P., 1979: A mobile facility for target/background characteristics at near millimeter wavelengths. Session 9, Workshop on Millimeter and Submillimeter Atmospheric Propagation Applicable to Radar and Missile Systems, 20-22 March 1979, Huntsville, Alabama.

Snider, D. E. and D. R. Brown, 1979: The transportable atmospheric characterization station. Session 9, Workshop on Millimeter and Submillimeter Atmospheric Propagation Applicable to Radar and Missile Systems, 20-22 March 1979, Huntsville, AL.

Acknowledgment: This work is supported by The U. S. Army Harry Diamond Laboratories under Contract No. DAAG39-78-C-0044.

TABLE 9. MMW/MMF DATA PROCESSOR REQUIREMENTS

INPUT:

1. Sample pulses 100 nsec long. (Triggering on the pulse).
2. Perform samples at 1000 Hz per channel.
3. Have two data processing collection systems.
   a). Transmitter data collection system must have 34 channels of input.
   b). Receiver data collection system must have 4 channels of input.
4. Transmission links must have at least 12 bit resolution.
5. Final data storage must be on 9 track tape.
6. A large mini-computer system (HP-1000 Model 45) must interface with the data and processors.

OUTPUT:

1. Gimbal control signals must be provided. The system contains 11 gimbals; seven at the transmitter van, and four at the receiver van. Each gimbal requires two bits of information for control, one a direction bit, the other a step bit.
2. Transmitter computers and processors must be interfaced to receiver computers, processors, and tape drivers. The information will be two way. The link is to be high speed over hard-wire or RF link, both must be provided for.
3. The mini-computers must be interfaced with White Sands met-van mini-computer over hardwire when the met-van is on site with the MMW/MMF.

MINI-COMPUTER:

1. The HP-1000 Model 45 is preferred due to software and it is complementary of the met-van Model 45.
2. It must have a graphics CRT terminal.
3. It must have a graphics printer-plotter.
4. Nine track 10 1/2" reel, 1600 BPI dual tape drives must be provided for merging files.
5. Distributed interface to the met-van computer must be provided for.
6. Software for antenna alignment must be developed.

Figure 1. Interior of Receive and Transmit Vans

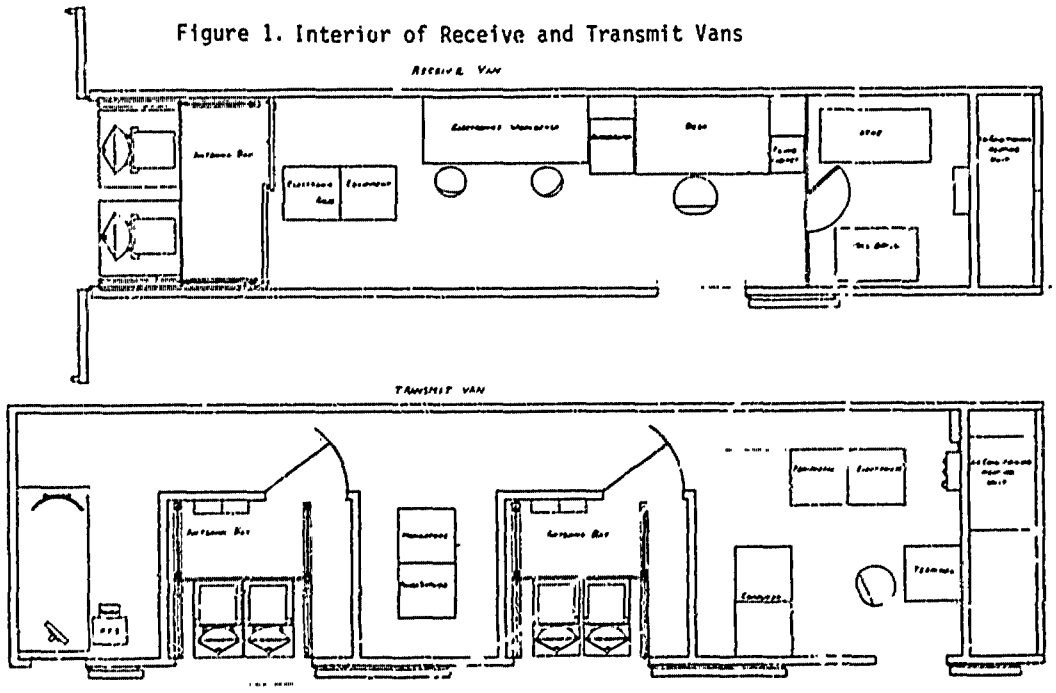

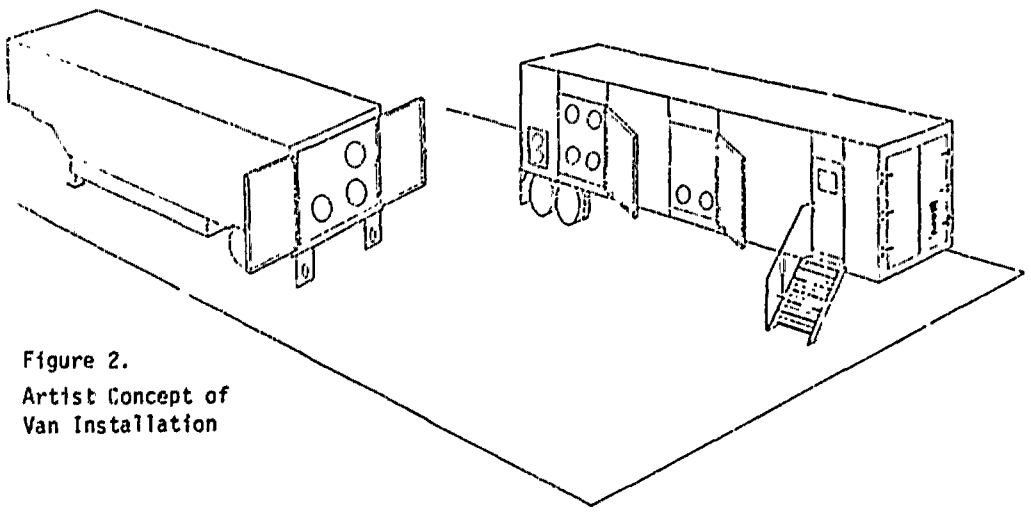

Figure 2.
Artist Concept of
Van Installation

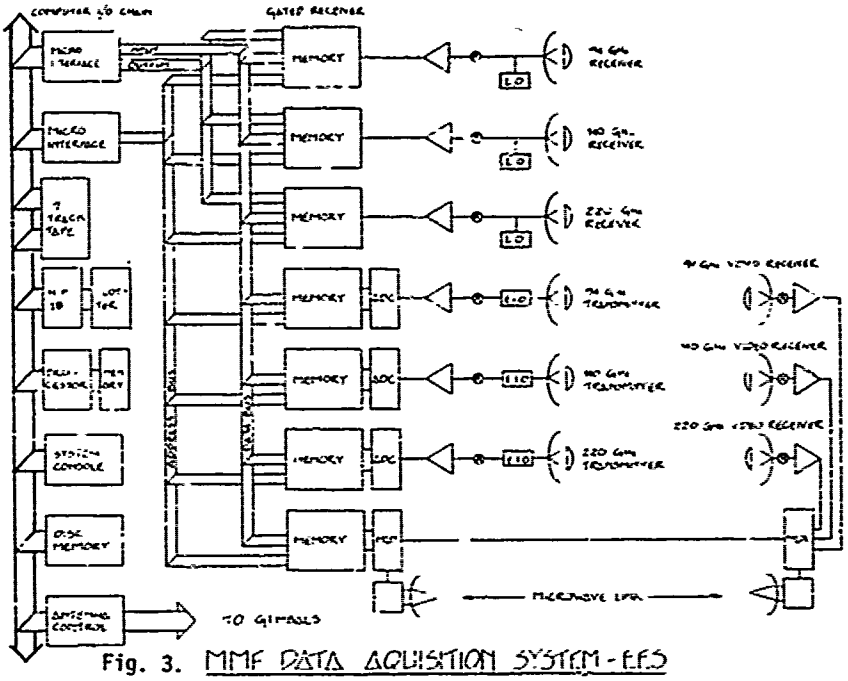

Fig. 3. MMF DATA ACQUISITION SYSTEM - E.E.S

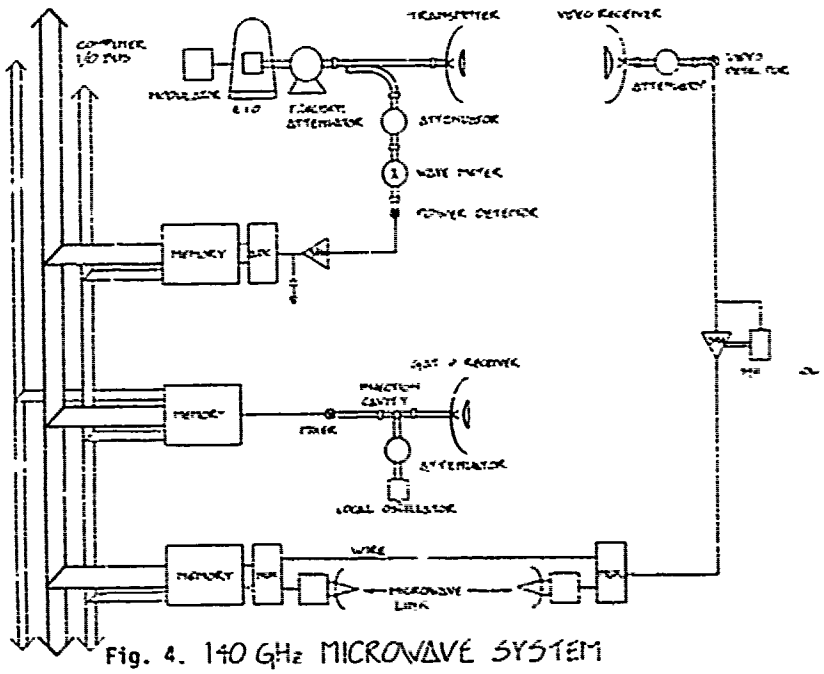

Fig. 4. 140 GHz MICROWAVE SYSTEM

THE TRANSPORTABLE ATMOSPHERIC CHARACTERIZATION STATION

Dr. Donald E. Snider and Douglas R. Brown

US Army Atmospheric Sciences Laboratory

White Sands Missile Range, New Mexico

ABSTRACT

The Atmospheric Sciences Laboratory, US Army, is developing a Transportable Atmospheric Characterization Station (TACS) in cooperation with Harry Diamond Laboratory to characterize the atmospheric propagation path during operation of the Mobile Measurement Facility (MMF). The system will consist of two vans containing a computerized data acquisition system, repair facilities and rudimentary living quarters, two tripods carrying particle size probes on servo mount, a 32 meter tower, diesel generator, and three or more remote stations deployed along the propagation path. The system is designed to measure the particle size distribution of rain, dust, or fog from 0.3 μ to 10.4 mm, and provide as complete a meteorological characterization of the test site as is portably possible.

1. INTRODUCTION

The Atmospheric Sciences Laboratory, WSMR, is developing a Transportable Atmospheric Characterization Station (TACS) in association with the Harry Diamond Laboratory Mobile Measurement Facility (MMF). Its purpose is to provide a detailed characterization of the near millimeter wave atmospheric propagation path. Many previous millimeter propagation measurements have been of limited use to the systems designer and atmospheric scientist because the measurements were not accompanied by adequate data on the physical state of the propagation path. Without this data it is impossible to relate the diverse measurements and compile a well defined millimeter wave data base.

The interaction with the atmosphere, generally negligible at lower radio frequencies, becomes of major significance as frequencies rise above 35 Gigahertz. Besides the everpresent absorption effects of gaseous oxygen and water vapor, various aerosols such as rain, fog, snow and particulates such as dust and smoke, make increasing contributions to the total atmospheric extinction at these frequencies. System operation parameters therefore become sensitive to the detailed atmospheric conditions and such conditions must be known if the extinction measurements are to be truly useful.

The TACS has been designed to provide path characterization. In this report we will describe the physical and operational characteristics of the system as it is being constructed. The TACS is not envisioned as a static system, however, a program to improve its sensing capabilities, in sensitivity, in area coverage, and parameters measured, is an integral part of its operating plan.

2. PHYSICAL DESCRIPTION

The TACS system will be based upon M109 Shop Vans. These are air transportable (C-141), 3 axle drive all terrain vehicles. Two such vans will be available. One unit will house the data acquisition system and perform experiment control, data compilation and storage, and tow one trailor. The other will provide the maintenance and repair facilities, rudimentary living space, and will tow the other trailor. Depending on the test requirements either one or both vans would be used.

The two trailors will be employed to transport and deploy a 32 meter meteorological tower, diesel generator and pedestal mount servo-controlled by the wind speed and direction. The tower and pedestal mount will be equipped with various sensors as described in Section 3.

The millimeter wave propagation path will be instrumented at regular intervals by ground based remote stations. These stations will be self-contained battery powered units and will communicate with the data acquisition van via radio or hardwire link. Again, their met equipment is discussed in the next section.

3. METEOROLOGICAL EQUIPMENT

Experiment control, data sequencing, manipulation, storage and reduction will be performed by a minicomputer based data acquisition system. This computer will poll the various remote sensors on the tower, the propagation path, and the servo mount; the data will then be collated by the computer and stored on magnetic tape. The data system has been designed to interface with the MMF computer to form a distributed processing system capable of total experiment control of both the TACS and MMF from either computer. Also, this will allow rapid data transfers between machines to permit backup data storage.

The most accurate met data will be collected by sensors based with the data van due to their general use of 110 volt 60 Hertz power. These instruments will also be used to calibrate the remote sensors which usually are less precise in operation. Table 1 describes the sensor measurement, range and accuracy for the van associated sensors.

TABLE 1 Van Equipment

PARAMETER	RANGE	ACCURACY
Particle Size	0.3μ to 12.4mm	Varies ±0.1μ to ±100μ
Rain Rate	≥0.25mm/hr	±5% typical
Dewpoint/ Frostpoint	-75°C to 50°C	±0.2°C
Temperature	-75°C to 50°C	±0.2°C
Pressure	488 torr to 800 torr	±0.5 torr
Wind Speed	≥0.6 mph	±0.15 mph
Wind Direction	0-360°	±2°
Sun/Sky Radiation	0-2.5gmcal/ cm^2min	±5%
Visible Contrast	0-100%	±5%
Visibility (Forward Scatter Meter)	60 meters to 6 km	±5%

The wind sensor can be either a 3 axis (UVW) sensor or a standard cup anemometer and vane.

The particle size measuring probes will be mounted on the servo controlled pedestal mount. This unit will be controlled to always face in azimuth into the wind, and in elevation to point along the rain vector. While the true rain vector is drop size dependent, the orientation of the probes will be such that the size measurement will not be biased by drops not falling along the probe axis. When there is no wind, the probes measuring sizes from 0.2μ to 1600μ will be aspirated to collect samples.

The tower instruments will be deployed at the 2, 4, 8, 16 and 32 meter levels. Table 2 is a compilation of their parameters, ranges and accuracies.

TABLE 2 Tower Equipment

PARAMETER	RANGE	ACCURACY
Relative Humidity	0 to 100%	±2.0%
Temperature	-40°C to 60°C	±0.8°C
Wind Speed (3 axis)	0.5mph to 45mph	±0.2mph
Down/Up Welling Radiation	0 to 2.5 gmcal/cm^2/ min	±5%

The tower data collection will be controlled by a local data logger and transmitted to the data van on command.

There will be initially 3 propagation path remote stations, the number to be expanded as funding permits. These units will also employ a data logger, to collect the data described in Table 3.

TABLE 3 Propagation Path Equipment

PARAMETER	RANGE	ACCURACY
Rain Rate	$\geq$0.25mm/hr	±5%
Relative Humidity	$\leq$15% to 99%	±3%
Temperature	-45°C to 65°C	±0.6°C
Sun/Sky Radiation	0 to 2.5 gmcal/cm^2/min	±5%

During tests, the TACS system will be operating generally on a sample repetition rate of better than 1 Hertz. These data will be stored in the data van as well as being transmitted to the NMF for collation with the millimeter wave data. At the test location, but while mm data are not being taken, we plan to sample the general meteorological sensors once every 15 minutes to provide a synoptic record of the test site weather.

Field tests of the TACS system will begin in the summer 1979. The system is planned to be fully operational with all sensors by December 1980.

4. FUTURE PLANS

Humidity measurements from the TACS will provide an adequate determination of water vapor content for the prediction of H_2O absorption. In adverse weather conditions, particularly rain, aerosol scattering becomes the dominant attenuator. The particle size measuring probes will provide an excellent determination of rain drop size distributions, but only at one point. This distribution can be integrated to give rain rate at this point; rain gauges must be relied on to give rain rate at other points. As the atmospheric propagation path will be characteristically 1 km in length, and rain cell sizes are generally below 100m, at least 10 remote stations with rain gauges would be required to minimally sample the path. To avoid the fine spacing of sensors, ASL is investigating the use of a Path Integrating Rain Gauge in development at NOAA (Wang et al., 1977). A few such instruments could provide an average rain rate over the entire propagation path.

Traditional rain gauges also find difficulty in measuring low rainfall rates accurately. The tipping bucket variety has unacceptably long integration times for rain rates below about 5 mm/hr. Since this is an important domain for MMW systems, rain sensors sensitive to low rain rates would be a valuable addition to TACS.

Further improvements and additions to TACS will be identified as the result of field testing and data reduction requirements.

REFERENCE

Wang, T. and R. S. Lawrence, 1977: Measurements of rain parameters by optical scintillation: computer simulation of the correlation method. Appl. Optics, 16, 3176-3179.

A METEOROLOGICAL MEASUREMENT SYSTEM FOR SUPPORT OF ATMOSPHERIC PROPAGATION STUDIES

John Hines

US Army Atmospheric Sciences Laboratory
White Sands Missile Range, NM 88002

Gail Bingham

Lawrence Livermore Laboratory
Livermore, California 94550

ABSTRACT

In support of laser system design and testing, the Atmospheric Sciences Laboratory (ASL) at White Sands Missile Range (WSMR), New Mexico, has designed, developed, and implemented a system for meteorological data acquisition, transmission, and processing. The system covers optical turbulence, wind, gases, and particulates. The system has been in operation for 2 years and is currently being used to characterize the atmosphere at a high energy laser facility at WSMR.

Optical turbulence instrumentation includes point measurements with a spatial temperature probe, integrated measurements over a 180-m horizontal path with an optical scintillometer, and vertical profiles up to 600 m with an acoustic sounder. Wind speed and direction are monitored with a UVW anemometer system.

Gases currently being monitored for concentration include water vapor, ozone, total hydrocarbons, methane, nitrous oxide, and carbon dioxide. Particulate measurements include those of size distribution, mass concentration, and scattering coefficient.

Stations at each data acquisition site acquire, preprocess, convert, transmit, and/or store data. The stations are linked to a central computer through bidirectional computer-controlled data links. The central computer handles the data collection, archiving, and formatting.

1. INTRODUCTION

The ASL at WSMR has been active in the study of atmospheric effects on electro-optical (EO) and laser systems for a number of years. Adequate characterization of the atmosphere for these systems required development of a specialized field research measurement system. Such a measurement system was initially developed in 1971 and first fielded in 1972.

In 1976 the ASL was requested to provide meteorological support at the High Energy Laser System Test Facility (HELSTF) at WSMR. This support consisted of two phases: (1) development of a data base at the HELSTF and (2) direct operational support. The research system is currently providing the data base at the HELSTF. However, in deference to project requirements for atmospheric data during operational support and in realization of the maintenance-intensive nature of the research system, it was recognized that a somewhat less sophisticated, but at the same time more flexible, system would be required for direct operational support. The development of the support system would then free the research system for other field studies of laser propagation

The primary purposes of this paper are: (1) to present a general description of the research field measurement system, (2) to describe the operational system for HEL support in detail, and (3) to comment on remote sensors currently under evaluation.

2. FIELD MEASUREMENT SYSTEM

2.1 Research

2.1.1 Design

Development of the field research system began in 1971 with the requirement to provide measurements of atmospheric conditions in support of field testing of EO and laser systems. The primary atmospheric effects requiring characterization were optical turbulence, cross-wind, and extinction coefficient (due to both gases and particulates). The research system, designated the Meteorological Optical Measuring System (MOMS III), was designed initially as a mobile data collection system with limited on-board processing capability.

The MOMS III system contains three major subsystems: (1) sensors, (2) data acquisition and transmission, and (3) data processing. The primary interface between the sensors and the data processing is a data input/patch network where any individual channel or group of channels can be routed as necessary. Sensor/signal calibration-attenuation and analog monitoring are accomplished before digital conversion. Raw and/or averaged data are then

recorded on magnetic tape; semireal-time evaluation requires computer manipulation with results displayed either graphically or numerically. Since this system was designed to provide research grade measurements, it has been used extensively to assist in the evaluation of specialized crosswind and optical turbulence point and remote sensors.

2.1.2 Sensors

The MOMS III system is currently used to provide a detailed data base at the HELSTF at WSMR. The near-surface data base for the natural background at this facility encompasses optical turbulence, crosswind, gases, and particulates. The instrumentation (primarily point sensors) used to provide the measurements is summarized in table 1.

2.1.2.1 Spatial Temperature Probe. This device was developed in-house at the ASL and measures temperature difference between vertically separated (20 cm) probes. The amplitude difference is converted to an rms signal calibrated at 1.0 V DC = 1°C. Specific processing yields the optical turbulence (C_N^2) value.

2.1.2.2 Wind Speed and Direction. The R. M. Young UVW orthogonal anemometer system measures winds between 0.2 and 23 m sec^{-1} with standard low-threshold propellers. The system is calibrated through spinning a component at 1800 rpm for a calibration value of 9.6 m sec^{-1}.

2.1.2.3 Water Vapor (H_2O). The General Eastern 1200 AP Dew Point/Temperature System measures the dewpoint via the cooled mirror/platinum thermometer method. Internal system calibration is provided. One unit has been calibrated at the National Bureau of Standards (NBS) and all other units are checked and compared to the NBS calibrated units.

2.1.2.4 Ozone (O_3). Ozone is monitored by a Dasibi ultraviolet (uv) absorption type analyzer. This analyzer ratios the signal from the source through the sample gas with ozone scrubbed (to set the 100 percent level) to the signal from the source through the sample gas with ozone. All sampling lines are teflon. Calibration is by generating ozone from a stable uv source.

2.1.2.5 Total Hydrocarbons/Methane (THC/CH_4). Total hydrocarbons and methane are measured with a Horiba Flame Ionization Detector (FID) type analyzer. This instrument ionizes any carbon atoms in the sample in a flame and measures the resulting current flow. The current flow is then converted to a display in ppm as carbon. To determine the methane content of the sample, the sample is first passed through

TABLE 1. ATMOSPHERIC POINT MEASUREMENTS

Element	Unit
Optical Turbulence	Spatial temperature probe (in-house)
Crosswind	R.M. Young UVW AN/GMQ-11 or WS-101
Gases (concentration)	
H_2O	General Eastern Dewpoint 1200 AP
O_3	Dasibi 1003 AH
THC/Methane	Horiba FIA-21
N_2O	Miran II
CO_2	Horiba AIA-23
Particulates	
Size distribution	Particle Measuring Systems DAS-64 w/CSASP-100 and ASASP-300 probes
Mass concentration	GCA Mass Monitor APM-1
Scattering coefficient	Meteorology Research Inc. Integrating Nephelometer 1550-B
Gases and/or Particulate	
Absorption coefficient	CO_2 and DF laser spectrophone (in-house)

a heated catalyst which oxidizes the higher hydrocarbons. This unit is calibrated through use of sample gases in known concentrations.

2.1.2.6 Nitrous Oxide (N_2O). Nitrous oxide is monitored by a Wilks Miran II analyzer, a straight infrared absorption photometer which has a spike filter in the absorption path to isolate the N_2O band. This instrument utilizes a white cell to obtain the necessary absorption path length. The instrument is not, however, completely species specific and appears to suffer from some, as yet indeterminate, interferences. The unit is calibrated through use of specific gas concentrations.

2.1.2.7 Carbon Dioxide (CO_2). Carbon dioxide is measured with a Horiba nondispersive infrared analyzer; but this analyzer, unlike the simple absorption cell type like the MIRAN, utilizes a compensating or correlation cell and an acoustic detector to greatly increase species specificity. In addition, a spike filter is also used to isolate a particular absorption band. The unit is calibrated through use of specific gas concentrations.

2.1.2.8 Particulates. Measurements of the size distribution of atmospheric particulates are made with a Particle Measuring Systems light-scattering aerosol counter (see table 1). By coupling these measurements with realistic assumptions about the complex refractive index and the shape of the particulates, Mie theory computations may be used to estimate the particulate extinction coefficient. The instruments to measure mass concentration and scattering coefficient have not been field tested.

2.1.2.9 Spectrophone. The laser spectrophone system was developed in-house at the ASL and provides relatively direct in situ field measurements of both the gas and particulate absorption coefficients. The basic approach was to measure the gaseous absorption with one spectrophone and the gaseous plus particulate contribution with another. The electrical difference between signals is the particulate contribution.

2.1.3 Data Acquisition

The system utilizes high maintenance, medium-life sensors requiring a large resource investment of time and manpower to set up, calibrate, and operate even over relatively short test periods, i.e., 24 to 72 hours. The system must be manned continuously to provide for quick response and minimum data loss during sensor/system failure.

Optical turbulence and crosswind are measured at selected tower levels. Gases and particulates are usually measured within a few meters of the ground.

2.1.4 Data Processing

The heart of the MOM III system is a Hewlett Packard 2100S minicomputer and associated peripherals. This system processes the data from the sensors.

The turbulence, wind, and gas data are sampled at a frequency of 1 Hz. These values are arithmetically averaged over 10 sec and the 10-sec averages are recorded on magnetic tape. Subsequently, the 10-sec samples are arithmetically averaged over 15 min. Measurements of particulate size distribution are cumulative over periods of 10 to 15 min. The processed data may be graphically displayed (CRT and/or hard copy) and tabulated.

2.2 Operational

2.2.1 Design

For direct operational support, the meteorological support system depicted in figure 1 was conceived. The system, designated the High Energy Laser - Meteorological Data Analysis System (HEL-MDAS), is to be fabricated, tested, and installed at the HELSTF by the summer of 1982. Measurements are made at fixed sites (firm power) along the centerline of the HEL firing corridor and from a network of mobile sites (battery/solar power). The former measurements are made at four locations: (1) 0-m test cell complex, (2) 500-m receiver/target site, (3) 1-km site, and (4) 2-km site. A 16-m bulwark sensor platform and a 32-m tower are located at the 0-m test cell complex. A gas/aerosol van and a 32-m tower are located at the 500-m receiver/target site. A single

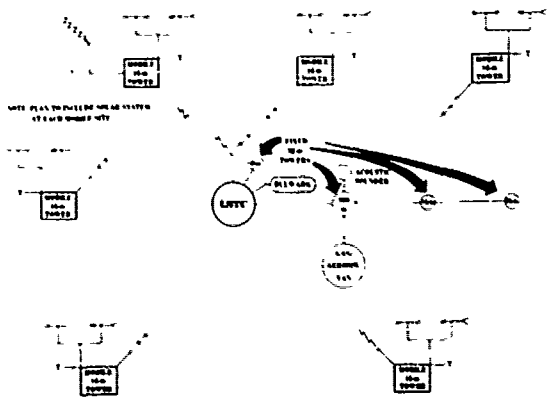

Figure 1. Conceptual HELMET support system for the HELSTF at White Sands Missile Range, New Mexico

32-m tower is located at each of the 1-km and 2-km sites. Measurements from the surrounding area are made from six portable 16-m towers. Data stations at each of the 12 sites electronically transfer information to the HEL-MDAS in the Laser Systems Test Center (LSTC). The HEL-MDAS handles the final data managing, archiving, and modeling.

2.2.2 Sensors

The overall sensor configuration is illustrated in figure 2.

2.2.2.1 Fixed 32-m Towers

a. Point Measurements. Standard sensor packages are located at the 8-, 16- and 32-m levels. The standard sensor package consists of wind speed and direction (WDS), temperature (T), barometric pressure (P) and, optimally, water vapor. Wind is measured by a cup and vane system, temperature by a shielded platinum sensor, pressure by a pressure transducer, and water vapor by an aspirated mirror-dewpoint/temperature system. Specialized sensors for gases and aerosols similar to those utilized in the research system are located at the 500-m site.

b. Path Measurements. Remote sensors for optical turbulence and crosswind are also located at certain levels.

2.2.2.2 Bulwark Sensor Platform. This site consists of a 16-m (approximately) meteorological tower rigidly affixed to the northeast face of the protective bulwark for test cell 1 at the 0-m test cell complex. Fixed point sensors located at the 16-m level provide near field effect measurements of wind speed and direction, optical turbulence, air temperature, and pressure. Additional point, integrated path, and/or path profile sensors may be incorporated in the future.

2.2.2.3 Mobile 16-m Towers. A 16-m crank-up tower with a sensor package of wind speed, wind direction, and temperature at the 8- and 16-m levels is located at each of six remote sites which are located at distances up to 8 km from the LSTC. The data are used as a basis for a 15- to 30-min predictive capability. Sensors, data acquisition, and relay link are battery/solar powered.

2.2.3 Data Acquisition, Preprocessing, and Transmission

2.2.3.1 General. Data stations are located at each data acquisition site to acquire, preprocess, convert, transmit, and/or store data. Multiple 8-channel data stations are installed at the bulwark sensor platform, at each of the four fixed 32-m towers, and at the gas/aerosol van. Single 8-channel data stations are located at each of the six mobile 16-m towers. All data stations slave to the HEL-MDAS via an appropriate bidirectional computer-controlled data link and transmit data to the HEL-MDAS on command. The fixed tower and gas/aerosol van stations communicate with the HEL-MDAS via a flexible RS-232-C compatible hardwire/fiber optic link; the link between the mobile tower stations and the HEL-MDAS is via an RS-232-C compatible radio link.

2.2.3.2 Equipment. In general, standard commercial or in-house modified standard commercial equipment is used. In either case, documentation is available. Hardware has been made as universal as possible by using the full power of the microprocessor to adapt with sensors and to allow maximum flexibility in data gathering and processing. Scaled versions of the same hardware and operation program instructions are employed for all towers and the van.

The initial controlling software has been developed to provide for flexibility in checkout and system testing. More advanced programs are developed as operational usage dictates. The remote stations are battery operated and use CMOS circuitry and power reduction techniques wherever possible. Data stations for the towers and van use identical cards with the multiplex board of the remote stations being only partially loaded, i.e., 8 channels. Figure 3 is a block diagram of the basic data station. Neither unit contains the EPROM data-storage system, but provision is made for future addition. The stations operate without the need for air conditioning, but will not have to operate in the direct sun. Each station is enclosed in a weatherproof container with some degree of air circulation.

a. Modems. The system is modem limited; i.e., it transmits data as accurately and rapidly as the link allows. Commercial modems are used for phone (hardwire) and/or fiber optic link. The radio modem was developed internally. Each remote station answers to its own Identification Address with query and reporting occurring on different frequencies.

b. Recording. The individual data collection/processor units do not currently provide any nonvolatile data storage capability. The processor systems are capable of expansion to include EPROM storage capability. In addition, an RS-232 compatible read/write cassette deck is available commercially and could be purchased for use with the system when a stand-alone mode is required.

2.2.3.3 Programming. The data collection systems are programmable at two levels.

a. Operational PROM Resident Program. The basic operational program with default values controlling channels to be scanned, gain setting, and integration time are stored in PROM and are automatically executed unless different values are set from keyboard or data link. The basic PROM resident executive program can be changed to allow the hardware to

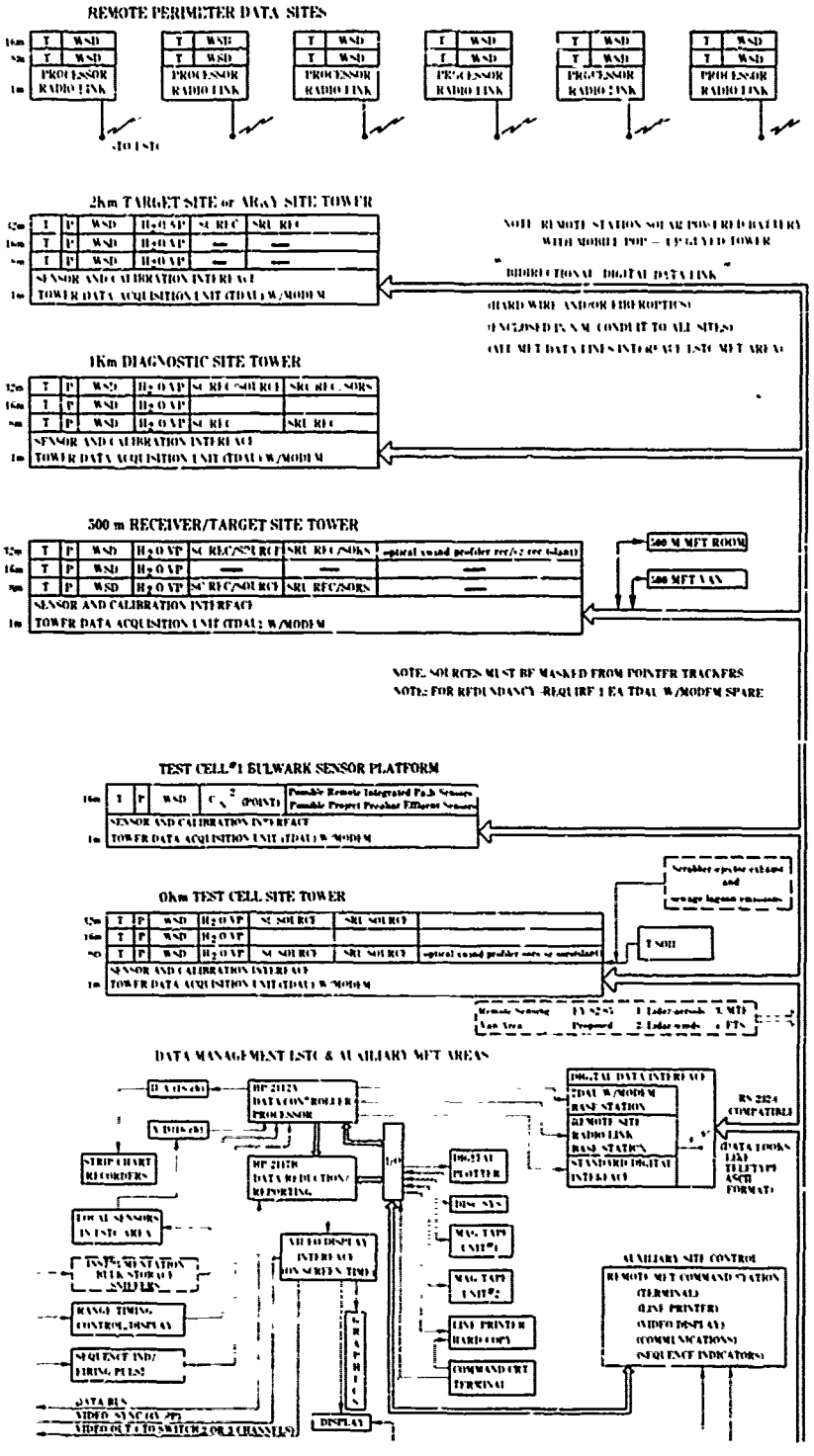

Figure 2. Block diagram of the HELMET Support System for the HELSTF at White Sands Missile Range, New Mexico.

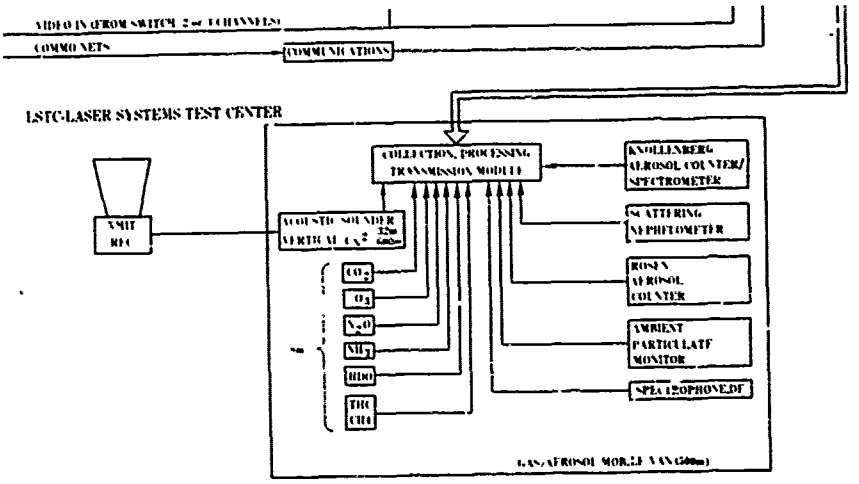

Figure 2 (cont)

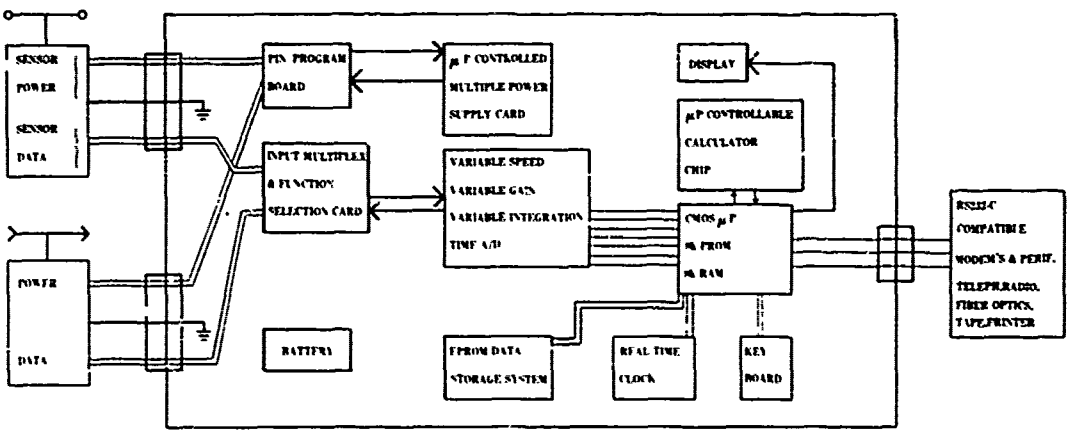

TOWER DATA ACQUISITION UNIT

ABBREVIATIONS

CH_4	METHANE
C_n^2	- OPTICAL TURBULENCE
H_2O VP	WATER VAPOR PRESSURE
IP	- INTEGRATED PATH
LSTC	LASER SYSTEMS TEST CENTER
MAG	MAGNETIC
μP	MICROPROCESSOR
NM	- NON METALLIC
P	- PRESSURE
REC	RECEIVER
SC	SCINTILLOMETER, HORIZ IP
SOURS	- SOURCE
SRU	- SATURATION RESISTANT XWIND SENSOR, HORIZ XWIND IP
SYNC	- SYNCHRONIZATION SIGNAL
TELEPH.	- TELEPHONE
T	TEMPERATURE
THC	- TOTAL HYDROCARBON
WND	- WIND SPEED/DIRECTION
XMIT	- TRANSMITTER
XWIND	- CROSSWIND

Figure 3. Block diagram of the remote station data acquisition units.

operate in any other desirable mode. Programming at this level, however, requires considerable knowledge of the system and the microprocessor language.

b. RAM Programming. Changes entered via keyboard or data link change operational program default values that control channels scanned, gain setting, integration time, average time, output processing subroutine used, clockset, and conversion factors. When the power to the unit is removed and then restored, these factors are lost and the PROM resident default values are executed.

2.2.4 Final Data Processing

The HEL-MDAS handles the long-term meteorological data storage and final data processing for HELSTF. The final data processing system is block diagrammed in figure 2. There are two Central Processing Units (CPU): The Data Controller/Processor (DCP) and the Data Reduction/Reporting (DRR). The DCP handles data collection, archiving, and formatting for efficient transfer to the information processing CPU. Model calculations and information display occupy the full capability of the DRR. The dual CPU concept also allows for backup operation (albeit at a reduced level) if one CPU should fail before or during a test.

The most accurate information is of no value if not available to the test director when needed. For long-range predictions, test personnel come to the LSTC Meteorological Center; but during the test, information is displayed in the HELSTF control rooms via video switch link. Graphical summary information is available real time on a CRT, and detailed information is available in hard copy from the line printer following a test. The CRT is divided into four graphical sections and a fifth section for flashing reverse format messages. The four graphical sections of the CRT contain:

Current meteorological conditions along anticipated beam path.

Short-term prediction of meteorological conditions along anticipated beam path.

Current trajectory and density of laser plume.

Predicted contour intensity plots of on-target irradiation calculated by using current meteorological conditions in a simple propagation code.

The fifth section is used to flag important meteorologically related events such as an approaching air mass discontinuity, plume drift into the beam path, or sensor failure.

3. REMOTE SENSORS

The basic instrumentation currently used either in the research or the operational support system is primarily point type, i.e., capable of sensing data at a single point or small volume. However, whereas point measurements may be adequate for characterizing the conditions along a fixed horizontal path near the ground, their utility for moving path scenarios (horizontal and slant) is certainly questionable. This led to the consideration, development (as required), and utilization of advanced or remote sensors. Table 2 summarizes the candidate sensors/systems. These sensors would provide either integrated path* or path profile† measurements. To date, two remote sensors, both developed by National Oceanic and Atmospheric Administration, have been evaluated and incorporated in the HEL-MDAS system: (1) optical turbulence scintillometer and (2) acoustic sounder.

The horizontal integrated path sensor for optical turbulence is an optical scintillometer. The scintillometer device uses a new optical technique to measure the refractive index structure parameter, C_N^2, over an integrated path through the use of large receiving optics and an extended incoherent transmitter. This technique avoids problems arising from the saturation of scintillation, thus allowing a C_N^2 measurement range from 10^{-16} to $10^{-12} m^{-2/3}$ over a usable path length of 150 to 500 m. The scintillometer has been validated for ranges of 3- to 32-m above ground at WSMR.

The vertical path profile sensor for optical turbulence is an acoustic sounder. The sounder utilizes an acoustic echo return technique to determine inversion levels and associated optical turbulence values derived from these inversion/temperature gradients. The sounder provides usable data to a height of 150 to 300 m with severe noise limitations at greater altitudes. The sounder has been validated for these ranges at WSMR.

The other remote sensors/systems listed in table 2 capable of providing wind and extinction coefficients due to gases and particulates are being evaluated.

*Integrated path - an averaged, but usually weighted, value measured between two points.

†Path profile - average values for each of several segments between two points.

4. SUMMARY

The ASL has developed two systems, one designed for research applications and the other for specific operational support, to study atmospheric effects on laser propagation. The research system utilizes maintenance-intensive, medium-life sensors with a large resource investment in time and manpower for development, test preparation, and real-time data quality checks. The operational system is designed to utilize low maintenance, long-life sensors with a large initial resource investment but lower operational costs.

An operational measurement system with one fixed tower site, one mobile site and a gas/aerosol van would cost $440K to duplicate at the present time:

Mobile site	$ 20K
Fixed tower site	30K
Gas/aerosol van	190K
Data transmission and processing	200K

The optical scintillometer and the acoustic sounder remote sensors are currently being used in data base evaluation. Other candidate remote sensors are being evaluated.

TABLE 2. ADVANCED SENSORS/SYSTEMS

Element	Sensor	Point (P) Integrated Path (IP) Path Profile (PP)	Horizontal (H) Vertical (V) Slant (S)
Optical Turbulence	Scintillometer	IP	(H)
	Acoustic Sounder	PP	(V)
Wind	FM-CW Radar	PP	(S)
	Pulsed Doppler Radar	PP	(V)
	Saturation Resistant Anemometer	IP	(H)
	Optical Crosswind Profiler	PP	(H)
	High Resolution Scanning Lidar	PP	(S)
	Laser Doppler Velocimeter	PP	(S)
	Tethered Aerodynamically Lifting Anemometer	P	(V)
Gases (concentration)	Fourier Transform Spectrometer	IP	(H)
	Differential Absorption Lidar	PP	(S)
Particulates	High Resolution Scanning Lidar	PP	(S)
Optical Turbulence, Crosswind, Gases, Particulates	Remotely Piloted Vehicle	PP	(S)

NEAR MILLIMETER WAVE BROADBAND ATMOSPHERIC PROPAGATION MEASUREMENTS

G. Wijntjes, N. Johnson and T. Quinn*
Block Engineering, Cambridge, MA 02139
and
R. G. Buser and R. S. Rohde
Department of the Army
Army Night Vision and Electro-Optics Laboratory
Fort Monmouth, NJ 07703

ABSTRACT

Broadband near-millimeter wave measurements to verify engineering aspects and to demonstrate radiometric performance of a Fourier transform-based propagation measurement system were performed at Block Engineering, Cambridge, MA facility.

The measurement system consisted of a rapid scan Michelson interferometer directly modulating the output of a high pressure mercury arc lamp. The modulated radiation was collimated by a 12-inch transmitter telescope and collected by a receiver consisting of an 8-inch telescope equipped with liquid helium cooled composite germanium bolometer detector. Measurements were made outdoors over a folded path. Spectral coverage was 9 to 100 cm^{-1} and all measurements have an unapodized spectral resolution better than 0.1 cm^{-1}. Data were collected on-line and processed by a Digilab Model DL-100 data system. A small amount of meteorological data were simultaneously recorded. Relative spectral transmission data having generally excellent signal to noise were obtained over distances of 12.5, 25, 50 and 100 m. These data are discussed and data handling procedures and problems encountered are reviewed. Future modifications to enhance and extend system performance are also described.

1. INTRODUCTION

To assess the potential of the near-millimeter wave spectral region for the active and passive sensing of military targets, a knowledge of atmospheric propagation under a wide variety of conditions is required. The goal of this work was to demonstrate that optical or direct detection techniques can be effective for the study of atmospheric propagation over significant pathlengths and also have adequate spectral and temporal resolution for sea level conditions. This goal has been achieved with the instrumentation described.

2. MEASUREMENT CONFIGURATION

A sketch showing the measurement configuration is given in Figure 1. It shows a transmitter consisting of a telescope and a source modulated by a rapid scan Michelson interferometer, a field mirror that can be moved to give different propagation paths, and a receiver consisting of a telescope and cryogenic detector.

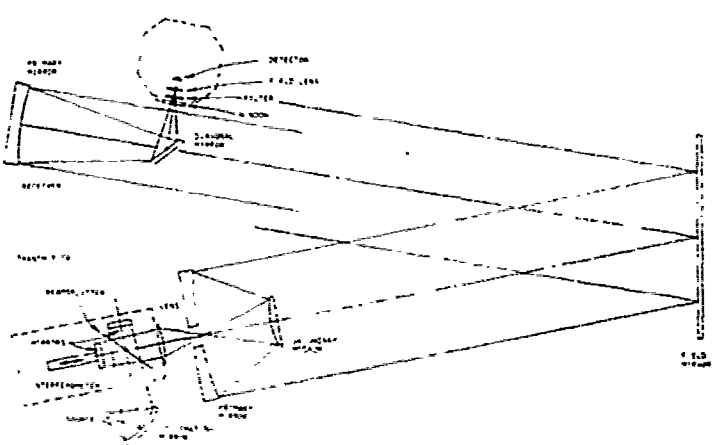

Figure 1. High Resolution Submillimeter Wave Atmospheric Transmission Measurement Configuration.

* Now at Honeywell Radiation Center, Lexington, MA.

It is probably worth reiterating the advantages of using an interferometer in this fashion. These are:

- High efficiency, since only one step of modulation is used. No additional choppers or other forms of modulation are involved.
- High source chopping frequencies, which result in complete elimination of signals due to background and foreground radiation.
- High scan rate, giving virtually total immunity to atmospheric scintillation and source instabilities.
- Broadband spectral response limited by detector and beamsplitter response.
- Low dynamic range in each high speed interferogram scan, allowing recording by simple analog recording techniques without loss of significance in typical long term data recording sequences.

A list of technical specifications is shown in Table 1.

3. RESULTS

Data presented were obtained over the period from 9 December to 15 December 1978. The data shown in Figures 2a - 2d are final measurements which resulted in relative transmission data over four different pathlengths. Measurement conditions at the time of the measurement are listed for each spectral plot. The relative data were obtained by ratioing against a "fudged" response obtained by a measurement with the transmitter and receiver head-to-head. The "fudging" involved approximate elimination of the remaining "zero range" absorption bands to avoid division by zero in ratioing. To the extent that the transmission in the window regions can be considered unity the data can be considered absolute. The effects of nonuniform wavelength response due to diffraction between a close-up measurement and a distant measurement have not been included. In general, the spectral data obtained are of high quality and show good agreement with previous data and with modeled results with several notable exceptions. Of special interest is a line at 11.9 cm^{-1} (observed by others† and sometimes erroneously assigned to CO) and a feature at 13.6 cm^{-1} (possibly due to an anomolous absorption variously assigned to dimers, clusters, and other causes).

Table 1. Measurement Study--Technical Specifications.

Spectral Range	100 to 1100 micrometer
Spectral Resolution	~0.06 cm^{-1} unapodized
Spectral Precision	<0.06 cm^{-1}
Retardation Rate	10.12 cm/second
Scan Rate (Nominal)	1.0 scan/second
Sampling Interval	40.4992 micrometers (64x)
Transmitter	
Aperture	12 inches diameter Cassegrain
Field of View	10 milliradians full angle
Source	High pressure mercury arc lamp
Source Modulator	Model 496 interferometer
Beamsplitter	Mylar film (50 micrometers)
Optical Efficiency	0.1, including beamsplitter
Receiver	
Aperture	8 inches diameter Newtonian
Field of View	7 milliradians full angle
Detector	Composite Ge:Ga bolometer (cold filtered)
NEP	5.5×10^{-12} watts/$Hz^{1/2}$
Temperature	4.2°K, liquid helium
Size	0.3 cm diameter
Optical Efficiency	0.5
Data System	
On-Line Processor	Digilab DL-100 (in-house)
Computer	NOVA 1200
Memory (Core)	32K words
Memory (Disk)	512K words
A/D Converter	12 bit, 100 kHz
Accessories	Video terminal, tape, plotter
Software	Emission package (Block)

† Gebbie, H. A. and Bohlander, R., Private Communication.

4. CONCLUSION AND SYSTEM IMPROVEMENTS

The results obtained show that optical techniques can be productive for studying properties of sea level atmospheres. In fact, the inherent broad spectral coverage in combination with a spectral resolution adequate to fully resolve the existing molecular line structure makes the optical or direct detection approach preferable over microwave techniques, not only in terms of results but also from a cost viewpoint.

System improvements that will be instituted before future measurements will be made are in two areas:

1. Improved long wavelength response. The present system has insufficient signal to noise at wavelengths longer than approximately 1 mm (9 cm^{-1}) precluding a direct comparison with data obtained by microwave radiometers. For example, typical microwave data have been obtained at 270 GHz (1.1 mm, 7.1 cm^{-1}), 150 GHz (2 mm, 5 cm^{-1}) and 94 GHz (3.2 mm, 3.13 cm^{-1}). This deficiency is not fundamental and it is expected that the response can be extended to at least 2 mm and possibly to 4 cm (30 GHz) by a number of changes. The required changes will also lead to a general improvement in signal to noise over the whole spectral region, which would allow an increase in operating range.

2. Improvements in system calibration. These will lead to a capability to give absolute transmission data in conjunction with local bulk atmospheric data, providing a complete and detailed understanding of the relationship between these parameters as well as accurate near-millimeter wave extinction coefficients.

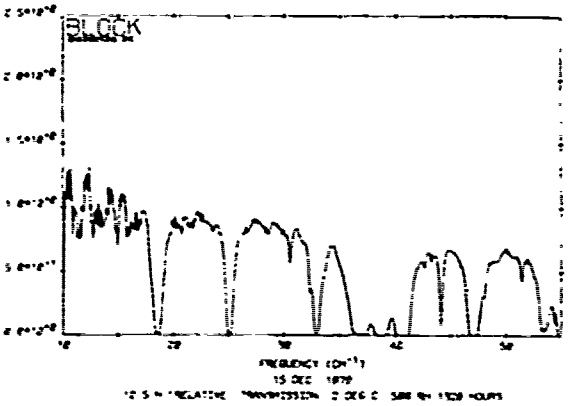

Figure 2a. 12.5 Meter Ratio. 46% R.H., 3°C.

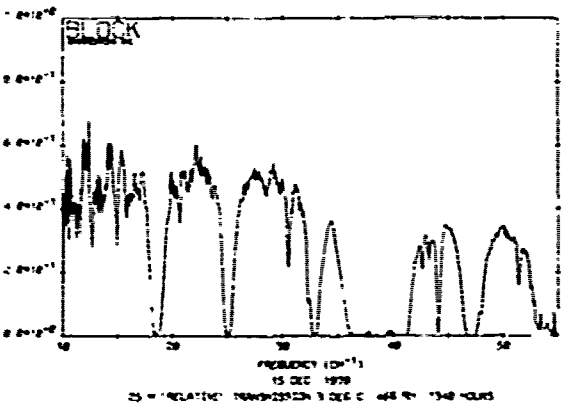

Figure 2b. 25 Meter Ratio, 46% R.H., 3°C.

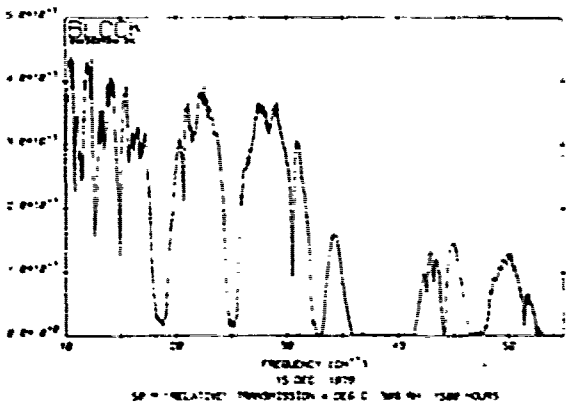

Figure 2c. 50 Meter Ratio, 39% R.H., 4°C.

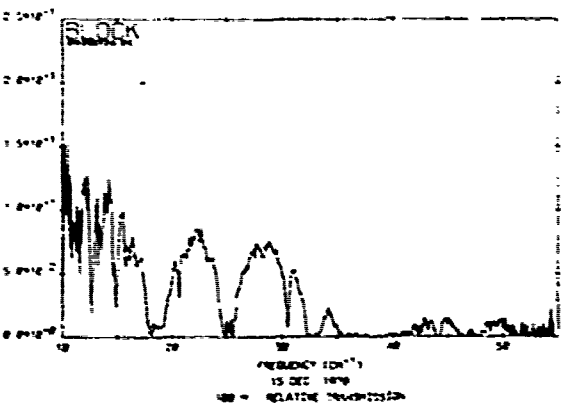

Figure 2d. 100 Meter Ratio, 37% R.H., 4°C.

ATMOSPHERIC ATTENUATION OF MILLIMETER AND SUBMILLIMETER WAVES

Vincent J. Falcone, Jr.

Air Force Geophysics Laboratory (AFSC)

Hanscom Air Force Base, MA

ABSTRACT

A computer model of atmospheric attenuation of millimeter and submillimeter waves for frequencies of 1-1000 GHz has been developed for clear, foggy, cloudy and precipitating (rain) atmospheres. The molecular absorption spectra of water vapor, oxygen, ozone, carbon monoxide, and nitrous oxide are calculated under clear conditions by an efficient computer algorithm of the AFGL HITRAN Code, named FASCODE-1. The hydrometeor attenuation of fog, clouds and rain typical of midlatitude conditions is addended to the FASCODE-1 molecular absorption model. The hydrometeor models include 4 fog models (both radiative and advective) with liquid water contents of $0.02 - 0.37\ gm^{-3}$, 8 cloud types with liquid water contents of $0.01 - 4.0\ gm^{-3}$ and rainfall rates of 10, 20, 50, 100, 150 $mmhr^{-1}$. The models can accommodate hydrometeor temperatures of -40° C. The operational computer programs of FASCODE-1 with aerosol extinction effects added permit calculation of worldwide atmospheric attenuation of microwave and millimeter radiation for an arbitrary input atmospheric model and geometry.

Manuscript not available

THE US ARMY METROLOGY AND CALIBRATION CENTER MILLIMETER AND SUBMILLIMETER WAVE PROGRAM

M. H. Sheldon

US Army Metr & Calbr Center

Redstone Arsenal, Alabama

ABSTRACT

The US Army Metrology and Calibration Center (USAMCC) of the US Army Missile Materiel Readiness Command (MIRCOM) has instituted a program of calibration standards support for millimeter and submillimeter wave activities of the Army. Our effort involves in-house programs as well as work at the National Bureau of Standards (NBS), other government agencies, and industry contractors.

We will describe our initial in-house 94-95 GHz (guided wave) calibration system which is expected to be in operation USAMCC in early 1979. Subsequent guided-wave systems will take advantage of integrated six-port network techniques evolved at lower frequencies now being applied to 94-95 GHz by efforts involving NBS and subcontractors, supported by the Calibration Coordinator Group (CCG) of the Army, Navy, and Air Force.

We will also describe our efforts to establish reliable (free-field) power/energy measurement standards for the far infrared/submillimeter spectral region (10 micrometers to about one millimeter).

Manuscript not available

DISTRIBUTION

	No. of Copies
US Army Missile Command Basic Distribution List	22
Defense Technical Information Center Cameron Station Alexandria, Virginia 22314	12
Colorado State University Department of Atmospheric Science ATTN: Prof. E. Reiter Fort Collins, Colorado 80523	1
Office of Naval Research/Code 221 ATTN: D. C. Lewis 800 N. Quincy Street Arlington, Virginia 22217	1
Pacific Missile Test Center Code 3253 ATTN: Charles Phillips Point Mugu, California 93042	1
Commander US Army Test and Evaluation Command ATTN: NBC Directorate AMSTE-EL -BAL Mr. Alfred H. Edwards Aberdeen Proving Ground, MD 21005	1 1 1 1
Commander US Army Cold Regions Research and Engineering Laboratories ATTN: Environmental Research Branch Mr. Roger H. Berger, CRREL-RP Hannover, New Hampshire 03755	1 1
Commander US Army Ballistics Research Laboratories ATTN: AMXBR-B -LA Ken Richer Aberdeen Proving Ground, Maryland 21005	1 1 1
Commander US Army Edgewood Arsenal ATTN: SMUEA-CS-O Operations Research Group Edgewood Arsenal, Maryland 21010	1 1
Commander US Army Frankford Arsenal ATTN: SMUFA-1140 Philadelphia, Pennsylvania 19137	1
Commander US Army Picatinny Arsenal ATTN: SMUPS-TV-3 Dover, New Jersey 07801	1
US Army Armament R&D Command ATTN: Murray Rosenbluth DRDAR-SCF-DD,65S Dover, New Jersey 07801	1
Optical Science Consultants ATTN: Dr. D. L. Fried P. O. Box 388 Yorba Linda, California 92686	1
Commander US Armament Development & Test Center ATTN: MAJ Francis Lomax CPT Edward H. Kelly Det 10, 2 Weather Sq. Eglin AFB, FL 32542	1 1
ADTC/XRCE ATTN: D. Dingus Eglin Air Force Base, Florida 32542	1
Commander AFATL/LMT Eglin Air Force Base, Florida 32544	1
Commander US Army Dugway Proving Ground ATTN: Meteorology Division Dugway, Utah 84022	1
Commander US Army Artillery Combat Developments Agency Fort Sill, Oklahoma 73504	1
Commander US Army Artillery & Missile School ATTN: Target Acquisition Department Fort Sill, Oklahoma 73504	1
Commander US Army Communications-Electronics Combat Development Agency Fort Huachuca, Arizona 85613	1
Commander Desert Test Center Fort Douglas, Utah 84113	1
Commander US Army CBR School Micrometeorological Section Fort McClellan, Alabama 36205	1
Commander USAF Air Weather Service (MATS) ATTN: Mr. Oscar Richard Ms. Hilda Snelling MAJ Kit G. Cottrell/AWS/DNP CPT William S. Weaving(7WW/LN) Scott Air Force Base, Illinois 62225	1 1 1 1

	No. of Copies
Commander US Army Combined Arms Combat Development Activity Fort Leavenworth, Kansas 66027	1
Chief of Naval Operations ATTN: Code 427 Department of the Navy Washington, DC 20350	1
Chief US Weather Bureau ATTN: Librarian Washington, DC 20235	1
Commander US Army Armament Command Rock Island, Illinois 61202	1
Commander US Army Foreign Science & Technology Center Federal Office Building 220 7th Street, NE Charlottesville, Virginia 22901	1
Commander US Army Training & Doctrine Command ATTN: ATORI Fort Monroe, Virginia 23351	1
Director Ballistic Missile Defense Advanced Technology Center ATTN: ATC-D ATC-O ATC-R ATC-T P. O. Box 1500 Huntsville, Alabama 35807	1 1 1 1
Commander US Naval Air Systems Command Washington, DC 20360	1
Chief of Naval Research Department of the Navy Washington, DC 20360	1
Commander US Naval Air Development Center Warminster, Pennsylvania 18974	1
Commander US Naval Electronics Lab Center San Diego, California 92152	1
Commander US Naval Surface Weapons Center Dahlgran, Virginia 22448	1
US Army Materiel Systems Analysis Activity ATTN: DRXSY-MP Aberdeen Proving Ground, MD 21005	1

	No. of Copies
ElectroScience Laboratory Department of Electrical Engineering The Ohio State University ATTN: Dr. Ronald K. Long Prof. Daniel B. Hodge Prof. Curt A. Levis 1320 Kinnear Road Columbus, Ohio 43212	1 1 1
Commander US Air Force, AFOSR/NP ATTN: LTC Gordon Wepfer Bolling Air Force Base Washington, DC 20332	1
Naval Surface Weapons Center ATTN: Mary Tobin WR42 White Oak, Maryland 20910	1
Pacific-Sierra Research Corporation ATTEN: Alan R. Shapiro Vice President 1456 Cloverfield Boulevard Santa Monica, California 90404	1
The Aerospace Corporation ATTN: Dr. D. T. Hodges, Jr. Mr. C. M. Randall Mr. Eugene Epstein Box 92957 2350 East El Segunda Boulevard Los Angeles, California 90009	1 1 1
Headquarters Department of the Army ATTN: DAEN-RDM/Dr. F. de Percin Washington, DC 20314	1
Headquarters Department of the Army Directorate of Army Research ATTN: DAMA-ARZ DAMA-ARZ-D Dr. Frank D. Verderame Washington, DC 20310	2 1 1
Dr. Robert J. Renard Department of Meteorology Naval Postgraduate School Monterey, California 93940	1
Dr. John J. DeLuisi NOAA/ERL-ARL' Boulder, Colorado 80303	1
Director US Army Night Vision Laboratory ATTN: Mr. John Johnson Mr. Joseph R. Moulton Dr. Richard R. Shurtz Dr. C. Ward Trussell, Jr. Fort Belvoir, Virginia 22060	1 1 1 1

	No. of Copies
Science and Technology Division Institute for Defense Analyses ATTN: Dr. Vincent J. Corcoran Dr. Robert E. Roberts Dr. Lucien M. Biberman 400 Army-Navy Drive Arlington, Virginia 22202	1 1 1
Director Naval Research Laboratory ATTN: Code 5300, Radar Division Code 5370, Radar Geophysics Br. Code 5460, Electromagnetic Propagation Br. Washington, DC 20390	1 1 1
Florida State University ATTN: Prof. T. A. Gleeson Tallahassee, Florida 32306	1
Mr. Darrell E. Burch Aeronutronic Division Philco-Ford Corporation Ford Road Newport Beach, California 92663	1
Deputy for Science and Technology Office, Director of Defense Research and Engineering ATTN: Military Assistant for Environmental Sciences Pentagon, Washington, DC 20301	1
LTC Robert E. Johnson TARDCC ATTN: ATFE-LO-MI Bldg 4505, Rm B-200 Redstone Arsenal, AL 35809	1
Mr. Ronald J. Nelson Science Applications, Inc. E/O Division, Albuquerque Operations Suite 216 2201 San Pedro N.E. Albuquerque, New Mexico 87110	1
Commander USA OTEA ATTN: CSTE-STS-I F. G. Lee 5600 Columbia Pk Falls Church, VA 22041	1
Dr. Gail Bingham Lawrence Livermore Laboratory Livermore, CA 94550	1
Mr. Don Hoock Physical Sciences Laboratory New Mexico State University Las Cruces, NM 88001	1
Control Data Corporation Research Division ATTN: Dr. Belmont Minneapolis, Minnesota 55440	1

	No. of Copies
Georgia Institute of Technology Engineering Experiment Station ATTN: Mr. Wayne Penn Mr. J. J. Gallagher Dr. E. K. Reedy Dr. R. A. Bohlander Dr. James Wiltse Mr. J. Hank Rainwater Dr. R. D. Hayes Dr. Robert McMillan Mr. Edward Martin Mr. J. L. Eaves Mr. Lucien C. Bomar Mr. R. C. Rogers Mr. P. B. Reinhart 225 North Avenue Atlanta, GA 30332	1 1 1 1 1 1 1 1 1 1 1 1 1 1
Commander/Director Corps of Engineers Waterways Experiment Station ATTN: WESEN/Mr. Jerry Lundien P. O. Box 631 Vicksburg, Mississippi 39180	1
Director Atmospheric Sciences Program National Sciences Foundation Washington, DC 20550	1
Director Bureau of Research and Development Federal Aviation Agency Washington, DC 20553	1
Commander US Army Aviation R&D Command ATTN: Dr. Gene Marner P. O. Box 209 12th and Spruce Streets St. Louis, Missouri 63166	1
Director US Army Air Mobility Research and Development Laboratory Ames Research Center Moffett Field, California 94035	1
Director of Meteorological Systems Office of Applications (FM) National Aeronautics & Space Admin. Washington, DC 20546	1
Environmental Research Insitute of Michigan Infrared and Optics Division ATTN: Anthony J. LaRocca Robert L. Spellicy P. O. Box 618 Ann Arbor, Michigan 48107	1 1
Kaman Nuclear ATTN: Lora Guy, Assistant Librarian Garden of the Gods Road Colorado Springs, Colorado 80907	1

	No. of Copies
Lockheed Missiles and Space Company Organization 62-41, Bldg. 562 ATTN: Dr. David M. Theobold Mr. Jerry Hopponen P. O. Box 504 Sunnyvale, CA 94086	1 1
Lockheed-California Company Department 72-25 ATTN: Dr. L. Baer Burbank, CA 91503	1
Massachusetts Institute of Technology ATTN: Department of Meteorology Cambridge, Massachusetts 02139	1
Meteorological & Geoastrophysical Abstract Editorial Office P. O. Box 1736 Washington, DC 20013	1
The Rand Corporation ATTN: Dr. S. J. Dudzinsky, Jr. Dr. D. Deirmendjian 1700 Main Street Santa Monica, CA 90406	1 1
Commander Center for Naval Analyses ATTN: Document Control 1401 Wilson Boulevard Arlington, VA 22209	1
Martin Company ATTN: Engineering Library Mail J1-398 Baltimore, Maryland 21203	1
National Bureau of Standards Boulder Laboratories ATTN: Library Boulder, Colorado 80302	1
Navy Representative National Climatic Center Arcade Building Asheville, North Carolina 28801	1 1
National Oceanic & Atmospheric Admin. National Climatic Center ATTN: Technical Library Arcade Building Asheville, North Carolina 28801	1
Director Defense Advanced Research Projects Agency 1400 Wilson Boulevard Arlington, Virginia 22209	1
Honeywell, Inc. Systems and Research Division ATTN: Dr. Paul Kruse Minneapolis, Minnesota 55413	1

	No. of Copies
Commander ARRADCOM ATTN: DRDAR-SCF-IM Mr. J. Heberley Dover, New Jersey 07801	1 1
Science Applications, Inc. ATTN: N. E. Feldman 101 Continental Blvd. Suite 310 El Segundo, CA 90245	1
Raytheon Company ATTN: A. V. Jelalian 528 Boston Post Road Sudbury, Massachusetts 01776	1
National Aeonautics & Space Admin. Marshall Space Flight Center ATTN: R-AERO-Y Marshall Space Flight Center, Alabama 35812	1
National Center for Atmospheric Research ATTN: Library Boulder, Colorado 80302	1
Director of Defense Research and Engineering Engineering Technology ATTN: Mr. L. Weisberg Washington, DC 20301	1 1
Office of Chief Communications-Electronics, DA ATTN: Electronics Systems Directorate Washington, DC 20315	1
Office, Assistance Chief of Staff for Intelligence, DA ATTN: ACSI-DSRSI Washington, DC 20310	1
Office of US Naval Weather Service US Naval Air Station Washington, DC 20390	1
Office, Assistant Secretary of Defense Research & Engineering ATTN: Technical Library Washington, DC 20301	1
Pennsylvania State University ATTN: Department of Meteorology University Park, Pennsylvania 16802	1
University of Washington ATTN: Department of Meteorology Seattle, Washington 98105	1
University of Chicago Department of Meteorology Chicago, Illinois 60637	1

	No. of Copies
Commander US Air Force Avionics Laboratory ATTN: MAJ Winston Crandall, ASD/W	1
CPT J. D. Pryce, AFAL/WE	1
Dr. B. L. Sowers, AFAL/RWI	1
Mr. Roger T. Winn, AFAL/WE	1
CPT William C. Smith, AFAL/RWI-3(WE)	1
Mr. Raymond Wasky	1
Mr. D. Rees	1
Wright Patterson Air Force Base Ohio 45433	
DA, ODCSLOG US Army Logistics Evaluation Agency New Cumberland Army Depot New Cumberland, PA 17070	1
University of Wisconsin ATTN: Prof. Weinman	1
Prof. E. Wahl Madison, Wisconsin 53706	1
US Army Engineering Topographic Laboratories Earth Sciences Division ATTN: ETL-GS-ES, Dr. W. B. Brierly Fort Belvoir, Virginia 22060	1
Commander US Army Research Office ATTN: Dr. R. Lontz	1
Dr. Frank DeLucia	1
Dr. James Mink	1
Dr. Hermann Robl P. O. Box 12211 Research Triangle Park, NC 27709	1
US Army Research & Standardization Group (Europe) ATTN: DRXSN-E-RX, Dr. A. K. Nedol Box 65, FPO New York 90510	2
US Army Materiel Development and Readiness Command ATTN: Dr. Gordon Bushy	1
Dr. James Bender	1
Dr. Edward Sedlak 5001 Eisenhower Avenue Alexandria, Virginia 22333	1
Commander US Army Tank Automotive R&D Command ATTN: DRDTA-RCAF	1
RCAF, Mr. Eugene Spratke Warren, Michigan 48090	1
Commander USA Mobility Equipment R&D Command ATTN: DRDME-ZK, Dr. Karl H. Steinbach Fort Belvoir, Virginia 22060	1

	No. of Copies
Commander US Army Harry Diamond Laboratories ATTN: Dr. Stan Kulpa	1
Dr. Joseph Nemarich	1
Mr. Edward P. Dudley	1
Mr. William H. Pepper	1
Mr. Michael S. Patterson	1
Mr. Z. Sztankay 2800 Powder Mill Road Adelphi, Maryland 20783	1
US Department of Commerce Institute for Telecommunication Science ATTN: Dr. Hans J. Liebe	1
Dr. M. C. Thompson, Jr. Boulder, Colorado 80303	1
HQ, AFSC/WER ATTN: LTC S. Pilipowskyj Andrews AF Base, MD 20331	1
Mr. Larry Weaver Hughes Aircraft Company Canoga Park, CA 91303	1
Mr. Frank Smith Norden Systems Norwalk, Connecticut 06856	1
Mr. Soonsung Hong MIT Lincoln Laboratory P. O. Box 73 Lexington, MA 02173	1
Dr. Kenneth P. Bochis The Analytic Science Corp. Six Jacob Way Reading, MA 01867	1
Dr. Apostle Cardiasmenos ALPHA Industries, Inc. TRG Division 20 Sylvan Road Woburn, MA 01801	1
Dr. Robert Crane Deputy Div. Mgr. Earth Resources & Atmospheric Physics Environmental Research & Technology, Inc. 696 Virginia Road Concord, MA 01742	1
Mr. Joseph Egger Technology Deputy Engr. Sys. Branch US Army Combat Development Experimentation Command Ft. Hunter-Liggett, CA 93928	1
Commander HQ Rome Air Development Center (AFSC) ATTN: Mr. Larry Telford	1
Mr. Edward E. Altshuler Hanscom Air Force Base, MA 01731	1

	No. of Copies
Mr. David Stringfellow Systems Technology Department Calspan Corporation Advanced Technology Center P. O. Box 400 Buffalo, New York 14225	1
SRC, Appleton Laboratory ATTN: Dr. Christopher Gibbins Mr. R. J. Emery Mr. D. T. Llewellyn-Jones Ditton Park, Slough, Berks UK	1 1 1
Mr. James H. Thompson, Sr. Scientist General Electric-TEMPO 816 State Street Santa Barbara, CA 93101	1
Dr. H. A. Gebbie Imperial College of Science and Technology University of London London, England	1
Dr. A. W. Straiton College of Engineering University of Texas at Austin Austin, Texas 78712	1
Keweenee Research Center Michigan Technological University ATTN: Mr. Gary Gimmestad Mr. S. M. Lee Houghton, MI 49931	1 1
Mr. Isaac Kliger Raytheon Company Bedford, MA 01730	1
Mr. A. Mintzer Raytheon Company Wayland, MA 01778	1
Block Engineering Corporation ATTN: Mr. G. Wijntjes Mr. N. Johnson Mr. T. Quinn 19 Blackstone St. Cambridge, MA 02139	1 1 1
Lockheed Corporation ATTN: Mr. Ray Baker Dr. Faison Gibson Mr. Charles Hayes Mr. Owen Hofer Mr. Bill Montgomery Mr. Larry Pinkley Mr. Francis Wang 4800 Bradford Dr., NW Huntsville, AL 35807	1 1 1 1 1 1 1
Air Force Geophysics Laboratories ATTN: OPI, Mr. John Selby Mr. V. Falcone OPA, Dr. R. Penn CRXL LKI, Mr. Lund Mr Gringorten Mr. Lenhard Mr. Grantham LYS, Mr. R. S. Hawkins LYW, Mrs. R. M. Dyer Mr. R. J. Donaldson LUP, Mr. B. A. Kunkel Hanscom AFB, Massachusetts 01731	1 1 1 1 1 1 1 1 1 1 1 1
Commander US Army Electronics R&D Command ATTN: DRSEL-RD-SM, Mr. M. Lowenthal DELET-MJ, Dr. H. Jacobs Dr. Lothar Wandinger DELCS-TA, Mr. Allan Tarbell DELCS-I-M, Dr. B. Gelernter DELCT, Dr. R. Buser Mr. R. S. Rohde Fort Monmouth, NJ 07703	1 1 1 1 1 1 1
Commander Naval Weapsons Center ATTN: Code 3173, Dr. Alexis Shlanta Mr. Robert Moore China Lake, CA 93555	1 1
Commander Atmospheric Sciences Laboratory US Army Electronics Command ATTN: DELAS-AS, Dr. E. H. Holt -DD, Mr. Rachele Mr. James D. Lindberg -EO-ME, Dr. D. R. Brown Dr. Donald Snider -AS-T, Mr. Robert Rubio -AS-P, Mr. John Hines -AS-P, Dr. Kenneth White Mr. H. Kobayashi -EO-S, Dr. Richard Gomez Dr. Louis Duncan -BE, Mr. Fred Horning Sci Appl Inc., Dr. Brent L. Bean White Sands Missile Range New Mexico 88002	1 1 1 1 1 1 1 1 1 1 1 1 1
IIT Research Institute ATTN: GACIAC, Mr. Smoots 10 West 35th Street Chicago, IL 60616	1
Dr. Martin Vogel DFVLR 551 8031 Oberpfaffenhofen Federal Republic of Germany	1

	No. of Copies
Dr. Albert W. Adey Dept. of Communications 300 Slater St. Ottawa, Ontario K1A 0C8 Canada	1
LTC Kervizic Direction des Recherches Etudes et Techniques 26 Boulevard Victor 75998 Paris Armees France	1
Dr. Jan Snieder Physics Laboratory-TNO Oude Waalsdorpeweg 63 The Hague The Netherlands	1
Dr. Logan Royal Signals and Radar Establishment Malvern, Worcs WR 14 3PS United Kingdom	1
Science Applications, Inc. ATTN: Dale Divis Michelle Farr Harold Jeffreys Suite 800 2109 Clinton Ave., W Huntsville, AL 35805	1 1 1
Mr. Alfred L. Bogush New Technology, Inc. 4811 Bradford Blvd., NW Huntsville, AL 35807	1
Mr. Larry Weaver Hughes Aircraft 3322 Memorial Parkway, SW Huntsville, AL 35801	1
Mr. Doug Kennedy VARIAN 500 Wynn Dr., NW Huntsville, AL 35805	1
Mr. Glenn Weathers M&S Computing Inc. Highway 20, W. Madison 35758	1
Mr. J. F. Osmundsen 818 Kerr Ave., Apt. 201 Urbana, IL 61801	1
Mr. Stephen L. Johnston 4015 Devon, SE Huntsville, AL 35801	1
Dr. J. G. Castle, Jr. 4018 Heatherhill Rd., SE Huntsville, AL 35802	1
DRCPM-LD ATTN: COL J. H. Reeves	1
DRCPM-VI ATTN: Mr. Herman R. Oswell	1
DRSMI-LP ATTN: Mr. Voigt	1
BMDSCOM ATTN: Mr. Henry Cummings	1
DRSMI-M ATTN: Mr. Louie Bowling Mr. Jim Brown Mr. M. H. Shelton Mr. James Christian	1 1 1 1
DRSMI-R ATTN: Dr. Kobler	1
DRSMI-RD ATTN: Dr. McCorkle Mr. Sullivan Mr. Conrad Mr. F. M. Belrose Mr. John Sinapole	1 1 1 1 1
DRSMI-RG ATTN: Mr. Huff	1
DRSMI-RK ATTN: Dr. Wharton Mr. Duerr Mr. Lewis Mr. Gregg Mr. Northrop Mr. Dreitzler Mr. Garrett Mr. W. B. Thomas Mr. L. B. Thorn	1 1 1 1 1 1 1 1 1
DRSMI-E ATTN: Mr. W. Y. Bishop Mr. Charles M. Crocker Mr. A. W. Presson Mr. Randolph Priddy Mr. Donald Roberson Mr. James M. Taylor Mr. Clifford Walker Mr. C. L. Northrop	1 1 1 1 1 1 1 1
DRSMI-RE ATTN: Mr. Lindberg Mr. W. Todd Mr. Robert Haraway Mr. William Pittman Mr. H. F. Anderson Mr. T. A. Barley Mr. C. H. Cash Mr. D. Crosswhite Mr. A. H. Green, Jr. Mr. Tony Hodgens Mr. H. Holt Mr. G. Rast 1LT Thomas Tullia Mr. J. Lomis Mr. Christopher Kulas Mr. Gene Widenhofer Mr. Lloyd Root	1 1 1 1 1 1 1 1 1 1 1 1 1 1 1 1

	No. of Copies
DRSMI-C	
ATTN: -OT, Mr. W. Blackledge	1
-OT, Mr. T. E. Dilworth, Jr.	1
-OD, Mr. R. H. Evans	1
-OG, Dr. Bruce Fowler	1
Mr. Kenneth Evans	1
Mr. J. A. Stanford	1
DRSMI-UR	
ATTN: Mr. Melvin L. Bartlett	1
DRCPM-MD-T	
ATTN: Mr. W. E. Wood	1
DRSMI-RR	
ATTN: Dr. Hartman	1
Dr. Bennett	1
-RRA, Dr. Essenwanger	25
Dr. Stewart	25
Mr. Dudel	1
Ms. Boyd	1
-RRD, Dr. J. A. Merritt	1
Dr. H. C. Meyer	1
Dr. C. M. Bowden	1
Dr. D. W. Howgate	1
RRO, Dr. J. D. Stettler	1
Dr. R. L. Morgan	1
Dr. C. R. Christensen	1
Dr. G. A. Tanton	1
Dr. W. L. Gamble	1
DRSMI-RH	
ATTN: COL DeLeuil	1
Dr. Julius Lilly	1
Mr. John Ehrlich	1
Commander/Director	
Office, Missile Electronic Warfare	
ATTN: DELEW-M-STO, Mr. Larsen	1
-TAS, Mr. R. Stocklos	1
, Mr. R. Lee	1
White Sands Missile Range	
New Mexico 88002	
The Boeing Aerospace Company	
ATTN: Raymond M. Wells	1
M/S 47-25 ORGN 2-2702	
P. O. Box 3999	
Seattle, Washington 98124	
National Center for Atmospheric Research	
ATTN: E. M. Patterson	1
Boulder, Colorado 80303	
Mr. T. C. Tarbox	
Bell Aerospace-TEXTRON	1
5719 Tannerhill Circle	
Huntsville, AL 35802	
Dr. Juengen H. Richter	
Code 532 (T)	1
NOSC	
San Diego, CA 92152	

	No. of Copies
Mr. Joseph Matava	
Electronic Warfare Laboratory, ERADCOM	
ATTN: DELEW-E	1
Ft. Monmouth, NJ 07703	
DRSMI-RPR	3
DRSMI-RPT (Record Copy)	1
(Reference Copy)	1